Yukon

Yukon
Exploration & Geology
2020

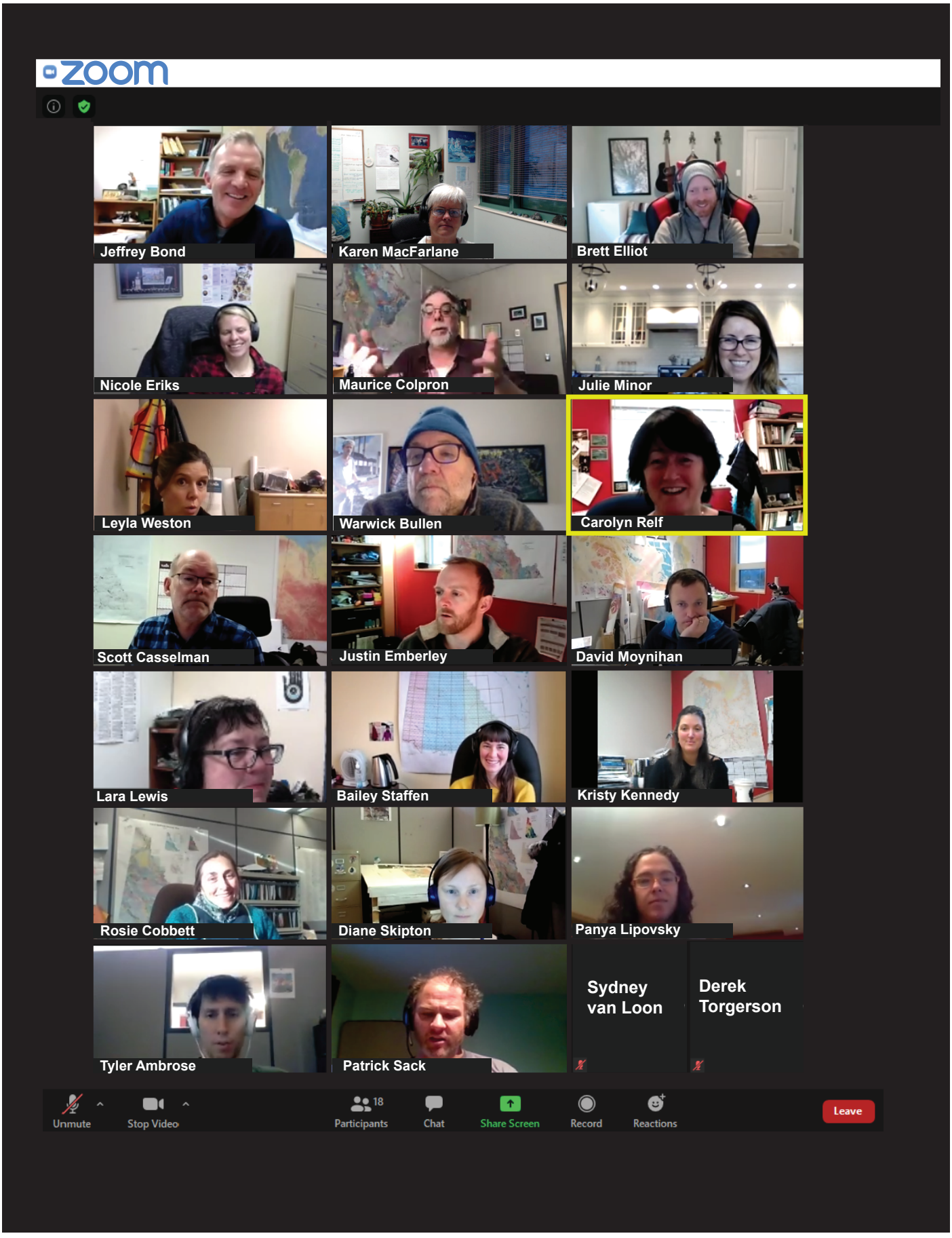
zoom
Jeffrey Bond
Karen MacFarlane
Brett Elliot
Nicole Eriks
Maurice Colpron
Julie Minor
Leyla Weston
Warwick Bullen
Carolyn Relf
Scott Casselman
Justin Emberley
David Moynihan
Lara Lewis
Bailey Staffen
Kristy Kennedy
Rosie Cobbett
Diane Skipton
Panya Lipovsky
Tyler Ambrose
Patrick Sack
Sydney van Loon
Derek Torgerson
Unmute
Stop Video
18
Participants
Chat
Share Screen
Record
Reactions
Leave

Yukon

Yukon Exploration & Geology 2020

Edited by
K.E. MacFarlane

Yukon Geological Survey
Energy, Mines and Resources
Government of Yukon

Published under the authority of the Department of Energy, Mines and Resources, Government of Yukon, https://yukon.ca.

Printed in Whitehorse, Yukon, 2021.

Publié avec l'autorisation du Ministères de l'Énergie, des Mines et des Ressources du gouvernement du Yukon, https://yukon.ca.

Imprimé à Whitehorse (Yukon) en 2021.

ISSN 1718-8326 (online version)

Yukon Geological Survey publications can be obtained from:
Yukon Geological Survey
102-300 Main Street
Box 2703 (K-102)
Whitehorse, Yukon, Canada Y1A 2C6

email geology@yukon.ca

Yukon Geological Survey website https://yukon.ca/en/science-and-natural-resources/geology.

In referring to this publication, please use the following citation:
Yukon Geological Survey, 2021. Yukon Exploration and Geology 2020, K.E. MacFarlane (ed.), 2021. Yukon Geological Survey, 176 p.

Front cover photograph: YGS staff atop an outcrop of Jurassic conglomerate; Bonneville Lakes in the background.

Preface

Yukon Exploration and Geology (YEG) papers and the Yukon Exploration and Geology Overview are two of the main publications of the Yukon Geological Survey (Energy, Mines and Resources, Government of Yukon). Individual YEG papers, with colour images, are available in digital format and can be downloaded from our website. The YEG Overview is available in digital format and in a limited colour print run.

YEG 2020 contains up-to-date information on mining and mineral exploration activity, studies by industry, and results of recent geological field studies. Information in this volume comes from prospectors, exploration and government geologists, mining companies, and students, all of whom are willing to contribute to public geoscience for the benefit of the scientific community, general public and mineral industries of Yukon. Their work is appreciated.

Despite the uncertainties of 2020, my colleagues at the Yukon Geological Survey continued to provide geoscience information to support informed decision making. For those who authored or reviewed YEG papers this year (and in some instances both), thank you. A special thank you to Nicole Eriks for being an extra set of eyes...

Input or suggestions that you may have to improve future YEG publications are welcomed. Please contact me at (867) 667-8519, or by email at karen.macfarlane@yukon.ca.

Karen MacFarlane

Yukon Exploration and Geology 2020

Table of Contents

Structural geology of the eastern Richardson Mountains, Yukon and Northwest Territories: Some field observations and a note of caution for palinspastic reconstructions

Nicolas Pinet
Natural Resources Canada, Geological Survey of Canada

Pinet, N., 2021. Structural geology of the eastern Richardson Mountains, Yukon and Northwest Territories: Some field observations and a note of caution for palinspastic reconstructions. *In:* Yukon Exploration and Geology 2020, K.E. MacFarlane (ed.), Yukon Geological Survey, p. 1–18.

Abstract

The Richardson anticlinorium is a major tectonic feature marking the eastern limit of the Cordilleran orogen in northern Yukon and Northwest Territories. Limited structural observations on the eastern flank of the Richardson anticlinorium indicate that the strain intensity increases significantly close to major faults that are associated with deformation zones tens to hundreds of metres wide. A predominant dextral sense of motion is documented for several major faults belonging to the Richardson fault array. However, second-order features exhibit highly variable kinematics. In several cases, strike-slip faults cut shallower dipping faults and follow steep bedding planes, suggesting that dextral motion occurred in a previously deformed and tilted sedimentary succession. The amount of displacement along the Richardson fault array is poorly constrained. Further investigation is warranted as potential large displacements may bear significant consequences on palinspastic reconstructions.

* nicolas.pinet@canada.ca

Introduction

Paleogeographic reconstructions need an appraisal of post-sedimentation deformation as major faults may have juxtaposed rock units originating from different sedimentary environments. However, early studies in frontier sedimentary basins generally focused on stratigraphic and sedimentologic analyses in order to build a regional-scale geological framework. At the reconnaissance stage, tectonic features are often implicitly considered as second-order importance for regional-scale basin reconstructions.

In 1961, the Geological Survey of Canada (GSC) initiated a large-scale geological mapping study, Operation Porcupine, that has described a thick Proterozoic to Tertiary sedimentary succession in northern Yukon and Northwest Territories. Facies changes in strata have been documented for both Paleozoic (Norford, 1996; Morrow, 1999) and Mesozoic (Dixon, 1996). These facies changes reflect paleogeographic features such as uplifts and troughs extending for tens to hundreds kilometres.

The aim of this paper is to report structural observations from the eastern Richardson Mountains. Despite uncertain offset along major structures, it is argued that displacement along the Richardson fault array should be kept in mind for palinspastic reconstructions.

Geological Framework

The Richardson Mountains mark the eastern limit of the Cordilleran orogen (Fig. 1), and corresponds to the north-northwest trending Richardson anticlinorium, which is up to 75 km in width. The Richardson anticlinorium is a north-plunging structure that includes deformed Proterozoic to Carboniferous rock units. It is bounded by generally flat to shallow-dipping strata of the Peel Plateau and Eagle Plain to the east and west of the anticlinorium respectively. To the south, the Richardson Mountains terminate at the east-west trending Ogilvie, Wernecke and Mackenzie mountains.

The sedimentary succession preserved in the Richardson anticlinorium consists of Cambrian to Early Devonian sediments deposited in water deeper than surrounding areas. This led several authors to interpret that the Paleozoic rocks of the Richardson Mountains were deposited in an elongated basin, approximately perpendicular to the northern continental margin (Richardson trough or aulacogen; Norris and Yorath, 1981; Pugh, 1983; Fraser and Hutchison, 2017; Strauss *et al.*, 2020).

Tectonic slivers of Proterozoic rocks constitute the oldest unit of the Richardson anticlinorium. In the central part the anticlinorium, the base of the exposed Paleozoic succession consists of a limestone unit (Ittlyd Formation) and a clastic-dominated assemblage (Slats Creek Formation). Predominantly fine-grained carbonate and siliciclastic strata of the Road River Group overlie this assemblage and include four recently formalized formations: from base up are the Cronin, Mount Hare, Tetlit and Vittrekwa formations (Strauss *et al.*, 2020). The black siliceous shale of the Canol Formation overlies the Road River Group as well as coeval rocks found in the Eagle Plain and Peel Plateau, and represents a regional marker interval (Fraser and Hutchison, 2017). The Canol Formation is conformably overlain by the Upper Devonian Imperial Formation, a thick sequence of predominantly mudstone and shale in its basal section, with more sandstone higher up in the succession (Allen, 2009; Fraser and Hutchison, 2017). On both sides of the anticlinorium, lower and middle Paleozoic strata are overlain by, or in fault contact with, upper Paleozoic and Mesozoic unconformity bounded rock assemblages.

The Richardson anticlinorium is cut by the Richardson fault array (RFA; Norris and Hopkins, 1977), a series of north-trending faults that extend from the Mackenzie Mountains to the Arctic Ocean. To the north, the RFA probably continues across the continental margin to connect with the Taglu and/or Eskimo Lakes fault zones (Lane, 1998), extending its total length to approximately 1000 km (Norris, 1996).

The Trevor and Deception faults, both part of the Richardson fault array, bound the Richardson anticlinorium to the east and west, respectively (Fig. 2). The RFA is seismically the most active structure in northern Yukon and Northwest Territories (Mazotti and Hyndman, 2002).

Kinematic interpretation of the RFA varies significantly in the literature. Norris and Yorath (1981) consider displacement by the RFA as dextral, while Eisbacher (1983) interprets it as sinistral. Alternatively, Norris (1985) indicates the RFA is experiencing mainly differential vertical motion during the early to mid-Tertiary, while Cecile (1984) considers a relatively minor (10 km or less) strike-slip motion.

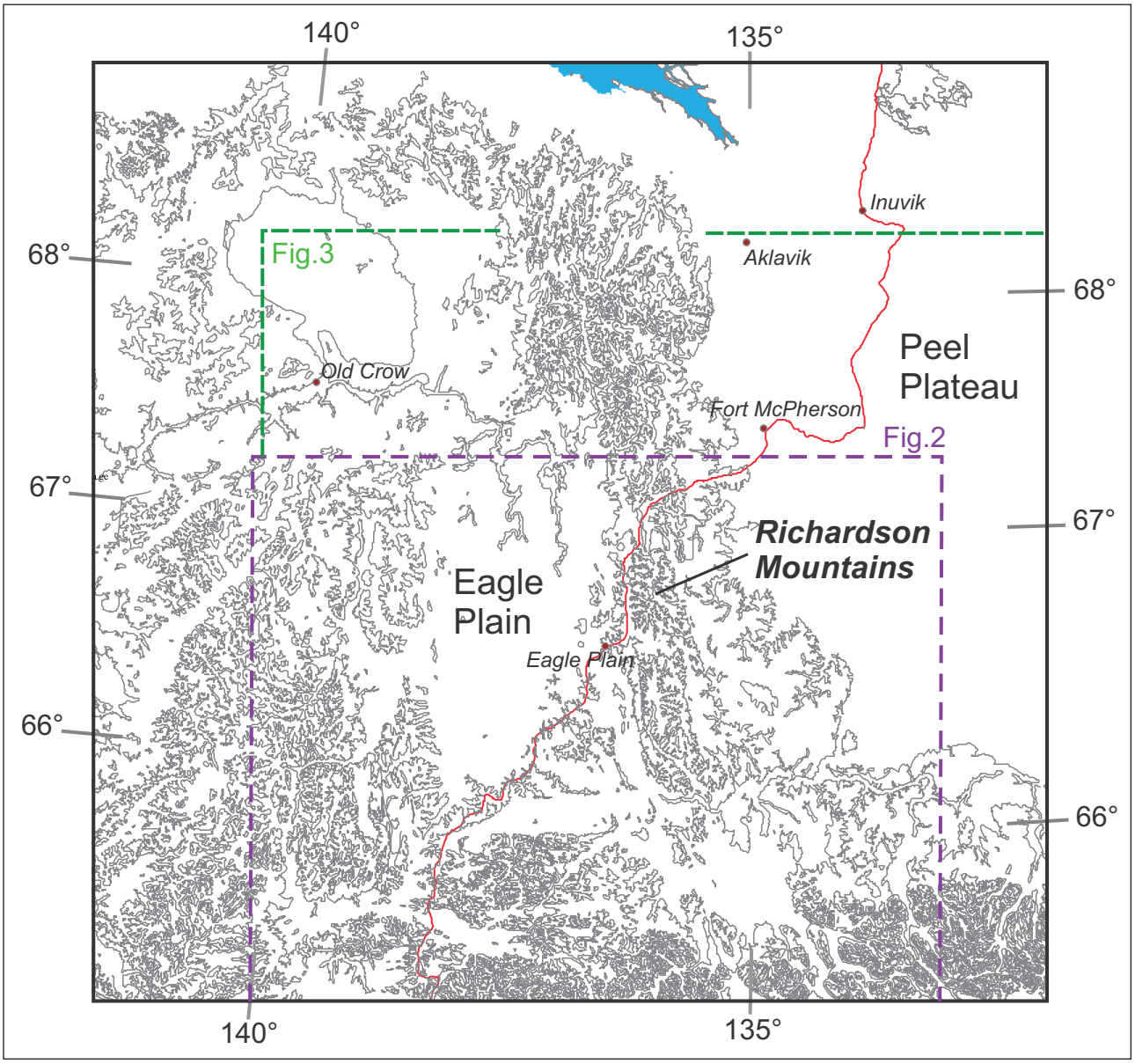

Figure 1. *Physiographic framework of the Richardson Mountains. The red line indicates the Dempster Highway.*

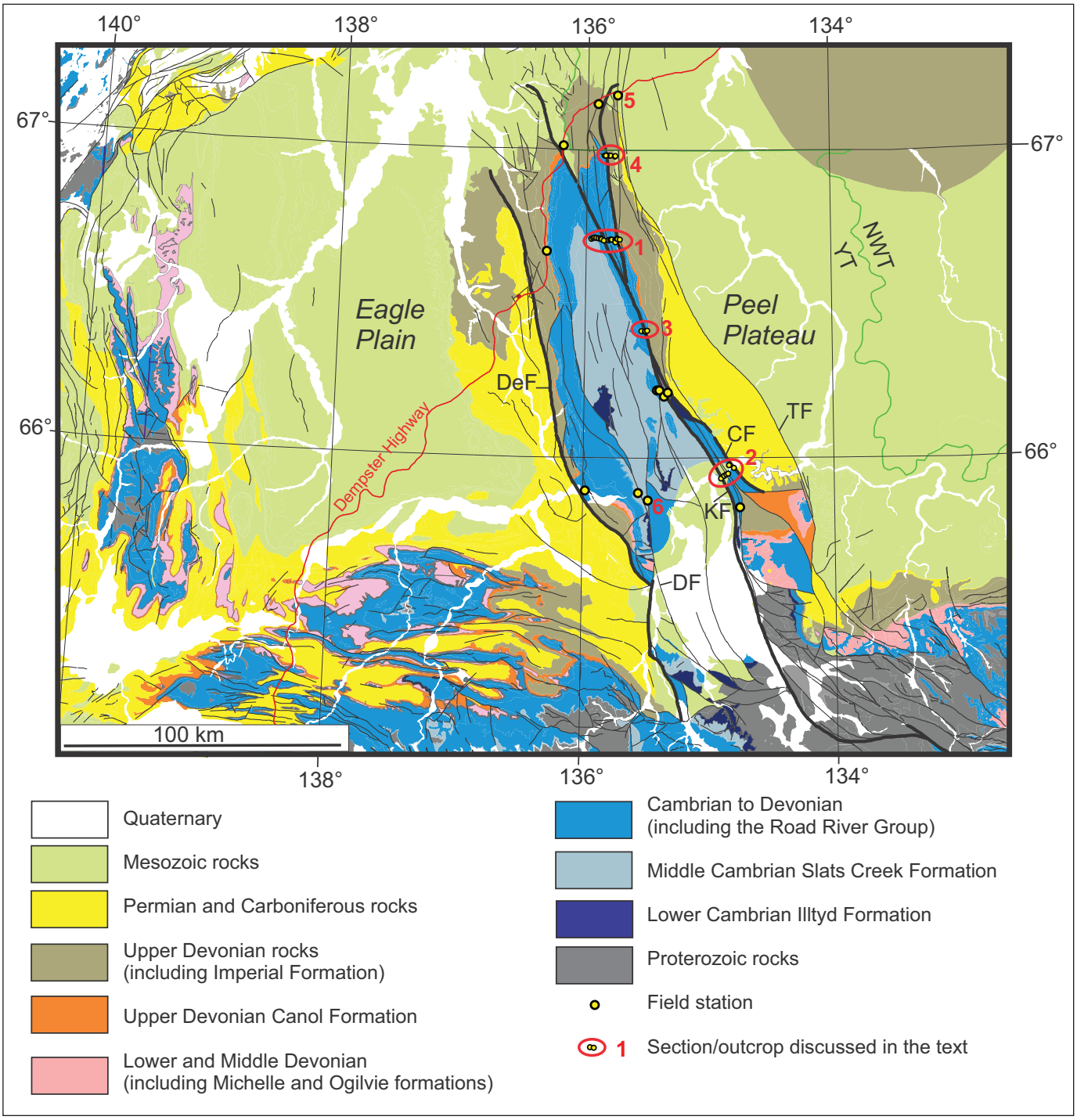

Figure 2. *Geological map of the Richardson Mountains and adjacent Eagle Plain and Peel Plateau (adapted from Norris 1981a to d). CF = Caribou fault; DF = Deslauriers fault; DeF = Deception fault; KF = Knorr fault; TF = Trevor fault; NWT = Northwest Territories; YT = Yukon; 1 = Tetlit River section; 2 = eastern Peel River section; 3=Trail River section; 4 = Vittrekwa River; 5 = Dempster Highway; 6 = western Peel River.*

Geophysical Framework

Fair to good quality seismic data are available for the Eagle Plain and Peel Plateau on both sides of the Richardson anticlinorium. These hydrocarbon exploration seismic lines generally end at the Richardson Mountains (Osadetz et *al.*, 2005; Rohr et *al.*, 2011) and the geometry of the anticlinorium is therefore poorly constrained. Based on the available seismic data set, Hall and Cook (1998) interpreted the Richardson anticlinorium as a pop-up structure formed above a regional detachment that extends westward beneath Eagle Plain.

A positive Bouguer gravity anomaly is centred on the Richardson anticlinorium (Fig. 3a). Gradients greater than 1 mGal/km characterize the east side of the anticlinorium. The boundaries of the gravity anomaly are enhanced on the map of the horizontal gradient of the Bouguer anomaly, and are almost coincident with mapped faults (Fig. 3b). As noted by Hall and Cook (1998), this anomaly probably reflects the presence of high-density Precambrian rocks in the core of the anticlinorium.

On the map of the residual total magnetic field, the RFA also corresponds to a clear boundary between domains with different long-wavelength anomaly signatures (Crawford et *al.*, 2010).

Structural Analysis

Structural observations were collected during the 2010 field season and precede the recent clarification of the Road River Group stratigraphy (Strauss et *al.*, 2020). For this reason, the recently formalized formations are not used in the following descriptions.

Tetlit section

A nearly continuous section of the east flank of the Richardson Mountains (Fig. 4; location 1 on Fig. 2) is found along the Tetlit River. Structural repetition of Canol Formation and part of the Imperial Formation occurs at this section.

Rock units dip almost invariably toward the east. The dips are generally shallow (<30°) except close to fault zones where bedding is steep (70 to 90°). Exposure of two main fault zones along the Tetlit River are informally referred to as the east and west Tetlit fault zones. On the published geological map, they correspond to fault splays of the Knorr fault (Norris, 1981c).

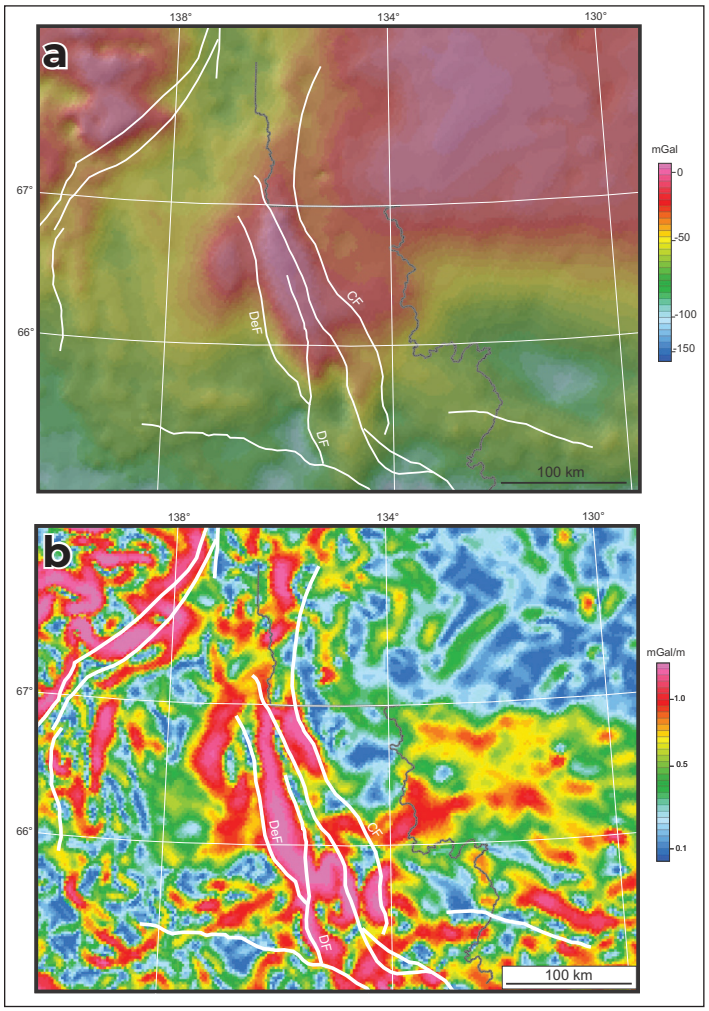

Figure 3. *Gravity maps of the Richardson Mountains and adjacent areas.* ***(a)*** *Bouguer anomaly map and* ***(b)*** *horizontal derivative of the Bouguer anomaly. White lines indicate main faults: CF = Caribou fault; DF = Deslauriers fault; DeF = Deception fault.*

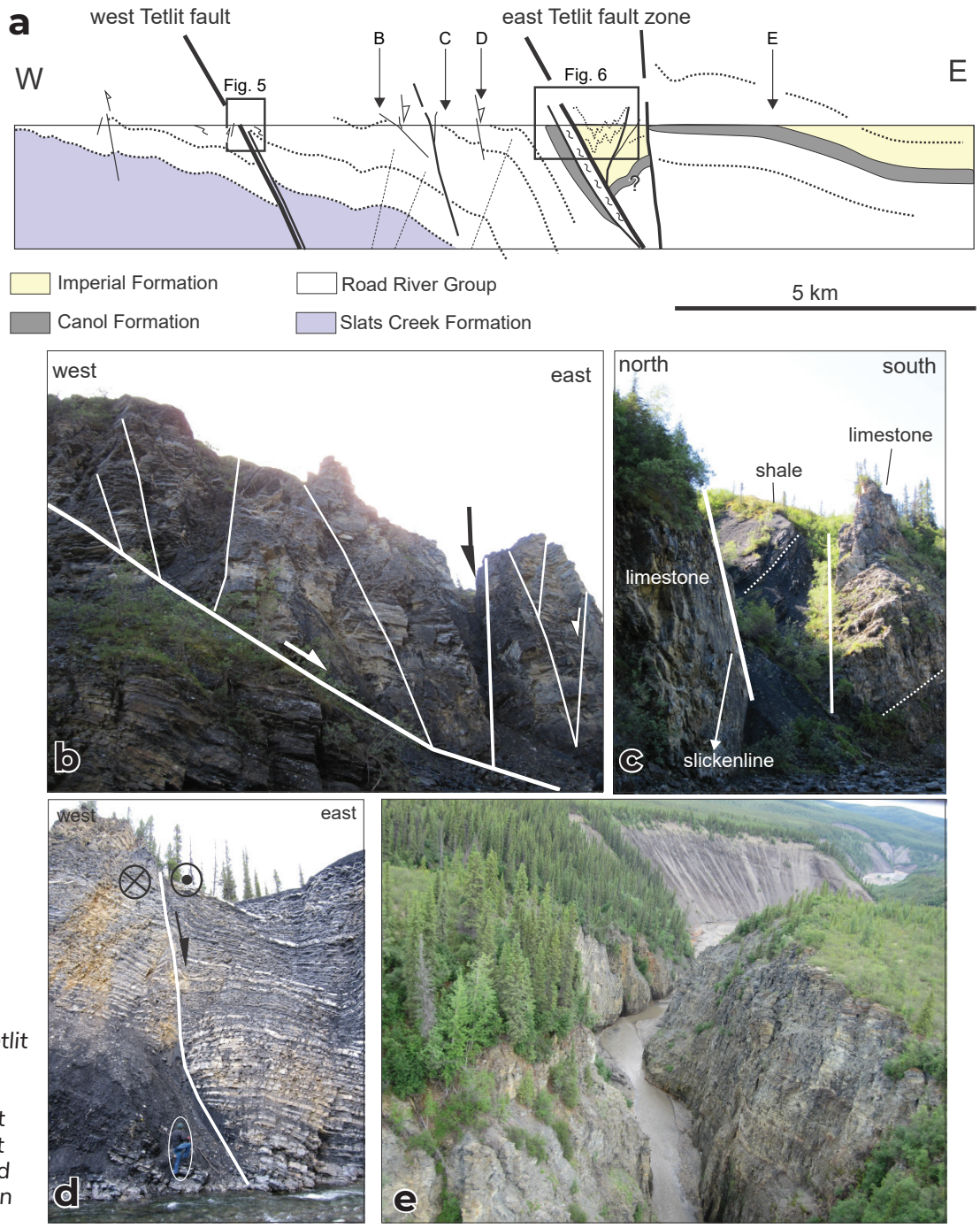

Figure 4. (a) *Cross section along the Tetlit River (location 1 on Fig. 2); no vertical exaggeration. Offset along the west Tetlit fault is unknown and shown for illustration purposes only. The eastern part of the section has not been studied in detail and the geometry of the Imperial Formation is based on a helicopter reconnaissance survey and on the study of Allen (2009). Locations for 4b to e indicated on section.* ***(b)*** *Brittle faults showing predominant normal motion, with a minor right-lateral component. Offsets along high angle faults are generally less than 1 m. Offset along shallow dipping fault is unknown. The width of the section pictured is approximately 20 m.* ***(c)*** *Brittle faults juxtaposing a shale-dominated unit against a limestone. A 5 m wide brecciated zone characterizes the main fault. The pitch of slickenlines found on the main fault plane is 45° suggesting that both the horizontal and vertical components of motion are significant. However, the sense of motion is unclear. The width of the section pictured is around 15 m. Dotted lines represent the bedding.* ***(d)*** *Brittle fault showing mixed right-lateral and normal motion. Geologist for scale (outlined by white oval).* ***(e)*** *Aerial view looking east, showing the contact between the Canol Formation (foreground) and the Imperial Formation (back).*

The east Tetlit fault zone marks the contact between a siltstone-dominated assemblage to the west and a limestone-dominated assemblage to the east, both belonging to the Road River Group. The fault trends N350 and is marked by a 4 m wide schistose zone (Fig. 5a) and a 120 m wide brecciated zone. Within the schistose zone, slickenlines on fault planes indicate predominant strike-slip motion (Fig. 5b) with an uncertain sense of slip. The brecciated zone corresponds to a cohesive tectonic breccia that contains centimetre to decimetre long angular fragments in a matrix formed by crushed rocks (Fig. 5c). Calcite veinlets and fractures (with a predominant N150 strike) are common in the brecciated zone.

The west Tetlit fault zone corresponds to a kilometre-wide deformation zone (Figs. 4 and 6). West of the main deformation zone, the contact between the shale-dominated upper part of the Road River Group and the Canol Formation dips steeply (70°) to the east. Within the Canol Formation, second-order faults associated with metre-thick cataclastic zones record predominantly right-lateral motions (Fig. 6a,b,c). The main zone of deformation is several hundred metres wide. It occurs in a fine-grained assemblage that includes fault bounded, elongated, competent blocks up to tens of metres in length (Fig. 6d,e). In a number of locations, several disconnected blocks are aligned with a plane parallel to bedding. The blocks are brecciated and bounded by deformed zones delineated by a scaly fabric. These blocks recorded significant bedding-parallel shearing, but the possibility that some blocks were olistoliths prior to deformation cannot be ruled-out.

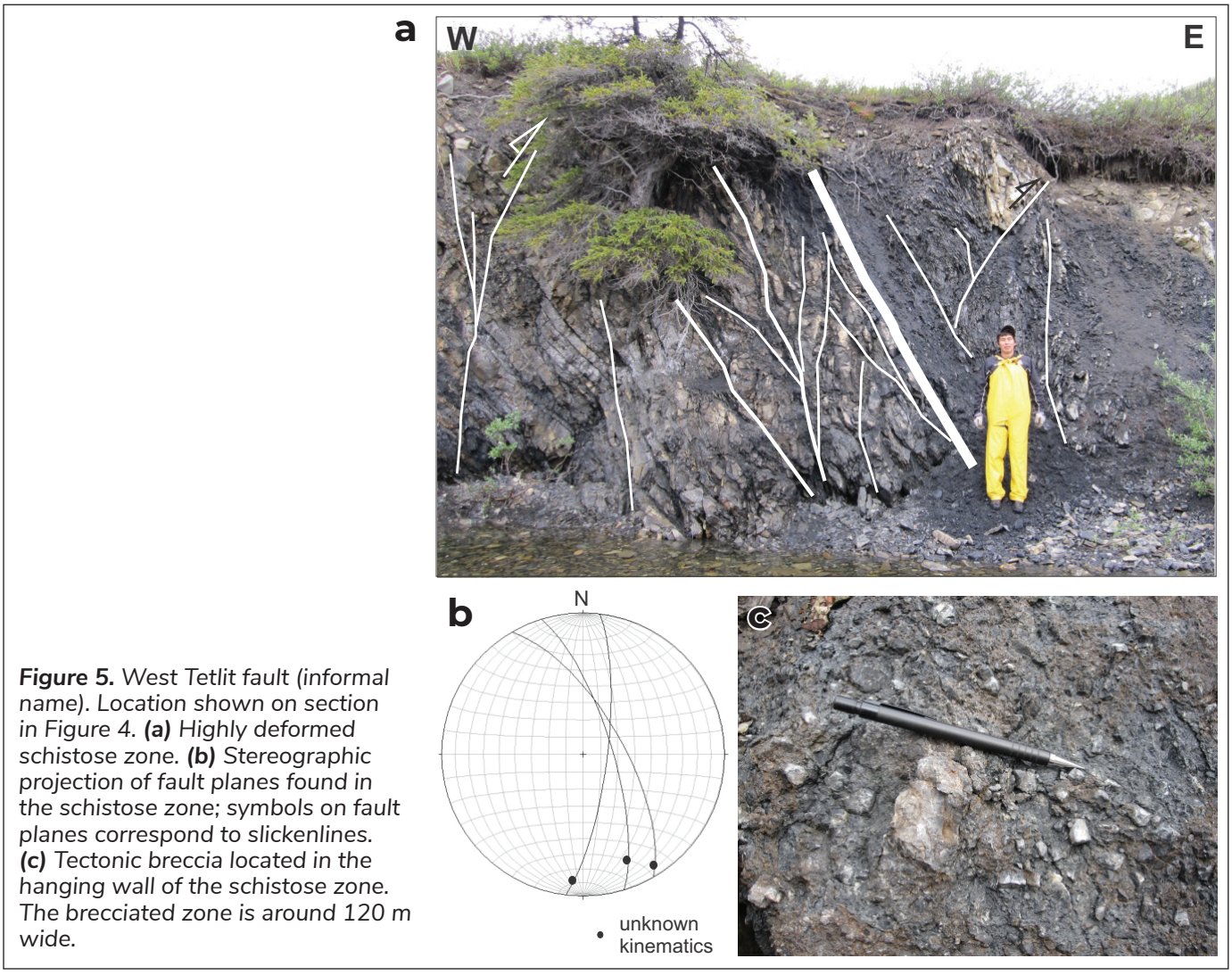

Figure 5. *West Tetlit fault (informal name). Location shown on section in Figure 4.* ***(a)*** *Highly deformed schistose zone.* ***(b)*** *Stereographic projection of fault planes found in the schistose zone; symbols on fault planes correspond to slickenlines.* ***(c)*** *Tectonic breccia located in the hanging wall of the schistose zone. The brecciated zone is around 120 m wide.*

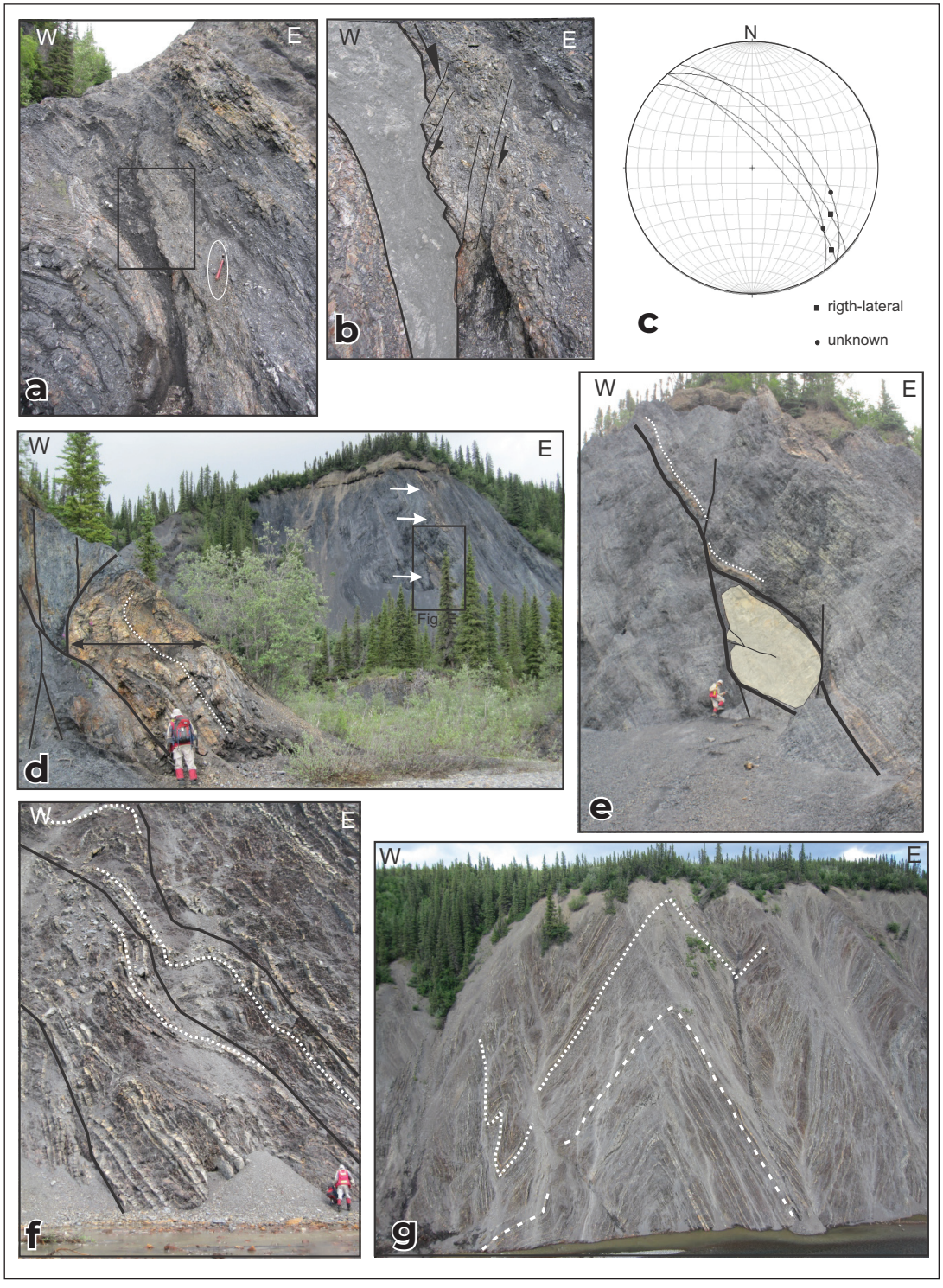

Figure 6. *East Tetlit fault zone (informal name). Location on section in Figure 4.* ***(a)*** *Fault zone in the Canol Formation. Hammer for scale (outlined by white oval).* ***(b)*** *Close-up of area outlined in 6a. Slickensided surfaces, as well as minor Riedel-type second-order shears, indicate predominant right-lateral motion.* ***(c)*** *Stereographic projection of striated fault planes in the east Tetlit fault zone. Symbols on fault planes correspond to slickenlines.* ***(d)*** *Fault-bounded block (black arrows) in a shale-dominated interval. The white dotted line represents bedding. White arrows mark other fault-bounded blocks.* ***(e)*** *Close-up of fault-bounded block in a shale dominated assemblage in area outlined in 6d. The white dotted line represents bedding. Geologist for scale.* ***(f)*** *Faults subparallel to bedding. Note the fault-bend folds associated with change in the fault dip ('fault ramp'). Geologist for scale.* ***(g)*** *Upright chevron folds. The outcrop is approximately 40 m high.*

West of the main deformation zone, the Imperial Formation exhibits numerous faults subparallel to bedding, and fault-bend folds are associated with change in the fault dip (Fig. 6f). The Imperial Formation also exhibits spectacular upright closed folds, hundreds of metres in wavelength, with angular hinge zones (Fig. 6g). The eastern fault within the east Tetlit fault zone corresponds to a steeply dipping deformation zone.

Second-order structural features in the footwall of the east Tetlit fault zone include brittle faults marked by deformation zones ranging in width from centimetres up to five metres (Fig. 4c). The orientations of slickenlines found on these second-order fault planes vary significantly suggesting a complete transition in time and/or space from faults with nearly downdip motion to strike-slip faults (Fig. 7). Faults having a normal component correspond to either discrete (Fig. 4d) or anastomosed features (Fig. 4b) allowing down-to-the-east motion. Folds are generally upright and wavelengths range from tens to hundreds of metres.

Deformation in the hanging wall of the east Tetlit fault zone corresponds to broad open folds involving the Imperial Formation (Allen, 2009; Fig. 4e).

Eastern Peel River section

Nearly continuous outcrops form a 5 km long section along the Peel River (Fig. 8; location 2 on Fig. 2) between the Knorr and Caribou faults of Norris (1981d). Due to the water level during fieldwork, most outcrops were not accessible. However, tectonic features are easily visible from several shoals in the riverbed.

Two main assemblages may be distinguished in the Road River Group: to the west, rocks consist of decimetre to metre thick layers of siltstone and limestone with shale intervals, whereas to the east, black shale predominates. The contact between fine-grained rocks belonging to the Carboniferous Ford Lake Shale that forms the eastern end of the studied section and the Road River Group is not exposed.

Folds are close to tight, and are overturned to the east (Fig. 8d). In the central part of the section, parasitic folds are asymmetric or 'S'-shaped, indicating that they belong to the western flank of a major syncline (Fig. 8a).

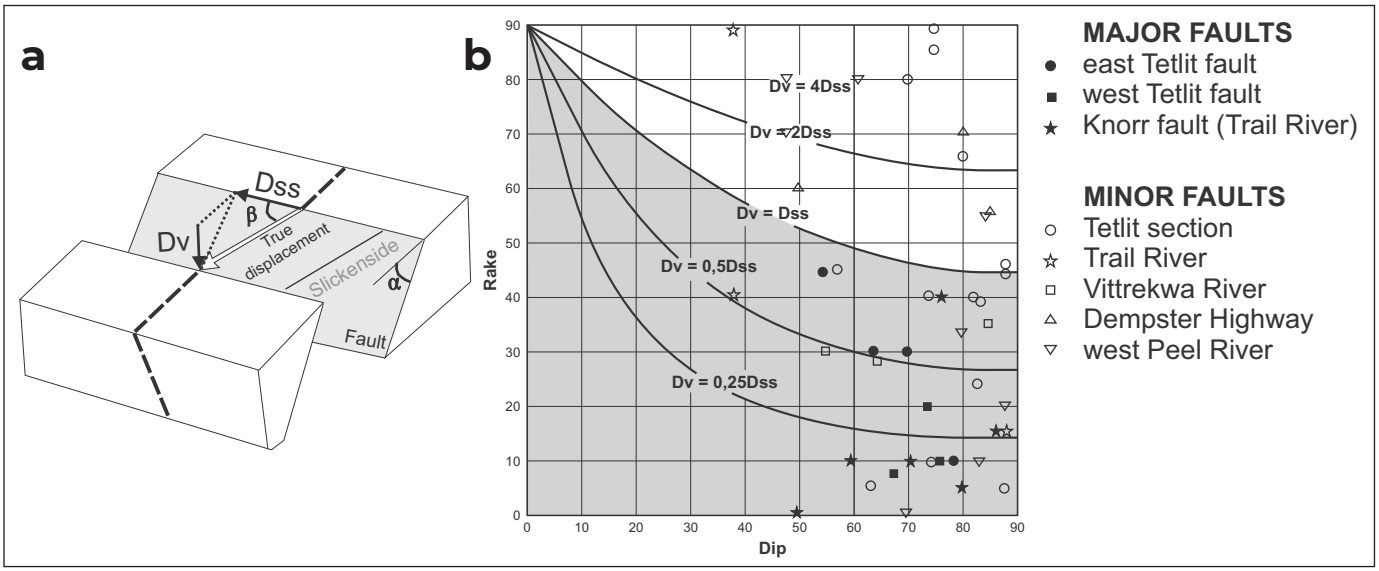

Figure 7. (a) *Relationship between the strike-slip (Dss) and vertical (Dv) components of displacement. α, dip of the fault plane; β, rake of the slickenline.* ***(b)*** *Diagram showing the kinematic of brittle faults based on fault dip and rake of slickenline. The field corresponding to faults with a predominant strike-slip motion (Dss>Dv) is shown in grey.*

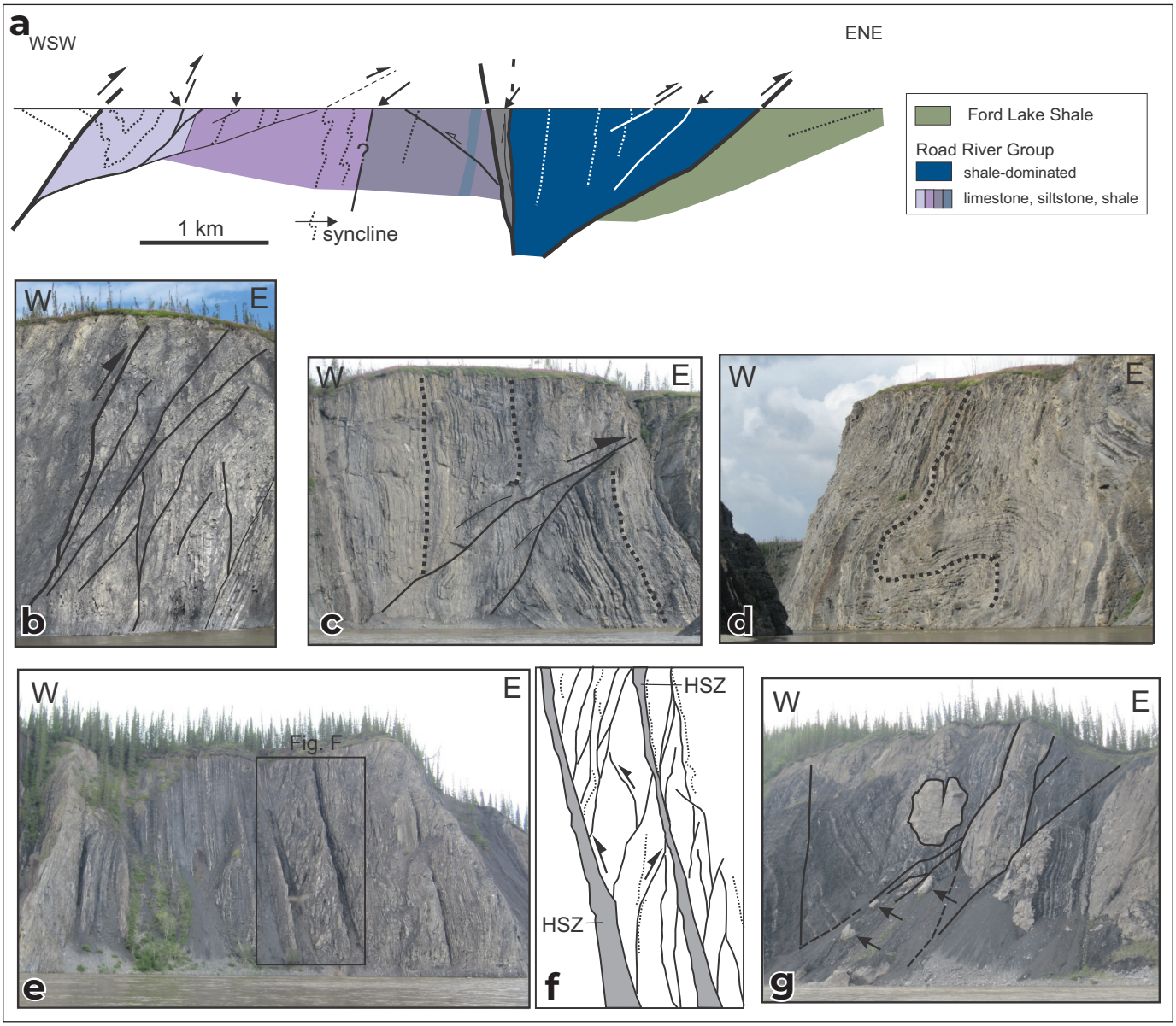

Figure 8. (a) *Cross section along the eastern Peel River (location 2 on Fig. 2). No vertical exaggeration. Arrows indicate the apparent sense of shear and do not take into account a potential strike-slip component.* ***(b)*** *Closely spaced steeply-dipping faults. Drag folds suggest apparent east-directed thrust motion along the faults.* ***(c)*** *Shallow-dipping faults recording apparent east-directed thrust motion.* ***(d)*** *Asymmetric east-verging folds.* ***(e)*** *Steeply dipping high-strain zone.* ***(f)*** *Sketch of the area outlined in 7e. The high-strain zone may record mainly strike-slip motion and cuts older second-order faults showing apparent east-directed thrust motion.* ***(g)*** *West-dipping faults, some of them bounding elongated more competent blocks (arrows).*

Moderate (30–40°; Fig. 8c) to steep (up to 70°; Fig. 8b) west-dipping faults are common along the Peel River section. Offset of marker beds and drag folds suggest east-directed thrusting. In the eastern part of the section, disconnected competent blocks are present in a shale-dominated assemblage (Fig. 8g). Shearing along block boundaries and faults cutting through the blocks attest to significant deformation.

A steep, east-dipping fault zone marked by several high-strain zones cuts west-dipping faults in the central part of the section (Fig. 8e,f). Based on the apparent dragging of the bedding and presence of west-dipping faults, the fault zone appears to be west-directed. However, the strike-slip component of motion may still predominate.

Trail River section

Along most of the studied segment of the Trail River section (Fig. 9; location 3 on Fig. 2), rock units dip toward the east, except close to a major fault zone that marks the northern extent of the Knorr fault of Norris (1981d). The conformable contact between the shale-dominated upper assemblage of the Road River Group and the Canol Formation is well exposed. The Imperial Formation overlies the Canol Formation to the east of the studied segment of the Trail River.

The main fault zone strikes ~N187 and corresponds to a steeply dipping, 10 m wide high strain zone that includes dismembered competent blocks in a fine-grained matrix. A brecciated zone, approximately 20 m in width and including subhorizontal to subvertical fracture planes, bounds the high strain zone to the east (Fig. 9d). Slickenlines found on second-order brittle fault planes indicate mainly right-lateral motion (Fig. 9e). This high strain zone (HSZ_2 on Fig. 9d) cuts a shallow dipping high strain zone (HSZ_1 on Fig. 9d) that divides two highly folded rock packages.

Second-order faults are common in the central part of the section (Fig. 9b,c) and include brittle structures showing either normal or thrust apparent motions. Bedding surfaces having slip indicators have been observed in several locations and are frequently cut by steeply dipping faults.

Vittrekwa River section

Within the studied section along the Vittrekwa River (location 4 on Fig. 2), the Imperial Formation dips steeply (average: 65–70°) generally toward the east. Brittle faults are common along the section and are generally steeply (>70°) dipping. High strain zones, one to three metres wide, parallel bedding, and record predominant right-lateral motions (Fig. 10). High strain zones are located in shale-rich intervals suggesting that beds were first tilted close to the vertical before strike-slip deformation in incompetent layers.

Shallow to moderately dipping (<50°) faults have been observed locally but their offsets and potential crosscutting relationships with high-angle faults remain unclear.

Dempster highway

The Trevor fault is partially exposed a few hundred metres north of the Dempster Highway (Fig. 11a; location 5 on Fig. 2). On the geological map of Norris (1981a), main structures trend N170 to N020 and put in contact the Upper Devonian Imperial Formation with Mesozoic rocks (attributed to the Jurassic North Branch Formation and Cretaceous Martin Creek Formation).

A north-trending deformation zone is well exposed in the eastern part of the section and separates a shale-dominated assemblage (Whitestone River Formation?) from locally micro-conglomeratic, grey, quartz-rich sandstones with a yellowish weathering colour (Kamik Formation?). The ~100 m deformation zone includes faults associated with decimetre-wide brecciated and/or schistose intervals with variable strikes and dips (Fig. 11b,d). Minor structures have no obvious pattern, but the slickenlines suggest two groupings (Fig. 11c). One group reflects mainly dip-slip motion on an array of subsidiary faults striking northwest. The other group indicates strike-slip motion on north-striking minor faults.

In the eastern part of the section, a fault-bounded block near the contact between the Mesozoic and Paleozoic assemblages attests to significant deformation. The fault that bounds the Imperial Formation toward the east is not exposed.

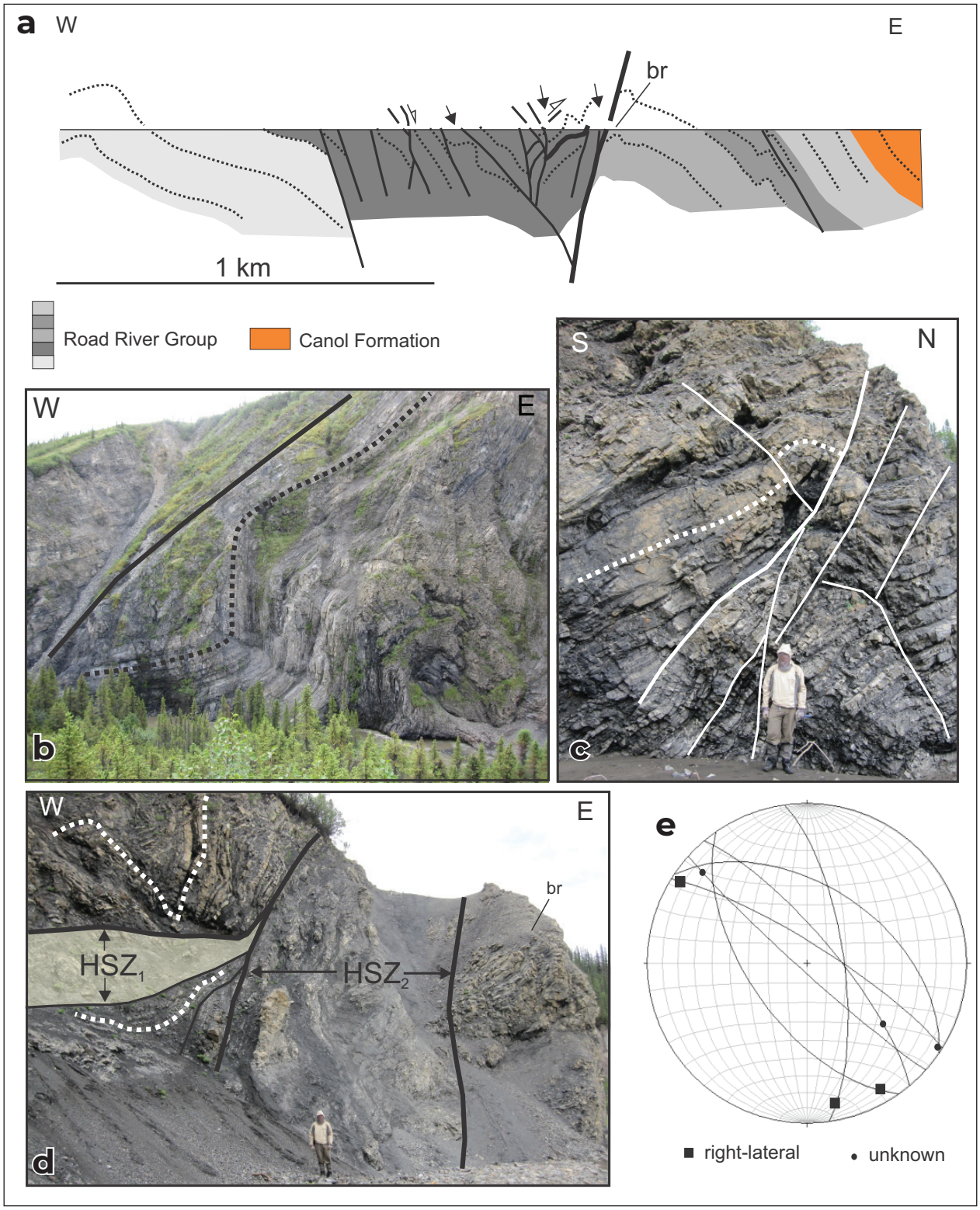

Figure 9. ***(a)*** *Cross section along the Trail River (location 3 on Fig. 2). No vertical exaggeration. Arrows indicate the apparent sense of shear and do not take into account a potential strike-slip component.* ***(b)*** *Asymmetric open fold;* ***(c)*** *second-order faults showing multiple cross-cutting relationships;* ***(d)*** *shallow-dipping high-strain zone (HSZ_1) cut by a steeply dipping high strain zone (HSZ_2) approximately 10 m wide. Rocks on the east side of HSZ_2 are brecciated (br); and* ***(e)*** *stereographic projection of striated fault planes found close to the HSZ_2. Symbols on fault planes correspond to slickenlines.*

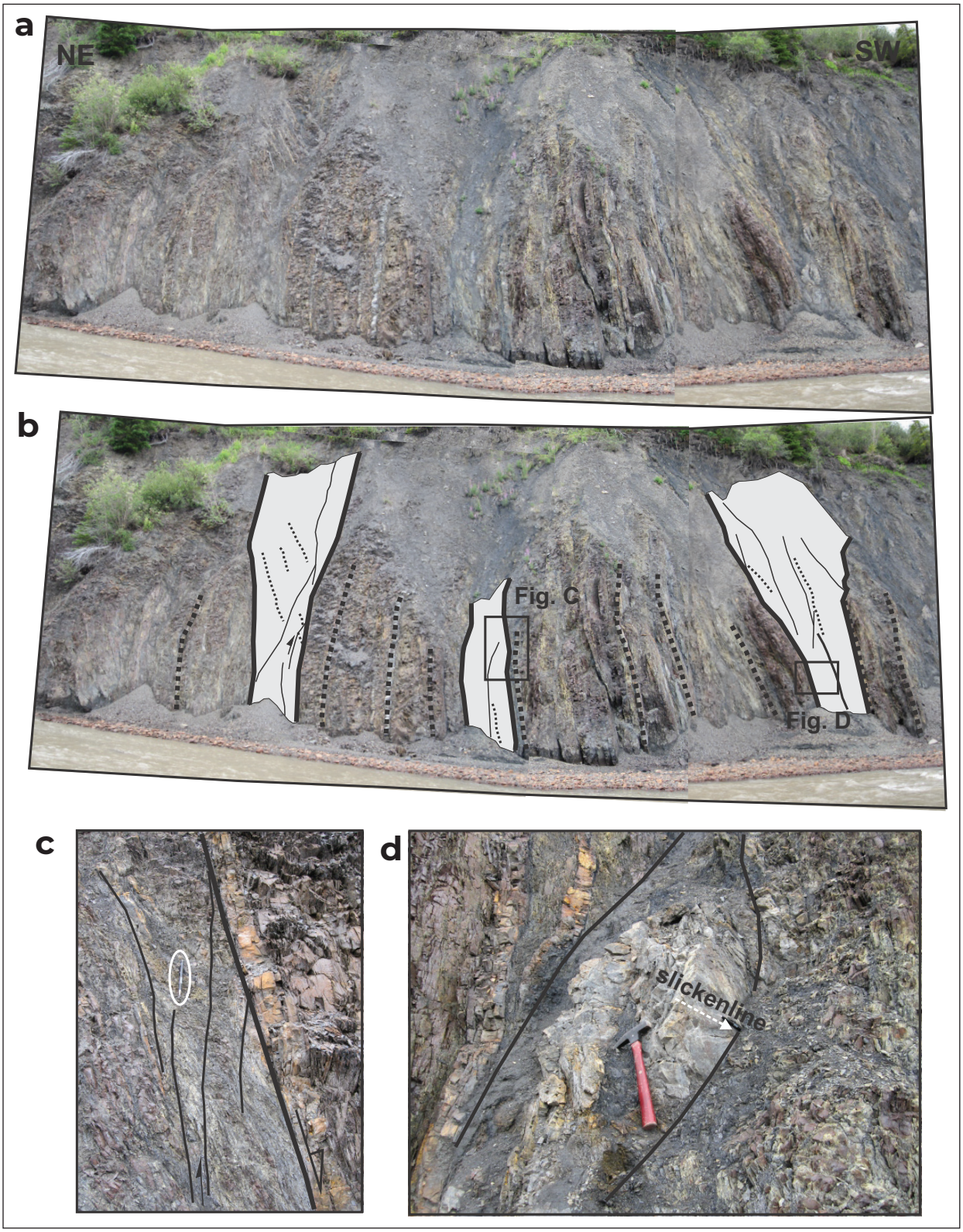

Figure 10. *Vittrekwa River (location 4 on Fig. 2).* ***(a and b)*** *(with annotations), steeply dipping faults characterized by 1 to 3 m wide deformation zones (in white on 10b) parallel to bedding.* ***(c)*** *Close-up of second order synthetic faults within a deformation zone (area outlined in 10b). Arrows indicate the apparent sense of shear and do not take into account a potential strike-slip component.* ***(d)*** *Closer view of one of the few striated surfaces found in deformation zones and recording predominant right-lateral motion (area outlined in 10b).*

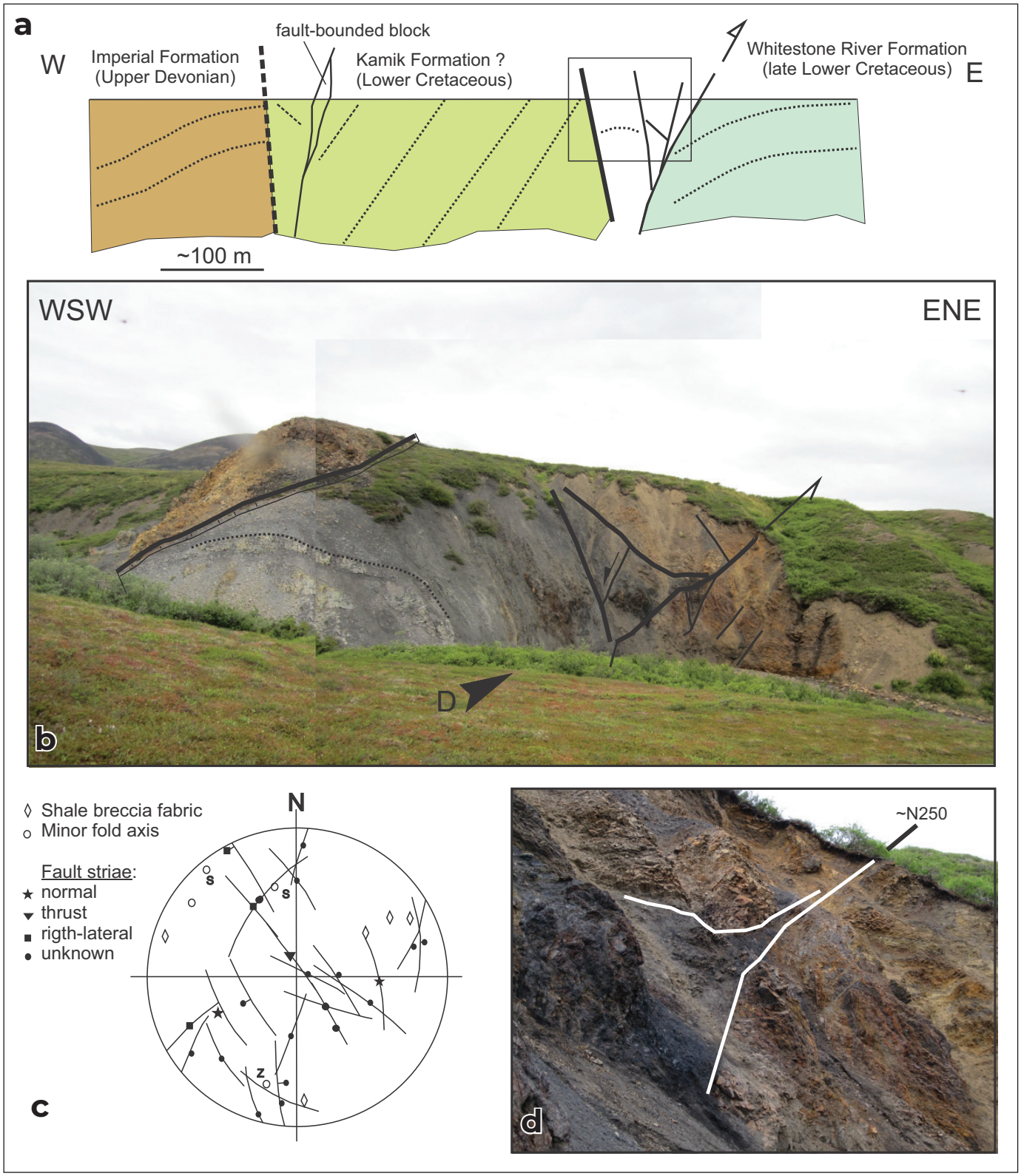

Figure 11. (a) *Cross section of the fault zone along the Dempster Highway (location 5 on Fig. 2).* ***(b)*** *View of the eastern fault zone showing the variability of fault strikes.* ***(c)*** *Stereographic projection of striated second-order fault planes. Only part of great circles (fault planes) is shown. Symbols on fault planes correspond to slickenlines.* ***(d)*** *Closer view of a steeply dipping (around 70°) N250 trending fault (from point of view indicated in 11b).*

Western Peel River

In the Peel River area, the Deslauriers fault puts in contact the Slats Creek Formation to the west and the Road River Group to the east (Norris, 1981d). The fault zone is not exposed in the Peel valley. However, an elongated butte forms an isolated outcrop near or at the location of the Deslauriers fault, a few hundred metres south of the Peel River (location 6 on Fig. 2). The butte consists of a light grey weathered, erosion-resistant massive limestone. The limestone is brecciated, has fractures spaced at 10 to 50 cm, and has abundant neoformed calcite (Fig. 12a). Brittle fault planes have various orientations. However, continuous planes tend to strike parallel to the elongation of the butte, approximately N335, and correspond to left-lateral strike-slip faults (Fig. 12b).

Discussion

The east flank of the Richardson anticlinorium exhibits highly variable strain intensities. Along most of the studied sections, rock units dip shallowly to the east and are characterized by broad open folds, hundreds of metres in wavelength, and have few brittle structures attesting to low internal deformation. However, close to major faults, marked by deformation zones up to several hundred metres in width, rock units are steep and highly strained. Clear evidence of bedding-parallel shearing in steeply dipping shale-dominated assemblages is documented at several locations, including along the east Tetlit fault. The amount of displacement along bedding-parallel shears is difficult to quantify, but is probably significant.

A predominant dextral sense of motion is documented for several major faults belonging to the Richardson fault array (east Tetlit fault, Trail River fault, Vittrekwa River structures; Fig. 7). This is in agreement with previous studies that suggest that strike-slip faulting predominates (Jeletsky, 1961, 1975) and with Paleogene (?) dextral faults documented elsewhere in northern Yukon (von Gosen *et al.*, 2019). The steep dip of major faults, as well as their kinematics, conflict with Hall and Cook's (1998) interpretation

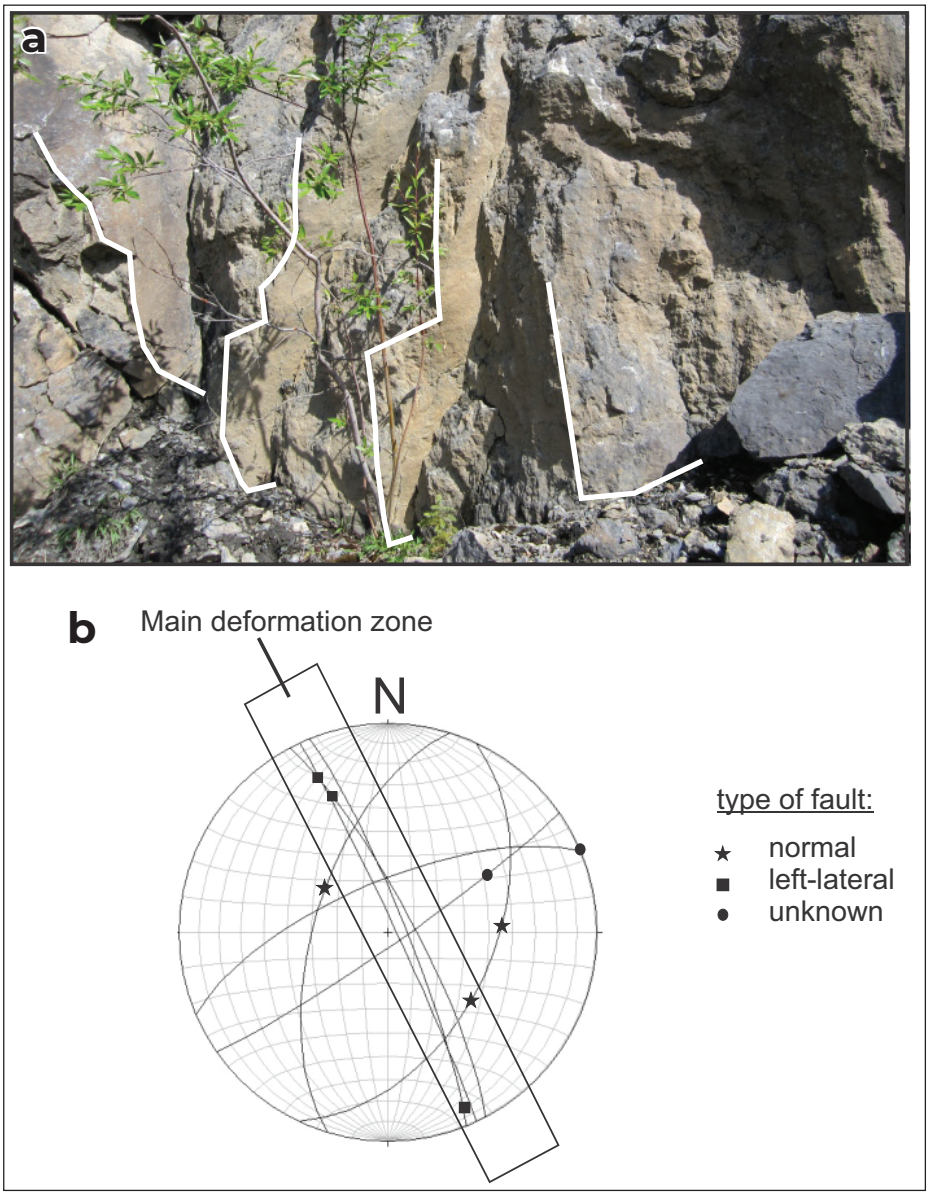

Figure 12. *Deslauriers fault near the Peel River (location 6 on Fig. 2).*
(a) *Closely spaced second-order fault planes (white lines).*
(b) *Stereographic projection of striated fault planes. Symbols on fault planes correspond to slickenlines.*

that the Richardson anticlinorium corresponds to a thrust-related pop-up structure formed above a regional detachment that roots westward beneath Eagle Plain.

Unambiguous evidence for left-lateral displacement has been documented along the Deslauriers fault (western Peel) in an elongated butte that corresponds to a tectonic block composed of limestone of uncertain age. This block may have experienced significant rotation and structures may have originally belonged to a group of N0 to N15 faults with left-lateral apparent displacements that have been mapped on the western flank of the Richardson anticlinorium (Norris, 1981b). Alternatively, these minor faults could belong to a distinct tectonic episode.

The Peel River section is characterized by a clear structural vergence toward the east. The significance of this change of deformation style in the southern Richardson Mountains is uncertain.

Second-order faults exhibit highly variable kinematics (Fig. 7) and both normal and thrust faults have been documented. In several cases (e.g., sections along the eastern Peel, Trail and Vittrekwa rivers), strike-slip faults cut more shallow dipping faults and/or follow steep bedding planes, suggesting that dextral motions affected a previously tilted and deformed sedimentary succession. However, crosscutting relationships are rare and it is unclear whether the various faults were active during a single progressive phase or several discrete deformation episodes. Polyphase deformation may explain the scattered distribution of bedding orientations.

Cecile (1984) used the apparent offset of the Canol Formation to estimate a less than 20 km displacement along the RFA. On the western flank of the Richardson Mountains, the Canol Formation has a clear geomorphologic signature (Norris, 1981b) and offset estimates are likely reliable. On the east flank, however, the signature is more subtle and the mapped location of the Canol Formation is more ambiguous. In addition, structural repetitions (such as the one observed on the Tetlit section) may contribute to the geometrical complexity on the eastern flank of the Richardson anticlinorium, which renders any displacement estimate highly uncertain.

However, the deformation documented in fault zones exhibits several characteristics (including width) generally associated with faults that experienced significant displacements. As such, possible large offset on the eastern flank of the Richardson anticlinorium should be considered along with independent evidence (present day seismicity; relatively steep gravity gradients; large wavelength magnetic anomaly pattern) that suggests the presence of regional-scale structure(s).

Consequently, the traditional interpretation of Paleozoic and Mesozoic succession thickness and facies variations essentially resulting from a complex paleogeography warrants further investigation. Such an interpretation may have led to invalid and/or imprecise palinspastic reconstructions because sedimentary rocks from distinct settings may have been tectonically juxtaposed along major faults.

Acknowledgements

This study was conducted as part of a GEM project led by Larry Lane; I thank him for giving me the opportunity to do some fieldwork. Tammy Allen shared her expertise on northern Yukon geology. Miranda Charlie, Yudii Mercredi and Adam Hayman provided valuable field assistance. This paper has been improved by the reviews of Sébastien Castonguay and Maurice Colpron. This is GSC contribution No. 20200527.

Reference

Allen, T.L., 2009. Field notes on the Upper Devonian Imperial Formation (NTS map sheet 106L), Tetlit Creek, east Richardson Mountains, Yukon. *In*: Yukon Exploration and Geology 2009, K.E. MacFarlane, L.H., Weston and L.R. Blackburn (eds), Yukon Geological Survey, p. 1–21.

Cecile, M.P., 1984. Evidence against large-scale strike-slip separation of Paleozoic strata along the Richardson-Hess fault system, northern Canadian Cordillera. Geology, vol., 12, p. 403–407.

Crawford, B.L., Betts, P.G. and Aillères, L., 2010. An aeromagnetic approach to revealing buried basement structures and their role in the Proterozoic evolution of the Wernecke Inlier, Yukon Territory, Canada. Tectonophysics, vol. 490, p. 28–46.

Dixon, J., 1996. Cretaceous and Tertiary. *In*: Geology and mineral and hydrocarbon potential of northern Yukon Territory and northwestern district of Mackenzie. Geological Survey of Canada, Bulletin 422, p. 301–317.

Eisbacher, G.H., 1983. Devonian-Mississippian sinistral transcurrent faulting along the cratonic margin of western North America: A hypothesis. Geology, vol. 11, p. 7–10.

Fraser, T.A. and Hutchison, M.T., 2017. Lithogeochemical characterization of the Middle-Upper Devonian Road River Group and Canol and Imperial formations on Trail River, eastern Richardson Mountains, Yukon: age constraints and a depositional model for fined-grained strata in the Lower Paleozoic Richardson trough. Canadian Journal Earth Sciences, vol. 54, p. 731–765.

Hall, K.W. and Cook, F.A., 1998. Geophysical transect of the Eagle Plains foldbelt and Richardson Mountains anticlinorium, northwestern Canada. Geological Society of America Bulletin, vol. 110, p. 311–325.

Jeletzky, A., 1961. Eastern slope, Richardson Mountains: Cretaceous and Tertiary structural history and regional significance. *In:* Geology of the Arctic, Volume I: University of Toronto Press, p. 532–583.

Jeletzky, J.A., 1975. An estimate of right-lateral displacement on Donna River Fault, northwestern district of Mackenzie, NWT Geological Survey of Canada, Paper 75-1, Part A, p. 541–543.

Lane, L.S., 1998. Latest Cretaceous-Tertiary tectonic evolution of northern Yukon and adjacent Arctic Alaska. American Association Petroleum Geologist Bulletin, vol. 82, p. 1353–1371.

Mazotti, S. and Hyndman, R.D., 2002. Yakutat collision and strain transfer across the northern Canadian Cordillera. Geology, vol. 30, p. 495–498.

Morrow, D.W., 1999. Lower Paleozoic stratigraphy of northern Yukon Territory and northwestern district of Mackenzie. Geological Survey of Canada, Bulletin 538, 202 p.

Norford, B.S., 1996. Ordovician and Silurian. *In*: Geology and mineral and hydrocarbon potential of northern Yukon Territory and northwestern district of Mackenzie. Geological Survey of Canada, Bulletin 422, p. 119–162.

Norris, D.K., 1981a. Geology, Fort McPherson, District of Mackenzie. Geological Survey of Canada, A-series map 1520A, scale 1:250 000.

Norris, D.K., 1981b. Geology, Eagle River, Yukon Territory. Geological Survey of Canada, A-series map 1523A, scale 1:250 000.

Norris, D.K., 1981c. Geology, Trail River, Yukon-Northwest Territories. Geological Survey of Canada, A-series map 1524A, scale 1:250 000.

Norris, D.K., 1981d. Geology, Wind River, Yukon Territory. Geological Survey of Canada, A-series map 1528A, scale 1:250 000.

Norris, D.K., 1985. Eastern Cordillera foldbelt in northern Canada: its structural geometry and hydrocarbon potential. American Association of Petroleum Geologists Bulletin, vol. 69, p. 788–808.

Norris, D.K., 1996. Physiographic setting. *In:* Geology and mineral and hydrocarbon potential of northern Yukon Territory and northwestern district of Mackenzie. Geological Survey of Canada, Bulletin 422, p. 7–20.

Norris, D.K. and Hopkins, W.S., 1977. The geology of the Bonnet Plume Basin, Yukon Territory. Geological Survey of Canada, Paper 76-8, 20 p.

Norris, D.K. and Yorath, C.J., 1981. The North American Plate from Arctic Archipelago to the Romanzof Mountains. *In*: The Arctic Ocean, A.E. Nairn, M. Churkin Jr. and F.G. Stehli (eds.), Springer Science + Business Media, New York, p. 37–103.

Osadetz, K.G., Chen, Z. and Bird, T.D., 2005. Petroleum Resource Assessment, Eagle Plain Basin and Environs, Yukon Territory, Canada. Yukon Geological Survey Open File 2005-2, Geological Survey of Canada, Open File 4922, 88 p.

Pugh, D.C., 1983. Pre-Mesozoic geology in the subsurface of the Peel River map area, Yukon Territory and district of Mackenzie. Geological Survey of Canada, Memoir 401, 61 p.

Rohr, K.M.M., Lane, L.S. and MacLean, B., 2011. Subsurface compressional structures and facies transitions imaged by seismic reflection data, eastern margin of Richardson Trough, Peel Plateau, Yukon. Bulletin of Canadian Petroleum Geology, vol. 59, p. 131–146.

Strauss, J.V., Fraser, T., Melchin, M.J., Allen, T.J., Malinowski, J., Feng, X., Taylor, J.F., Day, J., Gill, B.C. and Sperling, E.A., 2020. The Road River Group of northern Yukon, Canada: early Paleozoic deep-water sedimentation within the Great American Carbonate Bank. Canadian Journal Earth Sciences, vol. 57, p. 1193–1219.

von Gosen, W., Piepjohn, K., McClelland, W.C. and Colpron, M., 2019. Evidence for the sinistral Porcupine shear zone in North Yukon (Canadian Arctic) and geotectonic implications. *In:* Circum-Arctic Structural Events: Tectonic Evolution of the Arctic Margins and Trans-Arctic Links with Adjacent Orogens, K. Piepjohn, J.V. Strauss, L. Reinhardt, and W.C. McClelland (eds.), Geological Society of America, Special Paper 541, p. 473–491.

New geochemistry from old drill holes at the Tom property, Macmillan Pass, Yukon

Tiffani A. Fraser
Yukon Geological Survey

Jack Milton
Fireweed Zinc Ltd.

Sofie A. Gouwy
Geological Survey of Canada

Fraser, T.A., Milton, J. and Gouwy, S.A, 2021. New geochemistry from old drill holes at the Tom property, Macmillan Pass, Yukon. *In:* Yukon Exploration and Geology 2020, K.E. MacFarlane (ed.), Yukon Geological Survey, p. 19–46.

Abstract

This paper presents new data from historical drill core and outcrop specimens from Macmillan Pass, Yukon. Whole rock lithogeochemical data are presented from analyses of core from three drillholes at the Tom property. The core covers intervals ranging from the Middle Devonian Road River Group (Sapper Formation) to the Upper Devonian Earn Group (Portrait Lake Formation–Fuller Lake Member) and includes the Macmillan Pass volcanic suite that occurs at the Road River–Earn Group contact. Samples were collected to characterize the depositional history of Middle–Upper Devonian fine-grained rocks in the region to aid with paleogeographical reconstructions, depositional models, improve age control and to aid in correlation of thick shale units. Baseline geochemical profiles and sedimentology for all fine-grained units indicate turbidity current deposition in a range of shelf to basinal settings and variable oxic to anoxic conditions. Additionally, eleven existing Middle Devonian conodont collections were re-examined to provide better biozone refinements and a tighter constraint of the contact between the Road River Group (Sapper Formation) and Earn Group (Portrait Lake Formation) to the Late Eifelian *australis-ensensis* biozones.

Organic carbon isotope data from the upper Sapper Formation immediately below the Macmillan Pass volcanic suite display a negative 3.2‰ excursion. This thin (≤15 cm) interval coincides with enrichment of trace elements Mo, Ni, Zn, Se, P, As, Ag, Au, Zn and P_2O_5. Isotope data combined with the updated conodont ages indicates an anomalous shale interval age-equivalent to the 'NiMo' or hyper-enriched black shale horizon observed regionally in Selwyn basin, Richardson trough and Kechika trough at the contact between the Road River Group and Canol Formation/Portrait Lake Formation (Earn Group). This interval is also coeval with the Kačák Event, a global biocrisis that spans the Eifelian–Givetian boundary and is characterized in the marine realm by a condensed section of black shale sedimentation, sea-level instability, a negative isotopic excursion and pelagic faunal changes (*i.e.*, massive extinction followed by a radiation). Whether the strata at Macmillan Pass records this global event requires further biostratigraphic control; however, its presence would be a significant marker for the Eifelian–Givetian boundary in eastern Selwyn basin. Unlike other NiMo occurrences elsewhere in Yukon, this anomalous shale interval at Macmillan Pass is overlain by volcanic rocks. The local influence of the Macmillan Pass volcanic suite on metal concentrations and on the carbon isotopic signature in underlying shale also requires further examination.

* tiffani.fraser@yukon.ca

Introduction

Yukon Geological Survey (YGS) examined historical core at Macmillan Pass (Mac Pass) in summer 2019 as a reconnaissance study for future fieldwork in the area. The research is part of a regional study looking at the lithogeochemistry of shale sections in Selwyn basin to define the regional stratigraphic framework and evolution of the basin to facilitate paleogeographical reconstructions, depositional models, improve correlation, and provide age control of thick shale units. This paper presents lithogeochemical and organic carbon isotopic data from selected drill core on the Tom property that provide baseline information on Middle–Upper Devonian shale packages in the region. Presented are geochemical profiles that offer proxies for paleoenvironmental sediment source and proximity to carbonate banks and shorelines, redox conditions of bottom water and associated organic matter preservation, and relative sea level change. A negative organic carbon isotopic excursion and enrichments of Ni, Zn and Mo near the upper contact between the Sapper Formation (Road River Group) and the Macmillan Pass volcanic suite may correlate to the global Kačák Event, a late Eifelian–early Givetian bioevent that records a sea-level transgression, anoxic conditions in the marine realm, and a turnover in pelagic fauna (e.g., House, 1996; Walliser, 1996; Schöne, 1997; DeSantis, 2010; Elwood et *al.*, 2011). We also explore the possibility that this metal-enriched interval of the uppermost Sapper Formation is the local expression of the Middle Devonian hyper-enriched black shale (HEBS) mineralization (locally known as the NiMo horizon) observed elsewhere in Selwyn basin and Richardson trough at the Eifelian–Givetian (Middle Devonian) boundary. Eleven slides containing conodonts from a previous bedrock mapping project in the Macmillan Pass region were re-examined for further age refinement. Presented herein are biozonal ranges for Early to Middle Devonian-aged conodont collections that constrain the contact between the Road River Group (Sapper Formation) and Earn Group (Portrait Lake Formation) to the Late Eifelian *australis-ensensis* biozones.

Location

Mac Pass is in eastern Yukon near the border with the Northwest Territories, at the northeastern end of the North Canol Road, ~200 km from the community of Ross River (Fig. 1). The region north of the Canol Road lies in the Traditional Territory of the First Nation of Na-Cho Nyäk Dun, and to the south of the road, the Traditional Territory of the Ross River Dena Council and Liard First Nation (Kaska Dena Council). Macmillan Pass proper forms a broad valley at the head of the South Macmillan River that transects the Selwyn Mountains at an elevation of ~1360 m. The surrounding landscape is mountainous with surrounding peaks attaining >2000 m.

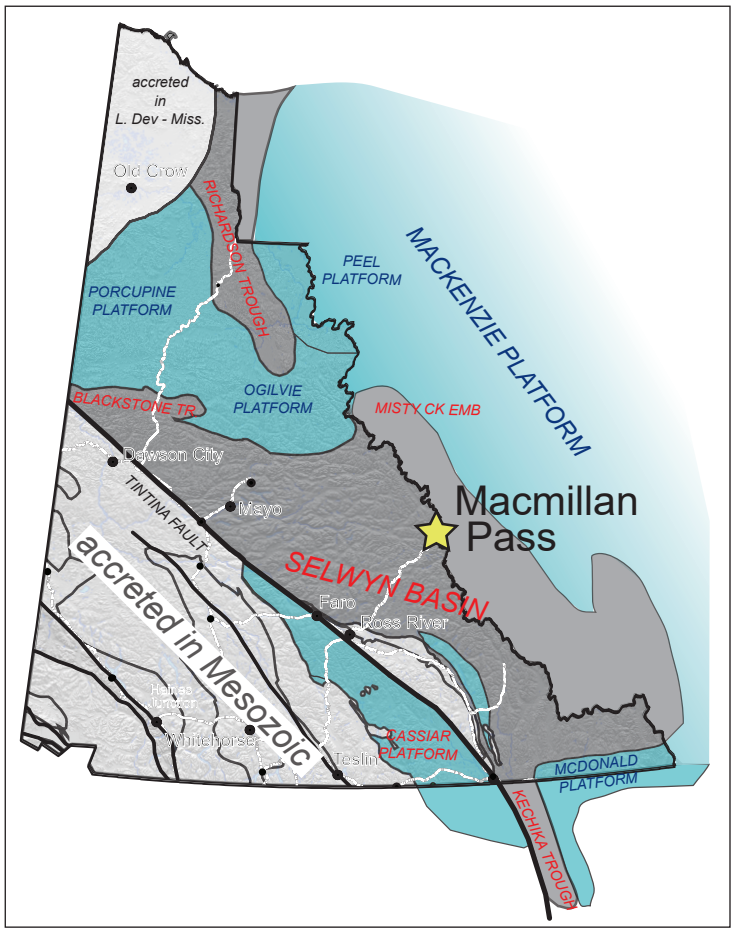

Figure 1. *Lower Paleozoic paleogeographic elements in Yukon (after Nelson and Colpron, 2007) highlighting Paleozoic carbonate platforms (blue) and basins (dark grey with red text) on the Laurentian margin. Macmillan Pass occurs in the east-central part of Selwyn basin at the border between Northwest Territories and Yukon. Younger terranes (Late Paleozoic and Mesozoic) are shown in light grey. White lines are roads.*

The Macmillan Pass region is known for the Tom and Jason Zn-Pb-Ag deposits, and the Boundary and End Zone mineralization systems (Fig. 2). Tom and Jason have a combined mineral resource of 11.2 Mt Indicated at 6.59% Zn, 2.48% Pb and 21.33 g/t Ag, in addition to 39.5 Mt Inferred at 5.84% Zn, 3.14% Pb and 38.15 g/t Ag (Arne and McGarry, 2018). Since discovery of the Tom deposit in 1951, the claims have undergone various ownership changes; in 2018 Fireweed Zinc Ltd. (Fireweed) acquired the Tom and Jason properties from Hudson Bay Mining and Smelting Company. A trailer camp and core storage facility are situated on the Tom property (63.1645°N, -130.1589°W). Fireweed has been drilling seasonally and using the camp since 2017.

Macmillan Pass Stratigraphy and Tectonic Setting

This paper uses the lithostratigraphic nomenclature of Abbott (2013), shown in Figure 3, however, it is recognized that different naming conventions occur in the literature (e.g., Carne, 1976; Abbott 1983; Abbott and Turner, 1991; Goodfellow and Rhodes, 1991) and that many names originated in publications from adjacent areas (e.g., Gordey and Anderson, 1993; Cecile, 1982, 2000).

Cambrian–Middle Devonian rocks of the area were deposited in Selwyn basin—a depocentre close to the NW margin of Laurentia (ancestral North America) that lay outboard of contemporaneous carbonate platforms (Gordey and Anderson, 1993; Gabrielse, 1967; Fig. 1). Neoproterozoic to lower Cambrian strata include clastic sedimentary rocks that formed during formation of the Laurentian margin, namely the Narchilla and Vampire formations (Fig. 3). These are overlain by latest early to middle Cambrian clastic and carbonate units (Sekwi, Gull Lake and Hess River formations) that record intermittent extension prior to the establishment of a more stable carbonate platform and basin configuration in the latest Cambrian to Ordovician (Dilliard et *al.*, 2010; Cecile, 1982; Gordey and Anderson, 1993; Fig. 1). At Macmillan Pass, Ordovician to Middle Devonian strata are assigned to the basinal Road River Group (Duo Lake, Steel and Sapper formations), which comprise siliceous shale, chert, variably calcareous siltstone and shale, and lesser limestone/dolostone. The Middle Devonian is marked by intermittent volcanism (Macmillan Pass volcanic suite), and black siliceous shale and chert deposition (Sapper Formation and Portrait Lake Formation–Niddery Lake Member). The Macmillan Pass volcanic suite is an informal stratigraphic term to describe carbonate-altered alkalic mafic volcaniclastic rocks that occur in at least two stratigraphic intervals: at the contact between the Earn and Road River Groups, and within the Macmillan Pass member, Portrait Lake Formation, Earn Group. During the Late Devonian, the North American margin transitioned to an active convergent margin (Nelson et *al.*, 2006) and the Mac Pass region experienced back-arc extension marked by normal faults and the deposition of the Earn Group coarse clastic sequence (chert pebble conglomerate of the Portrait Lake Formation–Macmillan Pass Member; Abbott and Turner, 1991). Sub-seafloor replacement of barite by sphalerite and galena occurred during Late Devonian time, resulting in formation of the Tom and Jason Zn-Pb-Ag ± Ba deposits (Magnall et *al.*, 2020). This mineralization event was occurring during a background of siliceous shale and chert deposition of the Fuller Lake Member (Portrait Lake Formation). Strata of the Selwyn basin region were later incorporated into the Mesozoic Cordilleran fold and thrust belt. In the study area, major Mesozoic right lateral strike slip faults (Macmillan and Hess fault zones; Fig. 2), that reflect pre-existing Devonian rift structures, divide the area into the North, Central and South blocks (Abbott, 1983; Abbott and Turner, 1991. The new data presented in this paper are from the Central Block, also the location of all Macmillan Pass Devonian Zn-Pb-Ag deposits, although some of the older conodont samples derive from the North Block (Fig. 2).

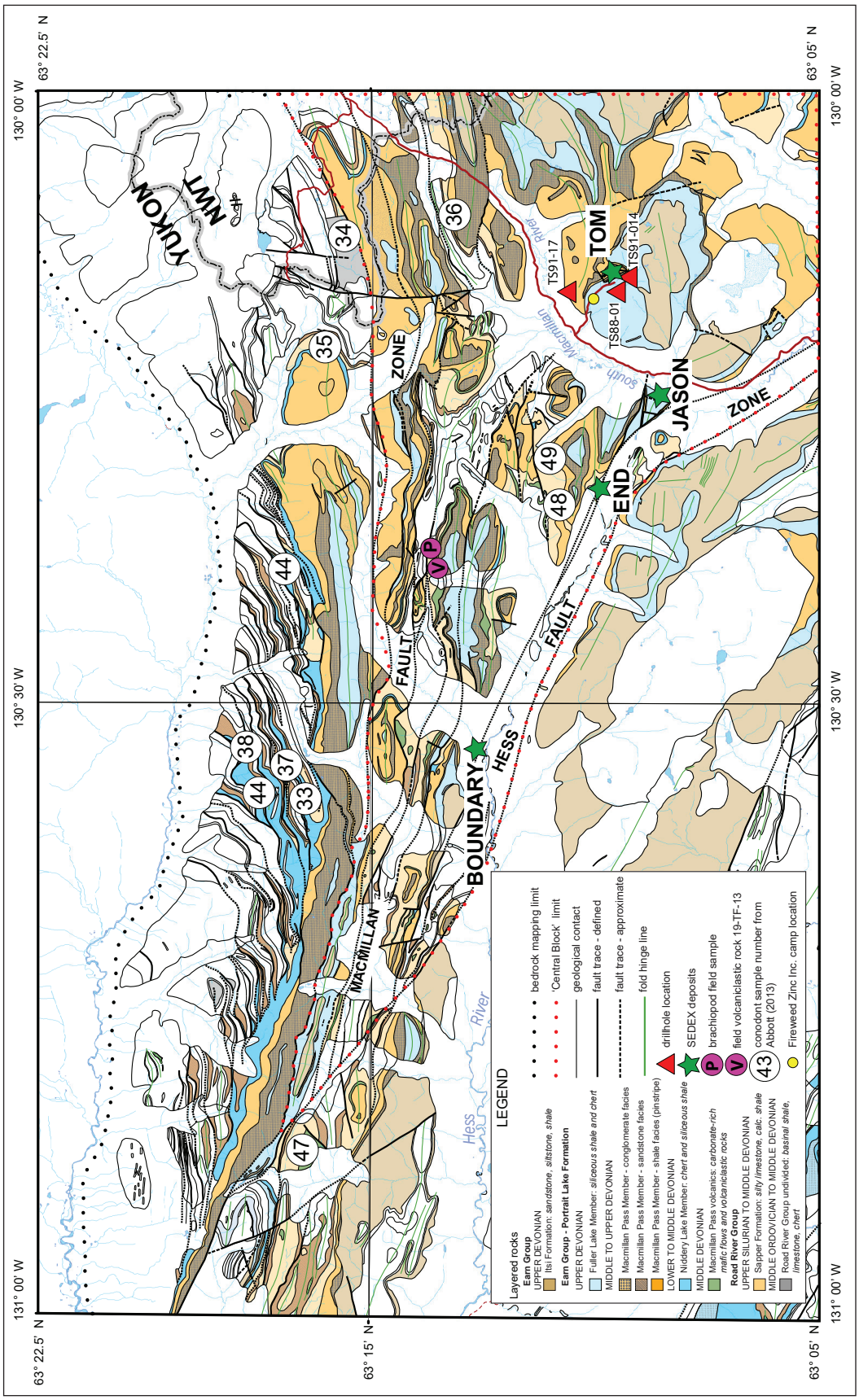

Figure 2. *Simplified geology map of Macmillan Pass area highlighting Devonian strata and the location of the 'Central Block' (after Abbott, 2013). Locations of the Zn-Pb-Ag deposits, drillholes and field data presented in this paper are included.*

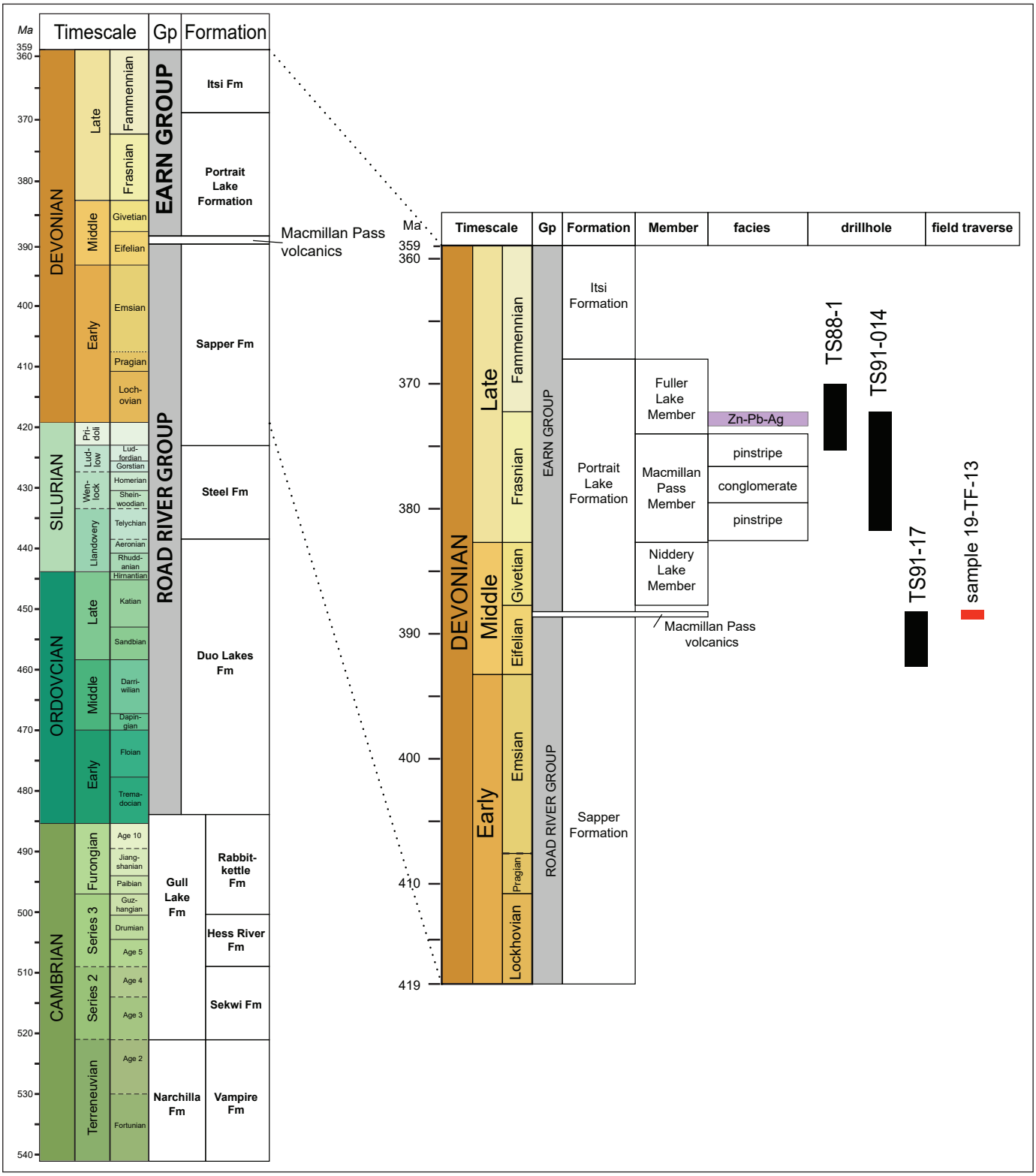

Figure 3. *Chronostratigraphy of the Devonian units at the Jason deposit, Macmillan Pass, Yukon, highlighting the Devonian section (after Abbott, 2013). Drillhole and field traverse strata examined in this study are highlighted. Geological timescale from Gradstein et al., (2012).*

Methods

Core logging and lithogeochemistry

Core looked at for this reconnaissance study are from holes drilled on the Tom property and include T88-1 (63.1553°N, -130.1535°W), TS91-17 (63.1760°N, -130.1765°W), and TS91-014 (63.1585°N, -130.1504W; Fig. 2), and were chosen because they covered extended parts of Devonian basinal rocks. Core was logged onsite; however, boxes 1–16 of TS91-014 are stored at the YGS Bostock Core Library in Whitehorse and were logged there. The focus of the study was to sample Devonian shale intervals to evaluate background shale lithogeochemistry, and therefore finer grained intervals were sampled and analyzed. Sample spacing was in 2 m increments for holes T88-1 and TS91-17 (n = 73 and 15, respectively), and 1 m for TS91-14 (n = 53). Whole rock lithogeochemistry, including total organic content for shales, was conducted at Bureau Veritas in Vancouver, BC using ICP-ES and ICP-MS instrumentation. Selected geochemical profiles that assist with paleoenvironmental interpretation such as terrestrial sediment source, proximity to carbonate platforms and continental shorelines, redox conditions and organic matter preservation, and relative sea level are presented in the results section. Geochemical results are provided in the Appendices.

Fifty-three shale samples from drillhole TS91-17 were analyzed for organic carbon isotope signatures at the Pacific Centre for Isotopic and Geochemical Research, Department of Earth Ocean and Atmospheric Sciences, The University of British Columbia, Vancouver, with a mass spectrometer. Carbon isotopic values are normalized to the Vienna PeeDee Belemnite (V-PBD).

Twenty-nine thin sections were made from the drill core, however, these were mainly limited to coarser grained intervals due to rock competency. Thin sections were prepared at Vancouver Petrographics using standard procedures.

The use of paleoenvironmental proxies

This study focuses on a subset of geochemical data used to 'blueprint' relatively monotonous shale intervals and to make high-level paleoenvironmental interpretations about their deposition. Proxies for terrestrial input used to distinguish relative proximity to a continental shoreline include the relationship between SiO_2 (%) and Zr (ppm) and the terrestrial input parameter (TIP; %) which is the sum of Al_2O_3, TiO_2, Na_2O and K_2O (%; after Hildred and Rice, 2012). These proxies assume that Zr and the oxides of Al, Ti, Na, and K are land-derived and immobile during diagenesis (Hildred and Rice, 2012; Tribovillard *et al.*, 2006), and that their relative increase/decrease can be related to sea level fluctuations and proximity of the basin to shoreline. A cross-plot of SiO_2 *vs.* Zr can indicate either a terrestrial source for the silica or a biogenic source, for positive and negative covariations, respectively. A high biogenic silica content in the sediments can indicate high bioproductivity in the water column by organisms that secrete silica tests (*e.g.*, radiolarian) and a low input of silica from terrestrial sources *i.e.*, further offshore. These terrestrial and silica source proxies would not apply in strata overwhelmed by a Zn-Pb-Ag mineralizing event, as silica can be sourced via hydrothermal inputs and oxides can be mobilized, thus erasing primary depositional characteristics (*e.g.*, Magnall *et al.*, 2015).

Redox conditions in sea bottom waters and degree of organic matter preservation can be cautiously identified from the total organic carbon content (TOC; weight %), under the premise that organic material is preserved under reducing conditions. Further, the enrichment factor (Ef) of Mo (*i.e.*, Mo normalized to Al using the formula $(Mo_{sample}/Al_{sample})/(Mo_{average\ shale}/Al_{average\ shale})$ from Tribovillard *et al.*, 2006) can be used to indicate redox conditions as Mo becomes relatively immobile and authigenically enriched as its solubility falls in oxygen-depleted water (Algeo and Rowe, 2012; Tribovillard *et al.*, 2006). Proxies for carbonate content, which can be used to indicate proximity to carbonate sediment sources, include CaO (%) and MgO (%); however distinguishing between primary and secondary carbonate is essential.

The marine $\delta^{13}C_{org}$ curve presented is used in an attempt to date and correlate Macmillan Pass Sapper Formation sediments to strata in other parts of Selwyn basin and beyond. The ratio of $^{13}C/^{12}C$ in the oceans and recorded in basinal sediments varies through time, and there are time intervals where well documented excursions, either positive or negative, have been identified regionally and/or globally (e.g., Saltzman and Thomas, 2012). The Devonian Period has several excursions, often associated with extinction events (e.g., basal Lochkovian positive excursion, late Eifelian Kačák-otomari negative excursion, Frasnian–Famennian Upper and Lower Kellwasser positive excursion events, and the terminal Devonian Hangenberg positive excursion; Saltzman and Thomas, 2012). A $\delta^{13}C_{org}$ excursion could indicate higher ocean bioproductivity and/or organic matter preservation as a result of high sea level, as the ratio of $^{13}C/^{12}C$ the ocean increases when there is a net deposition of organic matter globally (Saltzman and Thomas, 2012). Conversely, a negative $\delta^{13}C$ excursion could represent lower ocean bioproductivity and/or lower organic matter preservation because of relative sea level regression, as the $^{13}C/^{12}C$ ratio in the ocean will decrease when there is a net oxidation of organic matter globally. However, interpreting sea level from this limited data set beyond the immediate region is challenging.

Field transect

Thirteen kilometres northwest of the Tom property, a field traverse through Sapper Formation and Macmillan Pass volcanic suite rocks investigated uppermost Road River strata in the region (Fig. 2). One sample of volcaniclastic rock (63.2282°N, -130.3811°W) was analyzed for whole rock geochemistry at ALS Minerals using XRF, ICP-AES and ICP-MS techniques. A Devonian brachiopod sample from the upper contact of the Sapper Formation was submitted to Robert Blodgett, Anchorage, AK, for identification.

Conodont biostratigraphy

Eleven slides made for conodont identification and reported in Abbott (2013; Fig. 2) were re-examined as part of this reconnaissance study. These samples were processed previously in the Geological Survey of Canada's paleontological laboratory in Calgary, and were retrieved from the archives for this study. The samples examined are of Middle Devonian age, from the Sapper Formation (n = 2), the Portrait Lake Formation (Niddery Lake Member; n = 8) and a shale clast in the Macmillan Pass volcanic suite (n = 1). This particular age range was selected to assist in correlation of this time interval to other areas in Selwyn basin and Richardson trough, the focus of previous and ongoing YGS shale research.

Lithology and geochemistry of drill core

TS88-01

Lithology

Drillhole TS88-01 is collared in the Fuller Lake Member (Portrait Lake Formation) rocks, transects Zn-Pb-Ag mineralization between 524 and 554 m depth and terminates at a depth of 649.8 m in the Macmillan Pass Member shale facies (Portrait Lake Formation; Fig. 4a). The Macmillan Pass Member is mainly rhythmically interbedded packages of fining upwards fine to very fine sandstone and siliceous siltstone and shale. The colour of the weathered surface is alternating brown/red (sandstone), medium grey (siltstone) and black (shale) which gives the unit a striped appearance (sometimes called the 'pinstripe' unit; Fig. 4b). Overall this unit is well indurated and core is competent, although there are some more rubbly sections which are fractured. Pyrite cubes are visible in sandier intervals (Fig. 4b), and disseminated pyrite is observed in shale sections. Individual fining upward intervals are variable but are mainly 5 to 10 cm thick, beginning with a basal sandstone that scours into underlying shale, and occasionally displays flame and load structures (Fig. 4b), fining upwards to siliceous siltstone and shale. Sandstone becomes less prominent towards the top of the member.

The Fuller Lake Member is dominated by siliceous shale and radiolarian chert, with lesser siltstone and minor fine to medium sandstone. The strata occur in rhythmically fining upward packages of silty siliceous shale to shale (or sandstone to shale in minor instances), generally 5 to 15 cm thick. The chert and shale are black on fresh surfaces, and weather medium to dark grey.

Weathered faces and fractures are sometimes coated with a yellow or green, and locally a light blue, weathering residue. In sandier sections, the core weathers orange/brown. Sandstone comprises mainly quartz, chert and lithic grains, is poorly sorted, and is cemented by carbonate with lesser quartz and locally with pyrite. Overall the core is competent; however, there are minor fractured intervals, and intervals of recessive, very soft, wafer-thin shale at the top of some fining upward intervals. Disseminated, nodular and laminated pyrite occurs throughout the member. Minor brecciated fault sections occur particularly in the upper 250 m of the hole.

A Zn-Pb-Ag mineralized zone in the lower Fuller Lake Member is 26 m thick and occurs as laminated barite, sphalerite and pyrite, with >5% interlaminated shale (Fig. 4c). Barite is white to yellowish white in colour, and where laminated with sphalerite, it is pink and light brown. Laminae are crenulated to wavy in appearance. The lower and upper contacts of the mineralized zone are gradational where barite laminae increase/decrease over ~30 cm thicknesses, respectively.

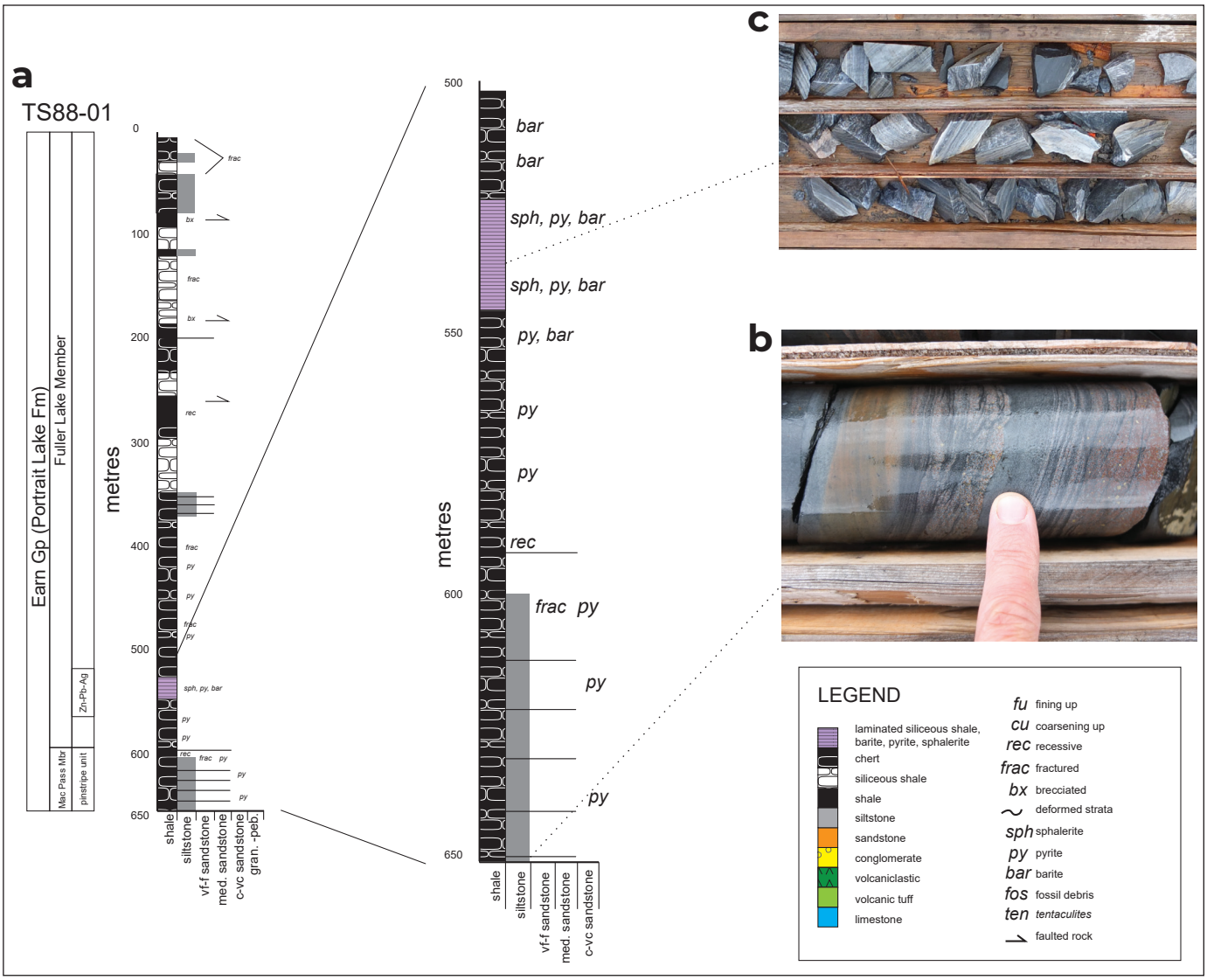

Figure 4. ***(a)*** *Lithology log of the TS88-01 core.* ***(b)*** *Strata from the Macmillan Pass Member ('pinstripe unit') at the base of the core (643.2 m). Note the weathering colour of the sandstone (red), siltstone (orange) and shale (dark grey to black), which gives the core a unique striped appearance. Finger is pointing just below the base of a fining upward unit of sandstone to shale, where loading of sandstone onto shale is apparent.* ***(c)*** *Laminated barite, shale and sphalerite from the Zn-Pb-Ag mineralized unit (530 m).*

Geochemistry

Whole rock geochemistry was conducted on samples collected between 509 and 650 m (Macmillan Pass and Fuller Lake members, including the Zn-Pb-Ag zone). Selected geochemical data are shown in Figure 5 and a full data set is offered in Appendix A. The Macmillan Pass Member pinstripe unit (596–649.8 m) has an average of 73% SiO_2, 143 ppm Zr and a TIP of 15%. While SiO_2 values remain constant throughout the unit, Zr and TIP values overall decrease towards the top of the unit. Total organic content averages 1.3 wt% and values increase in the upper 2 m of the unit. The Ef Mo averages 7.2; values are more than double the average in the upper 2 m. Carbonate content in the unit is low; CaO and MgO average <1%, with a very slight increase in the interval 622–628 m. Elements associated with mineralization in this unit including Ba, Zn and Pb are low, averaging 0.6%, 7 ppm and 27 ppm, respectively.

The lower Fuller Lake Member (556–594 m) averages 75% SiO_2, 92 ppm Zr and 9% TIP, and all values decrease towards the top of the unit. TOC averages 3.8% with the highest value of 6.4% in a recessive, sooty shale unit at 590.6 m. Overall, TOC decreases slightly towards the top of the unit. The Ef Mo values average 29 and trend overall higher toward the top of the unit. Carbonate content is very low at <1% for both CaO and MgO. Elements associated with mineralization all increase significantly moving up in the lower Fuller Lake Member. Both Ba and Zn increase from minimal values to the upper limits of the instrumentation detection (5% and 10 000 ppm respectively) and Pb trends from <100 ppm to >300 ppm in the top 6 m in the unit.

The Zn-Pb-Ag mineralized interval (523–556 m) has an average of 29% SiO_2, 33 ppm Zn and 2.5% TIP, which are the lowest values of the strata measured in the core in this study. These values are not credible for use as proxies, as their presence does not represent primary

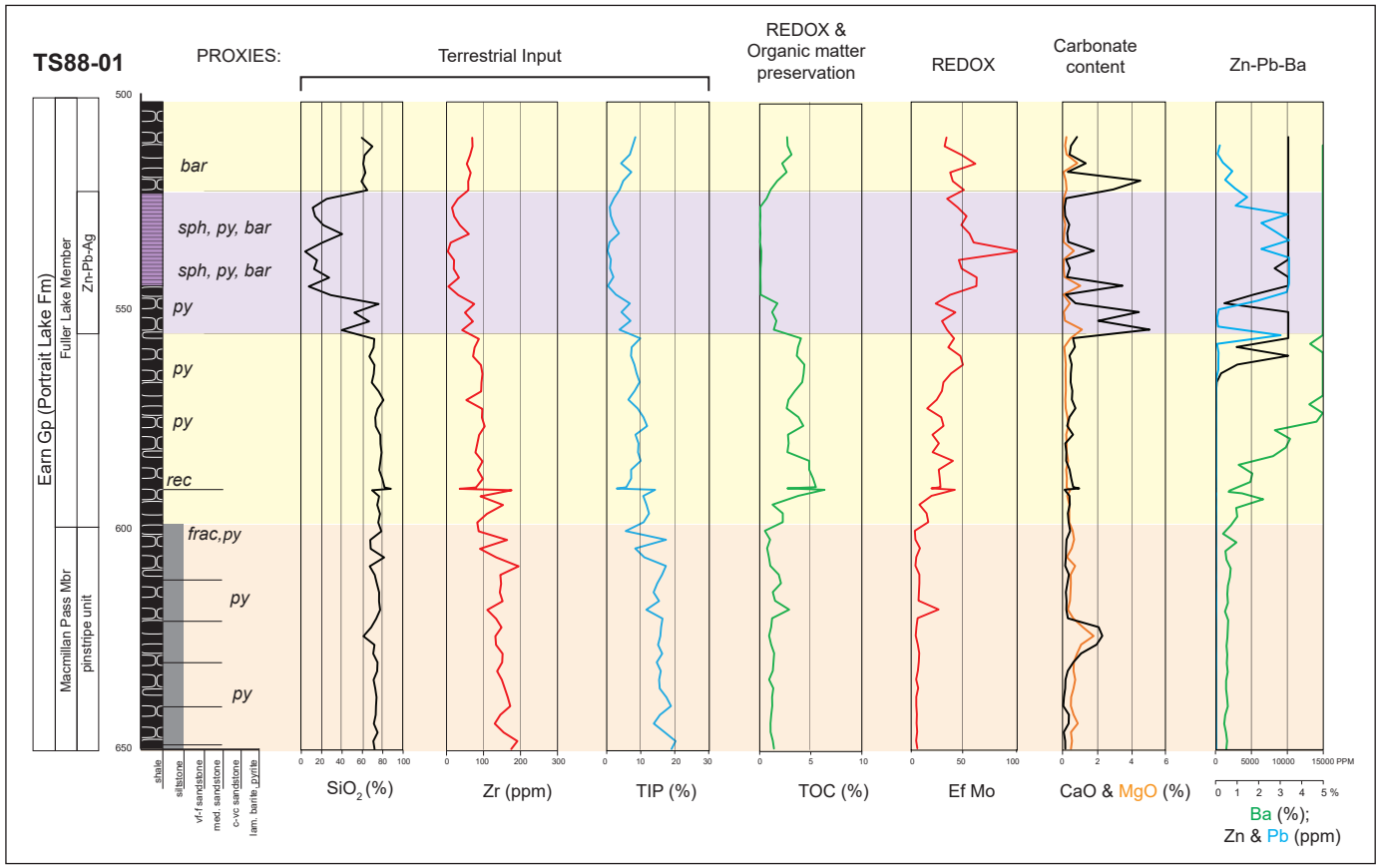

Figure 5. *Selected lithogeochemistry from the TS88-01 drillhole.*

depositional conditions. TOC values are also very low, averaging 0.5% while Ef Mo measures 49 with a peak value of 103 at 536 m. Carbonate content peaks in the base of the section at 51% CaO and 1.1% MgO, and trends downwards towards 0.2 and 0.1%, respectively, at the top of the unit. For elements associated with mineralization, Ba is consistently >5%, all but three samples of Zn are >10 000 ppm, and Pb is more variable, pushing the upper limits of the instrument at 10 000 ppm in five samples or being as low as 164 ppm. While Ba and Zn remain consistently high over the contact with the overlying Fuller Lake Member shale, Pb concentrations trend downward.

The upper Fuller Lake Member (510–523 m) averages 63% SiO_2, 63% Zr, 6.1% TIP and 2.3% TOC, all lower values than in the lower Fuller Lake Member below the Zn-Pb-Ag interval. Ef Mo is 43 and carbonate content decreases from 3.0% at the base to <1% at the top of the section, averaging 1.6%. MgO values are all <1%. Ba and Zn levels are all above the instrumentation thresholds of 5% and 10 000 ppm, respectively, and Pb declines from base to top from 4288 to 554 ppm, with an overall average of 1747 ppm.

SiO_2 and Zr values were plotted against each other to assess the source of silica and proximity to paleoshorelines. Zr is assigned as a proxy for a terrestrial source, whereby a positive SiO_2 *vs.* Zr relationship is suggestive of a land source for the silica and a negative relationship suggestive of a biological source, e.g. radiolarian, from within the water column (e.g., Wright *et al.*, 2010; Fraser and Hutchison, 2017). The plotted data, grouped according to unit, are presented in Figure 6a. A strong positive trend ($R^2 = 0.90$) is shown for the mineralized interval, which is best interpreted as a "terrestrial + hydrothermal" silica source. A weak terrestrial trend occurs for the upper Fuller Lake Member ($R^2 = 0.16$), a weak biogenic trend is shown for the lower Fuller Lake Member ($R^2 = 0.21$), and no trend was noted for the Macmillan Pass Member ($R^2 = 0.06$).

TS91-014

Lithology

Drillhole TS91-014 is collared in a Zn-Pb-Ag mineralized zone of the lower Fuller Lake Member (Portrait Lake Fm) and terminates at a depth of 522.4 m in the Macmillan Pass Member shale ('pinstripe' unit; Fig. 7a). This core was logged to a depth of 394.8 m as strata below this are duplicated by faulting. The Macmillan Pass Member shale interval occurs as rhythmically interbedded packages of fining upwards, fine to very fine sandstone, siltstone and shale between 100 and 394 m depth. Sandstone intervals weather orange/red/brown, siltstone weathers medium grey and red, and shale weathers dark grey, and weathering gives the unit a striped appearance (Fig. 7b). Cycles are variable in thickness, mainly 2–30 cm thick, and are generally dominated by siltstone and silty shale, however, sandstone comprises 5–30% of the cycles. Siltstone and shale are planar laminated, and sandstone may be cross-laminated. Sandstone and siltstone grains are chert and quartz, which are cemented with carbonate. Cycle bases, particularly where sandstone is present, are often erosive and may show flame and load structures. The core is competent with brecciation of some faulted intervals. Pyrite is abundant, particularly in sandstone intervals, although it can be observed in all lithological units as nodules, laminae or dissemination.

A 2.5 m thick interval of chert pebble conglomerate with carbonate cement occurs at a depth of 142.35 m; which fines upward to coarse-grained sandstone. The Macmillan Pass Member conglomerate facies proper occurs as a thick interval between 49.8 and 100 m depth. The conglomerate is dominated by pebble-sized chert and lesser quartz and lithic (sandstone, siltstone, shale) clasts with localized cobbles (6 cm maximum clast length observed). Chert grains are black, grey and white, and quartz grains are white. Clasts are mainly subangular to subround. Sorting is poor, and both matrix and clast-supported strata occur (Fig. 7c). Chert pebble clasts in a deformed shale matrix with up to 20% sparry carbonate matrix and pervasive pyrite mineralization mark the basal contact of the Macmillan Pass Member. The contact appears relatively sharp and is interpreted as conformable.

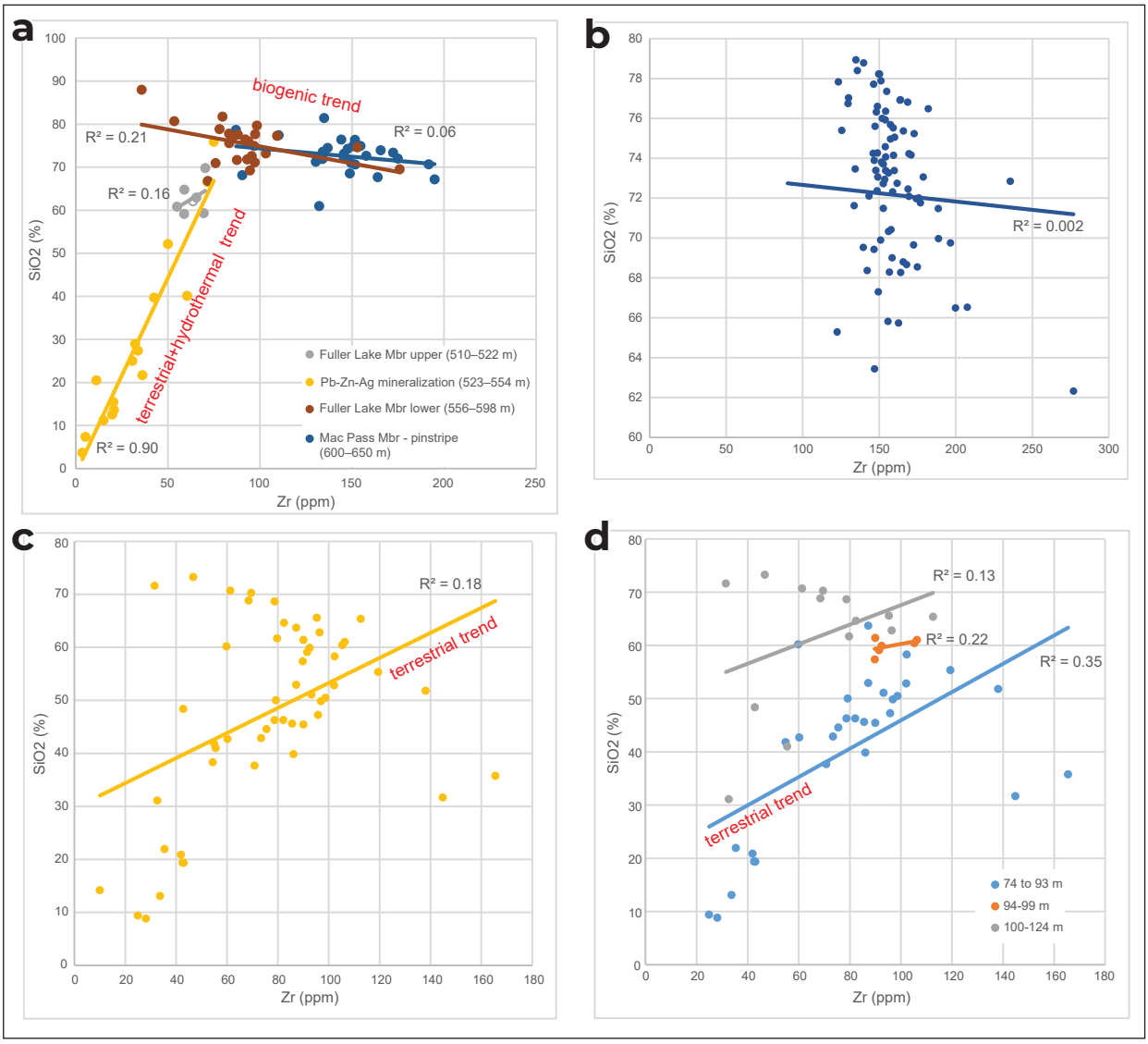

Figure 6. *SiO_2 versus Zr cross-plots for the* **(a)** *TS88-01 drillhole;* **(b)** *TS91-014 drillhole;* **(c)** *TS91-17 drillhole (full data set); and* **(d)** *TS91-17 drillhole (divided data set).*

The Fuller Lake Member is a variably siliceous, black, laminated shale. Its lower contact is characterized by brecciated to stratified shale with abundant pervasive pyrite. The contact zone is unconsolidated, appears weathered or rotten, and has abundant grey and brown mineral precipitate. Below the Zn-Pb-Ag interval, the Fuller Lake shale has abundant pyrite, both laminated and pervasive, and is crosscut by ≤1 cm thick barite veins. The Zn-Pb-Ag unit is hosted by laminated shale and comprises wavy/crenulated laminae of shale, pyrite, sphalerite and barite, which occur as black, green, pink and white laminae, respectively (Fig. 7d). Small, synsedimentary faults and dewatering structures are observed. Shale becomes more dominant towards the upper part of the mineralized unit (Fig. 7e) and grades into a black, laminated siliceous shale that is unconformably overlain at surface by a post-glacial, Holocene thin (<1 m) unit of iron-stained ferricrete pebble conglomerate.

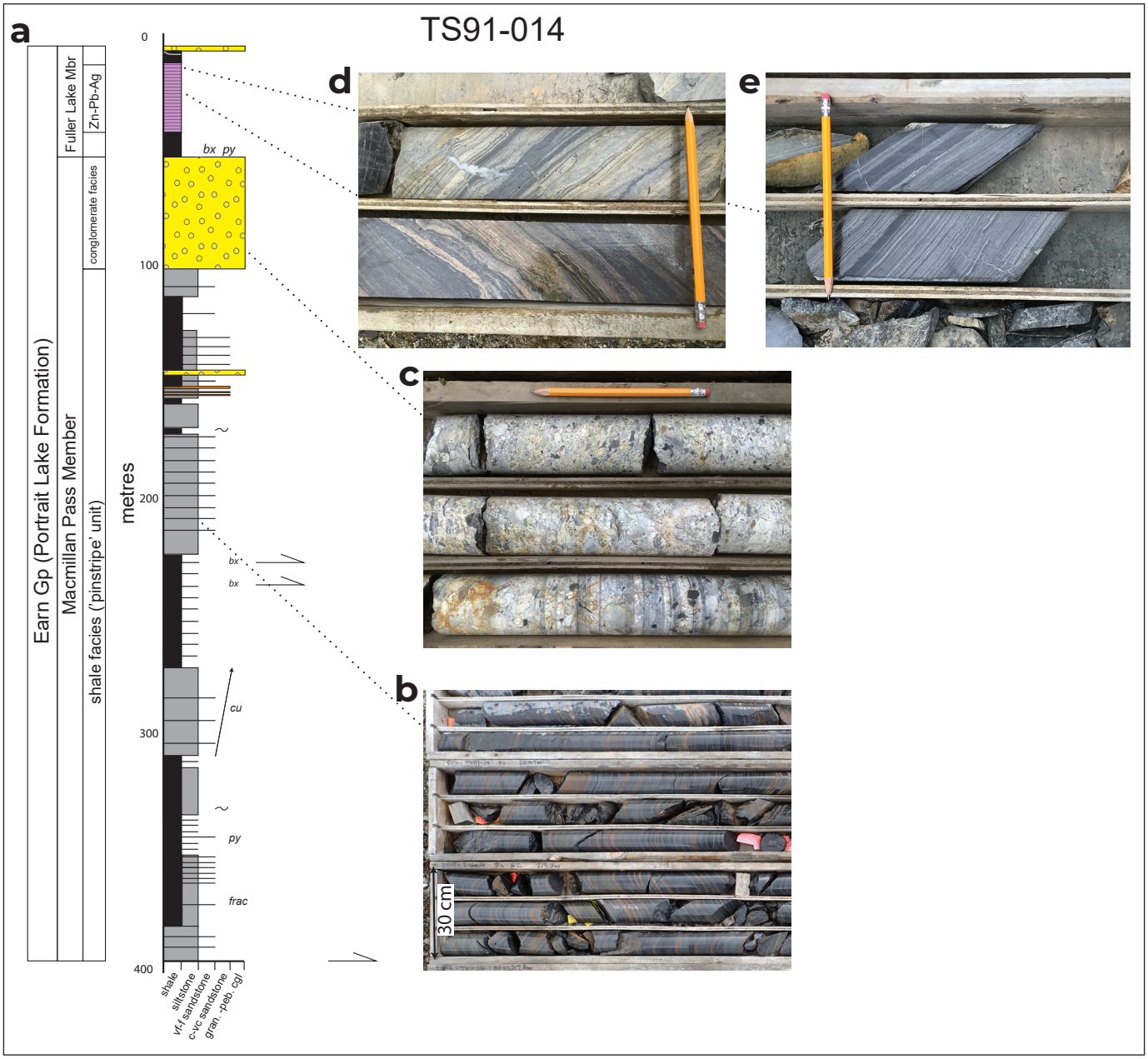

Figure 7. ***(a)*** *Lithology log of the TS91-014 core. Legend in Figure 4.* ***(b)*** *Macmillan Pass Member shale facies, showing 'pinstriped' nature of the core due to the interbedding of iron-oxidized sandstone and siltstone with shale (red and black laminae, respectively).* ***(c)*** *Chert pebble conglomerate of the Macmillan Pass Member conglomerate facies.* ***(d)*** *Stratified shale, pyrite, sphalerite and barite in the Fuller Lake Member, laminated pink-grey facies.* ***(e)*** *Stratified shale and barite in the uppermost laminated black facies as it grades upsection to a siliceous shale.*

Geochemistry

Geochemical analyses were conducted on samples collected between 103.6 and 394.0 m in the Macmillan Pass Member–pinstripe unit (Fig. 8). SiO_2 ranges from 54 to 79% with an average of 72%, and values become slightly more enriched near the top of the unit. Zr averages 157 ppm and ranges from 90 to 277 ppm. Zr enrichment is slightly elevated in the intervals between 286 and 210 m and 360.1 and 370 m; it is reduced in the upper part of the unit between 103.6 and 130 m. TIP values average 16%, ranging from 7 to 28%, with a very slight overall decrease towards the top of the unit. Average TOC values are very low in this unit at 0.8% with all but six values <1%; slightly higher values are observed in the top 47 m of the section. Ef Mo increases gradually from the base to the top of the unit and averages 3.2. Carbonate content is low at <1% with some slightly higher values associated with siltier intervals (e.g., 162 m, 186 m, 210 m and intermittently between 314 and 382 m). Ba concentration is constant throughout the interval averaging 0.3%. Zn concentration is below 180 ppm and is cyclical in nature with the highest value of 180 ppm at 114 m. Pb concentration shows an overall increasing trend upsection with a maximum value of 65 ppm at a depth of 134 m.

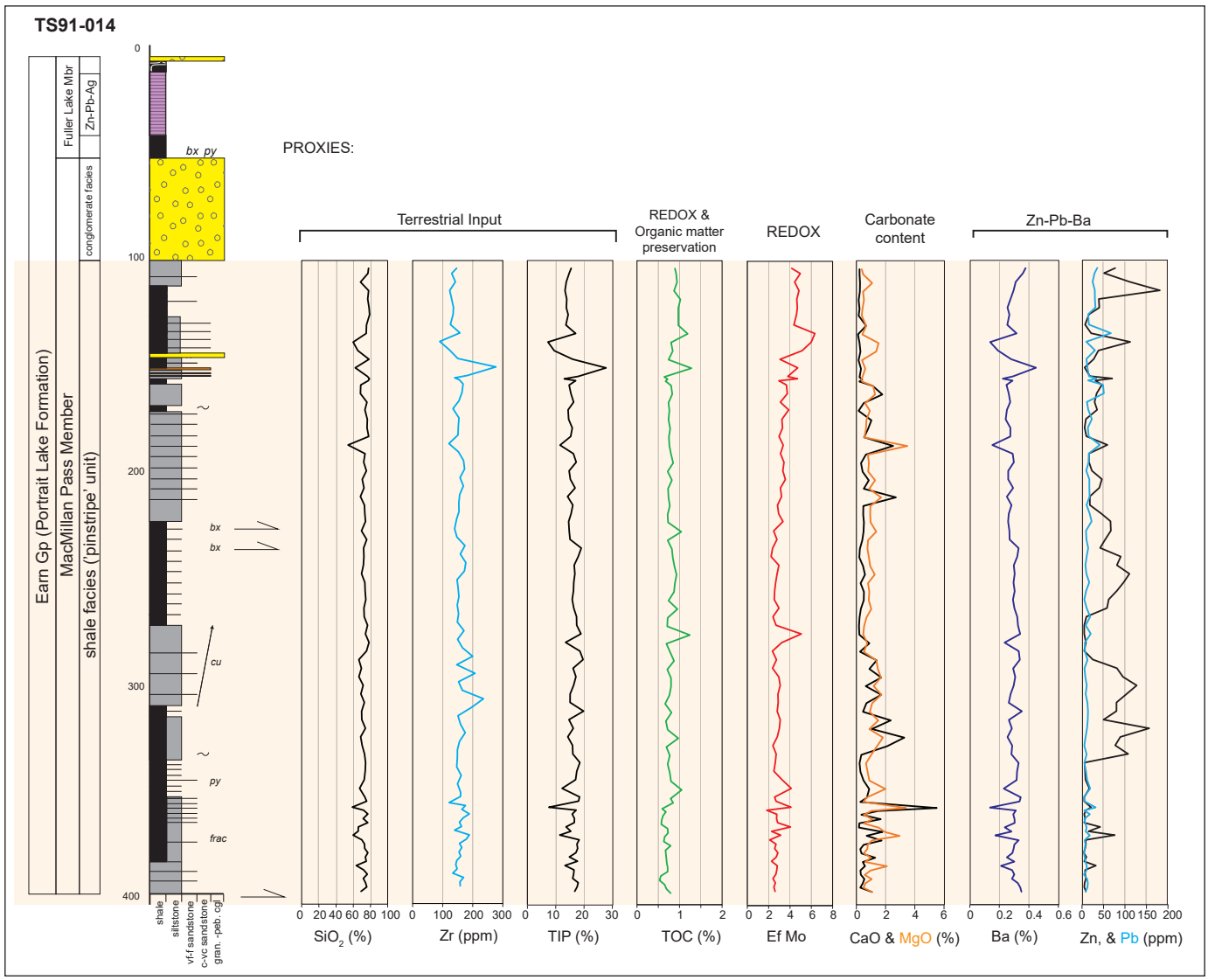

Figure 8. *Selected lithogeochemistry from the TS91-014 drillhole. Legend as in Figure 4.*

The SiO_2 versus Zr plot shows a scatter with no detrital or biologic trend for the silica (Fig. 6b). It is possible that plotting of specific intervals (e.g., fine grained or coarse grained) may indicate shorter episodes of one or the other but this level of detail is beyond the scope of this reconnaissance work.

TS91-17

Lithology

Of the core evaluated, hole TS91-17 covers the oldest stratigraphy. The hole is collared in the Macmillan Pass volcanic suite and terminates at a depth of 127 m in wackestone and micrite of the Sapper Formation (Road River Group; Fig. 9). Organic-rich interlaminated shale/mudstone, lesser siltstone and very minor fine sandstone characterize the Sapper Formation in this hole. Shale/mudstone is mainly dark grey to black on fresh surfaces, weathers dark grey and sometimes bluish-black, and varies between competent and very recessive and sooty. Shale is fissile while mudstone has no visible sedimentary structures. These fine-grained strata are often variably siliceous or calcareous, interbedded, especially towards the upper part of the unit. Siltstone is medium grey on fresh surfaces, weathers green and greenish-grey and is competent. Shale and siltstone are laminated in normally graded rhythmic successions. Mudstone has no visible sedimentary structures. Interbedded wackestone and micrite occur in the lower 2.5 m of the core (Fig. 9b). Wackestone contains fossil debris including crinoids, bivalves and bryozoans, and micrite is laminated with localized small fossil fragments.

The Sapper Formation is sharply overlain by the Macmillan Pass volcanic suite (Fig. 9c), which in this hole occurs as volcaniclastic rock comprising vesicular basalt clasts cemented by carbonate (Fig. 9d). This rock is resistant, medium grey on fresh surfaces and weathers greenish grey with variable brown/orange-staining. Basalt clasts are poorly sorted, range up to 15 mm in length (pebble-sized), and vary from angular to subround. The rock may be either matrix or clast-supported. The proportion of sparry carbonate cement is up to 85%, which also infills vesicles in basalt. The basal contact is sharp with the bottom 5 cm of the unit incorporating shale clasts. A 10 cm tuffaceous interval occurs at a depth 70.0 m, which is dark grey on fresh surfaces and weathers greenish-grey with a white and orange powdery residue. This tuff is very porous and forms a sharp contact, possibly a chilled margin, with the under and overlying volcaniclastic rocks.

Geochemistry

Systematic geochemical analysis was performed on the Sapper Formation up to its upper contact with the Macmillan Pass volcanic suite (Figs. 10 and 11). SiO_2 averages 48%, ranging from 9 to 73%. Higher SiO_2 values generally occur below 94 m, although not consistently. SiO_2 negatively correlates with CaO ($R^2 = 0.8$) showing an alternating pattern of siliceous shale interbedded with calcareous shale. These cycles are thicker below 94 m (e.g., 5–7 m thick) and thinner between 74 and 94 m (e.g., up to 2 m), although in some instances this may be an artifact of sample spacing. Zr values average 77 ppm with the highest values in the uppermost 4 m. A cross-plot of SiO_2 vs Zr shows that all samples trend weakly towards a terrestrial silica source ($R^2 = 0.18$; Fig. 6c), with samples becoming more strongly correlated in the upper parts of the hole at 74 to 93 m ($R^2 = 0.35$ *vs* 0.22 for samples from 94–99 m and $R^2 = 0.13$ for samples from 74–93 m; Fig. 6d). TIP values are <10% between 100 and 126.5 m, average 18% from 93–100 m, and average 10% in the upper part of the hole between 74 and 93 m. Average TOC for the data set is 4.7% with extremely high values of 8.1, 12.4 and 10.4% (average) associated with sooty, recessive shale intervals at 112, 84 and 74–75 m, respectively. Ef Mo values covary with TOC ($R^2 = 0.5$); the highest values (>200 ppm) occur from 120–123 m, 112, 84 and 74–75 m. Carbonate content is highest (>20%) in the lowermost 2 m of the section, is <20% between 93 and 125 m, and is variably high (maximum 47%) and low (minimum 4%) in the upper ~one-third of the data set (74–93 m). Ba averages 0.3% with a notable high value of 2.6% in a recessive shale at 106 m. Zn is mostly <30 ppm with exceptions up to 123 ppm associated with sooty shale intervals at 112, 84 and 74–75 m and a cherty shale at 88 m. Pb values average 43 ppm and range from 3–89 ppm. Ni is plotted with this data set as a redox sensitive element, which shows an overall increase in trend towards the top of the section, particularly in the

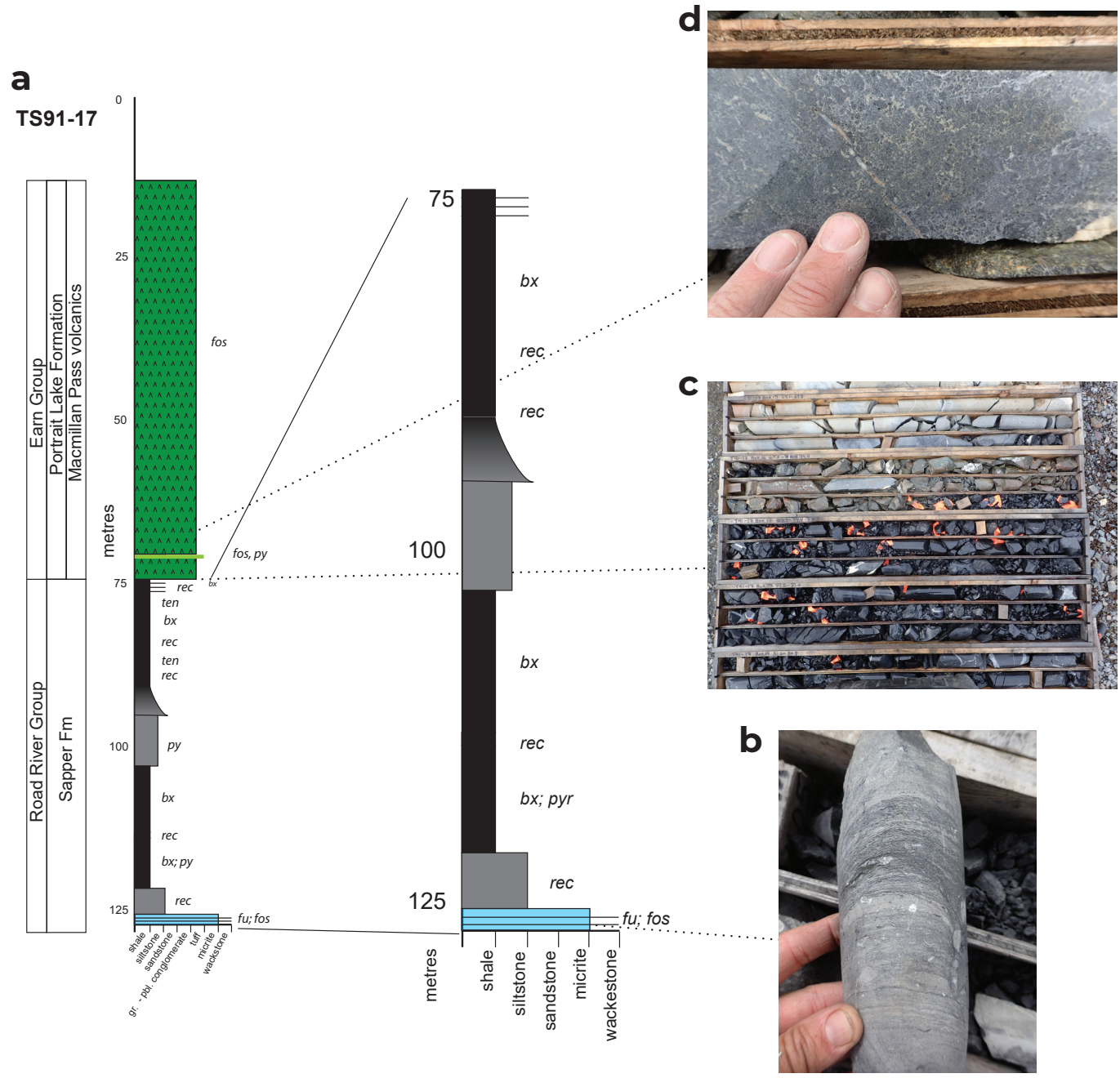

Figure 9. (a) *Lithology log of the TS91-17 core. Legend in Figure 4.* ***(b)*** *Micrite and fossiliferous wackestone at the base of the TS91-17 drillhole (124 m).* ***(c)*** *Contact zone between the Sapper Formation (black rocks in bottom two core boxes) and Macmillan Pass volcanic suite (grey rocks in upper two core boxes).* ***(d)*** *Close-up of volcaniclastic rocks from the Macmillan Pass volcanic suite (72 m).*

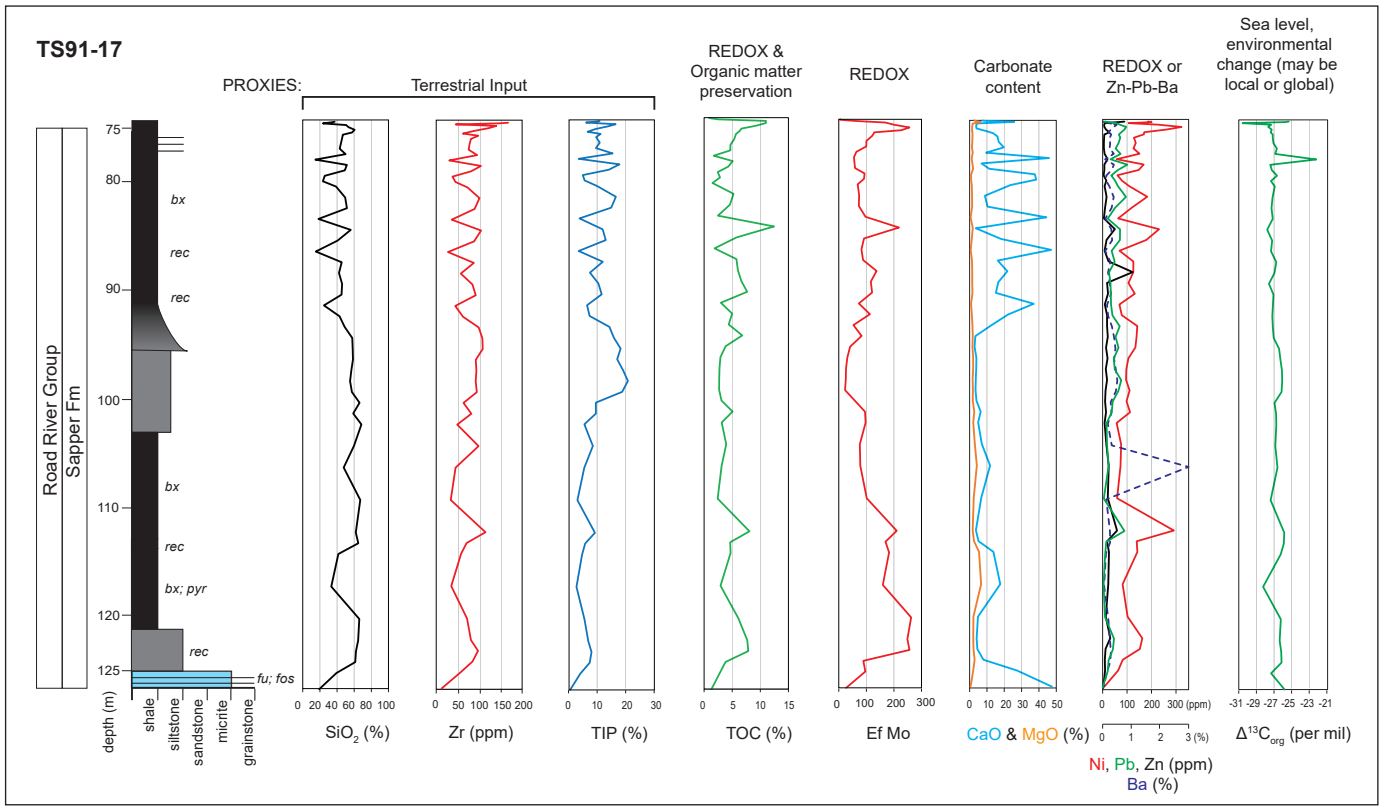

Figure 10. *Selected lithogeochemistry from the TS91-17 drillhole. Legend as in Figure 4.*

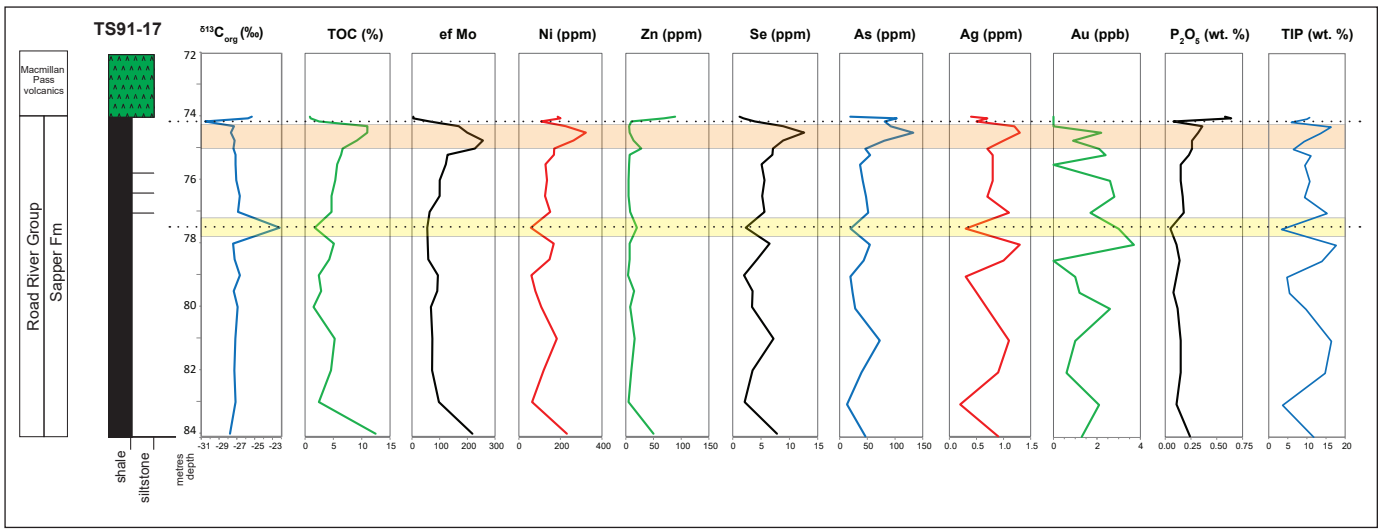

Figure 11. *Geochemistry of the uppermost Sapper Formation from the TS91-17 drillhole. The orange highlighted box indicates the interval of enhanced trace element concentrations in the uppermost Sapper Formation, which immediately precedes a prominent negative 3.5‰ $\delta^{13}C_{org}$ excursion. The yellow highlighted box indicates the interval of lower trace element values and a positive 4.8‰ $\delta^{13}C_{org}$ excursion.*

upper 12 m (74–86 m). Ni spikes occur in sooty shale at 112 and 74.5 m (231 and 323 ppm, respectively). $\delta^{13}C_{org}$ values hover at -27‰ (average of -26.8). There are notable excursions in the uppermost part of the section including a positive one at 77.5 m (-22.2‰), and a negative/positive one at 74.15–74.0 m (-30.56‰ and -25.32‰). More minor excursions occur at 117 m (-28.24‰), 113 m (-25.89‰) and 97 m (-26.1‰).

Details of the trace element geochemistry (Ef Mo, Ni, Zn, Se, As, Ag, Au P_2O_5), TOC, TIP (%) and $\delta^{13}C_{org}$ values from the upper 10 m of the Sapper Formation are shown in Figure 11. There are significant concentration fluctuations in many of the data sets but the overall trend shows an up-section increase in elemental, TOC and TIP concentrations toward the upper contact with the overlying Macmillan Pass volcaniclastic rocks. In contrast, the $\delta^{13}C_{org}$ data show a relatively stable background state of ~-27‰, with a large positive excursion of 4.8‰ at 77.5 m and a prominent negative excursion of 3.5‰ at a depth of 74.15 m. The 77.5 m positive $\delta^{13}C_{org}$ excursion is associated with lower values in all trace elements, TIP, and TOC, except for Zn and Au (yellow highlighted section on Fig. 11). The negative excursion at 74.15 m is associated with a relative depletion in all elements, TOC and TIP, but interestingly is immediately preceded by prominent concentrations in all trace elements (except for P_2O_5 and Zn, which have subdued peaks), TIP and TOC (orange highlighted box on Fig. 11).

The Macmillan Pass volcanic/volcaniclastic rocks were not systematically analyzed from this hole; however, a field sample from immediately above the Sapper Formation contact (19-TF-13; 63.22817°N; -130.38109°W) was submitted for whole rock geochemistry (Fig. 12). The full geochemical data set is provided in Appendix D (sample ID 19-TF-13). The sample is pervasively altered to carbonate (19% CaO; 8% MgO) and has a loss on ignition of more than 15%, rendering the trace element concentrations (especially rare earths) unsuitable for interpretation of primary tectonic processes due to element mobility.

Figure 12. *Outcrop of Macmillan Pass volcanic suite (19-TF-13; 63.22817°N, -130.38109°W).*

Paleontology

Table 1 reports the samples re-examined for conodont zonal refinement[1] and includes Map ID numbers from Abbott (2013) for easy correlation to the bedrock map (Fig. 2; Abbott, 2013). Figure 13 displays the conodont biozonation ranges for each re-examined sample. All samples, except three, show some refinement to the age, albeit minor in some cases. Conodont biozones for two samples from the upper contact of the Sapper Formation range from *australis* to *ensensis* zones (middle–late Eifelian). The stratigraphically lowest Niddery Lake Member samples (Abbott, 2013; Nos. 33, 34, 35, 36) also cover some or all of this same range, with No. 33 ranging up to the *ansatus* (middle *varcus*) zone. Samples within the Niddery Lake Member (*i.e.*, not at the lower contact) range from *costatus* to *varcus* zones (latest Eifelian to early Givetian; Nos. 43 and 37), although two are much older *nothoperbonus-inversus* (No. 38) and *inversus-costatus* zones (No. 44) which

1 *Note that a full description of conodont fossils is offered in Gouwy, 2020, available through the Yukon Geological Survey.*

are Emsian and Emsian–Eifelian, respectively. It is important to note that the No. 38 sample was submitted with a (?)Road River designation so it may not be actually Niddery Lake Member. Samples 38 and 44 occur within the same bedrock polygon in Abbott (2013), which may suggest that the contact was approximated in the area, and that the samples actually are from the older Road River Group (Sapper Formation).

A single ventral valve of brachiopod collected from the contact between the Sapper Formation and Macmillan Pass volcanic suite is tentatively identified as *Spinatrypina*? sp. (Fig. 14). If correctly identified, the specimen is of late Early Devonian to Early Late Devonian in age and is widespread in rocks of this age in western North America (Blodgett, 2020).

Discussion

Paleoenvironmental interpretation

Sapper Formation, Macmillan Pass Member (shale facies or pinstripe unit), and the Fuller Lake Member geochemistry and sedimentology provide the means for a general characterization and paleoenvironmental interpretation of these Devonian shale intervals. As the nature of this study is reconnaissance, only high-level geochemical interpretations have been made, recognizing that the use of geochemical proxies has limitations and further studies will provide a more robust interpretation than is presented here.

The Macmillan Pass Member shale (pinstripe) unit is a siliceous unit (generally 70–80% SiO_2), that has little to no carbonate content, a significant terrestrial input (high TIP and Zr values) and redox indicators that suggest

Table 1. *Previous and current ages from 11 Devonian conodont slide samples re-examined for this study. Original data set from Abbott (2013). Shaded boxes under "Refined Age" column delineate a tighter age constraint as a result of this study.*

Abbott, 2013							Gouwy, 2020		
Map ID	NTS 50K	GSC No.	Formation	Stratigraphic position	Latitude (°N)	Longitude (°W)	Previous Age	Refined Age	Conodont biozone ranges
33	105O/7	C-087690	Portrait Lake Fm; Niddery Lake Mbr	lower part	63.2700	-130.5833	Middle Devonian–Eifelian	Middle Devonian, Eifelian–Givetian	*australis-ansatus*
34	105O/7	C-089951	Portrait Lake Fm; Niddery Lake Mbr	lower contact	63.2597	-130.1056	Middle Devonian–Eifelian	Middle Devonian, middle Eifelian	*australis-kockelianus*
35	105O/8	C-089962	Portrait Lake Fm; Niddery Lake Mbr	lower contact	63.2764	-130.2056	Middle Devonian–Eifelian	Middle Devonian, Eifelian	*australis-ensensis*
36	105O/1	C-089976	Portrait Lake Fm; Niddery Lake Mbr	lower contact	63.2250	-130.0833	Middle Devonian–Eifelian	Middle Devonian, middle Eifelian	*australis-kockelianus*
37	105O/7	C-087692	Portrait Lake Fm; Niddery Lake Mbr	within unit	63.2750	-130.5500	Middle Devonian–Givetian	Middle Devonian, Givetian	*rhenanus/varcus-latifossatus/semialternans*
38	105O/7	C-087538	Portrait Lake Fm; Niddery Lake Mbr	within unit	63.3000	-130.5333**	late Early Devonian–Emsian	Early Devonian, Emsian	*nothoperbonus-inversus*
43	105O/8	C-102309	Portrait Lake Fm; Niddery Lake Mbr*	within unit	63.2833	-130.3833	Middle Devonian	Middle Devonian–Eifelian	*costatus-ensensis*
44	105O/7	C-087689	Portrait Lake Fm; Niddery Lake Mbr	within unit	63.2900	-130.5700	Early Devonian–Emsian	Early Devonian, middle-late Emsian	*inversus-costatus*
47	105O/7	C-087687	shale in Macmillan Pass volcanics	lower part of unit	63.0000	-130.0000	Middle Devonain, middle Eifelian–early Givetian	Middle Devonian, middle–late Eifelian	*kockelianus-ensensis*
48	105O/1	C-087554	Sapper Fm	upper contact	63.1700	-130.3500	Middle Devonian–Eifelian	Middle Devonian, middle–late Eifelian	*australis-ensensis*
49	105O/1	C-108165	Sapper Fm	upper contact	63.1806	-130.2833	Middle Devonian–Eifelian	Middle Devonian, middle–late Eifelian	*australis-kockelianus*

* may be Road River Group

** exact location uncertain

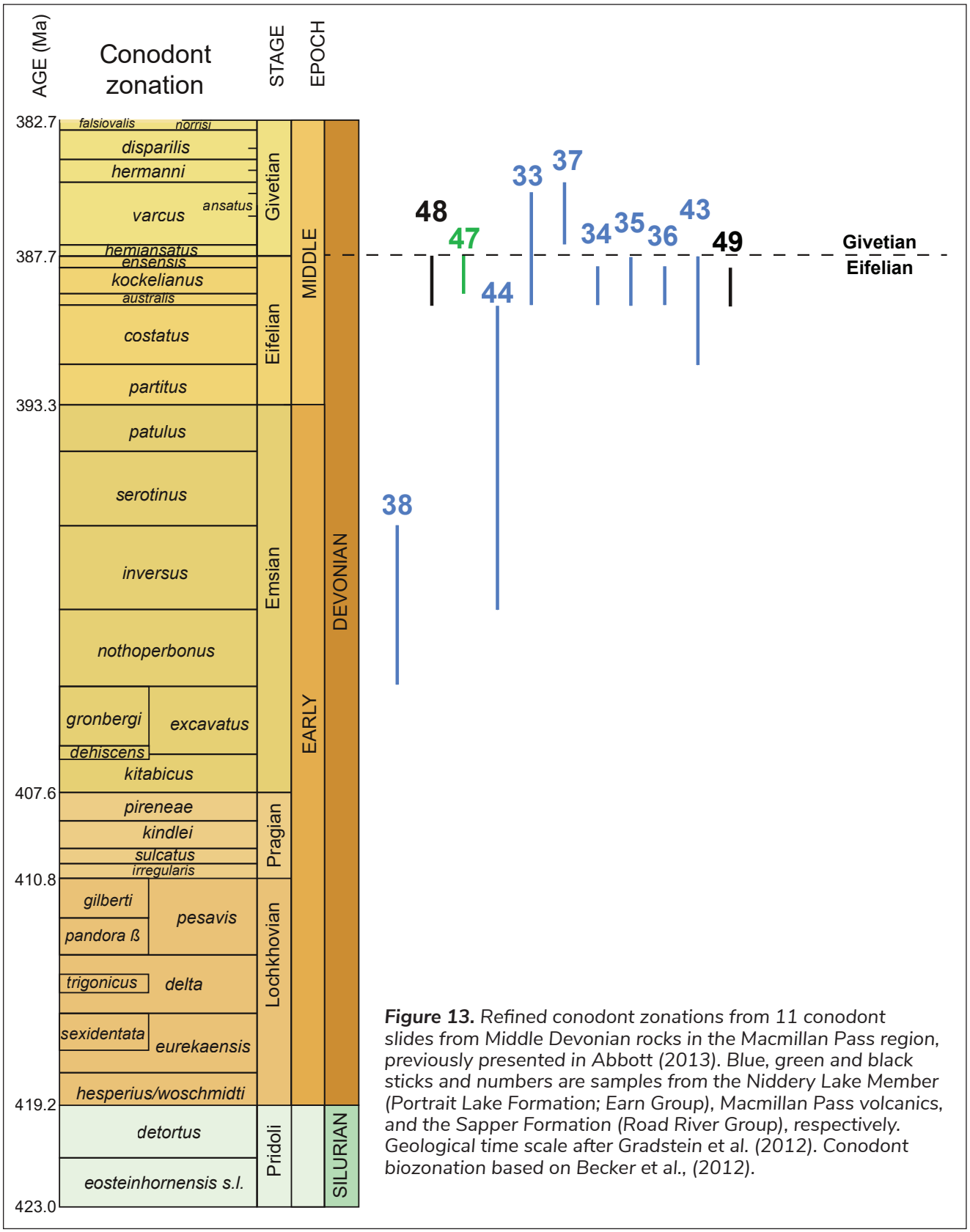

Figure 13. *Refined conodont zonations from 11 conodont slides from Middle Devonian rocks in the Macmillan Pass region, previously presented in Abbott (2013). Blue, green and black sticks and numbers are samples from the Niddery Lake Member (Portrait Lake Formation; Earn Group), Macmillan Pass volcanics, and the Sapper Formation (Road River Group), respectively. Geological time scale after Gradstein et al. (2012). Conodont biozonation based on Becker et al., (2012).*

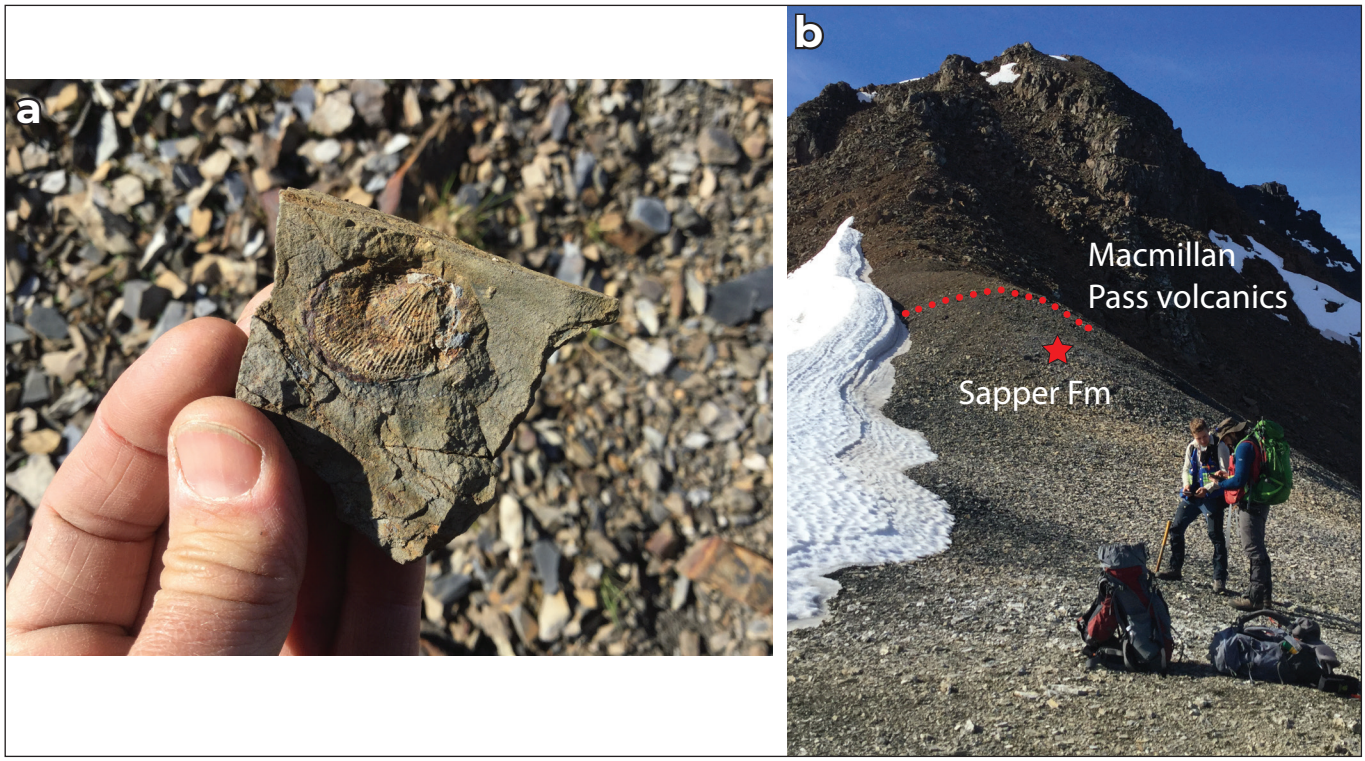

Figure 14. *Brachiopod sample in the uppermost Sapper Formation (63.1553°N, -130.1535°W) tentatively identified as Spinatrypina sp., late Early Devonian to Early Late Devonian.*

the depositional environment was oxic (low TOC and Ef Mo values). The combination of geochemistry with the sedimentology, which includes rhythmic fining upwards sandstone to shale successions and basal scours and load structures, suggests turbidity current deposition (Bouma units Tcde) onto a middle to outer shelf setting.

The Fuller Lake Member (Portrait Lake Formation), where not affected by Zn-Pb-Ag mineralization (*i.e.*, 556–596 m in TS88-01), is the most siliceous of the units investigated (average 75% SiO_2). The silica is likely biologically sourced, as shown by the moderate but notable negative SiO_2 *vs.* Zr trend and the low Zr and TIP average values (92 ppm and 9%, respectively). Redox indicators such as Ef Mo and TOC are moderate, and carbonate content insignificant. The rhythmically bedded siliceous shale and chert with lesser siltstone, lack of coarse-grained strata, and moderate indicators for anoxic conditions and biogenic chert suggest an outer slope to basinal setting where turbidity current deposition (Bouma units Tde) sourced both biogenic (radiolarian) and terrestrial silica, and periods of intermittent anoxia resulted in organic carbon preservation. Determination of euxinia (*i.e.*, anoxia with sulphur present) is difficult to determine with the data presented here, and unfortunately cannot be effectively compared with Magnall *et al.*'s (2018) paleoredox analysis of Fuller Lake Member strata at the Tom property. Their study employed proxies such as Fe-speciation and Mo isotopes to characterize the depositional environment of the host sediments of the massive sulphide deposits as ferruginous (*i.e.*, anoxia in the absence of sulphur) with the sulphur for metal-enrichment controlled instead by high primary productivity and enhanced carbon burial, as indicated by TOC/P ratios <106:1 (the Redfield ratio; Redfield, 1958). Interestingly, the TOC/P ratios determined in this current study do compare to the findings of Magnall *et al.* (2018), where values are lower than 106:1 (average 28:1), suggestive of effective carbon supply and burial. By inference, we could suggest anoxic or ferruginous conditions for Fuller Lake Member deposition; however, this interpretation is highly speculative without further research.

The Zn-Pb-Ag mineralizing event overwhelmed the background oceanic conditions during Fuller Lake Member deposition resulting in high concentrations of Ba, Pb, Zn and other elements. Other differences from Fuller Lake Member background conditions include lower SiO_2 and oxide concentrations, minimal to no organic matter preservation, moderate carbonate content and elevated Mo. Primary depositional characteristics cannot be effectively interpreted from the proxy data presented herein. The Fuller Lake Member chert above the Zn-Pb-Ag interval (510–523 m in TS88-01) still contains high amounts of Ba and Zn, and appears to be still affected by the mineralizing event. This suggests oceanic conditions are likely not at background levels but it appears all values are trending towards the lower Fuller Lake Member ones.

The Sapper Formation samples in TS91-17 show much more variability in geochemistry than the other units in this study and a four-fold division of the unit facilitates interpretation. The bottom two metres of the section is dominated by carbonate with disseminated fossil debris, suggesting off-shelf deposition in proximity to a carbonate source with very little terrestrial clastic input and under oxic conditions. Between 100 and 124 m depth, shale is moderately siliceous (average 62%) and the silica trends weakly towards a terrestrial source. Terrestrial input in this section is low (<10%), and organic matter content and Ef Mo values are high (4.8% and 149, respectively), suggesting less oxic conditions than farther up or at the base of the section, and likely intermittent anoxic or dysoxic conditions during deposition. Laminated shale and mudstone in rhythmic, normally graded intervals suggest distal turbidite deposition (Bouma units Tde) in a middle shelfal setting. A small excursion in the $\delta^{13}C_{org}$ curve at 112–113 m could indicate higher sea level as it is immediately followed by an increase in TOC and Ef Mo suggesting good organic matter preservation and thus anoxia. The interval from 94–99 m shows a coarser grained sediment (siltstone) fining up to a shale. It has the highest average TIP values of the section, while TOC is lower (average 3.6%) and Ef Mo and carbonate component are the lowest in the section. The trends throughout this interval suggest deposition on an inner to middle shelf transitioning to a lower shelf during a sea level transgression. The upper part of the section, from 74–92 m, shows a high degree of geochemical variability suggesting rapidly fluctuating sea level and associated terrestrial input, silica source, redox conditions, and proximity to a carbonate source. The paleoenvironmental significance of this upper section is discussed in more detail in the next section.

The Kačák Event in the Sapper Formation

Conodont biostratigraphy places the uppermost Sapper Formation in the terminal Eifelian *australis* to *ensensis* conodont zones. The latter half of this time period is marked globally by black shale deposition called the Kačák-oto*mari* Event (herein Kačák; House, 1985; Walliser, 1985; Walliser and Bultynck, 2011). Kačák corresponds to a multi-phased global sea level rise with associated rapid facies changes, significant biotic turnover (*i.e.*, extinction followed by rapid radiation events), and anoxia which produced sediments rich in organic carbon (House, 1996; House, 2002; Desantis and Brett, 2011). The Kačák Event is marked by two phases. The first phase, the oto*mari* Event, is based on the onset of the dacryoconarid lineage of *Nowakia* oto*mari* that occurred at the boundary between the *kockelianus* and *ensensis* conondont zones (388.2 Ma; timescale from Becker *et al.*, 2012). The second is the Kačák Event s.s., named after the Kačák Shale in the Bohemian Massif, immediately before the Eifelian–Givetian boundary (387.7 Ma), which is characterized by the onset of black shale deposition and numerous faunal extinctions among goniatid ammonites (*e.g.*, House, 1996; Walliser, 1996; Schöne, 1997; DeSantis, 2010; Elwood *et al.*, 2011). Evidence for the Kačák Event is recorded in Germany (*e.g.*, House, 1996; Schöne, 1997; Konigshof *et al.*, 2016), Spain (*e.g.*, House, 1996; Garcia-Lopez *et al.*, 2002), Czech Republic (Hladikova *et al.*, 1997), Belgium (Jamart and Denayer, 2020), Scotland and England (House, 1996; Marshall *et al.*, 2007), France (House, 1996), Austria (DeSantis and Brett, 2011), Morocco (House, 1996; Walliser and Bultynck, 2011; Becker *et al.*, 2013), Falkland Islands (Marshall, 2016), Brazil (Horodyski *et al.*, 2014), Bolivia (Troth *et al.*, 2011); China (House, 1996; Qie *et al.*, 2018), Australia (House, 1996) and Vietnam (Konigshof *et al.*, 2017). In North America it

has been observed in the eastern United States as a three-part bioevent which includes (oldest to youngest) the Bakoven, Stony Hollow and Kačák Events that occur in the Upper Eifelian *australis*, *kockelianus* to *ensensis* conodont biozones, respectively (DeSantis and Brett, 2011). In Canada, it is likely recorded in the top of the Hume Formation and base of the Hare Indian Formation in the Mackenzie Mountains (Uyeno *et al.*, 2017), and possibly in an anomalous, metal-enriched horizon in Yukon at the contact between the Road River Group and Canol Formation (Fraser and Hutchison, 2017; Gadd *et al.*, 2019a); however, more work is required to determine proof of a biocrisis.

Robust studies characterizing the Kačák Event rely on documenting pelagic biostratigraphic changes (*i.e.*, conodonts and ammonoids), and geochemical, isotopic and magnetic susceptibility patterns, or combinations thereof, at a high sampling resolution over these thin intervals. The reconnaissance nature of this study, limited available core through these strata, and the lack of fossils does not allow for such detail. Certain indicators in the data suggest the Kačák and the Eifelian–Givetian boundary sediments may be present at the Tom property, including trace element enrichments over a thin stratigraphic interval, indicators for rapid sea level rise and subsequent anoxia, and a marked negative $\delta^{13}C_{org}$ excursion which is a hallmark characteristic at many locales. Thin, condensed sections caused by low to no sedimentation in a period of high sea level (e.g., 50 cm at Mech Irdane, Morocco; Ellwood *et al.*, 2011; Walliser and Bultynck, 2011) and 30 cm in the Appalachian Basin, eastern U.S. (Bakoven member of the Union Springs Formation, *Macellus* subgroup; Sageman *et al.*, 2003) are a global geological expression of the Kačák in basinal settings. Due to the paleogeographical basinal setting of Selwyn basin during Middle Devonian time, we would expect a similar condensed section in the rock record. Elevated metal concentrations as a reduction in "normal" sedimentation (or terrigenous sediment starvation) caused by sea level transgression tends to favour enrichment of rare earth and heavy metals from allogenic sources (e.g., windborne dust, volcanic ash, and cosmic dust) as well as from authigenic chemical reactions that are able to occur more effectively (Fraser and Hutchison, 2017; after Schutter, 1996). A zone of trace element enrichment, including Mo, Ni, Zn, Se, P, As, Ag, Au, Zn and P_2O_5 (orange box on Fig. 11), in the black shales of the uppermost Sapper Formation in drill hole TS91-17 suggests a condensed section of sedimentation. Note that Zn and P_2O_5 show only minor enrichments in phase with other elements but become more enriched at the top of the section.

Evidence for anoxia at marine Kačák localities are typically shown by sharp increases in concentration of redox-sensitive elements (e.g., Mo, V, and U), and spikes in TOC which suggest significant organic carbon burial (e.g., Mech Irdane in (Ellwood *et al.*, 2011), the Eifel area of Germany (Konigshof *et al.*, 2016) and the Barrandian basin in Czech Republic (Hladikova *et al.*, 1997)). In all of these localities, the trend towards anoxia is rapid, co-occurring over a thin stratigraphic interval, and consistent with a transgressive sea level. In the uppermost Sapper Formation in drillhole TS91-17, we see strong enrichments in redox sensitive elements Mo, U, V, and Ni (Fig. 11 and Appendix C), as well as a spike in TOC values (up to 11%) over a thin stratigraphic interval. A prominent negative $\delta^{13}C_{org}$ or $\delta^{13}C_{carb}$ in sediments is a diagnostic feature of the Kačák in many localities: New York State ($\delta^{13}C_{org}$ -2.0‰; Sageman *et al.*, 2003); the Eifel region in Germany ($\delta^{13}C_{carb}$ -4.0‰ and $\delta^{13}C_{org}$ -1.0‰; Konigshof *et al.*, 2016); the Ardennes region in Belgium ($\delta^{13}C_{carb}$ -3‰; Konigshof *et al.*, 2016); and at Mech Ardane, Morocco (~$\delta^{13}C_{carb}$ -8.0‰; Ellwood *et al.*, 2011). A negative $\delta^{13}C_{carb}$ excursion is also observed in brachiopod shells from Morocco and Germany (-1.5‰; van Geldern *et al.*, 2006). The shift in $\delta^{13}C_{org}$ values in the uppermost Sapper Formation in TS91-17 is -3.2‰, which is on par with the other excursions observed globally. These geochemical characteristics, combined with the age control from the refined conodont dates of samples at the Sapper Formation–Macmillan Pass volcanic suite contact make a strong case for the expression of the Kačák Event at the Tom property.

Is there a relationship between the $\delta^{13}C_{org}$ excursion in the Sapper Formation and the NiMo horizon?

The uppermost Sapper Formation at Macmillan Pass is coeval (within error) with the hyper-enriched black shale (HEBS) unit or 'NiMo' horizon observed regionally in Selwyn basin, Richardson trough and Kechika trough at the contact between the Road River Group and Canol Formation (or lowermost Portrait Lake Formation of the Earn Group). This is a thin (<14 cm, average ~3 cm thick), shale-hosted, stratabound Ni-Mo-Zn and PGE mineralization horizon, with anomalous Au, As, Ce, P, Ba and U (Hulbert *et al.*, 1992; Goodfellow *et al.*, 2010; Gadd *et al.*, 2019b; Henderson *et al.*, 2019). Re-Os geochronology and conodont biostratigraphy date the horizon as 385–390 Ma (Gadd *et al.*, 2019a). The horizon may be the expression of the combined Kačák and younger *pumilio* and Taghanic bioevents in an extremely condensed section (Gadd *et al.*, 2019a). The revised conodont dates from strata at the Sapper Formation–Macmillan Pass volcanic suite suggest that this contact and the NiMo horizon are time equivalent features in the basin, which should assist in future mapping and correlation exercises. The observation of two different expressions of the Kačák Event in the Laurentian margin, *i.e.*, sulphide mineralization versus black shale deposition, is beyond the focus of this study; it would involve considerations of paleo ocean chemistry, redox conditions, tectonics and paleogeography at a much larger scale.

Questions surrounding the influence of the Macmillan Pass volcanic suite

Unlike other NiMo localities in Selwyn basin and Richardson trough, volcanic/volcaniclastic rocks at Macmillan Pass sharply overlie the Road River Group. These volcanic rocks are interpreted to be the result of differential subsidence and block faulting on the margin of Laurentia, and the initiation of low temperature hydrothermal activity that reached a maximum during Zn-Pb-Ag deposition in the Late Devonian (Abbott and Turner, 1991). In the TS91-17 hole, the Macmillan Pass volcanic suite sharply overlies the Sapper Formation, with what appears to be a conformable contact. Abbott and Turner (1991) note that although the Middle Devonian volcanic rocks are mainly at the basal contact of the Earn Group and sharply overlie the Road River Group, they may also be intercalated with the uppermost Road River Group; at the Boundary Creek deposit the volcanic rocks are intercalated with chert conglomerate and diamictite in the Macmillan Pass Member. This suggests that volcanism was intermittent and not a single event. Two questions arise from the overlap in timing of volcanism with NiMo development in Selwyn basin and Richardson trough. The first question is whether this volcanism has created a local effect on trace metal concentrations and TOC, and an associated disturbance to the carbon partitioning at the Eifelian–Givetian boundary. If not, we may not be seeing the global Kačák Event in the upper Sapper Formation but rather a localized event. The second question is whether Middle Devonian volcanism at Macmillan Pass played a role in the development of the NiMo horizon elsewhere in the basin. Answering these questions are beyond the scope of this report, but would be interesting starting points for future Middle Devonian studies in Yukon.

Conclusions

Core logging, lithogeochemistry, and a reassessment of conodont data were conducted on Middle Devonian sediments at the Tom deposit, Macmillan Pass, Yukon. Updated descriptions and lithogeochemical characteristics of shale dominant units are presented, which can be used to assess depositional environment and that aid in regional mapping and correlation are presented herein.

The Macmillan Pass Member shale (pinstripe) unit is a siliceous, rhythmically interbedded fining upwards, fine to very fine sandstone and siliceous siltstone and shale unit that was deposited in a turbidity current onto a middle to outer shelf setting in an oxic environment.

The Fuller Lake Member (Portrait Lake Formation), where not affected by Zn-Pb-Ag mineralization, is a variably siliceous, black, laminated shale. The silica is likely biologically sourced from radiolarian combined with terrestrial input, and deposition is interpreted to be via turbidity currents into an outer slope to basinal setting far from a carbonate rock source. Redox proxies

suggest periods of intermittent anoxia that resulted in intervals of enhanced organic material preservation. The Zn-Pb-Ag mineralizing event flooded Zn and Pb into the system, and is observed as interlaminated shale, barite, pyrite and sphalerite with associated carbonate.

Finally, the Sapper Formation of the Road River Group is a dominantly organic-rich interlaminated shale/mudstone with lesser siltstone and very fine sandstone and lesser limestone. It shows a range of depositional environments including off-shelf proximal to a carbonate source to turbidity current deposition on the middle to inner shelf. The terminal 20 m of the Sapper Formation is characterized by geochemical variability suggesting paleoenvironmental instability, including fluctuating sea level and associated proximity to carbonate and terrestrial sources, silica source, and redox conditions. This instability was followed by a volcanic event that may or may not have affected these uppermost sediments.

The uppermost Sapper Formation highlights a thin interval of metal enrichment, high TOC, markers for anoxia and a negative 3.5‰ $\delta^{13}C_{org}$ excursion that may be an expression of the Kačák Event. The Kačák is a global biocrisis spanning the Eifelian–Givetian boundary and characterized in the marine realm by a condensed section of sedimentation, sea-level instability, and pelagic faunal changes (*i.e.*, massive extinction followed by a radiation). Further study is required to determine whether the strata at Macmillan Pass reflect this global signal, or are localized and caused by volcanic activity. Also, further research into the hypothesis as to whether these strata are a local expression of geochemical events responsible for the NiMo horizon elsewhere in Selwyn basin and Richardson trough is required.

Ackowledgements

The authors thank many YGS colleagues including Rosie Cobbett for assistance on the geochemistry of the Macmillan Pass volcaniclastic sample, David Moynihan for discussions on regional geology, Bailey Staffen for GIS assistance, and Maurice Colpron and Carolyn Relf for supporting the advancement of shale studies in Yukon. Michael Gadd from GSC–Ottawa is acknowledged for discussions on the NiMo/HEBS horizon in Yukon. Amanda O'Conner is thanked for excellent field assistance. The staff of Fireweed Zinc Inc. are gratefully thanked for their 2019 hospitality.

References

Abbott, J.G., 1983. Structure and Stratigraphy of the MacMillan Fold Belt: Evidence for Devonian Faulting. Exploration and Geological Services Division, Yukon Region, Indian and Northern Affairs Canada, Open File 1983-1, 16 p., 3 maps at 1:50 000 scale.

Abbott, J.G., 2013. Bedrock geology of the Macmillan Pass area, Yukon and adjacent Northwest Territories (NTS 105O/1, 2 and parts of 105O/7, 8, and 105P/4, 5; 1:50 000 scale). Yukon Geological Survey, Geoscience Map 2013-1.

Abbott, J.G. and Turner, R.J. 1991. Character and paleotectonic setting of Devonian stratiform sediment-hosted Zn, Pb, Ba deposits, Macmillan Fold Belt, Yukon. *In:* Mineral deposits of the northern Canadian Cordillera, Yukon-northeastern British Columbia, Geological Survey of Canada, Open File 2169, p. 99–136.

Algeo, T.J. and Rowe, H. 2012. Paleoceanographic applications of trace-metal concentration data. Chemical Geology, vol. 324–325, p. 6–18.

Arne, D. and McGarry, L., 2018. NI 43-101 Technical Report on the Macmillan Pass Zinc-Lead-Silver Project, Watson Lake & Mayo Mining Districts, Yukon Territory, Canada. CSA Global Canada Geosciences Ltd. Report prepared for Fireweed Zinc Ltd., Jan. 10, 2018, http://www.fireweedzinc.com/resources/presentations/FWZ_MacPass_ResourceUpdate_20180110.pdf, [accessed Nov. 13, 2020].

Becker, R.T., Gradstein, F.M. and Hammer, O. 2012. The Devonian Period. *In:* The Geologic Time Scale 2012, F.M. Gradstein, J.G. Ogg, M. Schmitz and G. Ogg (eds.), Elsevier, p. 559–601.

Becker, T., El Hassani, A. and Tahiri, A., 2013. International Field Symposium on "The Devonian and Lower Carboniferous of northern Gondwana" Field Guidebook. Institut Scientifique, Rabat, 150 p.

Blodgett, R.B., 2020. Report on fossils collected by Yukon Geological Survey during 2019 summer field season. Unpublished report, March 24, 2020.

Carne, R.C., 1976. Stratabound barite and lead-zinc-barite deposits in eastern Selwyn Basin, Yukon Territory. Department of Indian and Northern Affairs, Open File Report EGS 1976-16, 41 p.

Cecile, M.P. 1982. The Lower Paleozoic Misty Creek Embayment, Selwyn Basin, Yukon and Northwest Territories. Geological Survey of Canada, Bulletin 335, 78 p.

Cecile, M.P., 2000. Geology of the northeastern Niddery Lake map area, east-central Yukon and adjacent Northwest Territories. Geological Survey of Canada, Bulletin 553, 120 p.

DeSantis, M.K. 2010. Anatomy of Middle Devonian Faunal Turnover in Eastern North America: Implications for Global Bioevents at the Eifelian-Givetian Stage Boundary. Unpublished PhD thesis, University of Cincinnati, 409 p.

Desantis, M.K. and Brett, C.E., 2011. Late Eifelian (Middle Devonian) biocrises: Timing and signature of the pre-Kačák Bakoven and Stony Hollow Events in eastern North America. Palaeogeography, Palaeoclimatology, Palaeoecology, vol. 304, p. 113–135.

Dilliard, K.A., Pope, M.C., Coniglio, M., Hasiotis, S.T. and Lieberman, B., 2010. Active synsedimentary tectonism on a mixed carbonate-siliciclastic continental margin: Third-order sequence stratigraphy of a ramp to basin transition, lower Sekwi Formation, Selwyn Basin, Northwest Territories, Canada. Sedimentology, vol. 57, p. 513–542.

Ellwood, B.B., Algeo, T.J., El Hassani, A., Tomkin, J.H. and Rowe, H. D. 2011. Defining the timing and duration of the Kačák Interval within the Eifelian/Givetian boundary GSSP, Mech Irdane, Morocco, using geochemical and magnetic susceptibility patterns. Palaeogeography, Palaeoclimatology, Palaeoecology, vol. 304, p. 74–84.

Fraser, T.A. and Hutchison, M.P. 2017. Lithogeochemical characterization of the Middle-Upper Devonian Road River Group, Canol and Imperial formations on Trail River, east Richardson Mountains, Yukon: age constraints and a depositional model for fine-grained strata in the Lower Paleozoic Richardson trough. Canadian Journal of Earth Sciences, vol. 54, p. 731-765.

Gabrielse, H. 1967. Tectonic evolution of the northern Canadian Cordillera. Canadian Journal of Earth Sciences, vol. 4, p. 271–298.

Gadd, M.G., Peter, J.M., Hnatyshin, D., Creaser, R., Gouwy, S. and T. Fraser, 2019a. A Middle Devonian basin-scale precious metal enrichment event across northern Yukon (Canada). Geology, vol. 48, p. 242–246.

Gadd, M.G., Peter, J.M., Jackson, S.E., Yang, Z. and Petts, D. 2019b. Platinum, Pd, Mo, Au and Re deportment in hyper-enriched black shale Ni-Zn-Mo-PGE mineralization, Peel River, Yukon Canada. Ore Geology Review, vol. 107, p. 600–614.

García-López, S., Sanz-López, J. and Sarmiento, G.N. 2002. The Palaeozoic succession and conodont biostratigraphy of the section between Cape Peñas and Cape Torres (Cantabrian coast, NW Spain). *In:* Palaeozoic conodonts from northern Spain, S. García-López and F. Bastida (eds). Eighth International Conodont Symposium held in Europe. Madrid, Publicaciones del Instituto Geológico y Minero de España, p. 125–161.

Goodfellow, W.D. and Rhodes, D., 1991. Geological setting, geochemistry and origin of the Tom stratiform Zn-Pb-Ag-barite deposits. In: Mineral deposits of the northern Canadian Cordillera, Yukon-northeastern British Columbia [Field Trip 14], J.G. Abbott and R.J.W. Turner (eds.), Geological Survey of Canada, Open File 2169, p. 177–241.

Goodfellow, W.D., Geldsetzer, H., Gregoire, C., Orchard, M. and Cordey, F. 2010. Geochemistry and origin of geographically extensive Ni(Mo, Zn, U)-PGE sulphide deposits hosted in Devonian black shales, Yukon. *In:* TGI-3 Workshop: Public geoscience in support of base metal exploration programme and abstracts. Geological Association of Canada, Cordilleran Section 2010, p. 15–18.

Gordey, S.P. and Anderson, R.G., 1993. Evolution of the northern Cordilleran miogeocline, Nahanni map area (105I), Yukon and Northwest Territories. Geological Survey of Canada, Memoir 428, 214 p.

Gouwy, S.A., 2020. Reassessment of 11 historical conodont samples from the Sapper and Portrait Lake formations from the Yukon (NTS 105O). Geological Survey of Canada (Calgary), Paleontological Report 2-SAG-2020, 8 p.

Gradstein, F.M., Ogg, J.G., Schmitz, J. and Ogg, G. (eds), 2012. The geologic time scale 2012, 1st ed. Elsevier, 1176 p.

Henderson, K.M., Williams-Jones, A.E. and Clark, J.R., 2019. Metal transport by liquid hydrocarbons: evidence from metalliferous shale and pyrobitumen, Yukon. *In:* Targeted Geoscience Initiative: 2018 report of activities, N. Rogers (ed.), Geological Survey of Canada, Open File 8549, p. 179–187.

Hildred, G.V. and Rice, C. 2012. Using High Resolution Chemostratigraphy to Determine Well-bore Pathways in Multilateral Drilling Campaigns: an Example from the Horn River Formation, British Columbia, Canada. *In:* Canadian Society of Petroleum Geologists, Canadian Society of Exploration Geophysicists, Canadian Well Logging Society Convention 2010, Calgary, Canada, online abstract, http://www.cspg.org/cspg/Conferences/Geoconvention/2012_Abstract_Archives.aspx, [accessed December 1, 2015].

Hladikova, J., Hladil, J. and Krobek, B., 1997. Carbon and oxygen isotope record across Pridoli to Givetian stage boundaries in the Barrandian basin (Czech Republic). Palaeogeography, Palaeoclimatology, Palaeoecology, vol. 132, p. 225–241.

Horodyski, R.S., Holz, M., Grahn, Y. and Bosetti, E., 2014. Remarks on sequence stratigraphy and taphonomy of the Malvinokaffric shelly fauna during the Kačák Event in the Apucarana Sub-basin (Parana Basin), Brazil. International Journal of Earth Sciences, vol. 103, p. 367–380.

House, M.R., 1985. Correlation of mid-Palaeozoic ammonoid evolutionary events with global sedimentary perturbations. Nature, vol. 313, p. 17–22.

House, M.R., 1996. The Middle Devonian Kačák Event. Proceedings of the Ussher Society, vol. 9, p. 79–84.

House, M.R., 2002. Strength, timing, setting and cause of mid-Palaeozoic extinctions. Palaeogeography, Palaeoclimatology, Palaeoecology, vol. 181, p. 5–25.

Hulbert, L.J., Gregoire, D.C., Paktunc, D. and Carne, R.C. 1992. Sedimentary nickel, zinc and platinum group element mineralization in Devonian black shales at the Nick Property, Yukon, Canada: a new deposit type. Exploration Mining Geology, vol. 1, p. 39–62.

Jamart, V. and Denayer, J., 2020. The Kačák event (late Eifelian, Middle Devonian) on the Belgian shelf and its effects on rugose coral palaeobiodiversity. Czech Geological Survey, Bulletin of Geosciences, vol. 95, p. 279–311.

Konigshof, P., Da Silva, A.C., Suttner, T.J., Kido, E., Waters, J., Carmichael, S,K., Janse, U., Pas, D. and Spassov, S., 2016. Shallow-water facies setting around the Kačák Event. *In:* Devonian Climate, Sea Level and Evolutionary Events, R.T. Becker, P. Konigshof and C.E. Brett (eds.). Geological Society, London, Special Publications 423, p. 171–199.

Konigshof, P., Narkiewicz, K., Hoa, P.T., Carmichael, S.K. and Waters, J.A., 2017. Devonian events: examples from the eastern Palaeotethys (Si Phai section, NE Vietnam). Palaeobiodiversity and Palaeoenvironments vol. 97, p. 481–496.

Magnall, J.M., Gleeson, S.A. and Paradis, S., 2015. The importance of siliceous radiolarian-bearing mudstones in the formation of sediment-hosted Zn-Pb ± Ba mineralization in the Selwyn basin, Yukon Canada. Economic Geology, vol. 110, p. 2139–2146.

Magnall, J.M., Gleeson, S.A., Poulton, S.W., Gordon, G,W., and Paradis, S., 2018. Links between seawater paleoredox and the formation of sediment-hosted massive sulphide (SHMS) deposits – Fe speciation and Mo isotope constraints from Late Devonian mudstones. Chemical Geology, vol. 490, p. 45–60.

Magnall, J.M., Gleeson, S.A. and Paradis, S., 2020. A new subseafloor replacement model for the Macmillan Pass clastic-dominant Zn-Pb ± Ba deposits (Yukon, Canada). Express Letter, Economic Geology, vol. 115, p. 953–959.

Marshall, J.E.A., Astin, T.R., Brown, J.F., Mark-Kurik, E., and Lazauskiene, J., 2007. Recognizing the Kačák Event in the Devonian terrestrial environment and its implications for understanding land-sea interactions. *In:* Devonian Events and Correlations. R.T. Becker, W.T. Kirchgasser (eds.), Geological Society London, Special Publication 278, p. 133–155.

Marshall, J.E.A., 2016. Palynological calibration of Devonian events at near-polar paleolatitudes in the Falkland Islands, South Atlantic. *In:* Devonian Climate, Sea Level and Evolutionary Events, R.T. Becker, P. Konigshof and C.E. Brett (eds.), Geological Society London, Special Publication 423, p. 25–44.

Nelson, J. and Colpron, M., 2007. Tectonics and metallogeny of the British Columbia, Yukon and Alaskan Cordillera, 1.8 Ga to the present. *In:* Mineral Deposits of Canada: A Synthesis of Major Deposit-Types, District Metallogeny, the Evolution of Geological Provinces, and Exploration Methods, W.D. Goodfellow (ed.), Geological Association of Canada, Mineral Deposits Division, Special Publication No. 5, p. 755–791.

Nelson, J.L., Colpron, M., Piercey, S.J., Dusel-Bacon, C., Murphy, D.C. and Roots, C.F. 2006. Paleozoic tectonic and metallogenetic evolution of pericratonic terranes in Yukon, northern British Columbia and eastern Alaska. *In:* Paleozoic Evolution and Metallogeny of Pericratonic Terranes at the Ancient Pacific Margin of North America, Canadian and Alaskan Cordillera, M. Colpron and J.L. Nelson (eds.), Geological Association of Canada, Special Paper 45, p. 323–360.

Qie, W., Ma, X., Xu, H., Qiao, L., Liang, K., Guo, W., Song, J., Chen, B. and Lu, J., 2018. Devonian integrative stratigraphy and timescale of China. Science China Earth Sciences, vol. 61, p. 1–23.

Redfield, A.C., 1958. The biological control of chemical factors in the environment. American Science, vol. 46, p. 205–222.

Sageman, B.B., Murphy, A.E., Werne, J.P., Ver Straeten, C.A., Hollander, D.J. and Lyons, T.W. 2003. A tale of shales: the relative roles of production, decomposition, and dilution in the accumulation of organic-rich strata, Middle-Upper Devonian, Appalachian basin. Chemical Geology, vol. 195, p. 229–273.

Saltzman, M.R. and Thomas, E. 2012. Carbon isotope stratigraphy. In: The Geologic Time Scale 2012. F. Gradstein, J. Ogg, M.D. Schmitz, and G. Ogg (eds.), Elsevier, p. 207–232.

Schöne, B.R., 1997. Der *otomari*-Event und seine Auswirkungen auf die Fazies des Rhenoherzynischen Schelfs (Devon, Rheinishces Schiefergebirge). Göttinger Arbeiten zur Geologie und Paläontologie, vol. 70, p. 1–140.

Schutter, S.R. 1996. The Glenwood Shale as an example of a Middle Ordovician condensed section. Geological Society of America, Special Paper 306, 55 p.

Tribovillard, N., Algeo, T.J., Lyons, T. and Riboulleau, A., 2006. Trace metals as paleoredox and paleoproductivity proxies: An update. Chemical Geology, vol. 232, p. 12–32.

Troth, I., Marshall, J.E.A., Racey, A. and Becker, R.t., 2011. Devonian sea-level change in Bolivia: A high palaeolatitude biostratigraphical calibration of the global sea-level curve. Palaeogeography, Palaeoclimatology, Palaeoecology, vol. 304, p. 3–20.

Uyeno, T.T., Peder, A.E.H., Uyeno, T.A., 2017. Conodont biostratigraphy and T-R cycles of the Middle Devonian Hume Formation at Hume River (type locality), north Mackenzie Mountains, Northwest Territories, Canada. Stratigraphy, vol. 14, p. 391–404.

van Geldern, R., Alvarez, F., Day, J., Jansen, U., Joachimski, M.M., Ma, X.P. and Yolkin, E.A. 2006. Carbon, oxygen and strontium isotope records of Devonian brachiopod shell calcite. Palaeogeography, Palaeoclimatology, Palaeoecology, vol. 240, p. 47–67.

van Hengstum, P.J. and Gröcke, D.R. 2008. Stable isotope record of the Eifelian–Givetian boundary Kačák-o*tomari* Event (Middle Devonian) from Hungry Hollow, Ontario, Canada. Canadian Journal of Earth Sciences, vol. 45, p. 353–366.

Walliser, O.H., 1985. Natural boundaries and commission boundaries in the Devonian. Courier Forschungsinstitut Senckenberg, vol. 75, p. 401–408.

Walliser, O.H., 1996. Global Events in the Devonian and Carboniferous. *In:* Global Events and Event Stratigraphy in the Phanerozoic, O.H. Walliser (ed.), Springer-Verlag, Berlin, p. 225–250.

Walliser, O.H. and Bultynck, P. 2011. Extinctions, survival and innovations of conodont species during the Kacák Episode (Eifelian-Givetian) in south-eastern Morocco. Bulletin de l'Institut Royal des Sciences Naturelles de Belgique, Sciences de la Terre, vol. 81, p. 5–25.

Wright, A.M., Ratcliffe, K.T., Zaitlin, B.A. and Wray, D.S. 2010. The application of chemostratigraphic techniques to distinguish compound incised valleys in low-accommodation incised-valley systems in a foreland-basin setting: an example from the Lower Cretaceous Mannville Group and Basal Colorado Sandstone (Colorado Group), Western Canadian Sedimentary Basin. *In:* Application of Modern Stratigraphic Techniques: Theory and Case Histories. SEPM Special Publication, vol. 94, p. 93–107.

Appendices (separate excel spreadsheet)

Appendix A.

Whole rock geochemistry from samples in the TS88-01 drillhole.

Appendix B.

Whole rock geochemistry from samples in the TS91-014 drillhole.

Appendix C.

Whole rock geochemistry and organic carbon isotopic signatures from samples in the TS91-17 drillhole.

Appendix D.

Whole rock geochemistry for the Macmillan Pass volcanic suite field sample, 19-TF-13.

Potential heat production from the Seagull and Teslin plutonic suites, southern Yukon: Geochemistry, geochronology, rock physical properties, and 3D geophysical inversion of Bouguer gravity data

Maurice Colpron*
Yukon Geological Survey

Nathan Hayward
Geological Survey of Canada

James L. Crowley
Boise State University

Colpron, M., Hayward, N. and Crowley, J.L., 2021. Potential heat production from the Seagull and Teslin plutonic suites, southern Yukon: Geochemistry, geochronology, rock physical properties, and 3D geophysical inversion of Bouguer gravity data. *In:* Yukon Exploration and Geology 2020, K.E. MacFarlane (ed.), Yukon Geological Survey, p.47–72.

Abstract

Cretaceous granitoid plutons of the Seagull and Teslin plutonic suites, east of Teslin, are evaluated for their potential radiogenic heat production. The Seagull suite comprises ultra-fractionated, A-type granites dated at *ca.* 103–101 Ma that have anomalous average heat production values (*A*) of 7.9 to 9.9 μW/m^3. The Teslin suite is older (*ca.* 121–109 Ma) and characterized by more intermediate granodiorite compositions that mostly have average *A* values of 2.0 μW/m^3, closer to global averages. Locally, anomalous *A* values of 4.5 to 11.4 μW/m^3 are associated with younger (*ca.* 110–108 Ma), more evolved granitic phases of the Teslin suite. The 3D inversion of Bouguer gravity data provides models that constrain the subsurface density character and extents of the Hake and Seagull batholiths, and estimated volumes of ~4624 and 2744 km^3, respectively. The combination of these results suggests that potential heat energy of ~36.5 MWt may be contained in the Hake batholith, and as much as 27.2 MWt in the Seagull batholith.

* *maurice.colpron@yukon.ca*

Introduction

As part of the Yukon Geological Survey's geothermal research program, a regional assessment of the potential radiogenic heat production from granitoid plutons was done using a compilation of published and archival lithogeochemical data for southern Yukon (Friend and Colpron, 2017; Yukon Geological Survey, 2020a). This analysis showed that Cretaceous plutons of the Seagull suite (103–96 Ma), which intrude the Yukon-Tanana terrane east of Teslin (Fig. 1), are some of the most radiogenic plutons in Yukon, with potential heat production values locally exceeding 10 $\mu W/m^3$ (Friend and Colpron, 2017). This region coincides with some of the shallowest Curie point depths mapped in Yukon, also suggesting potentially higher crustal heat flow (Witter and Miller, 2017; Witter *et al.*, 2018). To further investigate the geothermal potential of the region, we visited plutons of the Seagull plutonic suite during the summer of 2019 and collected additional samples for lithogeochemical analysis and rock physical property measurements. Samples from the older Teslin plutonic suite (123–108 Ma), which intrudes the western Yukon-Tanana terrane near Teslin, were also collected to fill a gap in the lithogeochemical data compilation.

In this paper, we summarize the geological and geochemical characteristics of plutons of the Seagull and Teslin plutonic suites, evaluate their potential radiogenic heat production, and present new chemical abrasion–thermal ionization mass spectrometry (CA-TIMS) U-Pb zircon dates for 4 of these plutons. The subsurface density character and extent of the Hake and Seagull batholiths—the most radiogenic plutons in the region—are modeled using 3D geophysical inversion of Bouguer gravity data building on the strategy of Hayward (2019). The 3D geometries and volume estimates derived from the gravity inversion are combined with radiogenic heat values to estimate the potential heat energy contained in these granitic bodies.

Geological Setting

The Seagull plutonic suite (103–96 Ma) comprises a series of highly fractionated A-type granites associated with tin (Sn), tungsten (W), tantalum (Ta) and niobium (Nb) mineralization in southern Yukon (Abbott, 1981; Liverton and Alderton, 1994; Liverton *et al.*, 2005; Liverton, 2016). East of Teslin, the Seagull, Hake and Thirtymile Range plutons define a northwest-trending belt of intrusions along the eastern edge of the Yukon-Tanana terrane, near its boundary with the Cassiar terrane (Fig. 1; Rasmussen, 2013; Colpron *et al.*, 2016). This younger, mid-Cretaceous suite of highly fractionated granites is flanked on both sides by older, Early Cretaceous calc-alkaline diorite and granodiorite plutons of the Teslin suite (123–115 Ma) to the west and the Cassiar suite (115–104 Ma) to the east (intruded into Cassiar terrane; Fig. 1). These three distinct Cretaceous plutonic suites apparently occur within distinct fault panels, although the Nisutlin River and Hidden Lake faults are both plugged by Early Jurassic plutons of the Lokken suite (195–184 Ma; Fig. 1; Roots *et al.*, 2004; Sack *et al.*, 2020), and the Ram Creek fault is truncated to the south by the Cassiar fault, which is inferred to have developed during or shortly after emplacement of the Cassiar batholith at *ca.* 110–95 Ma (Gabrielse *et al.*, 2006). Thus, intrusion of the Seagull and Teslin suites occurred after development of the regional structures affecting the Yukon-Tanana terrane in this area. Older phases of the Teslin suite are locally deformed in the Deadman Creek batholith (Gordey *et al.*, 1998; this study), and development of the structural fabric is possibly related with displacement along the nearby Teslin fault (Fig. 1).

The Seagull plutonic suite is primarily composed of reduced, ilmenite-bearing, biotite leucogranite to monzogranite, but also includes local lepidolite–(zinnwaldite)–albite–fluorite–topaz leucogranite and rare hornblende lamprophyre (Liverton and Alderton, 1994; Rasmussen, 2013). The main exposures of the Seagull suite in southern Yukon occur in the Seagull and Hake batholiths, and the Thirtymile Range pluton, and satellite stocks and dikes (Fig. 1). The granite is texturally variable, ranging from fine to coarse grained, from equigranular to K-feldspar porphyritic,

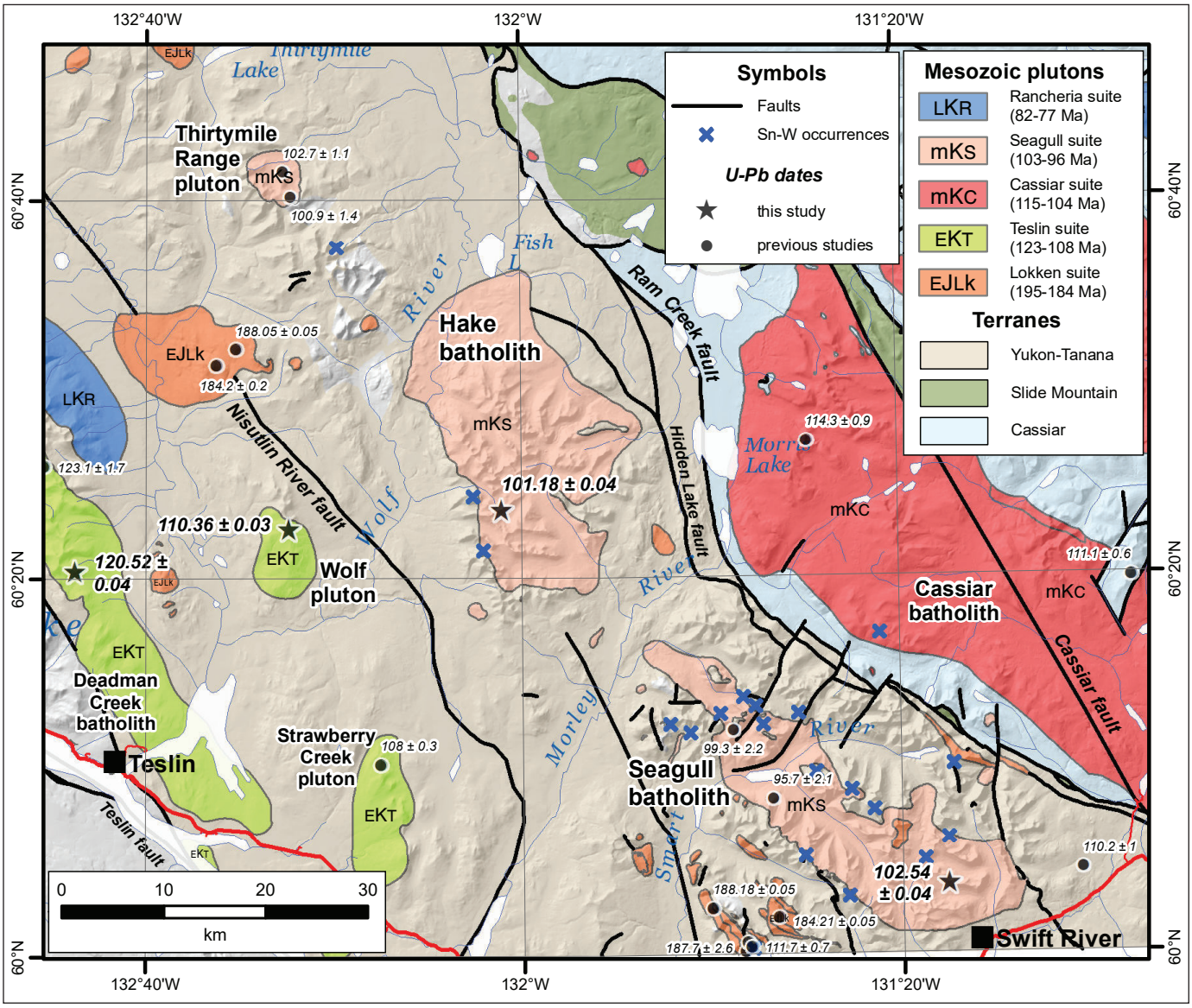

Figure 1. *Simplified geological map of the Teslin–Wolf Lake area, southern Yukon, showing the distribution of Mesozoic plutons and associated Sn-W occurrences (geology after Yukon Geological Survey, 2020b; mineral occurrences from Yukon Geological Survey, 2020c). Previous U-Pb dates for Jurassic and Cretaceous plutons are from the Yukon Geological Survey (2020d) compilation. New U-Pb dates presented here are shown by stars.*

and locally megacrystic (Fig. 2a–c). The K-feldspar (microcline) is commonly perthitic, and rapakivi texture is partially developed in parts of the Hake batholith (Fig. 2d). Smoky quartz is common in coarser grained phases (Fig. 2a). Miarolitic cavities with tourmaline–fluorite ± beryl ± topaz fills, pegmatite pods and quartz–tourmaline orbicules with aplitic margins indicate a shallow emplacement depth for plutons of the Seagull suite (Liverton and Alderton, 1994; Rasmussen, 2013; Liverton, 2016). The plutons are inferred to be connected at depth and represent the apex of a large, regional batholith approximately 100 km long by 20 km wide (Liverton *et al.*, 2005).

The Teslin suite, near the town of Teslin, was also investigated for its potential heat generation. In our study area, the Teslin suite comprises the Deadman Creek batholith and the Wolf and Strawberry Creek plutons (Fig. 1). The Teslin suite is composed mainly

of biotite ± hornblende diorite and granodiorite. The rocks are fine to coarse grained, and locally very coarse grained, and vary from equigranular to K-feldspar porphyritic to locally pegmatitic. Medium to coarse-grained, equigranular, biotite granite and leucogranite are common in the Strawberry Creek and Wolf plutons (Fig. 2e). Fine-grained hornblende diorite occurs locally along the eastern margin of the Deadman Creek batholith. Older diorite and granodiorite phases in the Deadman Creek batholith are locally foliated (Fig. 2f), but in general granodiorite and granite phases are undeformed.

Geochronology

Previous U-Pb zircon dates of the Teslin suite are presented in Gordey *et al.* (1998). These results were obtained using multi-grain zircon fractions that were air-abraded and analyzed by ID-TIMS at the Geological Survey of Canada. For most samples, zircon fractions are discordant and generally yielded imprecise dates. An older, lineated granodiorite phase in the Deadman Creek batholith is dated at 123.1 ± 1.7 Ma, whereas Bt granite from the northern margin of the pluton is 109 ± 2 Ma (Gordey *et al.*, 1998). A sample of coarse-grained biotite granite from the Strawberry Creek pluton is 108.0 ± 0.3 Ma (Fig. 1).

Zircons from the Seagull suite were previously analyzed by LA-ICPMS at the University of British Columbia. Two samples of granite from the northern part of the Seagull batholith yielded $^{206}Pb/^{238}U$ weighted mean dates of 95.7 ± 2.1 and 99.3 ± 2.2 Ma (Fig. 1; Mortensen *et al.*, 2006). In the Thirtymile Range pluton, a K-feldspar porphyritic granite yielded a $^{206}Pb/^{238}U$ weighted mean date of 102.7 ± 1.1 Ma, whereas an equigranular biotite granite phase is 100.9 ± 1.4 Ma (Fig. 1; Mortensen *et al.*, 2007).

We selected four samples of Cretaceous granitoid rocks for more precise analyses of single zircon crystals using the CA-TIMS method at Boise State University (Table 1; Appendix 1). Two samples of granite were collected from the Seagull and Hake batholiths (Seagull suite); for the Teslin suite, we collected a foliated granodiorite in the Deadman Creek batholith and a leucogranite in the Wolf pluton (Fig. 1). For each sample, zircon grains were first imaged by cathodoluminescence (CL) and selected spots were analyzed by laser ablation–inductively coupled mass spectrometry (LA-ICPMS; see Appendix 1 for methods; CL images are presented in Appendix 2 and LA-ICPMS data in Appendix 3). These results were then used to select zircon crystals for CA-TIMS. Weighted mean $^{206}Pb/^{238}U$ dates were calculated from equivalent dates (probability of fit [pof] >0.05) using Isoplot 3.0 (Ludwig, 2003). Errors on the weighted mean dates are given as ± *x* / *y* / *z*, where: *x* is the internal error based on analytical uncertainties only, including counting statistics, subtraction of tracer solution, and blank and initial common Pb subtraction; *y* includes the tracer calibration uncertainty propagated in quadrature; and *z* includes the ^{238}U decay constant uncertainty propagated in quadrature. Internal errors should be considered when comparing our dates with $^{206}Pb/^{238}U$ dates from other laboratories that used the same tracer solution or a tracer solution that was cross-calibrated using EARTHTIME gravimetric standards (Condon *et al.*, 2015). Errors including the uncertainty in the tracer calibration should be considered when comparing our dates with those derived from other geochronological methods using the U-Pb decay scheme (e.g., LA-ICPMS). Errors including uncertainties in the tracer calibration and ^{238}U decay constant should be considered when comparing our dates with those derived from other decay schemes (e.g., $^{40}Ar/^{39}Ar$, ^{187}Re-^{187}Os). Errors are given at 2σ.

Thirty-one zircon grains from 19MC-040, foliated granodiorite from the Deadman Creek batholith, yield LA-ICPMS dates between 132 ± 7 and 110 ± 5 Ma. Twenty-two dates yield a weighted mean of 120 ± 2 Ma (Mean Squared Weighted Deviation [MSWD] = 1.3, pof = 0.19). Six grains were analyzed by CA-TIMS. Four dates yield a weighted mean of 120.52 ± 0.04 / 0.07 / 0.15 Ma (MSWD = 0.8, pof = 0.48; Fig. 3a). This is the interpreted igneous crystallization age. One grain with a date of 120.70 ± 0.09 Ma is interpreted as containing an inherited component. One grain with a date of 119.82 ± 0.09 Ma is interpreted as having domains that suffered Pb loss despite chemical abrasion.

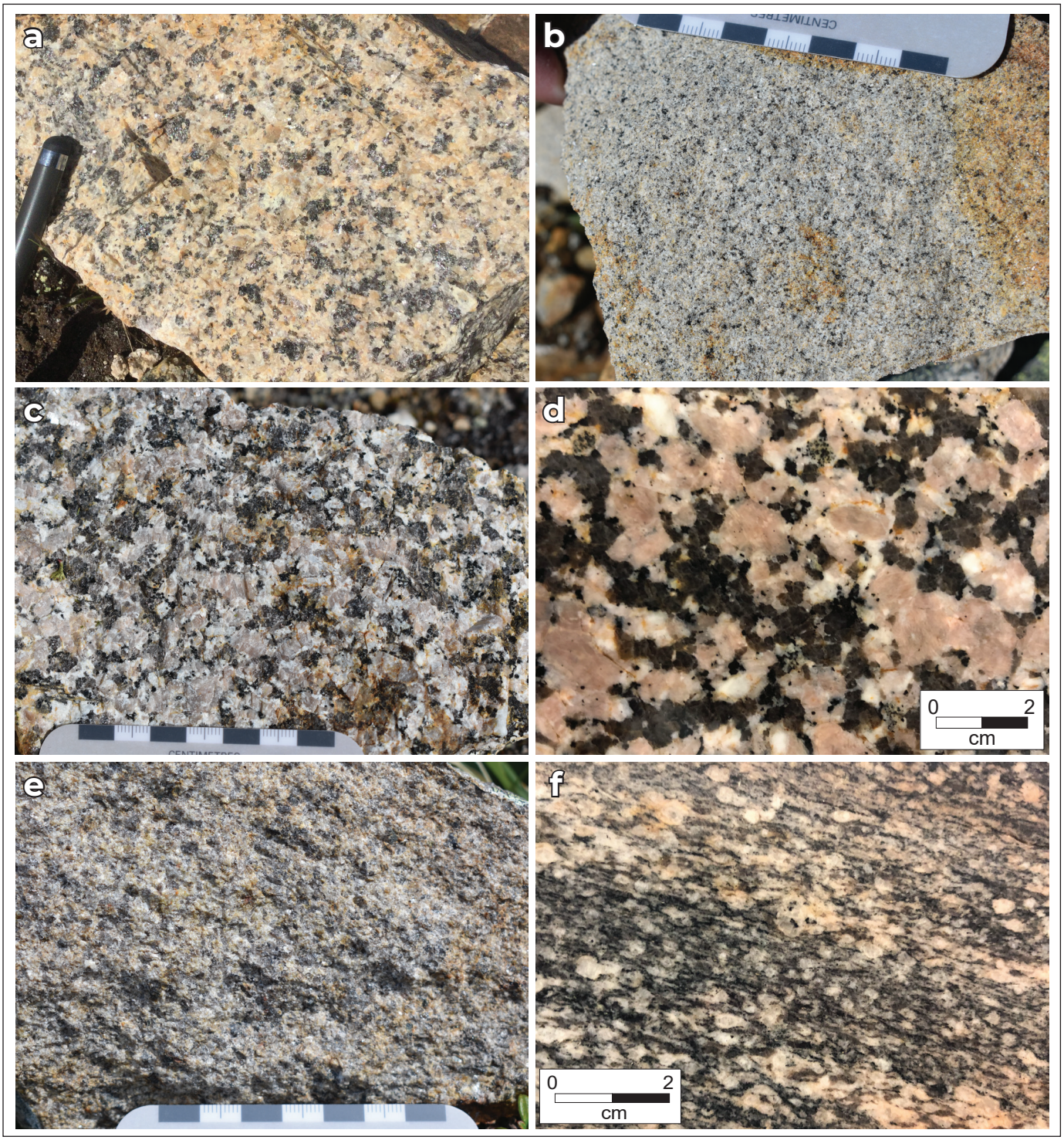

Figure 2. *Representative lithology of the Seagull, Hake and Wolf plutons.* **(a)** *coarse-grained, equigranular leucogranite from the southern part of the Seagull batholith. Note the coarse smoky quartz.* **(b)** *fine-grained biotite granite, central Seagull batholith.* **(c)** *coarse-grained, K-feldspar porphyritic, biotite granite from the Hake batholith. Note the smoky quartz.* **(d)** *partial development of rapakivi texture in the Hake batholith.* **(e)** *medium-grained, equigranular, biotite granite from the Wolf pluton.* **(f)** *foliation in granodiorite of the Deadman Creek batholith.*

Table 1. *CA-TIMS zircon U-Pb isotopic data.*

									Radiogenic Isotope Ratios					
	Th	^{206}Pb*	mol %	Pb*	Pb$_c$	^{206}Pb	^{208}Pb	^{207}Pb		^{207}Pb		^{206}Pb		corr.
Sample	U	x10^{-13} mol	^{206}Pb*	Pb$_c$	(pg)	^{204}Pb	^{206}Pb	^{206}Pb	% err	^{235}U	% err	^{238}U	% err	coef.
(a)	(b)	(c)	(c)	(c)	(c)	(d)	(e)	(e)	(f)	(e)	(f)	(e)	(f)	
19MC-040														
z1	0.550	1.0595	99.46%	56	0.48	3339	0.176	0.048532	0.150	0.126420	0.201	0.018901	0.073	0.788
z3	0.623	1.0438	99.60%	77	0.35	4509	0.199	0.048629	0.132	0.126524	0.185	0.018878	0.075	0.816
z2	0.636	0.6421	99.53%	66	0.25	3831	0.203	0.048692	0.148	0.126646	0.200	0.018872	0.072	0.809
z4	0.586	0.5822	99.34%	47	0.32	2754	0.187	0.048638	0.196	0.126495	0.245	0.018871	0.073	0.746
z5	0.445	0.9920	99.64%	81	0.30	4948	0.142	0.048516	0.119	0.126127	0.173	0.018863	0.071	0.849
z6	0.573	1.3062	99.72%	110	0.30	6483	0.183	0.048509	0.110	0.125427	0.165	0.018761	0.072	0.860
19MC-048														
z7	0.410	0.4584	99.39%	48	0.23	2973	0.131	0.048071	0.218	0.106500	0.260	0.016075	0.077	0.652
z2	0.567	2.0922	98.77%	25	2.14	1510	0.181	0.048034	0.143	0.106385	0.197	0.016070	0.074	0.824
z6	0.449	1.4114	99.59%	72	0.48	4429	0.144	0.048107	0.099	0.106437	0.157	0.016054	0.071	0.900
z3b	0.428	1.0407	99.87%	221	0.12	13565	0.137	0.048098	0.096	0.106298	0.153	0.016036	0.071	0.889
z3a	0.401	1.9700	99.92%	369	0.13	22790	0.128	0.048135	0.078	0.106378	0.138	0.016036	0.072	0.921
z5	0.294	2.3519	99.90%	290	0.19	18434	0.094	0.048150	0.071	0.106410	0.137	0.016036	0.075	0.944
z4	0.122	3.8832	99.96%	641	0.14	42877	0.039	0.048240	0.064	0.106558	0.130	0.016028	0.072	0.960
19MC-052														
z2	0.305	4.3695	99.94%	443	0.23	28093	0.098	0.048131	0.069	0.105205	0.132	0.015860	0.071	0.948
z4	0.414	1.3024	99.62%	76	0.42	4688	0.132	0.048124	0.118	0.105168	0.172	0.015857	0.071	0.846
z5	0.272	3.7587	99.93%	431	0.20	27577	0.087	0.048172	0.067	0.105190	0.132	0.015845	0.073	0.955
z1a	0.283	3.0042	99.91%	325	0.22	20744	0.091	0.048105	0.070	0.105013	0.134	0.015840	0.071	0.948
z1b	0.258	2.1049	99.91%	315	0.16	20253	0.082	0.048118	0.070	0.104929	0.133	0.015823	0.070	0.958
z6	0.296	2.0043	99.82%	158	0.30	10090	0.095	0.048100	0.085	0.104865	0.145	0.015819	0.071	0.914
z3	0.629	2.7527	99.91%	351	0.20	20420	0.201	0.048083	0.070	0.104802	0.133	0.015815	0.070	0.955
19MC054														
z6	0.811	1.0293	99.82%	183	0.15	10172	0.259	0.048328	0.098	0.115102	0.156	0.017282	0.071	0.895
z4	0.329	2.1726	99.92%	359	0.14	22587	0.105	0.048331	0.088	0.115024	0.144	0.017269	0.071	0.883
z5	0.532	0.9539	99.71%	105	0.23	6265	0.170	0.048344	0.115	0.115035	0.170	0.017265	0.071	0.859
z3	0.618	0.4530	99.51%	63	0.19	3669	0.198	0.048229	0.190	0.114750	0.239	0.017264	0.075	0.752
z2	0.578	0.9000	99.74%	118	0.19	6959	0.185	0.048294	0.106	0.114905	0.163	0.017264	0.071	0.891
z1	0.525	2.6265	99.93%	455	0.14	27189	0.168	0.048309	0.076	0.114925	0.137	0.017262	0.071	0.929

(a) z1, z2, etc. are labels for analyses composed of single zircon grains that were annealed and chemically abraded (Mattinson, 2005). Letters a and b denote fragments from the same grain.

(b) Model Th/U ratio calculated from radiogenic ^{208}Pb/^{206}Pb ratio and ^{207}Pb/^{235}U date.

(c) Pb* and Pbc are radiogenic and common Pb, respectively. mol % ^{206}Pb* is with respect to radiogenic and blank Pb.

d) Measured ratio corrected for spike and fractionation only. Fractionation correction for analyses done with tracer solution BSU1B is 0.18 ± 0.03 (1 sigma) %/amu (atomic mass unit) for single-collector Daly analyses, based on analysis of EARTHTIME ^{202}Pb-^{205}Pb ET2535 tracer solution. Fractionation correction for analyses done with tracer solution ET2535 is based on measurement of ^{202}Pb/^{205}Pb in the tracer solution.

(e) Corrected for fractionation and spike. Common Pb in zircon analyses is assigned to procedural blank with composition of ^{206}Pb/^{204}Pb = 18.04 ± 0.61%; ^{207}Pb/^{204}Pb = 15.54 ± 0.52%; ^{208}Pb/^{204}Pb = 37.69 ± 0.63% (1 sigma). ^{206}Pb/^{238}U and ^{207}Pb/^{206}Pb ratios corrected for initial disequilibrium in ^{230}Th/^{238}U using a D(Th/U) of 0.20 ± 0.05 (1 sigma).

(f) Errors are 2 sigma, propagated using algorithms of Schmitz and Schoene (2007) and Crowley *et al.* (2007).

(g) Calculations based on the decay constants of Jaffey *et al.* (1971). ^{206}Pb/^{238}U and ^{207}Pb/^{206}Pb dates corrected for initial disequilibrium in ^{230}Th/^{238}U using a D(Th/U) of 0.20 ± 0.05 (1 sigma).

Table 1 *continued. CA-TIMS zircon U-Pb isotopic data.*

	Isotopic Dates							
Sample	$^{207}Pb/^{206}Pb$	±	$^{207}Pb/^{235}U$	±	$^{206}Pb/^{238}U$	±	included in weighted mean?	
(a)	(g)	(f)	(g)	(f)	(g)	(f)		***Weighted Mean Calculations***
19MC-040								
z1	124.22	3.54	120.88	0.23	120.71	0.09		$^{206}Pb/^{238}U$ ± random (+tracer) [+decay constant]
z3	128.95	3.10	120.97	0.21	120.56	0.09	x	**120.52** **± 0.04** (0.07) [0.15]
z2	131.98	3.47	121.08	0.23	120.53	0.09	x	
z4	129.34	4.62	120.94	0.28	120.52	0.09	x	MSWD = 0.8
z5	123.46	2.79	120.61	0.20	120.47	0.08	x	pof = 0.48
z6	123.11	2.59	119.98	0.19	119.82	0.09		n = 4
19MC-048								
z7	101.71	5.15	102.76	0.25	102.80	0.08		$^{206}Pb/^{238}U$ ± random (+tracer) [+decay constant]
z2	99.87	3.39	102.65	0.19	102.77	0.08		**102.54** **± 0.04** (0.06) [0.13]
z6	103.46	2.33	102.70	0.15	102.67	0.07		
z3b	103.04	2.27	102.57	0.15	102.55	0.07	x	MSWD = 0.5
z3a	104.85	1.83	102.65	0.13	102.55	0.07	x	pof = 0.71
z5	105.57	1.68	102.68	0.13	102.55	0.08	x	n = 4
z4	109.98	1.51	102.81	0.13	102.50	0.07	x	
19MC-052								
z2	104.67	1.62	101.57	0.13	101.44	0.07		$^{206}Pb/^{238}U$ ± random (+tracer) [+decay constant]
z4	104.29	2.79	101.54	0.17	101.42	0.07		**101.18** **± 0.04** (0.06) [0.13]
z5	106.64	1.58	101.56	0.13	101.34	0.07		
z1a	103.37	1.66	101.39	0.13	101.31	0.07		MSWD = 0.5
z1b	103.99	1.65	101.32	0.13	101.20	0.07	x	pof = 0.60
z6	103.12	2.01	101.26	0.14	101.18	0.07	x	n = 3
z3	102.30	1.66	101.20	0.13	101.15	0.07	x	
19MC054								
z6	114.28	2.30	110.62	0.16	110.45	0.08	x	$^{206}Pb/^{238}U$ ± random (+tracer) [+decay constant]
z4	114.43	2.08	110.55	0.15	110.37	0.08	x	**110.36** **± 0.03** (0.06) [0.13]
z5	115.09	2.71	110.56	0.18	110.35	0.08	x	
z3	109.46	4.48	110.30	0.25	110.34	0.08	x	MSWD = 1.4
z2	112.65	2.50	110.44	0.17	110.34	0.08	x	pof = 0.22
z1	113.34	1.79	110.46	0.14	110.33	0.08	x	n = 6

Twenty zircon grains from 19MC-054, leucogranite from the Wolf pluton, yield LA-ICPMS dates between 121 ± 4 and 105 ± 2 Ma. Fifteen dates yield a weighted mean of 109 ± 1 Ma (MSWD = 1.2, pof = 0.22). Six grains were analyzed by CA-TIMS and yield a weighted mean date of 110.36 ± 0.03 / 0.06 / 0.13 Ma (MSWD = 1.4, pof = 0.22; Fig. 3b). This is the interpreted igneous crystallization age.

Seventeen zircon grains from 19MC-048, coarse-grained granite from the Seagull batholith, yield LA-ICPMS dates between 106 ± 3 and 100 ± 2 Ma. All dates yield a weighted mean of 103 ± 1 Ma (MSWD = 1.5, pof = 0.10). Six grains were analyzed by CA-TIMS, with two fragments from one grain being analyzed separately. The four youngest dates yield a weighted mean of 102.54 ± 0.04 / 0.06 / 0.13 Ma (MSWD = 0.5, pof = 0.71; Fig. 3c). This is the interpreted igneous crystallization age. Three grains with dates of 102.80 ± 0.08 to 102.67 ± 0.07 Ma are interpreted as containing inherited components.

Twenty-four zircon grains from 19MC-052, coarse-grained granite from the Hake batholith, yield LA-ICPMS

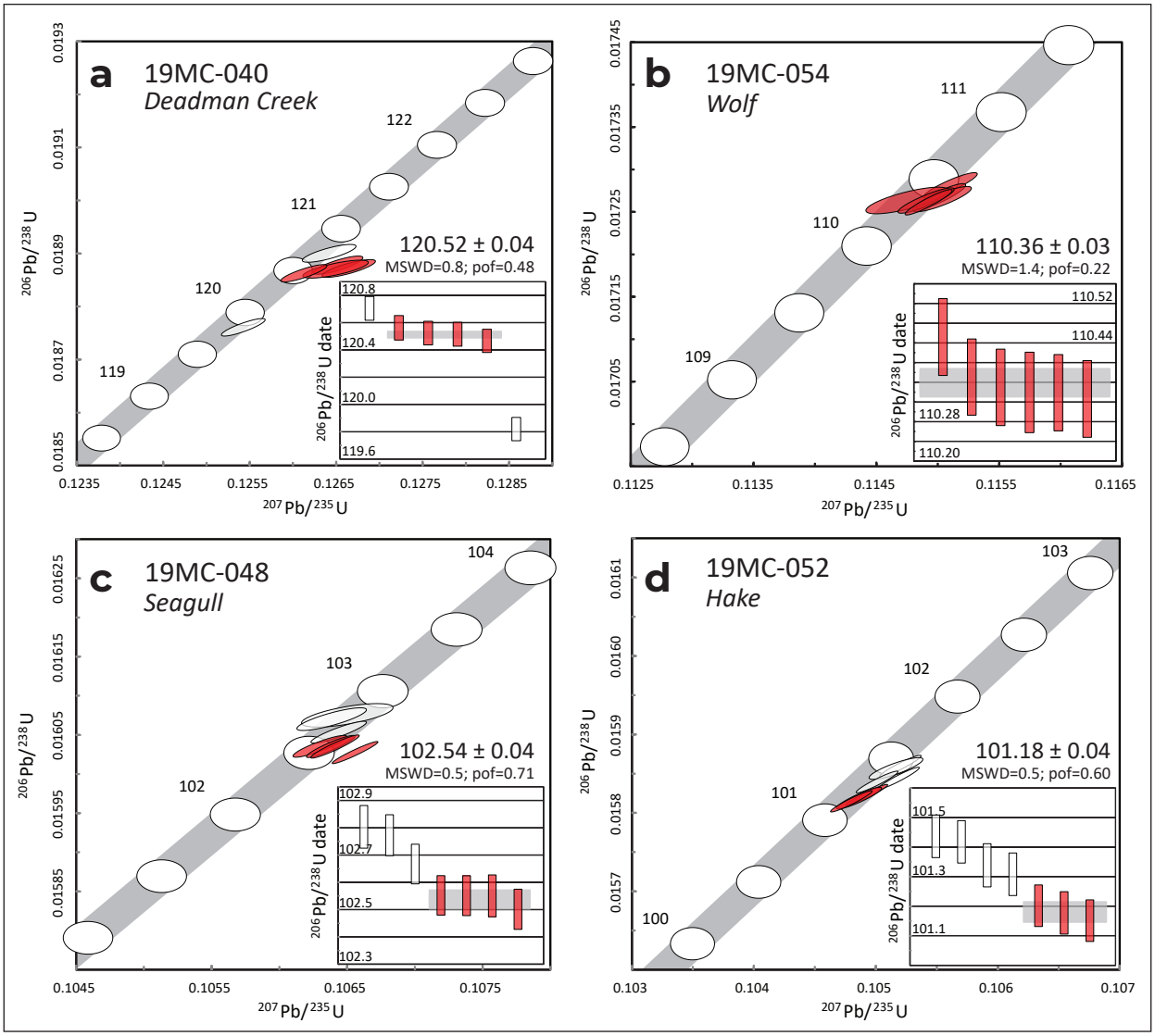

Figure 3. *Concordia diagram and ranked plot of $^{206}U/^{238}Pb$ dates (insets) for zircon analyzed by CA-TIMS (Table 1).* ***(a)*** *Deadman Creek batholith, 19MC-040;* ***(b)*** *Wolf pluton, 19MC-054;* ***(c)*** *Seagull batholith, 19MC-048;* ***(d)*** *Hake batholith, 19MC-052. The concordia curve is shown by the light grey band which includes uncertainties in decay constant. The weighted mean date was calculated with Isoplot 3.0 (Ludwig, 2003) and is represented by grey box behind the error bars on the ranked plot in inset. Analyses used in weighted mean calculation are shown in red. MSWD = Mean Square of Weighted Deviation; pof = probability of fit. All errors are at 2σ.*

dates between 108 ± 3 and 97 ± 5 Ma. Nineteen dates yield a weighted mean of 102 ± 1 Ma (MSWD = 1.2, pof = 0.22). Six grains were analyzed by CA-TIMS, with two fragments from one grain being analyzed separately. The three youngest dates yield a weighted mean of 101.18 ± 0.04 /0.06 / 0.13 Ma (MSWD = 0.5, pof = 0.60; Fig. 3d). This is the interpreted igneous crystallization age. Three grains with dates of 101.44 ± 0.07 to 101.31 ± 0.07 Ma are interpreted as containing inherited components.

Geochemistry

Lithogeochemical analyses were previously published for plutons of the Seagull suite, but <25% of samples were analyzed for the full suite of trace elements (including heat producing elements such as Th and U; Liverton and Alderton, 1994; Liverton *et al.*, 2005; Rasmussen, 2013). No previous geochemical data were published for plutons of the Teslin suite. We collected 6 new samples from the Seagull and Hake batholiths to complement previous data for the Seagull suite, and 9 samples from the Deadman Creek, Wolf and Strawberry Creek plutons to fill the gap for the Teslin suite (Table 2). Samples collected for this study were analyzed by fusion XRF and ICPMS at ALS Global laboratories in Vancouver, B.C. (all data are available online; Yukon Geological Survey, 2020a).

Samples from the Seagull suite generally have high SiO_2 contents (>70%, average 75%) and plot in the granite field of the total alkali *vs.* silica diagram of Le Bas *et al.* (1986; Fig. 4a). They are relatively sodic, with mostly alkali-calcic to alkalic compositions on the modified alkali-lime index (MALI) diagram (Fig. 4b), and straddle the peralkaline and peraluminous fields on the alumina saturation index (ASI) diagram (Fig. 4c). Granites of the Seagull suite are ultra-fractionated with strong enrichment in Th, Rb, U, $_{\Sigma}$REE, Li, B, F^- and Cl^-, elevated HREE, and depletion in CaO, MgO, Al_2O_3, Ba, Eu, Ti and P (Fig. 4d; Liverton and Alderton, 1994; Liverton *et al.*, 2005; Rasmussen, 2013; Liverton, 2016; Yukon Geological Survey, 2020a). Their Rb/Sr ratios are >2 (and up to ~9500) and $^{87}Sr/^{86}Sr_{100}$ range from 0.706 to 0.708 (Liverton and Alderton, 1994; Rasmussen, 2013). They have all the characteristics of A-type granites (Fig. 4e–f). The strongly fractionated granites of the Seagull suite stand as the most evolved plutons in the northern Cordillera (Rasmussen, 2013).

Samples from the Teslin suite have SiO_2 ranging from 58 to 77% (average 68%; Fig. 4a) and major and trace element compositions more typical of peraluminous, calc-alkaline granitoid rocks (Fig. 4b–f; Yukon Geological Survey, 2020a).

Potential Heat Generation

The decay of radioactive elements converts mass into radiation energy, which is an exothermic reaction that produces heat. While all naturally radioactive isotopes can generate some heat, significant heat production only occurs from the decay of ^{238}U, ^{235}U, ^{232}Th and ^{40}K. Therefore, potential heat production is governed by the concentrations of U, Th and K in the rock (Rybach, 1981). In igneous rocks, radiogenic heat production is dependent on the bulk chemistry of the rock and decreases from acidic (*e.g.*, granite) through basic to ultrabasic rock types (Rybach, 1981; Rybach and Buntebarth, 1982, 1984; Hasterok and Webb, 2017). Thus, granites with anomalously high concentrations of U, Th and K, such as plutons of the Seagull suite, are prime targets for calculating potential radiogenic heat production (*A*) using the equation of Rybach (1981):

$$A\ (\mu W/m^3) = \rho\ (9.52cU + 2.56cK + 3.48cTh) \times 10^{-5}$$

where *c* is the concentration of U and Th in ppm, and K in %; and ρ is the rock density (in g/cm^3). Heat production constants of the natural radio-elements U, Th, K are 9.525×10^{-5}, 2.561×10^{-5} and 3.477×10^{-9} W/kg, respectively (Rybach, 1981). Global averages for heat production (*A*) in typical granites range from 2.5 to 2.8 μW/m^3 (Hasterok and Webb, 2017).

The heat production calculations (*A*) for granites of the Seagull suite range between 0.3 and 22.9 μW/m^3, with an average of 6.7 μW/m^3 (n = 70) (Fig. 5; Appendix 4; Friend and Colpron, 2017; Colpron, 2019). More than 50% of the samples yielded *A* values >6.0 μW/m^3 with an average of 9.1 μW/m^3. Of these samples, only 15 were analyzed for all three radiogenic elements (Th, U and K), indicating that estimates of radiogenic

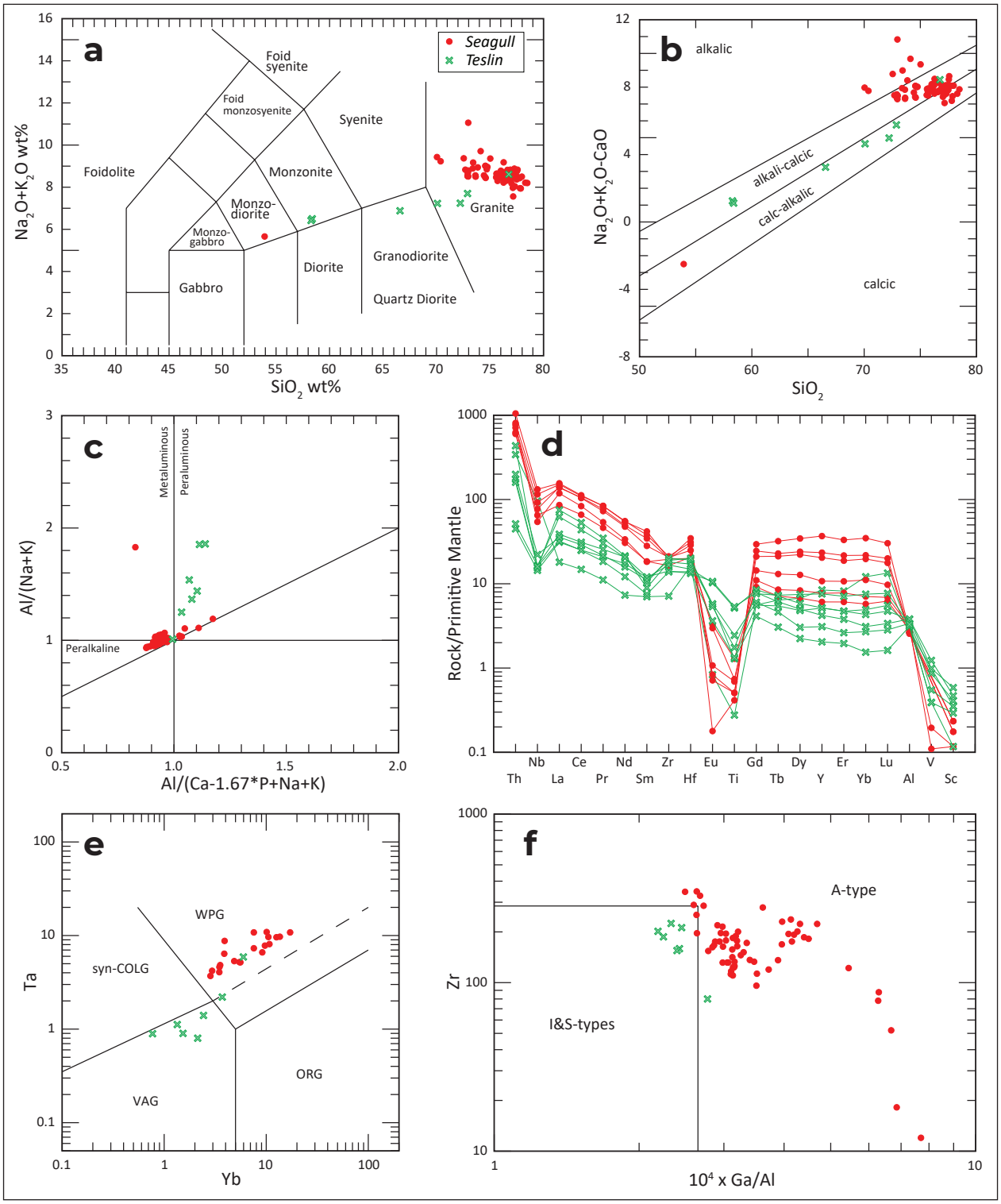

Figure 4. *Geochemical discriminant diagrams for the Seagull and Teslin plutonic suites.* **(a)** *Total alkali vs. SiO_2 diagram of Le Bas et al. (1986).* **(b)** *MALI diagram.* **(c)** *ASI diagram of Shand (1943).* **(d)** *Primitive mantle normalized trace element plot; normalization values of Sun and McDonough (1989).* **(e)** *Ta vs. Yb diagram of Pearce et al. (1984). ORG = ocean ridge granite; syn-COLG = syn-collisional granite; VAG = volcanic arc granite; WPG = within-plate (A-type) granite.* **(f)** *Zr vs. $10^4 \times$ Ga/Al diagram of Whalen et al. (1987).*

heat production are likely minimum values for ≥60% of samples. Seagull suite samples with A >6 μW/m³ generally have cTh >50 ppm (high ~100 ppm) and cU typically >10 ppm (Colpron, 2019; Yukon Geological Survey, 2020a). Samples with A >10 μW/m³ all have cU >20 ppm (high of 58 ppm).

Plutons of the Teslin suite have a wider range of compositions, from mafic to felsic (Fig. 4a), and generally yield heat production values that are closer to global averages, with A values being mostly between 0.9 and 3.1 μW/m³ and averaging 2.0 μW/m³ (Fig. 5; Appendix 4; Colpron, 2019). Two samples from the northern part of the Deadman Creek batholith (near Johnson's Crossing; not shown in Fig. 5) have more felsic compositions and A values of 4.5–5.0 μW/m³ (see Colpron, 2019). One sample from the Wolf pluton is strongly anomalous with A = 11.4 μW/m³ (Fig. 5).

For samples where all three radiogenic elements were analyzed, a ternary plot of Th-U-K relative to their respective heat production constants show that both Th and U are the main heat producing elements in the Seagull suite granites, with Th being dominant

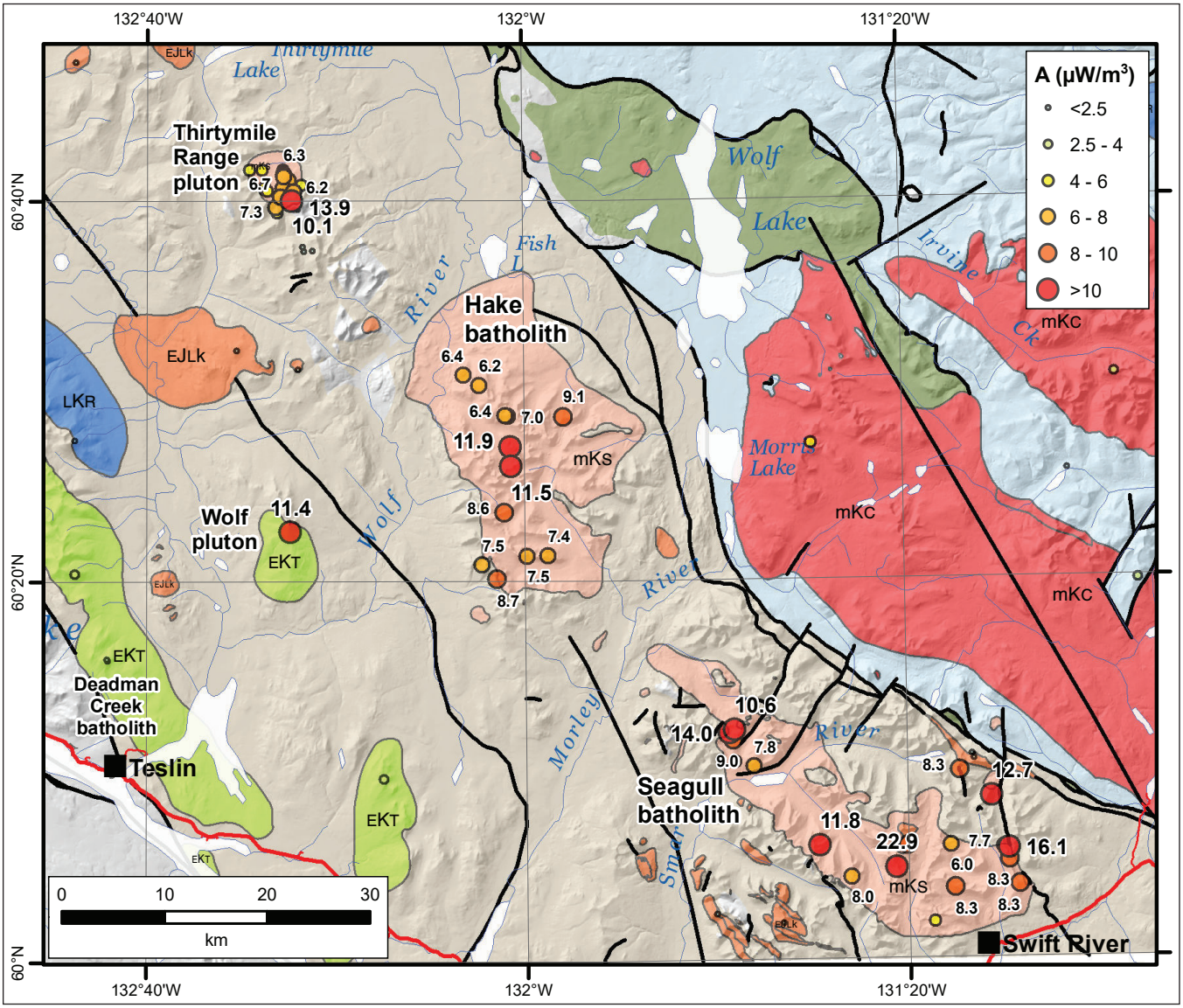

Figure 5. *Potential radiogenic heat production (A) from Mesozoic granitoids in the Teslin–Wolf Lake area of southern Yukon (after Friend and Colpron, 2017; Colpron, 2019). Heat production values were calculated using the equation of Rybach (1981). Lithogeochemical data are from the compilation by the Yukon Geological Survey (2020a). Only samples with A values >6 μW/m³ are labelled; complete list of values are given in Appendix 4 and Colpron (2019).*

in most samples (Fig. 6). The K contribution to heat production in granites of the Seagull suite is negligible. For all Cretaceous plutons, K_2O ranges from 2.5 to 6%, with most samples in the Seagull suite between 4.8 and 5.3% (average of 4.96%), and 2.6 and 3.9% for the Teslin suite (average of 3.19%; Appendix 4). In the Teslin suite, the generally low concentrations in Th (<17 ppm) and U (<5.7 ppm) in most samples result in proportionally more significant K contributions to heat production, although most samples have low to average A values (Fig. 5; Appendix 4). The few samples with anomalous A values all have cTh >29 ppm; the sample from the Wolf pluton, with A = 11.4 μW/m³, has cU = 33.2 ppm (Fig. 6; Appendix 4).

In both the Seagull and Hake batholiths, all samples are anomalous relative to global averages of heat production, with A ranging from 4.4 to 22.9 μW/m³, and >85% of samples have A values >6 μW/m³ (Fig. 5). The average A values for the Hake and Seagull batholiths are 7.9 and 9.9 μW/m³, respectively. Many of the samples with A <10 μW/m³ are lacking analyses for uranium (Colpron, 2019; Yukon Geological Survey, 2020a), suggesting that, although heat production seems primarily driven by cTh, the combination of anomalous Th and U concentrations yields the highest radiogenic heat production potential.

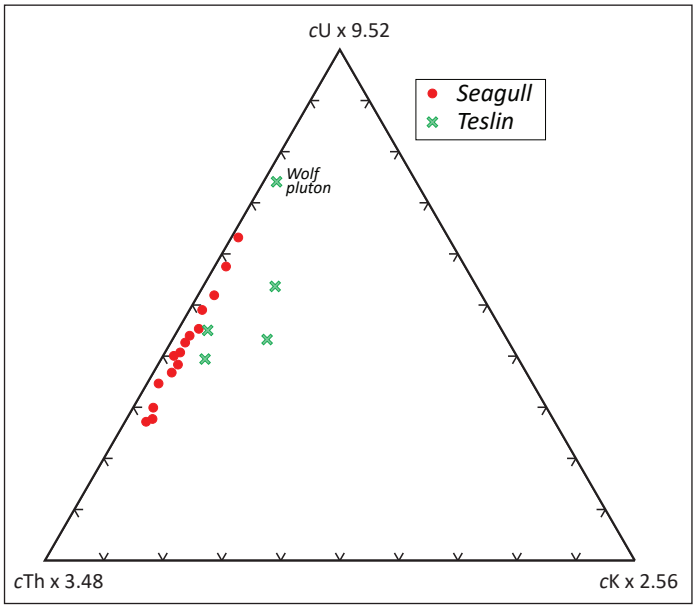

Figure 6. *Ternary Th-U-K diagram illustrating relative contributions to potential heat production calculations.*

A radiometric survey of the Seagull batholith acquired by UCore Rare Minerals Inc. in 2014 (Fig. 7; Kalkowski et *al.*, 2015) provides a means of evaluating the overall Th and U enrichments in this pluton. Figure 7 illustrates that Th enrichment is widespread in the Seagull batholith, whereas U is more concentrated in the southeastern part of the batholith. Samples with A >10 μW/m³ generally correspond with coincident Th and U anomalies. The radiometric survey for the Seagull batholith shows that coincident Th and U anomalies are more widespread in the southeastern portion of the pluton, where some of the highest heat production values are measured (up to 16.1 and 22.9 μW/m³; Figs. 5 and 7), and therefore this region is more prospective for potential radiogenic heat production. It is notable that U ± Th anomalies follow the fault at the eastern edge of the Seagull batholith, and that some of the highest heat production values occur along this same trend (Fig. 7).

Gravity Modeling

Bouguer gravity data for a broad area centered on the Hake and Seagull batholiths (Fig. 8) were gridded at 2 km from data acquired from the Geophysical Data Repository (Geological Survey of Canada, 2019). The data are reduced using a standard crustal Bouguer density of 2670 kg/m³. The Canadian Geodetic Survey and Geological Survey of Canada acquired the regional gravity data (Geological Survey of Canada, 2019) between 1944 and 2015 at a nominal station spacing of ~10 km. All data are tied to the International Gravity Standardization Network 1971 (IGSN 71; Morelli, 1974).

The three-dimensional geometry and character of low-density sources associated with intrusive rocks were investigated through the 3D inversion of Bouguer anomaly data, using the GRAV3D software package (Li and Oldenburg, 1998). The inverse problem is solved by minimizing the data misfit between the observed and predicted anomaly subject to model constraints; a trade-off parameter was used to balance the data fit and model smoothness.

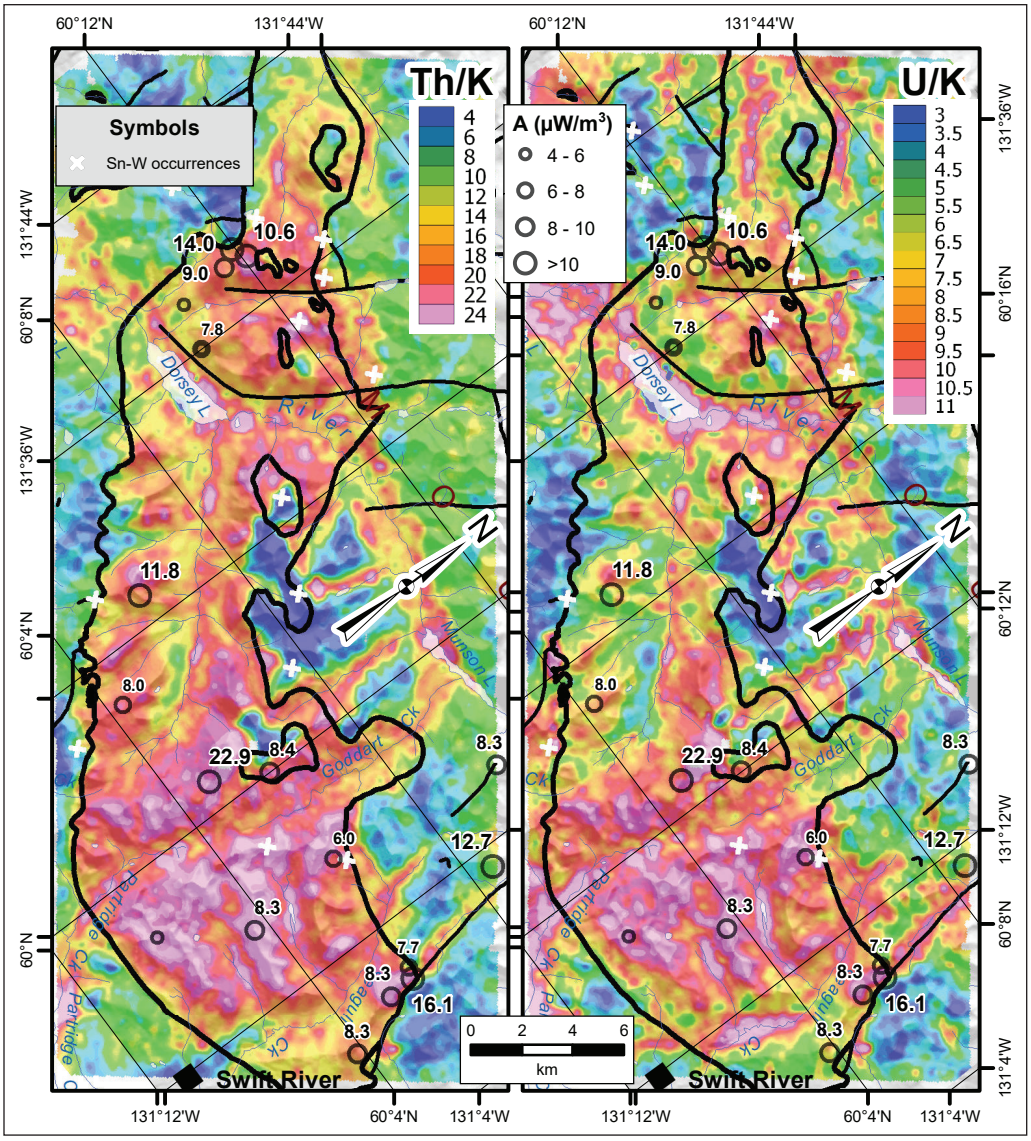

Figure 7. *Airborne radiometric survey results for the Seagull batholith (after Kalkowski et al., 2015).* ***(a)*** *Th/K map.* ***(b)*** *U/K map. Heat production values are from Appendix 4 and Colpron (2019). Note that all values in the Seagull batholith have A >4 μW/m³. Also note that the geographic frame is rotated with North pointing to the upper right.*

The input gravity data were sampled at original survey locations (2854 stations) from the 2 km grids. Model testing determined that upward continuation of the Bouguer data by 5 km was required to minimize model artefacts resulting from shallow-sourced perturbations and noise (Fig. 9a). In order to focus the inversions on the gravitational field associated with local sources, the regional field was removed by subtracting the long-wavelength component of the Bouguer anomaly following its upward continuation to 50 km (Fig. 9b). Surface topography was defined by a grid sampled from ETOPO1 (Amante and Eakins, 2009).

A mesh with a core cell size of $2 \times 2 \times 1$ km was determined from numerous test models to be a good compromise between model smoothness, size, and artefacts. The borders and base of the mesh were padded by increasingly larger cells to a distance/depth of 70/1000 km, respectively, to limit artefacts at model edges. As the inversions are focused on the gravity effects of low-density sources, only negative density contrasts were permitted. Specific gravity data measured from samples collected in the Hake and Seagull batholiths (Table 2) were used to define density constraints during modeling.

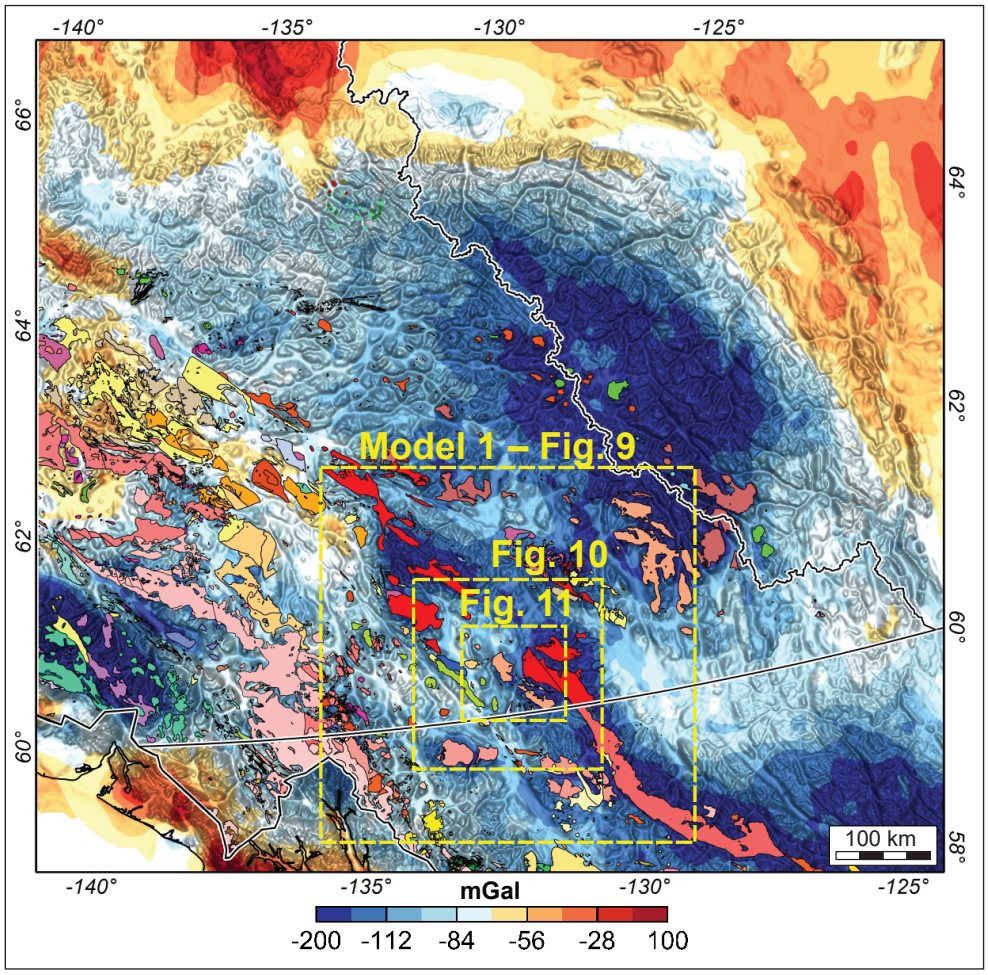

Figure 8. *Bouguer gravity of southern Yukon and surrounds overlain by topography. Coloured polygons show the distribution of mapped intrusive rocks (Cui et al., 2013; Yukon Geological Survey, 2020b). Yellow dashed box shows the locations of models presented below.*

A suite of three models was constructed for the intrusions, based on their combined rock physical property density ranges. The inversions were guided by a reference model with a negative density contrast equal to the higher value of sample density range, and the model bounded to only permit density contrast within the lower limit of the density range (Table 2). For example, the batholiths were initially modeled (Figs. 10 and 11a) with a range of -124 kg/m^3 (lower model bounds) to -58 kg/m^3 (reference density) corresponding to the range of rock physical property data (2546 to 2612 kg/m^3 relative to the Bouguer density of 2670 kg/m^3). The predicted model provided a good fit to the observed gravity with a RMS error of 1.02 mGal. Subsequent models were calculated for the density contrast ranges expanded by ± 10 (Fig. 11b; -134 to -48 kg/m^3) and ± 20 kg/m^3 (Fig. 11c; -144 to -38 kg/m^3), to assess the impact on the models should the intrusions have a wider range of density than constrained by rock physical properties.

The pattern of low-density zones in the models (e.g., Fig. 10) primarily reflect the distribution of relatively lower density intrusive rocks (Figs. 1 and 8). Models (Fig. 11) show low density sources associated with the Hake batholith and Thirtymile Range pluton, despite their limited surface extent and sparsity of gravity observations (Fig. 9a). The surface extent of the Hake batholith is well represented by the model

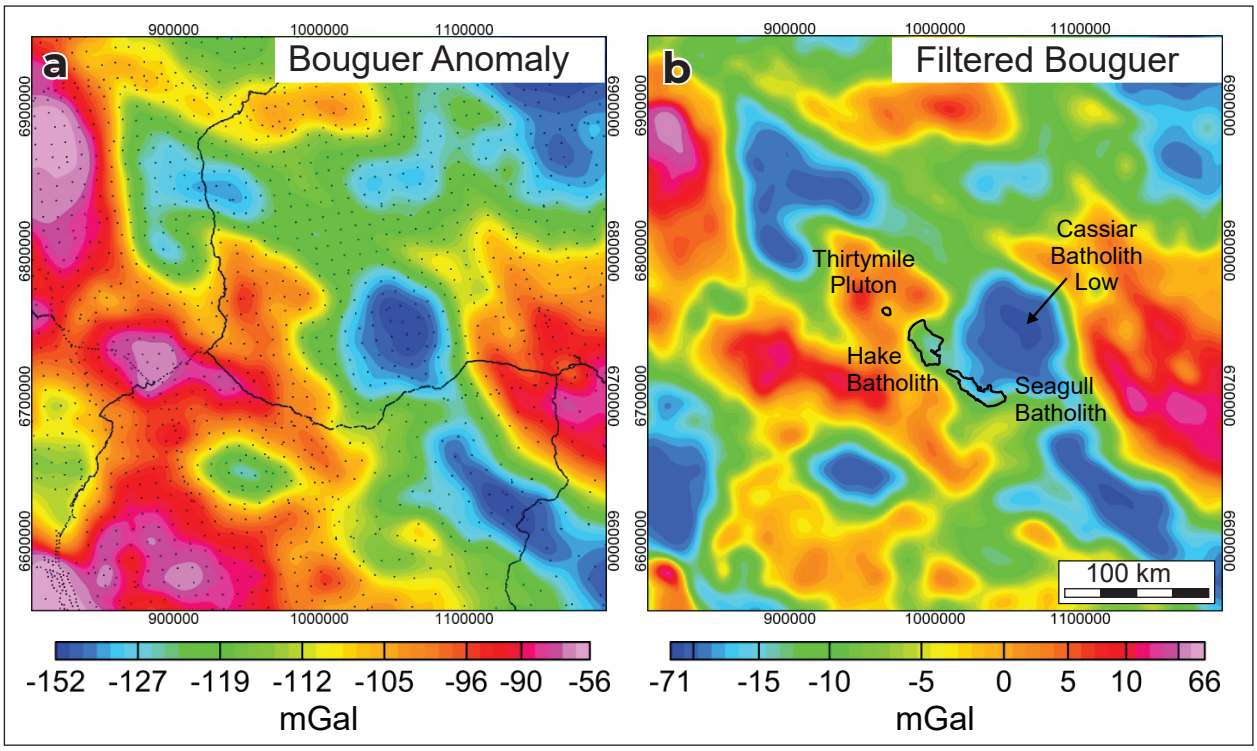

Figure 9. ***(a)*** *Bouguer anomaly, upward continued by 5 km, of the model area. Black dots show gravity station locations, more concentrated along roads.* ***(b)*** *Bouguer anomaly of the model area following removal of the regional field (Bouguer anomaly upward continued to 50 km). Black polygons show the mapped location of the Hake and Seagull batholiths, and Thirtymile pluton (Yukon Geological Survey, 2020b).*

(Fig. 11a), constrained by the rock physical properties in the range of -124 to -58 kg/m^3, but as with the Thirtymile Range pluton, the model may suggest a slightly greater lateral extent for the intrusion at depth. The volume of the Hake batholith is estimated at ~4624 km^3 with a maximum depth of ~11 km (Table 3). For an expanded density range (-134 to -48 kg/m^3), the lateral extent of the intrusion (Fig. 11b) is only slightly increased along with its depth and volume (Table 3). However, for a density range of -144 to -38 kg/m^3, the modeled intrusion (Fig. 11c) greatly exceeds its mapped expression and its estimated volume and depth are significantly greater.

For the Seagull batholith, the -124 to -58 kg/m^3 model (Fig. 11a) shows a source of similar lateral extent, but that is slightly displaced towards the northeast of its mapped expression. Its volume is estimated at ~2744 km^3 with a maximum depth of ~9 km. Increasing the density range (-134 to -48 kg/m^3 and -144 to -38 kg/m^3) results in predicted sources (Fig. 11b,c) that exceed the scale of the mapped expression. Estimates of volume and depth increase steadily in accordance (Table 3).

Discussion

Ultra-fractionated, A-type granites of the Seagull suite (Fig. 4) have heat production values (A) that are between 2 and 6 times higher than global averages (2.5–2.8 µW/m^3; Rybach, 1981; Hasterok and Webb, 2017), despite the fact that more than 60% of samples were not analyzed for a full suite of heat producing elements (Fig. 5; Appendix 4; Friend and Colpron, 2017; Colpron, 2019). The 6 samples collected from the Hake and Seagull batholiths for this study were analyzed for a full suite of trace elements and yielded A values ranging from 8.3 to 22.9 µW/m^3 (Fig. 5; Colpron, 2019; Yukon Geological Survey, 2020a), suggesting that for samples with incomplete analyses, heat production

Table 2. *Sample descriptions, locations and rock physical property data.*

Sample [1]	Latitude	Longitude	Lithology	Pluton	Magnetic susceptibility (10^{-3} SI units)[2]	Density (kg/m³)[3]	Density range (relative to Bouguer density of 2670 kg/m³)
Teslin plutonic suite							
19MC-036	60.161219	-132.248483	Medium-grained, equigranular Bt granite	Strawberry Creek pluton	3.52	2622	-48 to -62
19MC-037	60.160259	-132.249158	Coarse-grained, equigranular Bt granite	Strawberry Creek pluton	2.31	2608	
19MC-038	60.264854	-132.733467	Fine-grained Bt-Hbl diorite	Deadman Creek batholith	0.235	2713	-131 to -69
19MC-039	60.265657	-132.734871	Fine-grained Bt-Hbl diorite	Deadman Creek batholith		2711	
19MC-040	60.340521	-132.792034	Foliated, K-feldspar porphyritic Bt-Hbl granodiorite	Deadman Creek batholith	0.2	2680	
19MC-042	60.440648	-132.85519	Foliated, K-feldspar porphyritic Bt granodiorite	Deadman Creek batholith	0.204	2605	
19MC-043	60.509529	-133.036268	Medium-grained, equigranular Hbl-Bt granodiorite	Deadman Creek batholith	4.27	2601	
19MC-044	60.508212	-133.030736	Fine-grained Hbl diorite	Deadman Creek batholith	25	2801	
19MC-046	60.587557	-133.211117	Very coarse grained, equigranular, Bt-Hbl granodiorite	Deadman Creek batholith	2.85	2634	
19MC-054	60.377727	-132.412548	Medium-grained, equigranular leucogranite	Wolf pluton	0.0618	2573	-97
Seagull plutonic suite							
19MC-047	60.064369	-131.139421	Coarse-grained, equigranular, Bt granite	Seagull batholith	0.0207	2562	-78 to -124
19MC-048	60.062013	-131.251974	Coarse-grained, equigranular, Bt granite	Seagull batholith	0.0292	2592	
19MC-049	60.080551	-131.353948	Fine-grained, equigranular, Bt granite	Seagull batholith	0.058	2586	
19MC-050	60.100482	-131.487644	Coarse-grained, K-feldspar porphyritic Bt granite	Seagull batholith	0.212	2546	
19MC-052	60.394268	-132.034807	Coarse-grained Bt granite with partilally developed rapakivi texture	Hake batholith	1.04	2612	-58 to -84
19MC-053	60.477356	-131.930008	Coarse-grained, K-feldspar porphyritic Bt granite	Hake batholith	0.64	2586	

Notes:

[1] Samples shown in **Bold** were selected for geochronology

[2] Magnetic susceptibility is average of 5 or more measurements on the outcrop using a SM-30

[3] Density was measured from hand sample in the Yukon Geological Survey laboratory

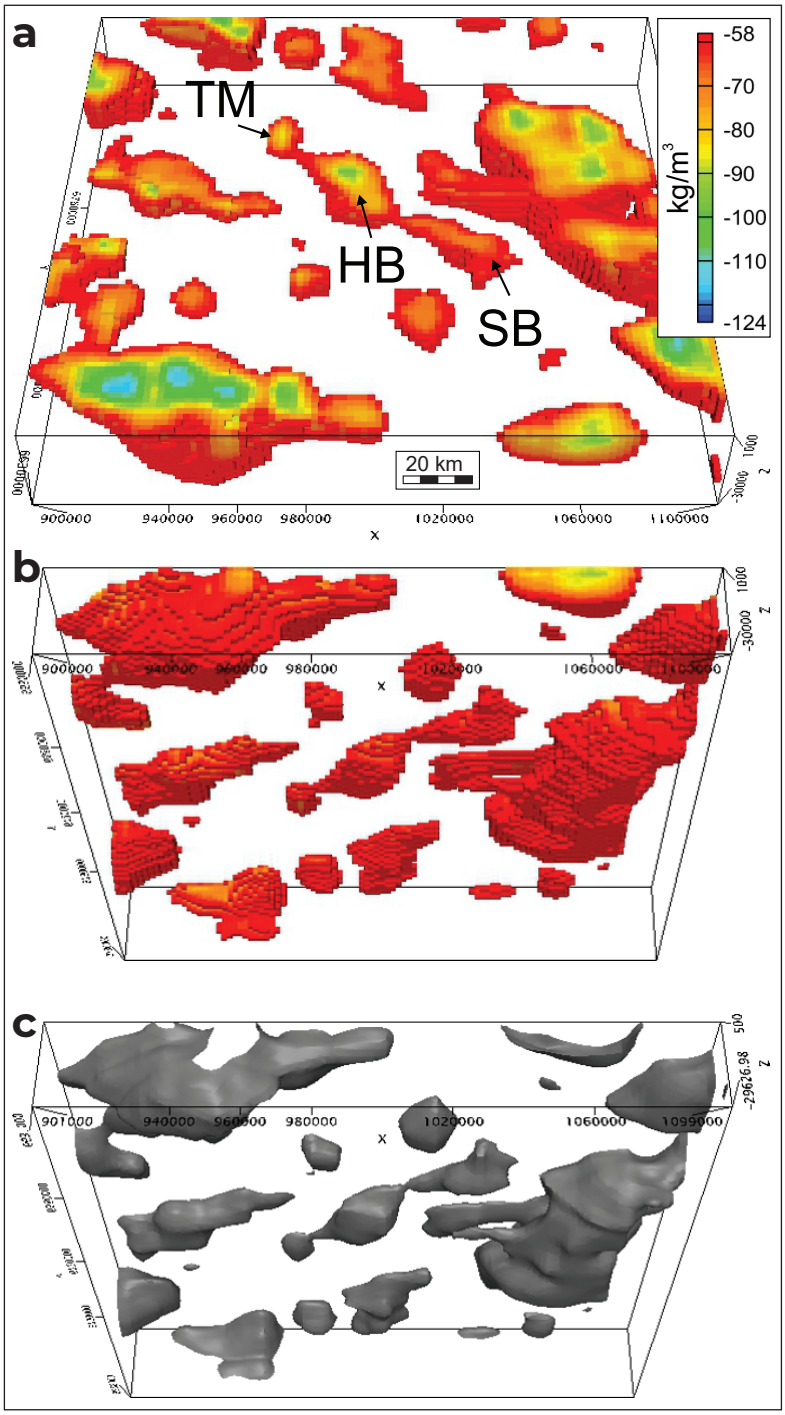

Figure 10. *3D Perspective views of the model density results from the Hake and Seagull batholiths for a density contrast range of -124 to -58 kg/m³.* **(a)** *View from above.* **(b)** *View from below* **(c)** *-58 kg/m³ isosurface viewed from below. See Figure 8 for location.*

values are likely underestimated by 30–60%; the relative contribution of cU in samples plotted in Figure 6. A radiometric survey of the Seagull batholith shows that although the whole batholith is highly radiogenic, the southeastern portion of the pluton near Swift River is likely more prospective for radiogenic heat production as coincident Th and U anomalies are more extensive in this region (Fig. 7).

Plutons of the Teslin suite have generally more intermediate compositions (Fig. 4) and A values that are equal to, or lower than, global averages (Fig. 5; Appendix 4; Colpron, 2019; Yukon Geological Survey, 2020a). Anomalous A values occur in more evolved granite phases of the Deadman Creek batholith (4.5–5.0 μW/m³; Colpron, 2019) and in one sample from the Wolf pluton, which has cU of 33.2 ppm resulting in A = 11.4 μW/m³ (Figs. 5 and 6; Yukon Geological Survey, 2020a). More detailed mapping of evolved granodiorite to granite phases in the Deadman Creek batholith would assist in identifying parts of the batholith more prospective for radiogenic heat production.

The new U-Pb zircon CA-TIMS dates for plutons of the Teslin and Seagull suites provide more precise age constraints that are generally in agreement with previously published dates (Fig. 1; Gordey *et al.*, 1998; Mortensen *et al.*, 2006, 2007). The older, foliated and lineated diorite to granodiorite phase of the Deadman Creek batholith is dated at *ca.* 121 Ma, whereas more evolved, post-tectonic granites in the Deadman Creek, Wolf and Strawberry Creek plutons yielded dates of *ca.* 110–108 Ma (Figs. 1 and 3). If local deformation in the Deadman Creek batholith is related to displacement along part of the Teslin fault system, then deformation along this segment of the fault had ceased by *ca.* 110 Ma. However, other segments of the fault may have been active into the Paleocene (Mihalynuk *et al.*, 2006).

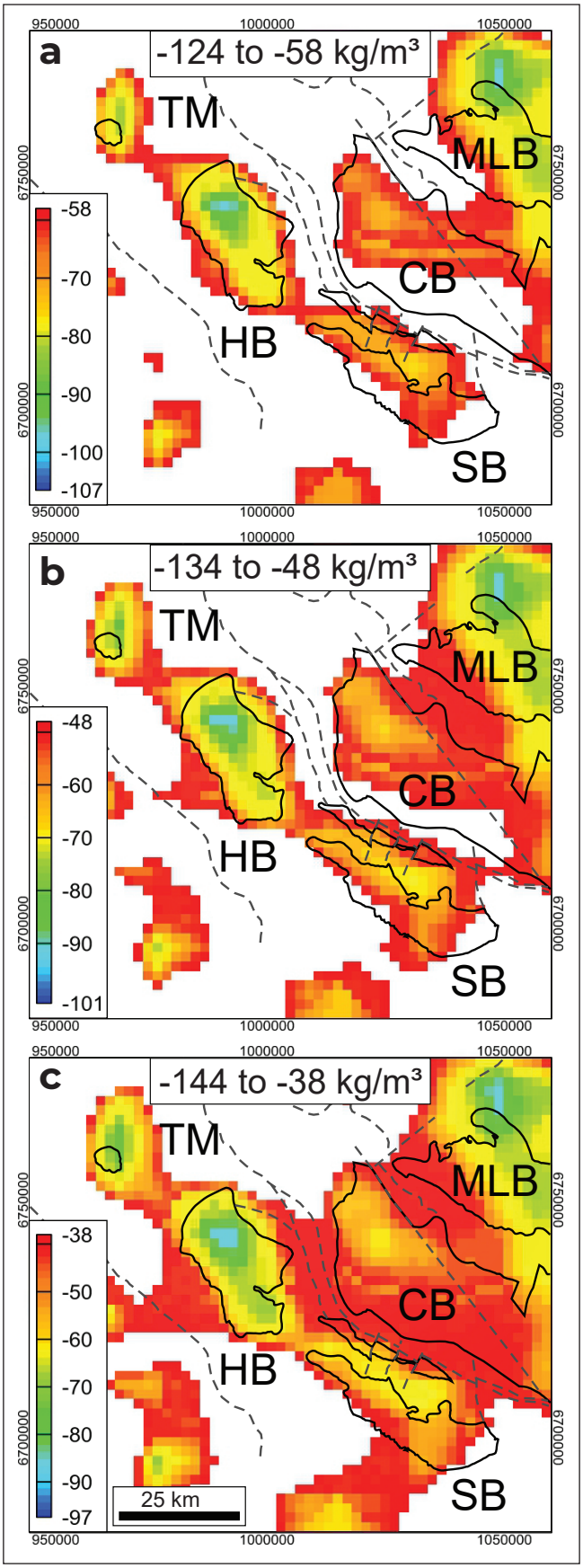

Granites of the Seagull suite are distinctly younger than the Teslin suite, with dates of *ca.* 103–101 Ma for the Thirtymile Range, Hake and Seagull plutons (Figs. 1 and 3). Previous LA-ICPMS dates from the northern part of the Seagull batholith are somewhat younger at 99–96 Ma (Mortensen *et al.*, 2006); this part of the batholith was not redated in this study using the more precise CA-TIMS method.

Gravity inversion model results that are based on measured rock physical properties (density contrast of -124 to -58 kg/m^3; Table 2) provide a good estimate for the extents of the Hake and Seagull batholiths (Table 3). Models for the Hake batholith are closely concordant with its mapped expression (Fig. 11). The volume of the pluton is estimated at ~4624 km^3 with a maximum depth of ~11 km (Table 3). The Seagull batholith is smaller with an estimated volume of ~2744 km^3 and a maximum depth of ~9 km (Table 3), but its modeled source is displaced to the northeast relative to its mapped expression (Fig. 11).

The apparent northeast displacement of the source associated with the Seagull batholith may indicate that the batholith dips towards the northeast and/or that the sparsely sampled gravity data are inadequate to accurately model the small intrusion. The majority of rocks adjacent to the pluton include typically higher density rocks of the Snowcap and Finlayson assemblages of the Yukon-Tanana terrane (Enkin, 2018; Yukon Geological Survey, 2020b). However, the Cassiar batholith (Fig. 11), which is associated with a large gravity low northeast of the Seagull batholith (Fig. 9), may be partly responsible for displacing the low-density source in the inversion results. Similarly, the location and scale of the small Thirtymile Range pluton are not well-defined by model results (Figs. 10 and 11), suggesting that smaller plutons may not be well constrained by the low spatial density of the

Figure 11. *Model density results for the Hake and Seagull batholiths, and Thirtymile Range pluton. Simplified geology from Yukon Geological Survey (2020b).*
(a) *Model density constraints -124 to -58 kg/m^3.*
(b) *Model density constraints -134 to -48 kg/m^3.*
(c) *Model density constraints -144 to -38 kg/m^3. Batholiths and plutons: TM = Thirtymile, HB = Hake, SB = Seagull, MLB = Marker Lake, CB = Cassiar.*

Table 3. *Estimated batholith volumes and maximum depths (below sea level) from density models using different reference densities.*

Range in Density Contrast (kg/m^3)	Density Range adjusted for Bouguer density (2670 kg/m^3)	Volume (km^3)	Max Depth (km)	Average A (μW/m^3)	Potential Heat Energy (MWt)
Hake batholith					
-124 to -58	2546 to 2612	4624	11	7.9	36.5
-134 to -48	2536 to 2622	6464	13	7.9	51.1
-144 to -38	2526 to 2632	11112	15	7.9	87.8
Seagull batholith					
-124 to -58	2546 to 2612	2744	9	9.9	27.2
-134 to -48	2536 to 2622	4928	13	9.9	48.8
-144 to -38	2526 to 2632	11612	18	9.9	115.0

gravity observations. Model resolution and accuracy would be improved with the acquisition of a denser grid of gravity data.

Both the Hake and Thirtymile Range plutons appear to have slightly larger extents at depth, but all plutons of the Seagull suite are relatively shallow with maximum depths of 9–11 km (Fig. 10; Table 3). The inversion model results may support the idea that these bodies are connected at depth (Liverton *et al.*, 2005), but the resolution of the input gravity data are not sufficient to be definitive and the relatively shallow maximum depths for these plutons limit the potential size of a regional batholith.

Using the volumes estimated by 3D inversion of regional Bouguer gravity data and average radiogenic heat production values, the Hake and Seagull batholiths contain potential heat energy of approximately 36.5 and 27.2 MWt, respectively (Table 3). When added to the elevated heat flow documented in the northern Cordillera (~105 ± 22 mW/m^2; Lewis *et al.*, 2003), the relatively thin crustal thickness (~32–35 km) and the shallow Curie point depths in the Teslin region (Witter and Miller, 2017; Witter *et al.*, 2018), these radiogenic heat sources could locally amplify near surface temperature gradients.

Lachenbruch (1970) has shown that shallow crustal heat flow and heat production in plutonic rocks have a near linear relationships such that:

$$q = 27 + 16.6A$$

where q is heat flow in mW/m^2 and A is the heat production in μW/m^3 (Beamish and Busby, 2016). This linear relationship shows little variation between differing crustal provinces (Lachenbruch, 1970; Hyndman and Lewis, 1999), and in the northern Cordillera Lewis *et al.* (2003) measured an average heat production (A) of 4.6 ± 2.4 μW/m^3, which corresponds to heat flow (q) of ~103 mW/m^2 within range of measured average heat flow of 105 ± 22 mW/m^2. When we apply Lachenbruch's (1970) equation to average heat production values for the Hake and Seagull batholiths, heat flow values of 158–191 mW/m^2 are suggested; these values are 50–80% above the regional average for the northern Cordillera (Lewis *et al.*, 2003).

Part of this energy could be harnessed if deep aquifers were heated and circulated to shallow depths. The granites themselves are likely poor targets for development of a geothermal reservoir, due to their expected poor porosity and permeability, except perhaps along faults (Fig. 1). A potential geothermal reservoir could however be developed in more porous limestone and marble of the Yukon-Tanana terrane mapped along the southern margin of the Seagull

batholith near Swift River (see Roots *et al.*, 2004). This portion of the Seagull batholith is the most radiogenic in the radiometric survey (Fig. 7), but the small modeled extent of the pluton at depth limits potential heating of the country rocks to its immediate margins. Crustal-scale thermal modeling, which is beyond the scope of the present study, is required in order to further evaluate the potential for the radiogenic granites to generate local geothermal anomalies.

The north-striking fault mapped north of Swift River is perhaps the most interesting target for geothermal exploration near the southeastern margin of the Seagull batholith (Fig. 1; Roots *et al.*, 2004). The fault is locally intruded by the Seagull batholith and appears to have provided a conduit during pluton emplacement, as suggested by Th and U anomalies following this structure in the radiometric survey (Fig. 7). A small satellite pluton of the Seagull suite was intruded along the fault to the north and has a heat production value of 12.7 μW/m^3, while samples collected at the eastern margin of the Seagull batholith have *A* ranging from 8.3 to 16.1 μW/m^3 (Fig. 5).

Radiogenic granites of the Cornubian province of SW England present an analogue for a potential geothermal system in plutons of the Seagull suite of southern Yukon (Beamish and Busby, 2016). Cornwall has the highest measured heat flow in England and this is directly related to radiogenic heat productions from the granites. It is the site of the only geothermal development project in the UK, where deep drilling (2500–4500 m) is targeting a permeable fault zone and the hot dry granite provides the heat source for an enhanced geothermal system (United Downs Deep Geothermal Power project; Ledingham *et al.*, 2019). Bottom hole temperatures of ~190°C are expected at United Downs and anticipated electricity generation ranges from 1–3 MWe. The southern Seagull batholith could be suitable for a similar geothermal energy generating system, but it should be noted that heat production values in the Seagull batholith (average of 9.9 μW/m^3) are 2–3 times higher than those measured in the Cornubian batholith (~2.5–5.0 μW/m^3; Beamish and Busby, 2016). This may suggest that temperatures sufficient for electricity generation could occur at shallower depths in the Seagull batholith compared to United Downs in Cornwall.

Conclusions

Ultra-fractionated, A-type granites of the Seagull plutonic suite are dated at *ca.* 103–101 Ma and have some of the highest potential for radiogenic heat production in southern Yukon (average of 9.1 μW/m^3). A radiometric survey of the Seagull batholith shows that heat producing elements are anomalous over large parts of this pluton, with the southeastern sector showing the highest potential for radiogenic heat production. The 3D inversion of regional Bouguer gravity resolves zones of low-density associated with the Seagull suite plutons and provide good density models on a mesh of 2 × 2 × 1 km, despite the relatively large gravity station spacing. Models for the Hake batholith match well its mapped extent and suggest an estimated volume of ~4624 km^3 with a maximum depth of ~11 km. The Seagull batholith is smaller with an estimated volume of ~2744 km^3 and a maximum depth of ~9 km, but its modeled source is displaced to the northeast relative to its mapped expression. Using the volumes estimated by 3D inversion of regional Bouguer gravity data and average radiogenic heat production values, the Hake and Seagull batholiths potentially hold heat energy of ~36.5 and 27.2 MWt, respectively.

Acknowledgements

Tiffani Fraser, Julie Minor, Carolyn Relf and Jeff Witter participated in field work for this study. Melissa Friend was instrumental in initiating the data compilation that led to initial assessment of potential radiogenic heat production in Yukon. Further development of the Yukon lithogeochemical dataset would not have been possible without help from Justin Emberley and Amanda O'Connor. Safe flying to field locations was provided by Capital Helicopters. Specific gravity measurements were obtained at the Yukon Geological Survey's rock property lab by Justin Emberley. Jeff Witter provided comments that helped enhance the paper. Funding for geothermal research at YGS was provided by the Government of Canada Canadian Northern Economic Development Agency's Strategic Initiatives in Northern Economic Development (SINED) Fund and the Government of Yukon. This is Geological Survey of Canada contribution 20200585.

References

Abbott, J.G., 1981. Geology of Seagull tin district. *In:* Yukon Geology and Exploration 1979-80, Indian and Northern Affairs Canada, Exploration and Geological Services Division, p. 32–44.

Amante, C. and Eakins, B.W., 2009. ETOPO1 1 Arc-Minute Global Relief Model: Procedures, Data Sources and Analysis. NOAA Technical Memorandum NESDIS NGDC-24. National Geophysical Data Center, NOAA. doi:10.7289/V5C8276M, [accessed October 2017].

Beamish, D. and Busby, J., 2016. The Cornubian geothermal province: heat production and flow in SW England: estimates from boreholes and airborne gamma-ray measurements. Geothermal Energy, vol. 4, p. 1–25. doi: 10.1186/s40517-016-0046-8.

Colpron, M., 2019. Potential radiogenic heat production from granitoid plutons in Yukon. Yukon Geological Survey, Open File 2019-16.

Colpron, M., Israel, S. and Friend, M., 2016. Yukon plutonic suites. Yukon Geological Survey, Open File 2016-37, 1:750 000 scale.

Condon, D.J., Schoene, B., McLean, N.M., Bowring, S.A. and Parrish, R., 2015. Metrology and traceability of U–Pb isotope dilution geochronology (EARTHTIME Tracer Calibration Part I). Geochimica et Cosmochimica Acta, vol. 164, p. 464–480.

Crowley, J.L., Schoene, B. and Bowring, S.A., 2007. U-Pb dating of zircon in the Bishop Tuff at the millennial scale. Geology, vol. 35, p. 1123–1126.

Cui, Y., Katay, F., Nelson, J. L., Han, T., Desjardins, P. J. and Sinclair L., 2013. British Columbia digital geology. British Columbia Ministry of Energy, Mines and Petroleum Resources, B.C. Geological Survey, Open File 2013-4.

Enkin, R.J. 2018. The Canadian Rock Physical Property Database - First Public Release, Geological Survey of Canada, Open File 8460, 126 p.

Friend, M. and Colpron, M., 2017. Potential radiogenic heat production from Cretaceous and younger granitoid plutons in southern Yukon. Yukon Geological Survey, Open File 2017-60, scale 1:1 000 000.

Gabrielse, H., Murphy, D.C. and Mortensen, J.K., 2006. Cretaceous and Cenozoic dextral orogen-parallel displacements, magmatism and paleogeography, north-central Canadian Cordillera. *In:* Paleogeography of the North American Cordillera: Evidence For and Against Large-Scale Displacements, J.W. Haggart, J.W.H. Monger and R.J. Enkin (eds.), Geological Association of Canada, Special Paper 46, p. 255–276.

Geological Survey of Canada, 2019. Geoscience Data Repository for Geophysical Data, Gravity, Point Data. Natural Resources Canada, http://gdr.agg.nrcan.gc.ca/gdrdap/dap/searcheng.php1, [accessed July 15, 2020].

Gerstenberger, H. and Haase, G., 1997. A highly effective emitter substance for mass spectrometric Pb isotope ratio determinations. Chemical Geology, vol. 136, p. 309–312.

Gordey, S.P., McNicoll, V.J. and Mortensen, J.K., 1998. New U-Pb ages from the Teslin area, southern Yukon, and their bearing on terrane evolution in the northern Cordillera. Geological Survey of Canada, Current Research 1998-F, p. 129–148.

Hasterok, D. and Webb, J., 2017. On the radiogenic heat production of igneous rocks. Geoscience Frontiers, vol. 8, p. 919–940.

Hayward, N., 2019. The 3D Geophysical Investigation of a Middle Cretaceous to Paleocene Regional Décollement in the Cordillera of Northern Canada and Alaska. Tectonics, vol. 38, p. 1–28, https://doi.org/10.1029/2018TC005295.

Hiess, J., Condon, D.J., McLean, N. and Noble, S.R., 2012. $^{238}U/^{235}U$ systematics in terrestrial uranium-bearing minerals. Science, vol. 335, p. 1610–1614.

Hyndman, R.D. and Lewis, T.J., 1999. Geophysical consequences of the Cordillera-Craton thermal transition in southwestern Canada. Tectonophysics, vol. 306, p. 397–422.

Jaffey, A.H., Flynn, K.F., Glendenin, L.E., Bentley, W.C. and Essling, A.M., 1971. Precision measurements of half-lives and specific activities of ^{235}U and ^{238}U. Physical Review C, vol. 4, p. 1889–1906.

Kalkowski, T., Dziuba, F. and Robinson, J., 2015. Staking, soil sampling, prospecting and airborne geophysics report – Seagull tin project. Yukon Energy, Mines and Resources, Assessment Report 096722, 50 p.

Krogh, T.E., 1973. A low contamination method for hydrothermal decomposition of zircon and extraction of U and Pb for isotopic age determination. Geochimica et Cosmochimica Acta, vol. 37, p. 485–494.

Lachenbruch, A.H., 1970. Crustal temperature and heat production: implications of the linear heat-flow relation. Journal of Geophysical Research, vol. 75, p. 3291–3300.

Le Bas, M.J., Le Maitre, R.W., Streckeisen, A. and Zanettin, B., 1986. A chemical classification of volcanic rocks based on the total alkalis-silica diagram. Journal of Petrology, vol. 27, p. 745–750.

Ledingham, P., Cotton, L. and Law, R., 2019. The United Downs Deep Geothermal Power Project. Proceedings, 44th Workshop on Geothermal Reservoir Engineering, Stanford University, California, p. 1–11.

Lewis, T.J., Hyndman, R.D. and Flück, P., 2003. Heat flow, heat generation, and crustal temperatures in the northern Cordillera: Thermal controls of tectonics. Journal of Geophysical Research, vol. 108, p. 2316.

Li, Y. and Oldenburg, D.W., 1998. 3D inversion of gravity data. Geophysics, vol. 63, p. 109–119.

Liverton, T., 2016. A-type granite plutons and tin skarn in southeast Yukon: Mindy prospect and surrounding granites of 105C/9. *In:* Yukon Exploration and Geology 2015, K.E. MacFarlane and M.G. Nordling (eds.), Yukon Geological Survey, p. 151–164.

Liverton, T. and Alderton, D.H.M., 1994. Plutonic rocks of the Thirtymile Range, Dorsey terrane: ultrafractionated tin granites in the Yukon. Canadian Journal of Earth Sciences, vol. 31, p. 1557–1568.

Liverton, T., Mortensen, J.K. and Roots, C.F., 2005. Character and metallogeny of Permian, Jurassic and Cretaceous plutons in the southern Yukon-Tanana terrane. *In:* Yukon Exploration and Geology 2004, D.S. Emond, L.L. Lewis and G.D. Bradshaw (eds.), Yukon Geological Survey, p. 147–165.

Ludwig, K.R., 2003. User's Manual for Isoplot 3.00. Berkeley Geochronology Center, Berkeley, CA, 70 p.

Mattinson, J.M., 2005. Zircon U-Pb chemical abrasion ("CA-TIMS") method: combined annealing and multi-step partial dissolution analysis for improved precision and accuracy of zircon ages. Chemical Geology, vol. 220, p. 47–66.

Mihalynuk, M.G., Friedman, R.M., Devine, F. and Heaman, L.M., 2006. Protolith age and deformation history of the Big Salmon complex, relicts of a Paleozoic continental arc in northern British Columbia. *In:* Paleozoic Evolution and Metallogeny of Pericratonic Terranes at the Ancient Pacific Margin of North America, Canadian and Alaskan Cordillera, M. Colpron and J.L. Nelson (eds.), Geological Association of Canada, Special Paper 45, p. 179–200.

Morelli, C., 1974. The international gravity standardization net 1971. International Association of Geodesy, Special Publication 4, 194 p.

Mortensen, J.K., Brand, A. and Liverton, T., 2007. Laser ablation ICP-MS zircon ages for Cretaceous plutonic rocks in the Logtung and Thirtymile Range areas of southern Yukon. *In:* Yukon Exploration and Geology 2006, D.S. Emond, L.L. Lewis and L.H. Weston (eds.), Yukon Geological Survey, p. 213–221.

Mortensen, J.K., Sluggett, C.L., Liverton, T. and Roots, C.F., 2006. Uranium-lead ID-TIMS and LA-ICP-MS ages for the Cassiar and Seagull batholiths, Wolf Lake map area, southern Yukon. *In:* Yukon Exploration and Geology 2005, D.S. Emond, G.D. Bradshaw, L.L. Lewis and L.H. Weston (eds.), Yukon Geological Survey, p. 257–266.

Pearce, J.A., Harris, N.B.W. and Tindle, A.G., 1984. Trace element discrimination diagrams for the tectonic interpretation of granitic rocks. Journal of Petrology, vol. 25, p. 956–983.

Rasmussen, K.L., 2013. The timing, composition, and petrogenesis of syn- to post-accretionary magmatism in the northern Cordilleran miogeocline, eastern Yukon and southwestern Northwest Territories. Unpublished PhD thesis, University of British Columbia, 788 p.

Roots, C.F., Nelson, J.L. and Stevens, R.A., 2004. Bedrock geology, Seagull Creek (105B/3), southern Yukon (1:50 000 scale). Yukon Geological Survey, Open File 2004-1.

Rybach, L., 1981. Geothermal systems, conductive heat flow, geothermal anomalies. *In:* Geothermal Systems: Principles and Case Histories, L. Rybach and L.J.P. Muffler (eds.), John Wiley & Sons, p. 3–31.

Rybach, L. and Buntebarth, G., 1982. Relationships between the petrophysical properties density, seismic velocities, heat generation, and mineralogical constitution. Earth and Planetary Science Letters, vol. 57, p. 367–376.

Rybach, L. and Buntebarth, G., 1984. The variation of heat generation. density and seismic velocity with rock type in the continental lithosphere. Tectonophysics, vol. 103, p. 335–344.

Sack, P.J., Colpron, M., Crowley, J.L., Ryan, J.J., Allan, M.M., Beranek, L.P., Joyce, N.L., Mortensen, J.K., Israel, S. and Chapman, J.B., 2020. Atlas of Late Triassic to Jurassic plutons in the Intermontane terranes of Yukon. Yukon Geological Survey, Open File 2020-1, 365 p.

Schmitz, M.D. and Schoene, B., 2007. Derivation of isotope ratios, errors and error correlations for U-Pb geochronology using ^{205}Pb-^{235}U-(^{233}U)-spiked isotope dilution thermal ionization mass spectrometric data. Geochemistry, Geophysics, Geosystems (G3), vol. 8, Q08006, doi:10.1029/2006GC001492.

Shand, S.J., 1943. Eruptive Rocks; Their Genesis, Composition, Classification, and Their Relation to Ore Deposits, with a Chapter on Meteorites. Hafner Publishing Co., New York, 444 p.

Sláma, J., Košler, J, Condon, D.J., Crowley, J.L., Gerdes, A., Hanchar, J.M., Horstwood, M.S.A., Morris, G.A., Nasdala, L., Norberg, N., Schaltegger, U., Schoene, B. Tubrett, M.N. and Whitehouse, M.J., 2008. Plešovice zircon — A new natural reference material for U–Pb and Hf isotopic microanalysis. Chemical Geology, vol. 249, p. 1–35.

Sun, S.S. and McDonough, W.F., 1989. Chemical and isotopic systematics of oceanic basalts: implications for mantle composition and processes. *In:* Magmatism in Ocean Basins, A.D. Saunders and M.J. Norry (eds.), Geological Society of London, Special Publication 42, p. 313–345.

Watson, E.B., Wark, D.A. and Thomas, J.B., 2006. Crystallization thermometers for zircon and rutile. Contributions to Mineralogy and Petrology, vol. 151, p. 413–433.

Whalen, J.B., Currie, K.L. and Chappell, B.W., 1987. A-Type granites: Geochemical characteristics, discrimination and petrogenesis. Contribution to Mineralogy and Petrology, vol. 95, p. 407–419.

Witter, J. and Miller, C., 2017. Curie point depth mapping in Yukon. Yukon Geological Survey, Open File 2017-3, 37 p.

Witter, J.B., Miller, C.A., Friend, M. and Colpron, M., 2018. Curie point depths and heat production in Yukon, Canada. Proceedings, 43rd Workshop on Geothermal Reservoir Engineering, Standford University, California, 11 p.

Yukon Geological Survey, 2020a. Yukon Lithogeochemistry data set. Yukon Geological Survey, http://data.geology.gov.yk.ca/Compilation/35#InfoTab, [accessed November 7, 2020].

Yukon Geological Survey, 2020b. Yukon Digital Bedrock Geology. Yukon Geological Survey, http://data.geology.gov.yk.ca/Compilation/3, [accessed November 7, 2020].

Yukon Geological Survey, 2020c. Yukon MINFILE – A database of mineral occurrences. Yukon Geological Survey, http://data.geology.gov.yk.ca/Compilation/24, [accessed November 7, 2020].

Yukon Geological Survey, 2020d. Yukon Geochronology – A database of Yukon isotopic age determinations. Yukon Geological Survey, http://data.geology.gov.yk.ca/Compilation/22, [accessed November 7, 2020].

Appendix 1

U-Pb Geochronology Methods

LA-ICPMS methods

Zircon grains were separated from rocks using standard techniques, annealed at 900°C for 60 hours in a muffle furnace, and mounted in epoxy and polished until their centers were exposed. Cathodoluminescence (CL) images were obtained with a JEOL JSM-300 scanning electron microscope and Gatan MiniCL. Zircon was analyzed by laser ablation inductively coupled plasma mass spectrometry (LA-ICPMS) using a ThermoElectron X-Series II quadrupole ICPMS and New Wave Research UP-213 Nd:YAG UV (213 nm) laser ablation system. In-house analytical protocols, standard materials, and data reduction software were used for acquisition and calibration of U-Pb dates and a suite of high field strength elements (HFSE) and rare earth elements (REE). Zircon was ablated with a laser spot of 25 µm wide using fluence and pulse rates of 5 J/cm^2 and 5 Hz, respectively, during a 45 second analysis (15 sec gas blank, 30 sec ablation) that excavated a pit ~15 µm deep. Ablated material was carried by a 1.2 L/min He gas stream to the nebulizer flow of the plasma. Dwell times were 5 ms for Si and Zr, 200 ms for ^{49}Ti and ^{207}Pb, 80 ms for ^{206}Pb, 40 ms for ^{202}Hg, ^{204}Pb, ^{208}Pb, ^{232}Th, and ^{238}U and 10 ms for all other HFSE and REE. Background count rates for each analyte were obtained prior to each spot analysis and subtracted from the raw count rate for each analyte. Ablation pits that appear to have intersected glass or mineral inclusions were identified based on Ti and P. U-Pb dates from these analyses are considered valid if the U-Pb ratios appear to have been unaffected by the inclusions. Analyses that appear contaminated by common Pb were rejected based on mass 204 being above baseline. For concentration calculations, background-subtracted count rates for each analyte were internally normalized to ^{29}Si and calibrated with respect to NIST SRM-610 and -612 glasses as the primary standards. Temperature was calculated from the Ti-in-zircon thermometer (Watson *et al.*, 2006). Because there are no constraints on the activity of TiO_2, an average value in crustal rocks of 0.8 was used.

Data were collected in one experiment in July 2020 and one in November 2020. For U-Pb and ^{207}Pb/^{206}Pb dates, instrumental fractionation of the background-subtracted ratios was corrected and dates were calibrated with respect to interspersed measurements of zircon standards and reference materials. The primary standard Plešovice zircon (Sláma *et al.*, 2008) was used to monitor time-dependent instrumental fractionation based on two analyses for every 10 analyses of unknown zircon. A secondary correction to the ^{206}Pb/^{238}U dates was made based on results from the zircon standards Seiland (530 Ma, unpublished data, Boise State University) and Zirconia (327 Ma, unpublished data, Boise State University), which were treated as unknowns and measured once for every 10 analyses of unknown zircon. These results showed a linear age bias of several percent that is related to the ^{206}Pb count rate. The secondary correction is thought to mitigate matrix-dependent variations due to contrasting compositions and ablation characteristics between the Plešovice zircon and other standards (and unknowns).

Radiogenic isotope ratio and age error propagation for all analyses includes uncertainty contributions from counting statistics and background subtraction. The standard calibration uncertainty for U/Pb is the local standard deviation of the polynomial fit to the fractionation factor of Plešovice versus time and for ^{207}Pb/^{206}Pb is the standard error of the mean of the fractionation factor of Plešovice. Errors without the standard calibration uncertainty are shown in the data table and are given below for single analyses. For groups of analyses that are collectively interpreted from a weighted mean date (*i.e.*, igneous zircon analyses), a weighted mean date is first calculated from equivalent dates (probability of fit >0.05) using Isoplot 3.0 (Ludwig, 2003) with errors on individual dates that do not include a standard calibration uncertainty. A standard calibration uncertainty is then propagated into the error on the date and is given below. These uncertainties are 0.8–0.9% (2σ) for ^{206}Pb/^{238}U and 0.4–0.5% (2σ) for ^{207}Pb/^{206}Pb. Age interpretations are based on ^{206}Pb/^{238}U dates. Errors are 2σ.

CA-TIMS methods

U-Pb dates were obtained by the chemical abrasion isotope dilution thermal ionization mass spectrometry (CA-TIMS) method from analyses composed of single zircon grains (Table 1), modified after Mattinson (2005). Zircon was removed from the epoxy mounts for dating based on CL images, and before LA-ICPMS data were collected.

Zircon was put into 3 ml Teflon PFA beakers and loaded into 300 ml Teflon PFA microcapsules. Fifteen microcapsules were placed in a large-capacity Parr vessel and the zircon partially dissolved in 120 ml of 29 M HF for 12 hours at 190°C. Zircon was returned to 3 ml Teflon PFA beakers, HF was removed, and zircon was immersed in 3.5 M HNO_3, ultrasonically cleaned for an hour, and fluxed on a hotplate at 80°C for an hour. The HNO_3 was removed and zircon was rinsed twice in ultrapure H_2O before being reloaded into the 300 ml Teflon PFA microcapsules (rinsed and fluxed in 6 M HCl during sonication and washing of the zircon) and spiked with the Boise State University mixed ^{233}U-^{235}U-^{205}Pb tracer solution (BSU-1B). Zircon was dissolved in Parr vessels in 120 ml of 29 M HF with a trace of 3.5 M HNO_3 at 220°C for 48 hours, dried to fluorides, and redissolved in 6 M HCl at 180°C overnight. U and Pb were separated from the zircon matrix using an HCl-based anion-exchange chromatographic procedure (Krogh, 1973), eluted together and dried with 2 µl of 0.05 N H_3PO_4.

Pb and U were loaded on a single outgassed Re filament in 5 µl of a silica-gel/phosphoric acid mixture (Gerstenberger and Haase, 1997), and U and Pb isotopic measurements made on a GV Isoprobe-T multi-collector thermal ionization mass spectrometer equipped with an ion-counting Daly detector. Pb isotopes were measured by peak-jumping all isotopes on the Daly detector for 160 cycles, and corrected for 0.16 ± 0.03%/a.m.u. (1σ) mass fractionation. Transitory isobaric interferences due to high-molecular weight organics, particularly on ^{204}Pb and ^{207}Pb, disappeared within approximately 60 cycles, while ionization efficiency averaged 10^4 cps/pg of each Pb isotope. Linearity (to ≥1.4×10^6 cps) and the associated deadtime correction of the Daly detector were determined by analysis of NBS982. Uranium was analyzed as UO_2^+ ions in static Faraday mode on 10^{12} ohm resistors for 300 cycles, and corrected for isobaric interference of $^{233}U^{18}O^{16}O$ on $^{235}U^{16}O^{16}O$ with an $^{18}O/^{16}O$ of 0.00206. Ionization efficiency averaged 20 mV/ng of each U isotope. U mass fractionation was corrected using the known $^{233}U/^{235}U$ ratio of the Boise State University tracer solution.

U-Pb dates and uncertainties were calculated using the algorithms of Schmitz and Schoene (2007), calibration of BSU-1B tracer solution of $^{235}U/^{205}Pb$ of 77.93 and $^{233}U/^{235}U$ of 1.007066 for, U decay constants recommended by Jaffey et *al.* (1971), and $^{238}U/^{235}U$ of 137.818 (Hiess et *al.*, 2012). $^{206}Pb/^{238}U$ ratios and dates were corrected for initial ^{230}Th disequilibrium using $D_{Th/U} = 0.20 \pm 0.05$ (1σ) and the algorithms of Crowley et *al.* (2007), resulting in an increase in the $^{206}Pb/^{238}U$ dates of ~0.09 Ma. All common Pb in analyses was attributed to laboratory blank and subtracted based on the measured laboratory Pb isotopic composition and associated uncertainty. U blanks are estimated at 0.013 pg.

Weighted mean $^{206}Pb/^{238}U$ dates are calculated from equivalent dates (probability of fit >0.05) using Isoplot 3.0 (Ludwig, 2003). Errors on weighted mean dates are given as ± x / y / z, where x is the internal error based on analytical uncertainties only, including counting statistics, subtraction of tracer solution, and blank and initial common Pb subtraction, y includes the tracer calibration uncertainty propagated in quadrature, and z includes the ^{238}U decay constant uncertainty propagated in quadrature. Internal errors should be considered when comparing our dates with $^{206}Pb/^{238}U$ dates from other laboratories that used the same tracer solution or a tracer solution that was cross-calibrated using EARTHTIME gravimetric standards. Errors including the uncertainty in the tracer calibration should be considered when comparing our dates with those derived from other geochronological methods using the U-Pb decay scheme (e.g., laser ablation ICPMS). Errors including uncertainties in the tracer calibration and ^{238}U decay constant (Jaffey et *al.*, 1971) should be considered when comparing our dates with those derived from other decay schemes (e.g., $^{40}Ar/^{39}Ar$, ^{187}Re-^{187}Os). Errors are 2σ.

Appendix 2 (online only)

CL images of zircon. (PDF)

Appendix 3 (online only)

LA-ICPMS data table (XLS)

Appendix 4 (online only)

Radiogenic heat production data and calculations for the Seagull and Teslin plutonic suite, east of Teslin. (XLS)

Updated geology of the Clark Lakes area in central Yukon (parts of 106D/2, 3, 6 and 7)

Diane Skipton
Yukon Geological Survey

Liam Maw
Institut national de la recherche scientifique

Skipton, D. and Maw, L., 2021. Updated geology of the Clark Lakes area in central Yukon (parts of 106D/2, 3, 6 and 7). *In:* Yukon Exploration and Geology 2020, K.E. MacFarlane (ed.), Yukon Geological Survey, p. 73–94.

Abstract

The Clark Lakes area is located along the northern boundary of the Selwyn fold belt, and is underlain by the Ediacaran to Cambrian Hyland Group. In the surrounding region, the Hyland Group and Paleozoic platformal carbonate rocks host several Au and polymetallic mineral deposits. The Clark Lakes area is bordered by regional-scale, southeast-striking thrust faults, which include the Dawson thrust to the northeast, and the Tombstone and Robert Service thrusts to the southwest. Based on stratigraphic relationships identified during 1:50 000-scale bedrock mapping, Hyland Group rocks in the Clark Lakes area are considered to belong to the Cryogenian–Ediacaran Yusezyu Formation, the Ediacaran Algae Formation and the Ediacaran–Terreneuvian Narchilla Formation. The Yusezyu Formation has been subdivided into five units based on dominant siliciclastic lithofacies, which form a broadly coarsening-upward sequence. The Yusezyu and Narchilla formations host gabbro sills, and quartz monzonite occurs locally in the upper Yusezyu Formation. Rocks in the Clark Lakes area exhibit a steeply northeast-to-southwest-dipping foliation that is axial planar to southeast-trending folds.

* diane.skipton@yukon.ca

Introduction

This article presents the results of 1:50 000-scale bedrock mapping conducted in 2019 in the Clark Lakes area of central Yukon, which includes parts of NTS sheets 106D/2, 3, 6 and 7. The Clark Lakes area is located along the northern boundary of the Selwyn fold belt, where the Neoproterozoic–Cambrian Hyland Group is juxtaposed against Paleozoic slope and shelf rocks of the Ogilvie Platform along the Dawson thrust zone (Figs. 1 and 2; Green, 1972a,b; Colpron et *al.*, 2013). The surrounding region hosts several mineral deposits (Fig. 2), including carbonate-hosted intrusion-related Au-Ag (Tiger), epithermal Ag-Au-Pb-Zn (McKay Hill), manto Ag-Pb-Zn (Clark), plutonic-related Au-Ag (Dublin Gulch), vein polymetallic Ag-Pb-Zn (Keno) and volcanogenic massive sulphide Au-Cu-Zn-Pb (Marg).

The region was initially mapped at 1:250 000-scale by the Geological Survey of Canada (Green, 1972a,b) as part of a helicopter-supported mapping project that included the Nash Creek, Larsen Creek and Dawson areas (Green, 1972a,b). More detailed (1:50 000-scale) bedrock mapping was undertaken in the Clark Lakes area in 2019 as part of a multi-year mapping and research project to address outstanding questions regarding stratigraphy, structural history and mineral potential.

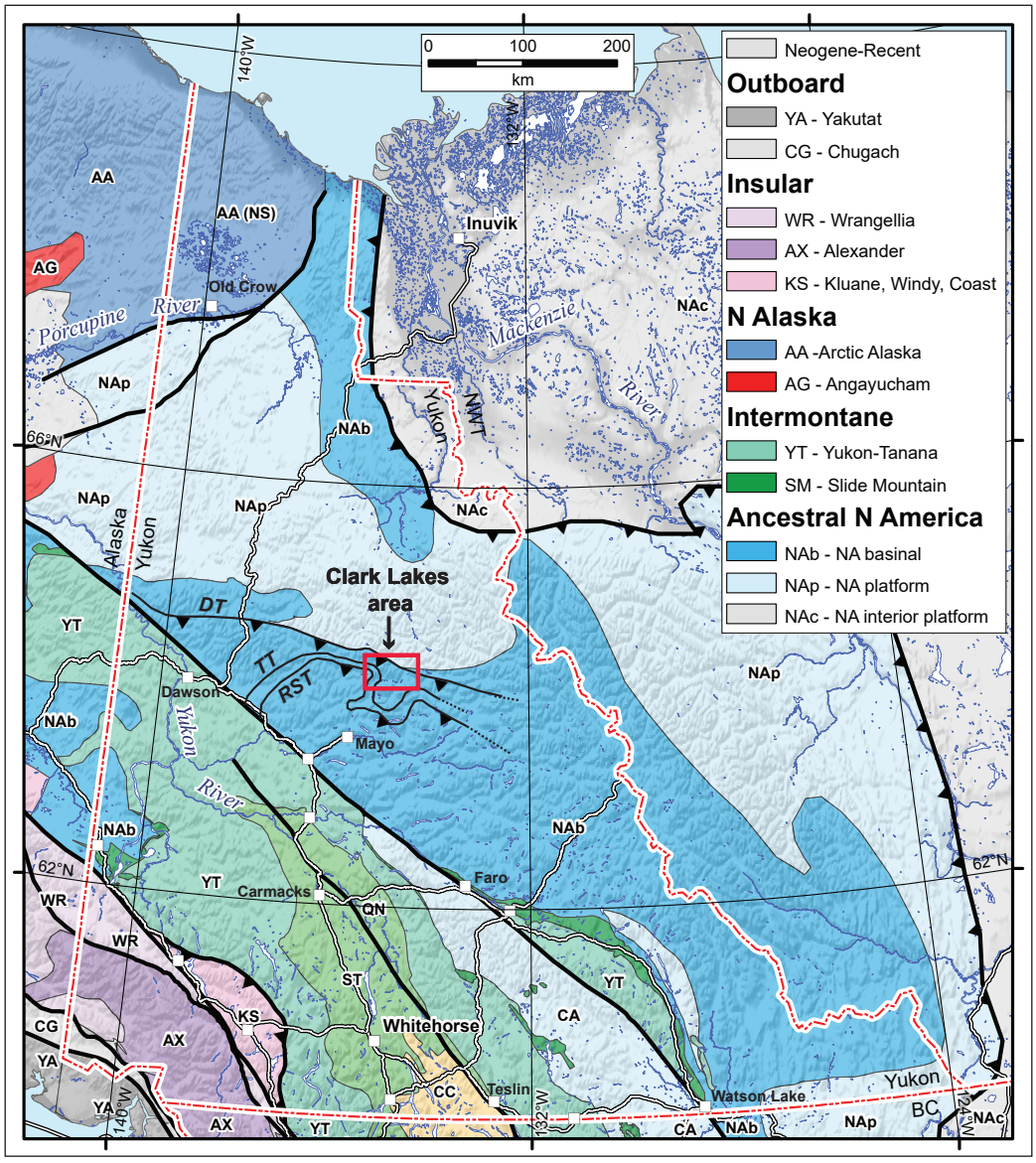

Figure 1. *Map of the geological terranes that comprise the northern Cordillera (Colpron et al., 2007). The study area (Clark Lakes area) is located in central Yukon, and outlined in red. DT = Dawson thrust; TT = Tombstone thrust; RST = Robert Service thrust.*

Geological setting and previous work

Previous mapping of the Clark Lakes area (Green, 1972a,b) showed that it is mostly composed of the Neoproterozoic Hyland Group (Fig. 2), including siliciclastic rocks of the Yusezyu Formation, with lesser carbonate rocks of the Algae Formation. On the geological compilation map of Yukon (Yukon Geological Survey, 2020a), the Hyland Group is juxtaposed over Carboniferous–Permian clastic rocks (Tsichu(?) Group) and Upper Cambrian–Devonian platformal carbonate rocks (Bouvette Formation) across the Dawson thrust zone (Fig. 2). The northeast-vergent Dawson thrust zone extends northwest–southeast across central Yukon, from the Ogilvie Mountains to the eastern Wernecke Mountains (Fig. 1). It records a protracted history that may have begun in the Neoproterozoic, with reactivation in the Paleozoic, and during Mesozoic (mid-Cretaceous?) shortening associated with Cordilleran orogenesis (Abbott, 1997c; Colpron *et al.*, 2013). Southwest of the Clark Lakes area, the Hyland Group is juxtaposed against the Devonian–Mississippian Earn Group along the Robert Service thrust, and the Earn

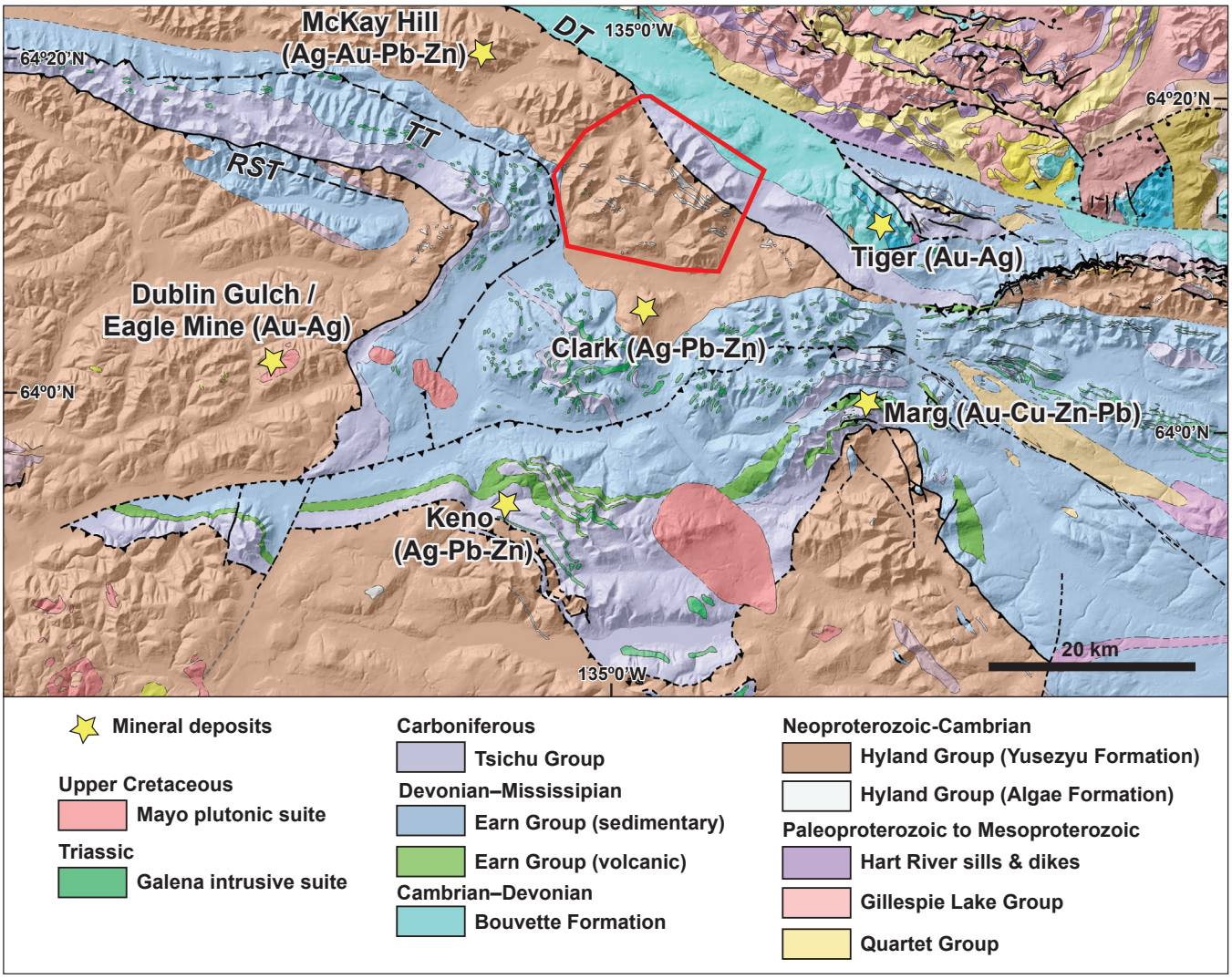

Figure 2. *Geological map of Paleoproterozoic to Carboniferous strata and younger plutons in the region of the Keno, Tiger and McKay Hill mineral deposits in central Yukon (from the digital compilation map of Yukon; Yukon Geological Survey, 2020a). The area mapped in 2019 (the Clark Lakes area; this study) is outlined in red, and was initially mapped at 1:250 000-scale (Green, 1972a). DT = Dawson thrust; TT = Tombstone thrust; RST = Robert Service thrust.*

Group is repeated by the Tombstone thrust (Figs. 1 and 2; Green and Roddick, 1962; Tempelman-Kluit, 1970; Thompson *et al.*, 1990; Anderson, 1987; Roots, 1988; Murphy, 1997). The southern and western edges of the Clark Lakes area are bordered by the Tombstone high-strain zone, a several-km thick interval of intensely deformed, lower-to-middle-greenschist-facies metasedimentary rocks (Devonian Earn Group, Mississippian Keno Hill Quartzite) in the hanging wall of the Tombstone thrust (Murphy, 1997). Shear-sense indicators in the Tombstone high-strain zone record top-to-the-northwest displacement (Murphy, 1997). Muscovite from the hanging wall of the Robert Service thrust, which is within the Tombstone high-strain zone, yielded $^{40}Ar/^{39}Ar$ dates of *ca.* 104–100 Ma, interpreted as the age of latest deformation (Mair *et al.*, 2006). The Clark Lakes area is considered to have reached lower-greenschist-facies (chlorite zone) conditions, in contrast with the sub-greenschist-facies conditions of the Hyland Group in the eastern Wernecke Mountains (Read *et al.*, 1991).

Several 1:50 000 and 1:75 000-scale mapping projects have improved our understanding of regional stratigraphic and structural relationships across the Dawson thrust zone in the Ogilvie and Wernecke mountains (Abbott, 1990a,b, 1997a,b,c; Colpron *et al.*, 2013; Moynihan, 2014, 2016a) and across the Tombstone and Robert Service thrust zones in the McQuesten River and Mayo areas (Murphy, 1997; Roots, 1997). However, due to less detailed (1:250 000-scale) mapping in the Clark Lakes area, the structural architecture of the area and stratigraphic correlations with Selwyn basin rocks elsewhere remained uncertain. Determining the structural and thermal history of the Clark Lakes area, and potential links with the major bounding thrust systems, is important for reconstructing the regional tectonic history and the geological setting of mineral deposits in the Dawson and Tombstone–Robert Service fault corridors. The 1:50 000-scale bedrock mapping of the Clark Lakes area is supported by new aeromagnetic data in the region (Kiss, 2020).

Stratigraphy

The Clark Lakes area mainly consists of siliciclastic and carbonate strata that have been tilted towards the southwest, such that the oldest rocks are closest to the Dawson thrust (Fig. 3). Based on lithofacies mapping and comparisons with stratigraphic relationships in the broader Selwyn basin (e.g., the eastern Wernecke Mountains and the Hyland River area; Colpron *et al.*, 2013; Moynihan, 2014, 2016b), the strata are considered equivalent to the Cryogenian–Ediacaran Yusezyu Formation, the Ediacaran Algae Formation and the Ediacaran–Terreneuvian Narchilla Formation of the Hyland Group. This interpretation is supported by U-Pb detrital zircon dating of sandstone in the Clark Lakes area, which yielded maximum depositional ages of *ca.* 665–725 Ma and detrital zircon populations that are similar to those of the Yusezyu Formation elsewhere in the Selwyn basin (J. Crowley and D. Skipton, unpublished data, 2020). Nonetheless, stratigraphic correlations between the Clark Lakes rocks and the Yusezyu, Algae and Narchilla formations are considered to be preliminary, and may be refined following additional bedrock mapping.

Hyland Group: Yusezyu Formation

The Clark Lakes area is dominantly underlain by siltstone, shale and sandstone of the Yusezyu Formation. The Yusezyu Formation exhibits an overall coarsening-upwards succession across the map area, whereby shale and siltstone-dominated sequences in the northeast grade upwards into more sandstone-rich units towards the southwest (Fig. 3). The Yusezyu Formation has been subdivided into five units based on predominant lithofacies. At the stratigraphically lowest level along the northeastern edge of the map area, the Yusezyu Formation is shale-dominated (PHYsh) and consists of grey, dark grey and green shale (mudstone) that is homogeneous to thinly laminated and locally phyllitic (Fig. 4a,b). In places, the shale contains thin, rhythmic interbeds of grey siltstone. The shale-dominated unit exhibits a gradational upper contact with a slightly

coarser-grained, siltstone-dominated unit (PHYsl) of the Yusezyu Formation; observed thicknesses of these units are estimated to be approximately 2 km and 1.5 km, respectively. The siltstone-dominated unit is mostly composed of green to grey siltstone to phyllite, which locally contain dark green-grey mudstone laminations or interbeds (Fig. 4c). The siltstone-dominated unit includes minor amounts of thin to medium-bedded, white siltstone to fine-grained sandstone, as well as dark grey and green shale (Fig. 4d). The contact between the Yusezyu Formation siltstone-dominated unit (PHYsl) and the overlying Yusezyu Formation "mixed" unit (PHYm) is marked by the first (*i.e.*, stratigraphically deepest) occurrence of medium-grained quartz arenite or quartz grit sandstone. The Yusezyu Formation mixed unit is the most predominant unit in the Clark Lakes area (Fig. 3), and is estimated to have an observed (deformed) thickness of approximately 800–1200 m. It consists of a heterogeneous mixture of siltstone (~55%), shale (~30%), and sandstone (~15%; Fig. 5a). These lithologic units typically form alternating intervals that are ~3 m to 10s of metres thick. Locally, sandstone and siltstone are rhythmically interbedded, forming medium to thick beds. The Yusezyu Formation mixed unit includes green and grey siltstone to phyllite; dark grey, green and, locally, maroon shale; and minor amounts of brown to grey quartz arenite and quartz grit, with local quartz-pebble conglomerate. The mixed unit also contains thick (up to ~500 m) intervals of sandstone (PHYss and PHYsc) that are laterally discontinuous and are interpreted to represent discrete channel deposits. Sandstone locally exhibits ripple cross-laminations or cross-bedding. The most abundant Yusezyu Formation sandstone unit (PHYss) is composed of medium to thick-bedded, brown to grey quartz arenite and quartz grit with local quartz-pebble conglomerate (Fig. 5b–e), and rare dark grey and green shale and siltstone to phyllite. The subordinate Yusezyu Formation sandstone unit (PHYsc) is distinguished by local dolomitic cement in sandstone, higher proportions of shale, siltstone and phyllite, and by rare intervals (<3 m thick) of limestone and dolostone.

Hyland Group: Algae Formation

The upper Yusezyu Formation (PHYm, PHYss, PHYsc) is overlain by the Algae Formation (PHa) along a sharp contact. The Algae Formation contains predominantly grey, fine-grained, massive to medium-bedded limestone (Fig. 6a,b) with local laminations, and lesser amounts of fine-grained, orange-weathered, medium-bedded dolostone. The Algae Formation in the Clark Lakes area has an estimated observed thickness of approximately 30–50 m, although the thickness is uncertain in places due to complex fold geometries (Fig. 3). As it is readily distinguishable from the Hyland Group siliciclastic rocks, the Algae Formation was used as a marker horizon for mapping. Additionally, the distinctive light grey weathering colour of the Algae Formation facilitated remote mapping of inaccessible areas, where exposure allowed, and enabled identification of complex, map-scale folds (Figs. 3b and 10e) that may otherwise have been masked within interbedded siliciclastic strata.

Hyland Group: Narchilla Formation

The Narchilla Formation (PCHn) overlies the Algae Formation along a sharp contact. The Narchilla Formation mostly consists of fine-grained siliciclastic rocks, including dark grey, green and maroon shale (Fig. 6c), and grey to green siltstone to phyllite (Fig. 10a). It contains lesser amounts of fine-grained, white, thinly bedded sandstone with local ripple cross-laminations (Fig. 6d), interbedded green-grey to white, fine-grained sandstone and siltstone (Fig. 10b), and rare occurrences of brown to grey quartz arenite and quartz grit. In the eastern Wernecke Mountains and the Hyland River area, the Narchilla Formation is sharply overlain by limestone conglomerate (or limestone) of the Gull Lake Formation (Moynihan, 2014, 2016b). In the Clark Lakes area, the Narchilla Formation represents the highest stratigraphic level of exposure, and its exposure is mostly limited to synclinal keels (Figs. 3 and 10e). As such, the thickness of the Narchilla Formation is poorly constrained in the map area, but it is estimated to be at least 500 m thick.

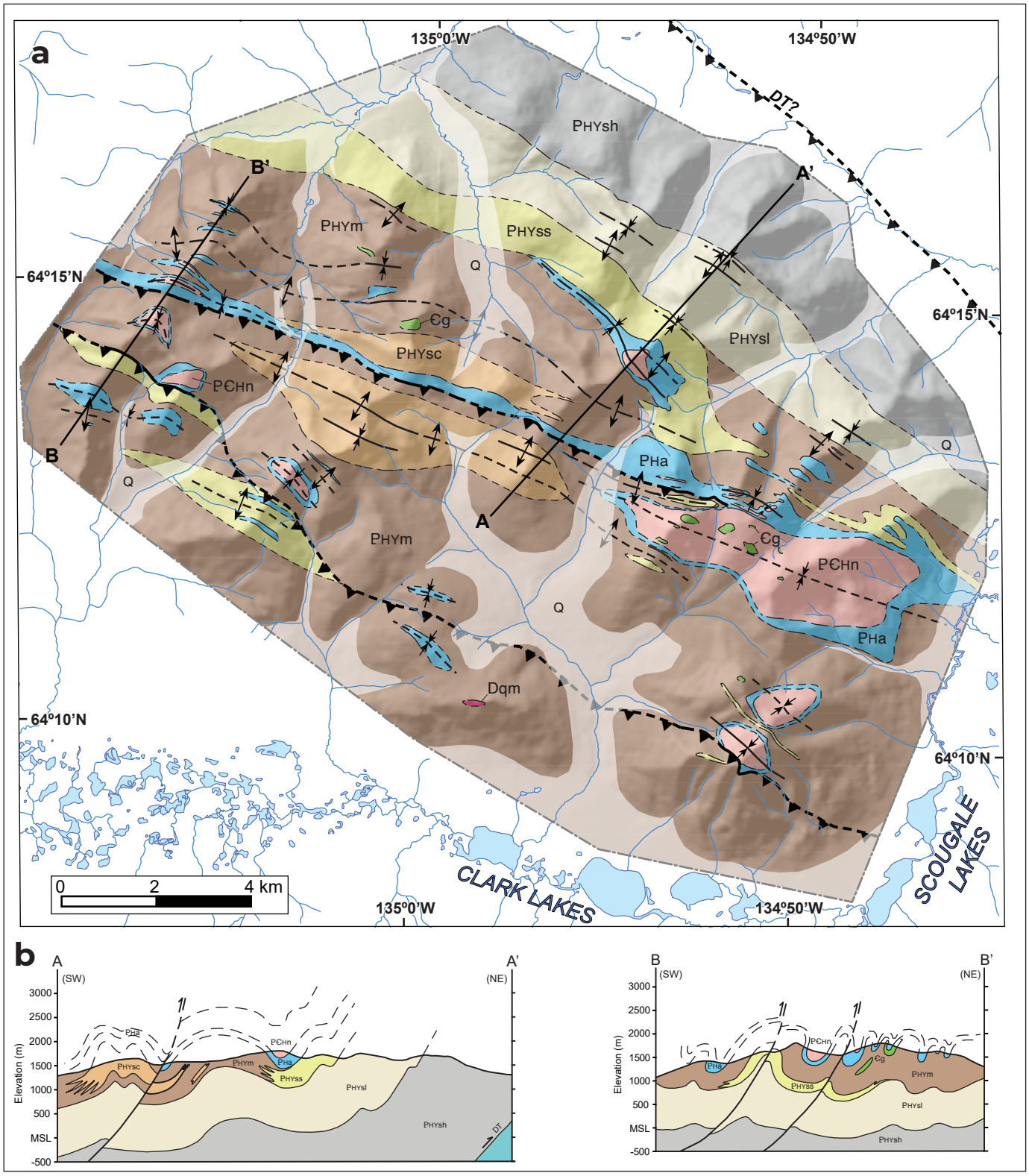

Figure 3. (a) *Preliminary geological map of the Clark Lakes area (parts of NTS 106D/2, 3, 6, 7) based on 1:50 000-scale bedrock mapping conducted in 2019. Map legend is provided in Figure 3c. DT?, inferred trace of Dawson thrust zone.* ***(b)*** *Cross sections corresponding to the preliminary geological map of the Clark Lakes area in Figure 3a. In cross section A-A', the location of the Dawson thrust zone (DT) is projected at depth from the estimated location of the thrust at surface (Fig. 3a).*

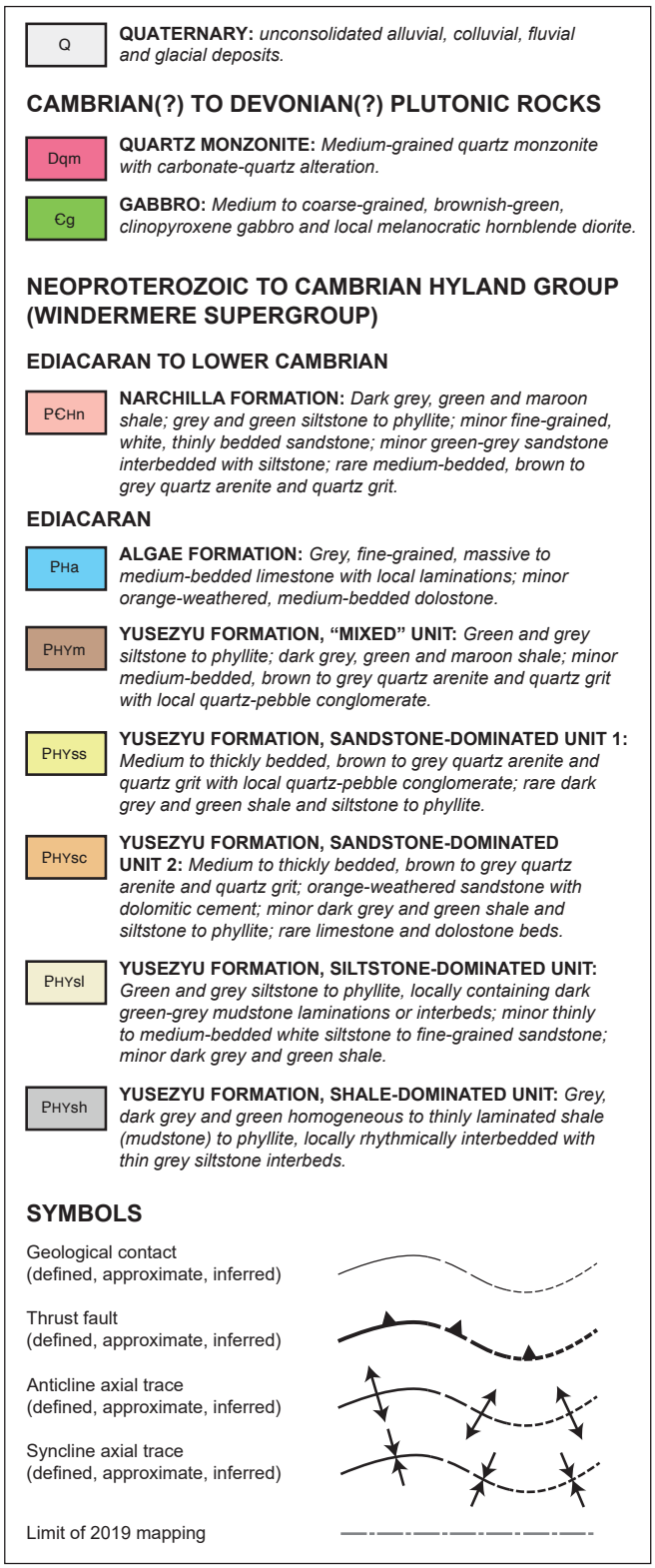

Figure 3. (c) *Legend corresponding to the preliminary geological map of the Clark Lakes area in Figure 3a.*

Intrusive rocks

Gabbro

Gabbro intrusions (Ꞓg) were emplaced into siltstone and shale of the Narchilla and upper Yusezyu formations on the eastern side and northwestern quadrant of the map area (Fig. 3). The intrusions form discontinuous sills and plugs with maximum dimensions estimated to be ~200 m at the bedrock surface (Fig. 7a). Gabbro is medium-grained, locally foliated, and has been extensively replaced by greenschist-facies minerals (chlorite, actinolite, epidote) and carbonate alteration (Fig. 7b,c). Igneous textures have been preserved locally, and relics of igneous clinopyroxene crystals are visible in thin section. In some places, igneous hornblende occurs instead of clinopyroxene, indicating that the intrusions have a compositional range from gabbro to, locally, melanocratic hornblende diorite. As the intrusions are hosted by the Narchilla Formation, they are inferred to be Terreneuvian or younger.

Whole rock geochemical compositions of the gabbro and hornblende diorite intrusions (Table 1) suggest that most (five) of the samples have alkali basaltic compositions that are transitional between those of typical oceanic island basalt and enriched mid-ocean ridge basalt (Fig. 8). Preliminary geochemical comparisons with Cambrian and younger mafic to intermediate rocks in the region (using data from: Abbott, 1997c; Yukon Geological Survey, 2020b; M. Colpron, pers. comm., 2020) suggest that the Clark Lakes gabbro and diorite are distinct from the Triassic Galena suite sills hosted by the nearby Earn Group. Instead, they may share affinity with Paleozoic sills, dikes and volcanic rocks (Dempster Volcanics), such as those in the Upper Hart River area (Abbott, 1997c; Yukon Geological Survey, 2020b). A sixth gabbro sample (19DS-115-2-1) from the Clark Lakes area is geochemically distinct, as it has a trachyte-phonolite composition and is enriched in several rare earth elements by an order of magnitude relative to the other gabbro and hornblende diorite samples (Table 1; Fig. 8).

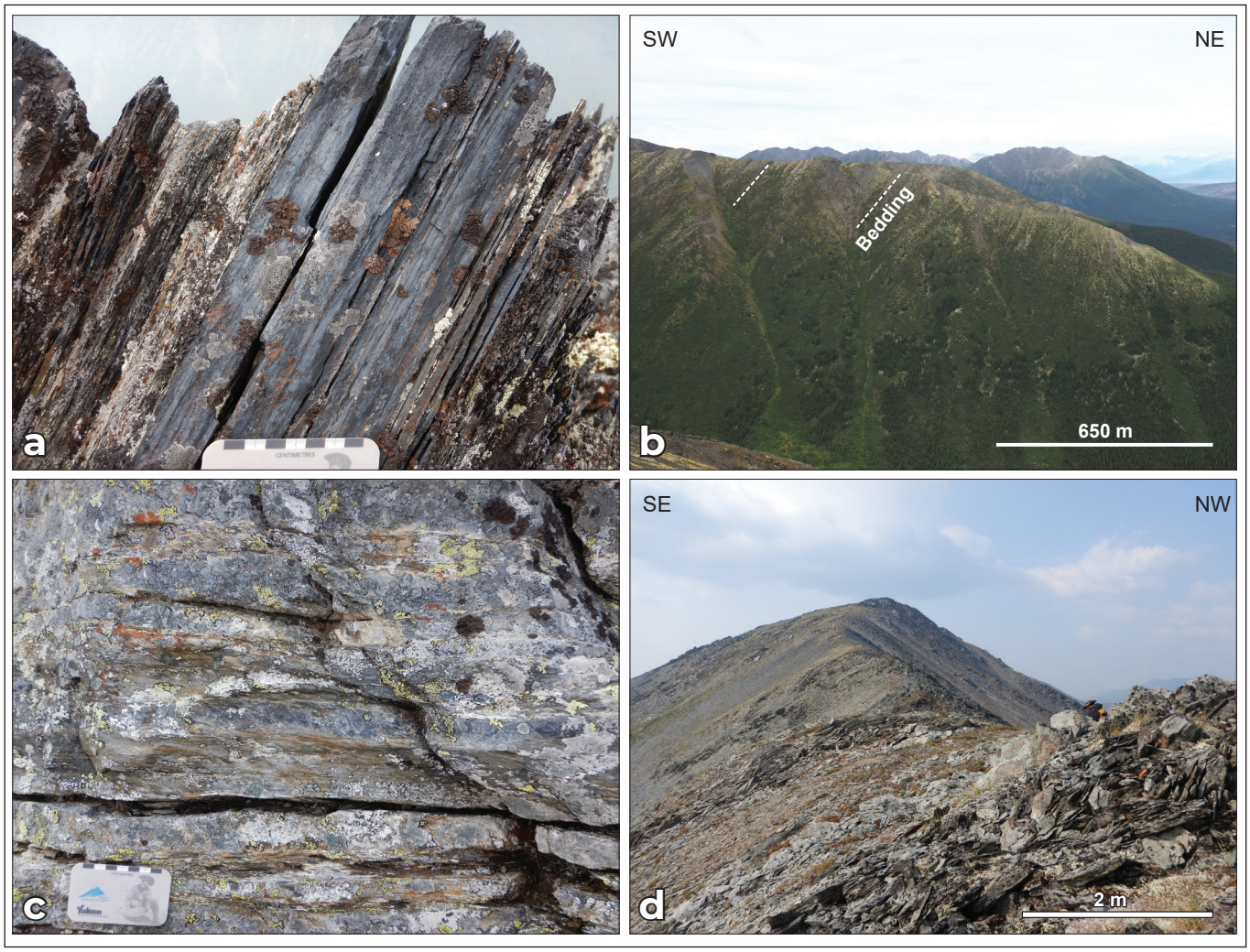

Figure 4. *Field photographs of the shale and siltstone-dominated units in the Cryogenian-Ediacaran Yusezyu Formation (Hyland Group).* ***(a)*** *Grey to dark grey, laminated mudstone (shale) in the Yusezyu Formation shale-dominated unit.* ***(b)*** *Ridge exposure of the Yusezyu Formation shale-dominated unit, exhibiting typical recessive weathering, with bedding dipping toward the southwest.* ***(c)*** *Rhythmically interbedded siltstone (light grey) and shale (brownish-grey) in the Yusezyu Formation siltstone-dominated unit.* ***(d)*** *Ridge exposure of the Yusezyu Formation siltstone-dominated unit, exhibiting characteristic grey weathering colour and rubbly outcrops of siltstone and shale.*

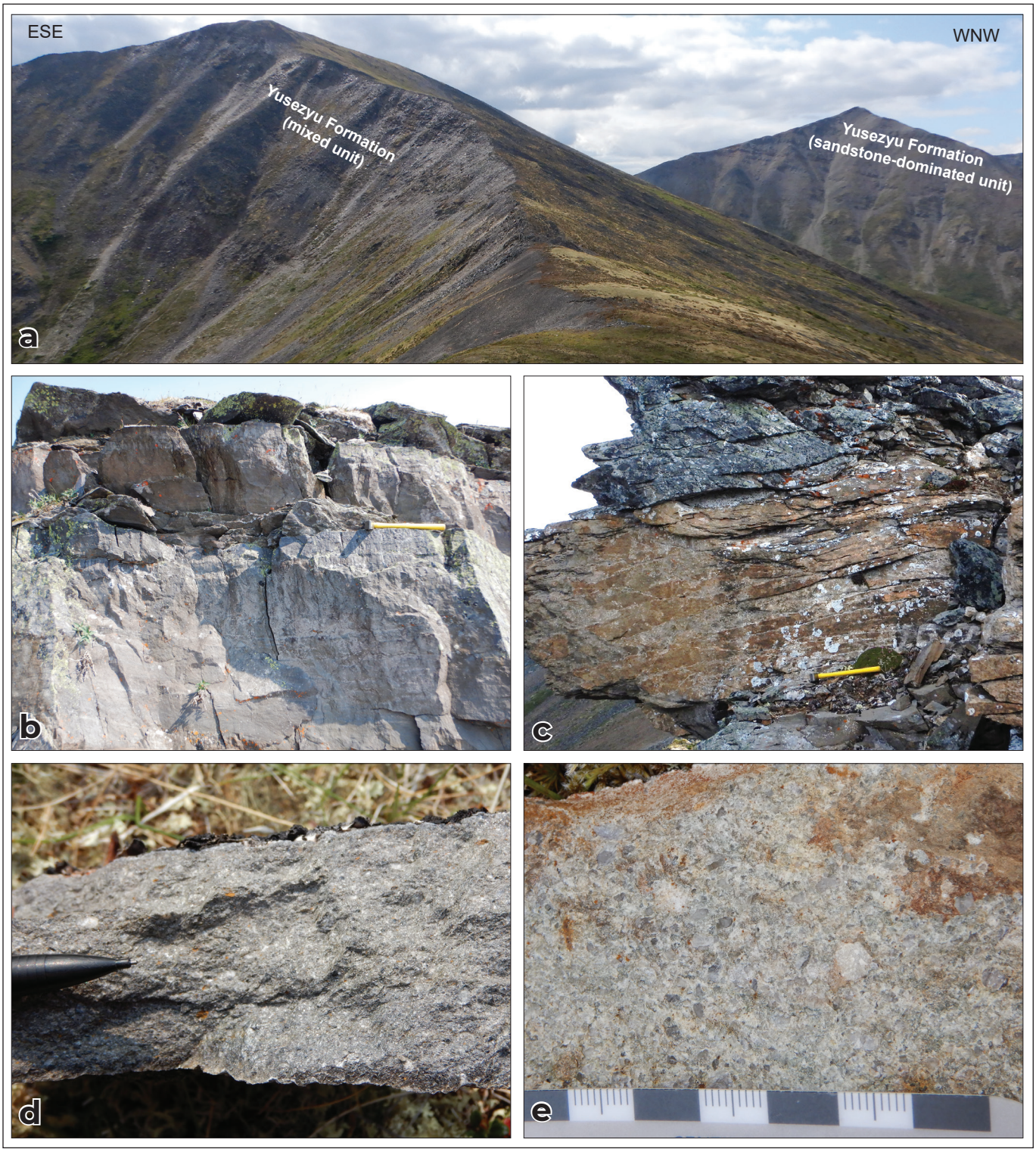

Figure 5. *Field photographs of the mixed (a) and sandstone-dominated units (a–e) in the Cryogenian-Ediacaran Yusezyu Formation (Hyland Group).* ***(a)*** *Field photograph showing recessively weathered siltstone and shale and non-recessively weathered sandstone in the Yusezyu Formation mixed unit in the foreground, and competent sandstone beds in the Yusezyu Formation sandstone-dominated unit in the background (horizontal field of view is ~3 km).* ***(b)*** *Medium to thickly bedded, brown quartz arenite.* ***(c)*** *Medium-bedded, brown-to-grey quartz arenite to quartz grit.* ***(d)*** *Brown-to-grey fresh surface of quartz arenite.* ***(e)*** *White to light grey fresh surface of quartz pebble conglomerate.*

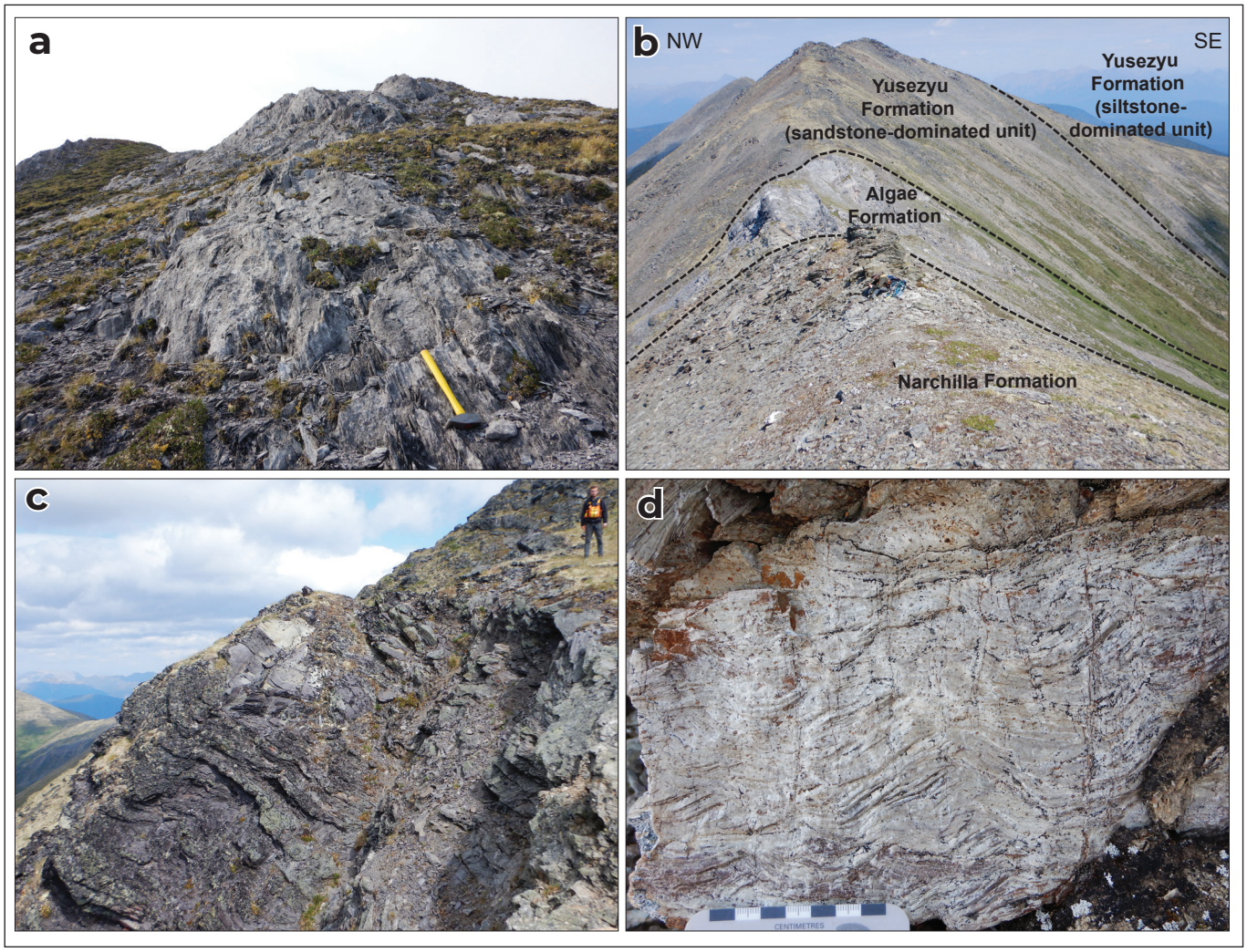

Figure 6. *Field photographs of the Ediacaran Algae Formation and the Ediacaran–Terreneuvian Narchilla Formation (Hyland Group).* ***(a)*** *Grey limestone of the Algae Formation, exhibiting a strong cleavage fabric (S2).* ***(b)*** *Light grey limestone of the Algae Formation overlain by siltstone of the Narchilla Formation and underlain by the Yusezyu Formation.* ***(c)*** *Maroon shale typical of the Narchilla Formation.* ***(d)*** *White-weathered, thinly bedded, fine-grained sandstone of the Narchilla Formation with ripple cross-laminations.*

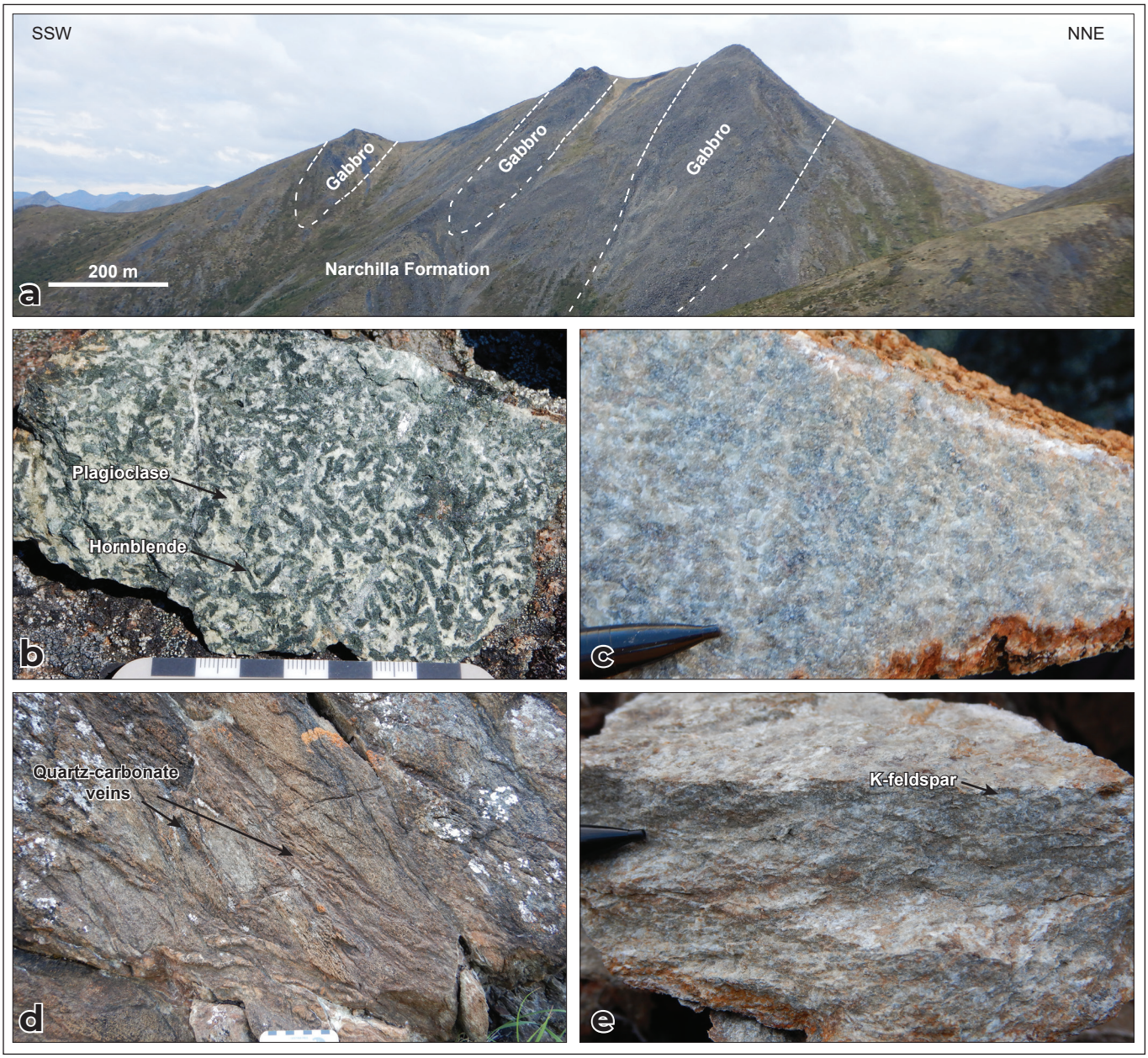

Figure 7. *Field photographs of gabbro, hornblende diorite and quartz monzonite.* ***(a)*** *Mountaintop exposure of gabbro intrusions hosted by shale and siltstone of the Narchilla Formation. Approximate gabbro contacts are represented by white dashed lines; widely spaced dashes indicate covered (inferred) contacts.* ***(b)*** *Fresh surface of medium to coarse-grained melanocratic hornblende diorite with primary igneous texture exhibited by plagioclase and hornblende. Hornblende has been mostly replaced by chlorite (sample 19DS-006-2-1 in Table 1).* ***(c)*** *Medium to coarse-grained gabbro that has been mostly replaced by greenschist-facies minerals (chlorite, epidote) and intense carbonate alteration, resulting in a pale green fresh surface that lacks igneous textures and a pitted, orange weathered surface.* ***(d)*** *Pitted, orange-brown weathered surface of quartz monzonite, with several quartz-carbonate veins.* ***(e)*** *Orange-grey fresh surface of quartz monzonite, in which original igneous minerals (e.g., K-feldspar) are barely identifiable due to intense carbonate-quartz alteration and sericitization.*

Table 1. *Whole-rock geochemical data of six gabbro and hornblende diorite samples from the Clark Lakes area. Major elements were analyzed using x-ray fluorescence (XRF) and trace elements were analyzed using inductively-coupled mass spectrometry (ICP-MS) by ALS Geochemistry.*

Sample	**19DS-006-2-1**	**19DS-007-1-1**	**19DS-034-1-1**	**19DS-040-1-1**	**19DS-111-2-1**	**19DS-115-2-1**
Lithology	**Hbl diorite**	**Gabbro**	**Gabbro**	**Gabbro**	**Gabbro**	**Gabbro**
Al_2O_3	15.29	14.90	15.08	13.61	6.69	10.67
BaO	0.02	0.02	0.01	0.01	0.01	0.03
CaO	9.83	16.00	12.15	9.60	15.55	9.85
Cr_2O_3	0.01	0.05	0.01	0.01	0.13	0.02
Fe_2O_3	15.50	8.04	12.37	17.54	8.27	16.17
K2O	0.03	0.01	0.02	0.08	0.24	0.14
MgO	5.36	8.74	5.80	4.86	5.46	8.14
MnO	0.26	0.15	0.18	0.24	1.16	0.42
Na_2O	3.15	1.93	0.44	0.52	1.08	0.05
P_2O_5	0.38	0.05	0.65	0.27	0.16	1.98
SiO_2	44.23	46.38	41.98	39.74	36.69	38.16
SrO	0.17	0.13	0.15	0.07	0.07	0.27
TiO_2	2.73	1.03	1.95	2.79	1.01	1.96
LOI	3.18	2.23	8.34	9.77	22.35	10.73
Total	101.35	99.83	99.28	99.34	99.17	99.06
Ba	69.30	61.60	27.80	25.30	44.20	240.00
Ce	64.50	23.90	102.50	44.70	17.10	1260.00
Cr	10.00	310.00	20.00	<10	930.00	90.00
Cs	0.09	0.08	0.07	0.22	0.68	0.43
Dy	5.63	2.79	6.03	4.44	1.88	39.20
Er	2.86	1.13	2.83	2.10	0.91	14.20
Eu	2.37	1.11	2.82	1.51	0.61	25.30
Ga	19.40	18.20	21.50	24.60	10.60	44.10
Gd	6.24	3.10	8.12	4.94	2.27	57.90
Ge	<5	<5	<5	<5	<5	<5
Hf	4.50	2.20	3.90	3.40	1.60	53.30
Ho	1.08	0.46	1.07	0.81	0.35	6.63
La	30.20	11.50	50.90	21.60	8.10	620.00
Lu	0.36	0.12	0.34	0.25	0.09	1.38
Nb	39.00	13.10	47.50	26.80	10.80	535.00
Nd	32.20	12.00	47.70	23.30	9.60	488.00
Pr	8.07	2.87	12.00	5.49	2.11	141.00
Rb	0.40	0.20	0.90	2.50	7.60	5.10
Sm	6.86	2.83	8.46	4.81	2.16	82.80

Table 1 *continued. Whole-rock geochemical data of six gabbro and hornblende diorite samples from the Clark Lakes area.*

Sample	**19DS-006-2-1**	**19DS-007-1-1**	**19DS-034-1-1**	**19DS-040-1-1**	**19DS-111-2-1**	**19DS-115-2-1**
Lithology	**Hbl diorite**	**Gabbro**	**Gabbro**	**Gabbro**	**Gabbro**	**Gabbro**
Sn	1.00	1.00	2.00	2.00	1.00	8.00
Sr	1605.00	1245.00	1405.00	661.00	644.00	2610.00
Ta	2.30	0.70	2.10	1.50	2.00	30.40
Tb	1.01	0.45	1.04	0.71	0.32	7.99
Th	2.51	1.42	6.12	3.14	0.91	46.60
Tm	0.36	0.16	0.34	0.25	0.10	1.81
U	0.65	0.31	1.67	1.18	0.44	18.00
V	495.00	244.00	288.00	598.00	80.00	42.00
W	<1	1.00	2.00	2.00	1.00	2.00
Y	28.10	12.60	29.10	21.40	9.30	159.00
Yb	2.27	1.09	2.57	1.67	0.71	10.20
Zr	181.00	82.00	201.00	153.00	57.00	2880.00
As	30.90	6.60	5.80	2.20	1.00	0.50
Bi	0.01	0.29	0.09	0.04	0.06	0.11
Hg	0.01	0.01	<0.005	<0.005	<0.005	0.05
In	0.01	0.01	0.02	0.05	0.03	0.23
Re	0.00	<0.001	<0.001	<0.001	<0.001	<0.001
Sb	0.32	0.50	0.07	0.05	0.05	0.29
Sc	3.00	4.00	5.70	15.60	9.80	2.10
Se	0.80	0.70	<0.2	<0.2	<0.2	0.20
Te	0.01	0.10	0.01	0.01	<0.01	0.03
Tl	<0.02	<0.02	<0.02	<0.02	<0.02	<0.02
Ag	<0.5	<0.5	<0.5	<0.5	<0.5	<0.5
Cd	<0.5	<0.5	<0.5	<0.5	0.60	<0.5
Co	61.00	32.00	40.00	62.00	77.00	16.00
Cu	169.00	233.00	136.00	143.00	30.00	9.00
Li	40.00	40.00	160.00	140.00	60.00	100.00
Mo	1.00	<1	<1	1.00	<1	<1
Ni	50.00	167.00	67.00	63.00	1110.00	78.00
Pb	9.00	96.00	36.00	28.00	62.00	20.00
Sc	19.00	53.00	18.00	22.00	11.00	2.00
Zn	142.00	43.00	105.00	184.00	159.00	401.00

Hbl = hornblende

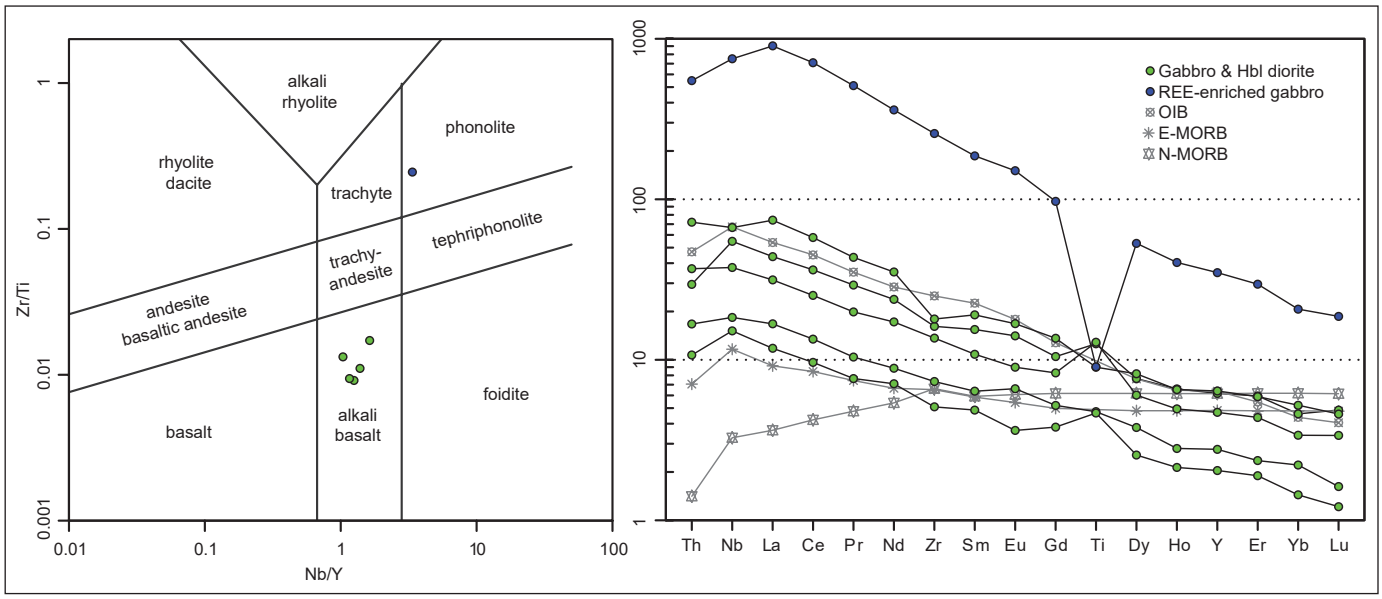

Figure 8. *Whole-rock geochemical compositions of gabbro and hornblende diorite samples from the Clark Lakes area plotted on* ***(a)*** *the classification diagram of Pearce (1996) and* ***(b)*** *a diagram showing selected rare earth and high field strength elements normalized to the primitive mantle values of Sun and McDonough (1989). In* ***(b)****, compositions of oceanic island basalt (OIB), enriched mid-ocean ridge basalt (E-MORB) and normal mid-ocean ridge basalt (N-MORB) are from Sun and McDonough (1989). REE, rare earth elements; Hbl, hornblende.*

Quartz monzonite

Foliated quartz monzonite (Dqm) was observed in the southern part of the map area, hosted in siltstone of the Yusezyu Formation mixed unit (Fig. 3). The geometry and extent of the quartz monzonite are poorly defined, mainly owing to heavy vegetation in the area. It consists of medium to coarse-grained K-feldspar, plagioclase feldspar and minor quartz, and has undergone pervasive carbonate and quartz alteration. The quartz monzonite has an orange-grey fresh surface, a pitted, orange-brown weathered surface, and contains abundant carbonate (± quartz) veins (Fig. 7d,e). At the micro-scale, K-feldspar commonly exhibits microcline ("tartan") twinning, and K-feldspar and plagioclase are strongly sericitized.

Metamorphism

The Clark Lakes area has undergone regional metamorphism at lower-greenschist-facies conditions. The siliciclastic rocks are characterized by metamorphic mineral assemblages containing white mica and chlorite (± epidote). In places in the southeastern quadrant of the map area, siltstone and phyllite also contain chloritoid porphyroblasts that are up to 1.5 mm long, or euhedral magnetite porphyroblasts up to 2 mm in diameter. Siltstone, shale and phyllite throughout the map area commonly contain ~0.5–2 mm-sized, brown to reddish-brown nodules/porphyroblasts with various shapes, including oval, rhombic, and irregular (blocky or patchy). Based on thin section analysis, at least some of these growths represent carbonate that has been partially to entirely replaced by (commonly Fe-rich) alteration assemblages, whereas others may represent altered pyrite. Pristine, euhedral carbonate rhombs occur locally. Carbonate is interpreted to have grown in the siliciclastic rocks as diagenetic nodules, or as porphyroblasts during lower-greenschist-facies metamorphism. In carbonate rocks, metamorphic minerals include white mica and, locally, tremolite, together with recrystallized calcite (and/or dolomite). In gabbro and diorite, metamorphic mineral assemblages consist of chlorite, epidote, actinolite, calcite and white mica (± titanite ± apatite). Quartz monzonite contains secondary white mica and chlorite that are consistent with lower-greenschist-facies metamorphism. The metamorphic mineral assemblages throughout the area indicate regional lower-greenschist-facies (chlorite zone) metamorphism (e.g., Spear, 1993).

Gabbro-to-diorite intrusions are surrounded by contact metamorphic aureoles in siltstone and shale host rocks. The aureoles are up to 2 m wide, and are characterized by a light green colour and a spotted hornfels texture formed by ~1–2 mm-wide, grey, oval-shaped porphyroblasts. Thin sections reveal that the original porphyroblastic mineral (possibly cordierite) has been replaced by aggregates of chlorite and quartz during regional lower-greenschist-facies metamorphism.

Deformation

On the geological compilation map of Yukon (Yukon Geological Survey, 2020a), the Dawson thrust cuts through Clark Lakes area, juxtaposing the Yusezyu Formation over the Carboniferous Tsichu(?) Formation (Fig. 2). However, 1:50 000-scale mapping at this location found no structural evidence of the Dawson fault, nor any juxtaposition of the Yusezyu and Tsichu formations. Instead, the formerly-defined trace of the Dawson fault corresponds approximately with the gradational stratigraphic boundary between the shale-dominated unit and the overlying siltstone-dominated unit in the Yusezyu Formation (Fig. 3). Grey to green shale of the Yusezyu Formation shale-dominated unit is distinct from the Tsichu Formation, which consists of black to silvery shale, carbonaceous phyllite and quartzite (e.g., Abbott, 1990a,b; Roots, 1997). Therefore, the Dawson thrust zone is projected to lie ~3 km farther to the northeast, along the valley that borders the main mountain range in the Clark Lakes area, which corresponds to a distinct linear feature on aeromagnetic maps (Figs. 3 and 9; Kiss, 2020).

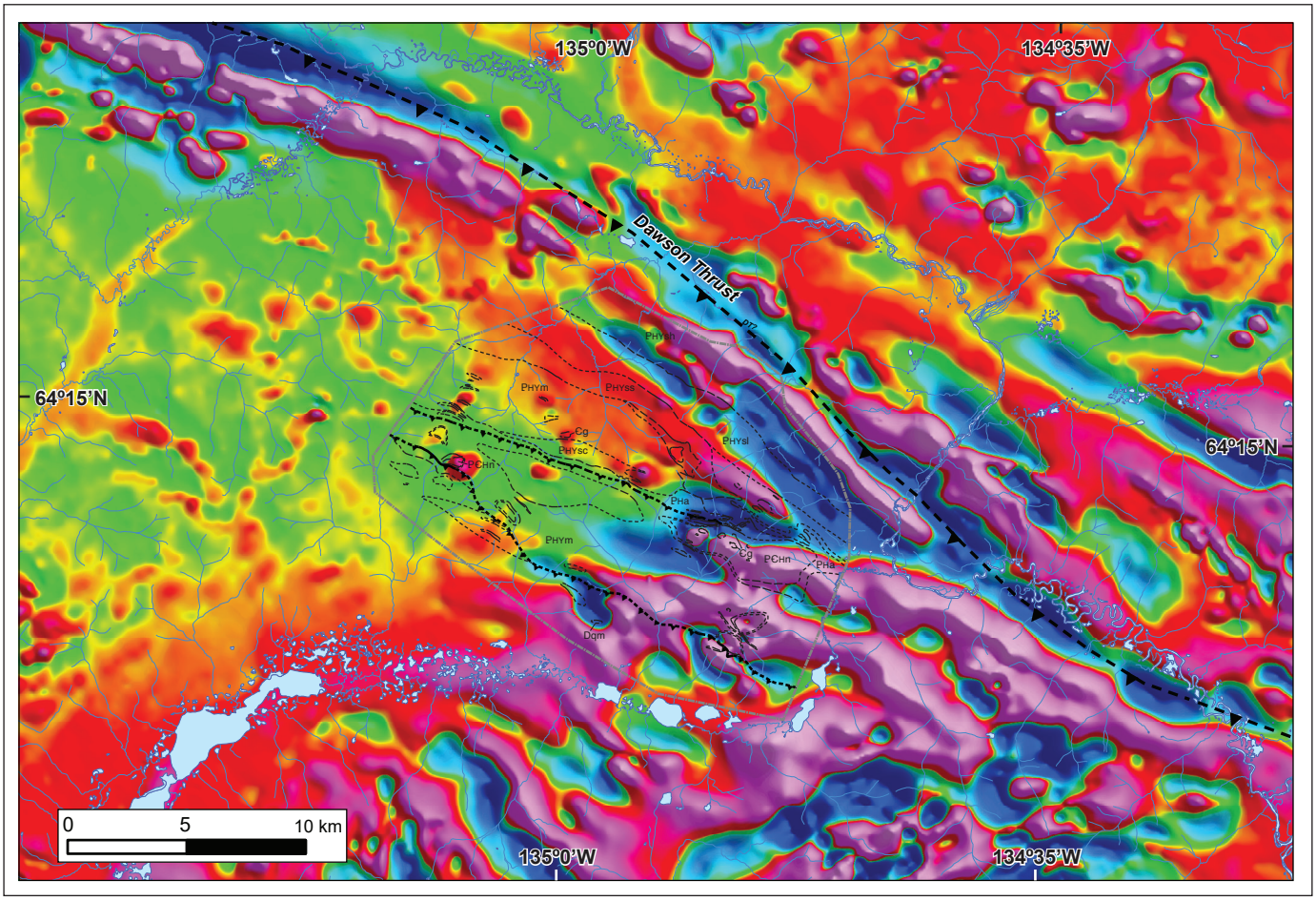

Figure 9. *Aeromagetic data (first vertical derivative; Kiss, 2020) overlain by geological contacts and faults from 1:50 000-scale mapping of the Clark Lakes area (Fig. 3a). The trace of the Dawson thrust in this figure is inferred primarily from the aeromagnetic data of Kiss (2020).*

Two regional foliations (S1 and S2) were identified during mapping of the Clark Lakes area. The sedimentary rocks exhibit a bedding-parallel foliation (S1) defined primarily by the alignment of very fine grained white mica and chlorite. Bedding and S1 are mostly southwest-dipping, although they dip with variable steepness towards both the southwest and northeast (Figs. 10a,b,e and 11a,b) as a result of later folding (F2).

The S1 foliation is crosscut by a southwest-northeast-dipping foliation (S2; Figs. 10a,b and 11c) defined by aligned fine-grained white mica (± chlorite), which commonly presents as a crenulation cleavage. The S2 foliation is generally steeply dipping, and is interpreted to have formed as an axial planar cleavage to folds (F2) with northwest-southeast-striking axial planes (Figs. 3 and 10c,e). F2 fold axes and crenulation lineations (L2) generally plunge shallowly towards the northwest or southeast (Figs. 10c,d and 11e,f). At the micro-scale, F2 folds form symmetric or asymmetric crenulations with wavelengths as small as 0.25 mm, which define a crenulation cleavage (S2). At the outcrop-scale, the F2 folds have wavelengths of ~30–60 cm (Fig. 10c), and include various types: open and close; symmetric and asymmetric; cylindrical and non-cylindrical; harmonic and disharmonic; upright to inclined; and parallel and kink folds. Larger F2 folds are common (Figs. 3 and 10e), with wavelengths ranging from <10 m to 10s of metres, and they also form map-scale folds (e.g., with wavelengths of ~0.5–3 km).

The variable dip directions exhibited by the S2 foliation, from steeply southwest to northeast, are attributed to the compounded effects of cleavage fanning and refraction in lithologic units of variable competencies (e.g., shale *vs.* siltstone *vs.* sandstone). In many places, the S2 foliation is oblique to bedding (and S1) at angles of up to 90°, a relationship that is typical of axial planar cleavage that formed in fold hinge zones (Fig. 10a,b), as well as in limbs of inclined folds. The S2 crenulation cleavage in some fine-grained rocks is sufficiently penetrative and so tightly spaced that bedding (and S1) is not discernable (or is only identifiable microscopically), precluding measurements of bedding-cleavage relationships in the field. In rocks that record only one foliation, and it is uncertain whether it is S1 or S2, the foliation is denoted "Sn" (Fig. 11d). Conversely, rocks in some places record only a bedding-parallel foliation (S1), and lack a late, non-bedding parallel foliation (S2), even at the micro-scale. This local absence of S2 is not grain-size, lithology or competency-dependent, suggesting that S2 may not be uniformly pervasive or penetrative throughout different stress-strain regimes within F2 folds. It is also possible that S2 is locally bedding-parallel, such that it transposes and is indistinguishable from S1 (e.g., in the limbs of isoclinal folds and/or in upright limbs of inclined folds).

The structural architecture of the Clark Lakes area is dominantly controlled by map-scale F2 folds, which have preserved upper stratigraphic levels, including the Algae and Narchilla formations, in synclinal keels (Figs. 3 and 10e). In several places, the underlying upper Yusezyu Formation is revealed in the cores of anticlines. Together with topographic relief, lateral facies changes and the non-cylindrical nature of the F2 folds, these relationships result in discontinuous lateral exposures of the Algae and Narchilla formations and the sandstone-dominated units in the Yusezyu Formation (Fig. 3a). Additionally, D2 thrust faults have locally transported the upper Yusezyu Formation to higher stratigraphic levels, such as above the Algae Formation (Figs. 3 and 10f). Thrust displacements are estimated to have been less than ~150 m, verging toward the northeast.

Gabbro-to-diorite intrusions exhibit a weak to moderate, southwest-to-northeast-dipping foliation that is localized along intrusion margins. Quartz monzonite exhibits a strong, southwest-dipping foliation defined mainly by the alignment of flattened K-feldspar and plagioclase grains. Microscopically, the K-feldspar and plagioclase grains exhibit undulose extinction and evidence of dynamic recrystallization and boudinage. As the gabbro-to-diorite intrusions and quartz monzonite each record only one foliation, it is uncertain whether the foliation is S1 or S2.

Both the S1 and S2 foliations are defined by lower greenschist-facies minerals and, therefore, they are both interpreted to have developed at lower-greenschist-facies conditions. Quartz in siliciclastic samples exhibits dynamic recrystallization textures, including grain boundary bulging, consistent with deformation under lower greenschist-facies conditions (e.g., Vernon, 2004).

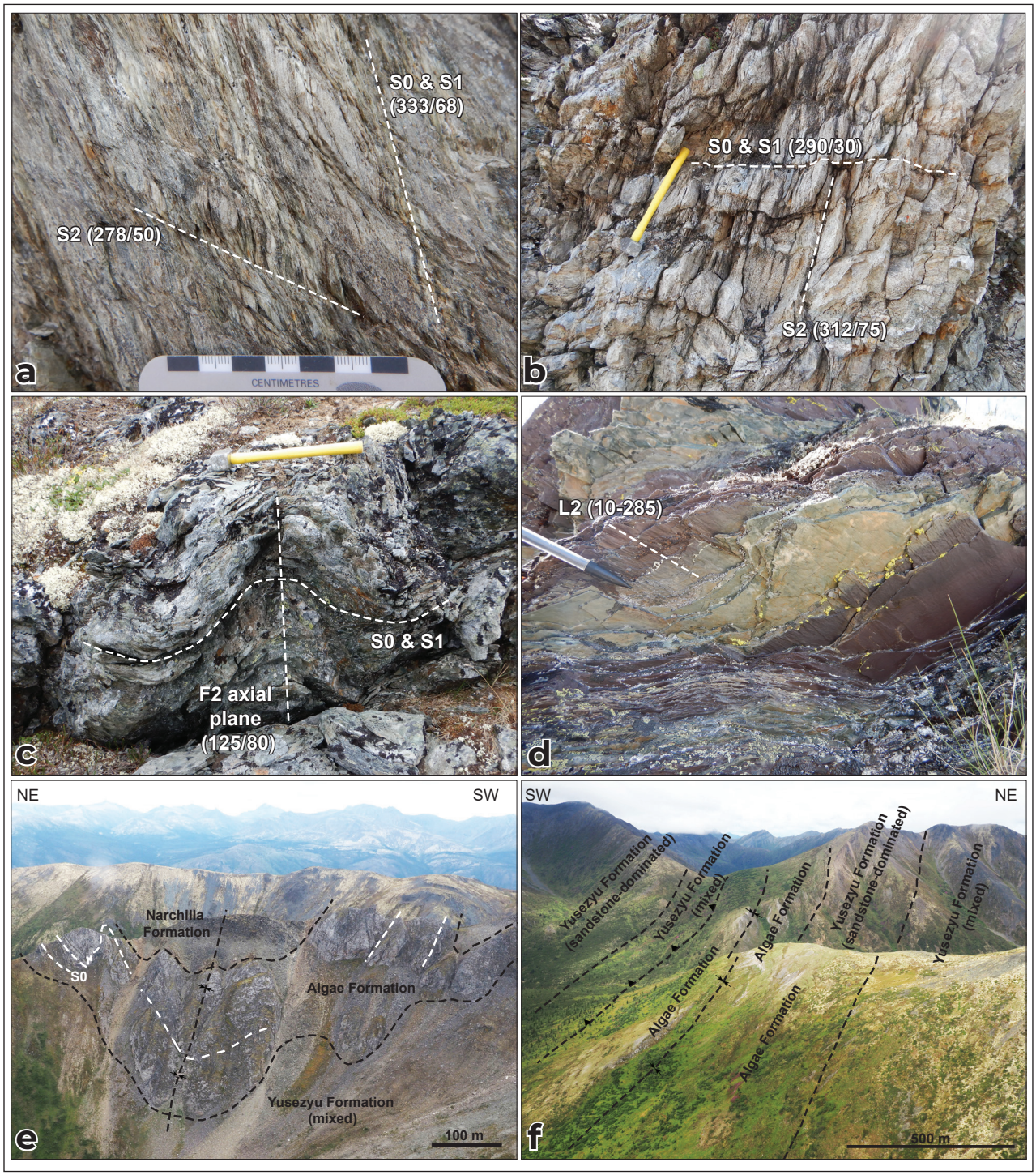

Figure 10. *Field photographs of structural relationships and deformation fabrics. Planar fabric orientations are presented in right-hand-rule format.* ***(a)*** *Bedding (S0) and bedding-parallel foliation (S1) crosscut by S2 cleavage in thinly interbedded siltstone (Narchilla Formation).* ***(b)*** *Bedding (S0) and bedding-parallel foliation (S1) crosscut by spaced cleavage (S2) in siltstone to fine-grained sandstone in the hinge zone of a map-scale synclinal F2 fold (Narchilla Formation).* ***(c)*** *An upright, open F2 fold in siltstone (Yusezyu Formation mixed unit), with a southeast-plunging axis (36–125).* ***(d)*** *Crenulation lineations (L2) in maroon to light-green shale (Yusezyu Formation mixed unit).* ***(e)*** *Cliff exposure of F2-folded rocks of the Yusezyu, Algae and Narchilla formations. The geometry of the fold is broadly synclinal, and smaller folds occur within the limbs of the syncline. The white dashed lines represent bedding traces; widely spaced dashes indicate low confidence in bedding orientations.* ***(f)*** *Panoramic view looking towards the northwest along a thrust fault that juxtaposed the Yusezyu Formation over the Algae Formation.*

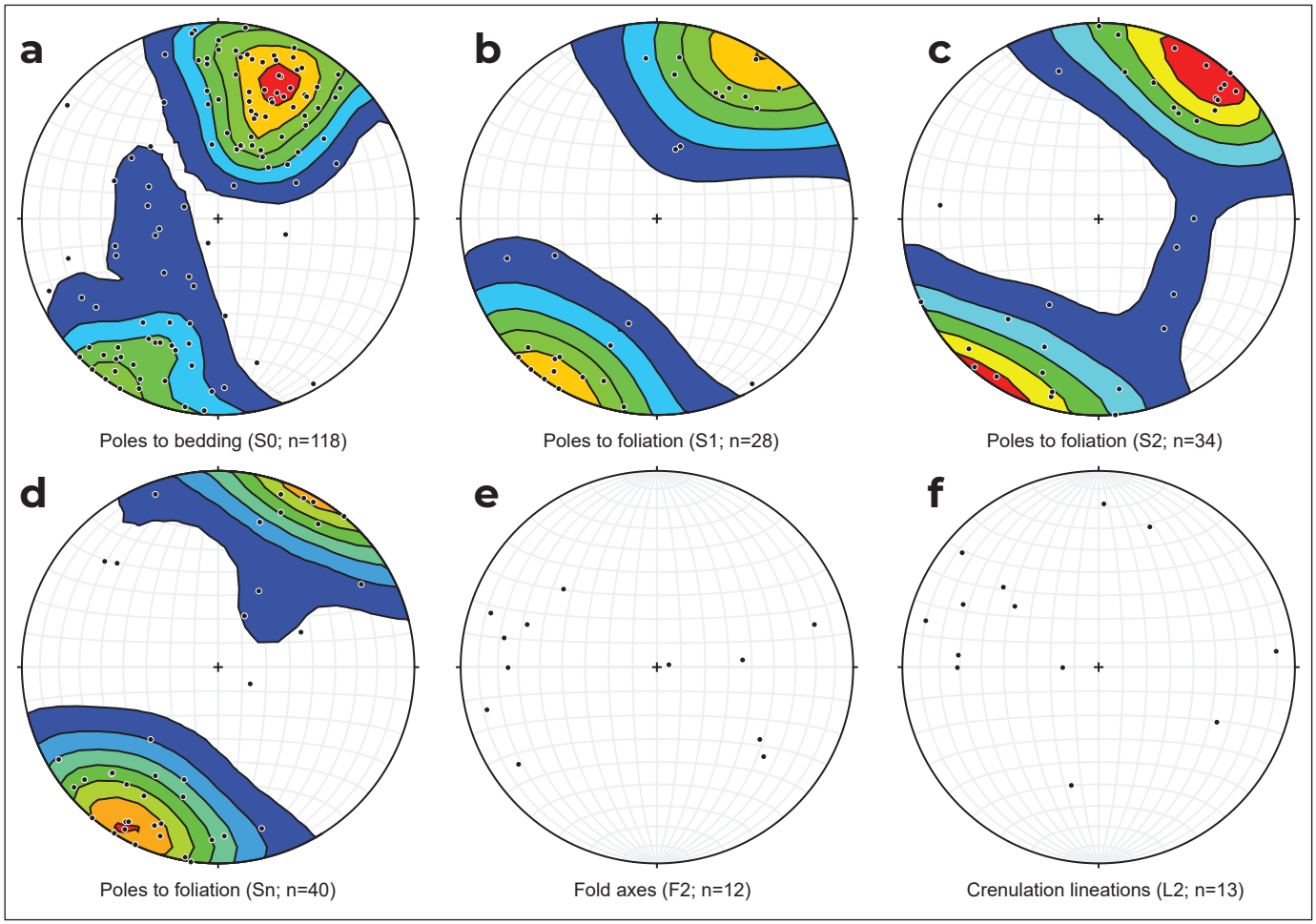

Figure 11. *Structural data from the Clark Lakes area plotted on equal-area projection stereonets (using Stereonet 10.0 software; R. Allmendinger, 2018). Data density distributions are represented by Kamb contours, for which the increasing warmth of contour colours corresponds to higher data density. (a) Poles to bedding (S0).* ***(b)*** *Poles to bedding-parallel foliation (S1).* ***(c)*** *Poles to S2 foliation, which crosscuts bedding and the bedding-parallel S1 foliation.* ***(d)*** *Poles to foliation of uncertain generation (Sn; i.e., S1 or S2; refer to text for details).* ***(e)*** *F2 fold axes.* ***(f)*** *L2 crenulation lineations. n, number of measurements.*

In summary, relationships between metamorphism and deformation suggest that the Clark Lakes area underwent burial to lower-greenschist-facies conditions, forming a bedding-parallel foliation (S1). Subsequent F2 folding and thrusting produced a crenulation cleavage (S2) at lower-greenschist-facies conditions. The orientations of D2 folds, thrusts and fabrics suggest that D2 formed during northeast-vergent shortening, which may have been related to major southeast-striking thrusts that border the Clark Lakes area. Given the northwest-vergent shear fabrics in the Tombstone high-strain zone (Murphy, 1997), it may be more likely that D2 deformation in the Clark Lakes area was related to the Dawson thrust rather than to the Tombstone and Robert Service thrusts. Notably, the thermal peak in the Clark Lakes area is higher-grade than the sub-greenschist-facies conditions recorded in stratigraphically equivalent rocks to the east beneath the Dawson thrust zone in the eastern Wernecke Mountains (Read *et al.*, 1991; Moynihan, 2014). The higher thermal peak conditions in the Clark Lakes area may have resulted from burial beneath the Tombstone and Robert Service thrust sheets.

Mineralization

As several Au and polymetallic mineral deposits occur within an ~30 km radius (Fig. 2), there is heightened interest in the Clark Lakes region; it has been classified as "prospective" to "highly prospective" by mineral potential models (Bullen, 2020). The Hyland Group has the potential to host mineral deposits, as demonstrated by the past-producing polymetallic (Ag-Pb-Zn) manto-style Clark deposit in Hyland Group limestone, located ~5 km south of the Clark Lakes map area (Fig. 2). The McKay Hill polymetallic vein Ag-Au-Pb-Zn deposit, which lies ~15 km along-strike from the Clark Lakes map area (Fig. 2), is hosted by siliciclastic and volcanic rocks that have been tentatively assigned to the Cambrian to Silurian Marmot Group (refer to Yukon MINFILE 106D 038).

Minor occurrences of sulphide mineralization were encountered during 2019 mapping of the Clark Lakes area (Fig. 12). The Narchilla Formation and the mixed and sandstone-dominated units of the upper Yusezyu Formation host quartz veins in several locations, which range in width from <1cm to ~20 cm and, less commonly, up to ~2 m (Fig. 12a). Some quartz veins are surrounded by orange, gossanous weathering and contain pyrite, or a red-brown alteration material, which may be limonite. Quartz veins are mostly discontinuous on the outcrop

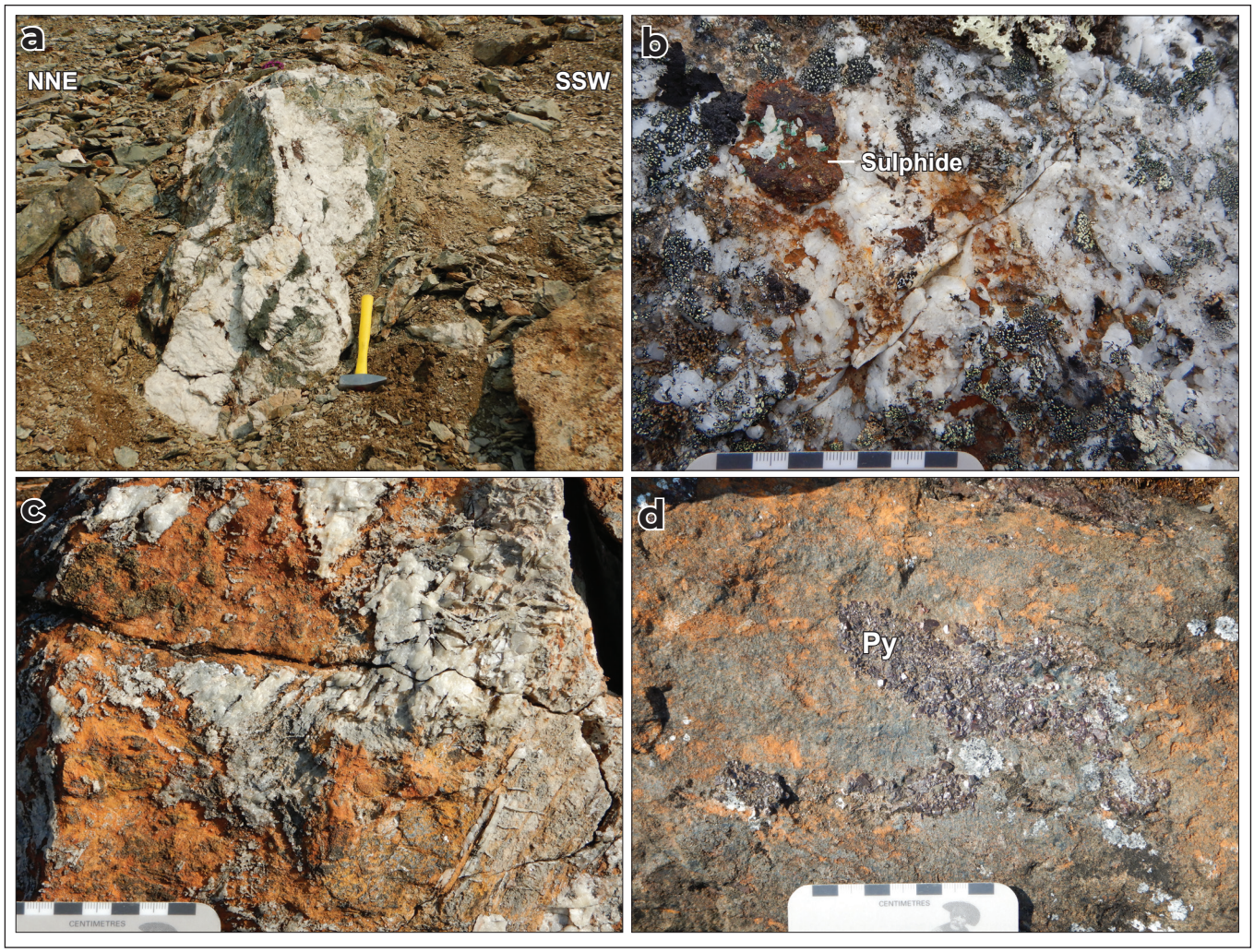

Figure 12. *Field photographs of quartz veins and sulphides hosted in the Hyland Group and gabbro in the Clark Lakes area.* ***(a)*** *A west-northwest-striking, ~1 m wide quartz vein hosted in green phyllite of the Narchilla Formation. The vein contains chlorite, carbonate, and minor rust-coloured alteration material (limonite?).* ***(b)*** *Red-brown-weathered sulphide (likely pyrite) in a 2–3 m wide quartz vein hosted in gabbro.* ***(c and d)*** *Quartz-carbonate veins hosted in orange-weathered carbonate near gabbro, with locally associated pyrite.*

scale, with some exceptions that are continuous over at least ~10 m. They have various orientations and locally form meandering networks, but they dominantly trend northwest–southeast, parallel to the regional structural grain (Fig. 12a). Siliciclastic rocks at various stratigraphic levels in the Yusezyu Formation exhibit discrete zones of silica alteration, which are up to 10s of metres wide and are generally northwest-southeast striking. This silica alteration is commonly associated with quartz veining and, in some places, with cataclastic texture. The silica-altered rocks have a distinctive white to light grey weathered surface, and a fresh surface that is either white with a "bleached" appearance or, less commonly, dark grey with the "siliceous" appearance of crystalline quartz. The predominant northwest-southeast strike of quartz veins and zones of silica alteration suggests that hydrothermal fluid flow and related mineralization were controlled—at least in part—by the northwest–southeast-striking structural grain of the area. Determining the style, architecture and timing of D2 deformation may help to understand fluid flow along the Dawson and Tombstone-Robert Service fault corridors and, therefore, the setting of hydrothermal mineral deposits in the region.

Quartz veins are also hosted by some gabbro intrusions in the Clark Lakes area. Gabbro on the eastern side of the 2019 map area hosts an ~2–3 m-wide quartz vein that contains minor pyrite (Fig. 12b). On the west side of the map area, an ~100 m wide interval of orange-weathered subcrops and rubble is interpreted to represent a skarn-like alteration zone coinciding with an intrusive contact between gabbro and the Algae Formation. Both gabbro and carbonate exhibit orange, locally gossanous weathering, and contain abundant quartz-carbonate veins with local pyrite (Fig. 12c,d).

The occurrence of quartz monzonite along the southern boundary of the area mapped in 2019 (Fig. 3a) raises the possibility of intrusion-related mineralization in the area. The quartz monzonite may share affinity with other felsic igneous rocks in the region (Fig. 2), some of which are associated with mineral deposits, including the Rackla granite (*ca.* 63–59 Ma; Kingston et *al.*, 2010) at the Tiger Au deposit, or the Dublin Gulch pluton (*ca.* 93.5–92.8 Ma; Murphy, 1997) at the Eagle Au Mine, which belongs to the Mayo Suite plutons (*ca.* 94–93 Ma; Hart et *al.*, 2004). Alternatively, if the quartz monzonite was deformed during the mid-Cretaceous (*e.g.*, by *ca.* 104–100 Ma deformation associated with the Tombstone high-strain zone; Mair et *al.*, 2006), it may share affinity with older felsic rocks, such as *ca.* 380–378 Ma (Murphy, 1997) felsic volcanic rocks in the Earn Group, host to the Marg volcanogenic massive sulphide deposit (Fig. 2).

Magnetic susceptibility

To facilitate geophysical interpretations, magnetic susceptibility measurements were obtained for major lithologic units at 150 sites across the Clark Lakes area in 2019. In total, 162 measurements were acquired using a ZH Instruments SM-30 Magnetic Susceptibility Meter. Each "measurement" is the average of five individual measurements from each lithology. Magnetic susceptibilities of the sedimentary rocks ranged from 0.01 to 0.2 SI units, whereas those of gabbro-to-diorite intrusions were typically between 0.2 and 0.5 SI units. Magnetite-bearing siltstone in the southeastern part of the map area produced elevated values of 1.00 to 50.0 SI units.

Acknowledgements

Maurice Colpron, Rosie Cobbett and David Moynihan and the Yukon Geological Survey bedrock geology group are thanked for field visits and helpful discussions. Julia Lane and Adam Coulter of ATAC Resources Ltd. are gratefully acknowledged for their logistical support. Transportation during fieldwork was provided by Horizon Helicopters. David Moynihan and Maurice Colpron are thanked for their helpful reviews of this article. Fieldwork was conducted in the traditional territory of the First Nation of Na-Cho Nyäk Dun.

References

Abbott, G., 1990a. Geological map of Mt. Westman map area (106D/1). Exploration and Geological Services Division, Yukon Region, Indian and Northern Affairs Canada, Open File 1990-1, scale 1:50 000.

Abbott, G., 1990b. Preliminary results of the stratigraphy and structure of the Mt. Westman area, central Yukon. Geological Survey of Canada, Current Research 1990-1E, p. 15–22.

Abbott, G., 1997a. Geology of NTS map area 116A/10, eastern Ogilvie Mountains, Yukon. Exploration and Geological Services Division, Yukon Region, Indian and Northern Affairs Canada, Geoscience Map 1997-2, scale 1:50 000.

Abbott, G., 1997b. Geology of Two Beaver Lake map area, eastern Ogilvie Mountains, Yukon (NTS 116A/11). Exploration and Geological Services Division, Yukon Region, Indian and Northern Affairs Canada, Geoscience Map 1997-3, scale 1:50 000.

Abbott, G., 1997c. Geology of the Upper Hart River Area, Eastern Ogilvie Mountains, Yukon Territory (116A/10, 116A/11). Exploration and Geological Services Division, Yukon Region, Indian and Northern Affairs Canada, Bulletin 9, 92 p.

Allmendinger, R., 2018. Stereonet 10.0. Cornell University, http://www.geo.cornell.edu/geology/faculty/RWA/programs/stereonet.html, [accessed November 20, 2020].

Anderson, R.G., 1987. Plutonic rocks in the Dawson map area, Yukon Territory. Geological Survey of Canada, Current Research 1987-1A, p. 689–697.

Bullen, W., 2020. New mineral potential mapping methodology for Yukon: Case studies from the Beaver River and Dawson regional land use planning areas. *In*: Yukon Exploration and Geology 2019, K.E. MacFarlane (ed.), Yukon Geological Survey, p. 23–42.

Colpron, M., Moynihan, D., Israel, S. and Abbott, G., 2013. Geological map of the Rackla belt, east-central Yukon (NTS 106C/1–4, 106D/1). Yukon Geological Survey, Open File 2013-13, 1:50 000 scale, 5 maps and legend.

Colpron, M., Nelson, J.L. and Murphy, D.C., 2007. Northern Cordilleran terranes and their interactions through time. GSA Today, vol. 17, no. 4/5, p. 4–10.

Green, L.H. and Roddick, J.A., 1962. Dawson, Larsen Creek, and Nash Creek map-areas, Yukon Territory (116B, C, E1/2, 116A and 106D). Geological Survey of Canada, Paper 62-7, 20 p., plus maps.

Green, L.H., 1972a. Geology, Nash Creek, Yukon Territory. Geological Survey of Canada, Department of Energy, Mines and Resources, Map 1282A, scale 1:250 000.

Green, L.H., 1972b. Geology of Nash Creek, Larsen Creek, and Dawson map-areas, Yukon Territory (106D, 116A, 116B, and 116C (E1/2)). Geological Survey of Canada, Memoir 364, 157 p.

Hart, C.J.R., Goldfarb, R.J., Lewis, L.L. and Mair, J.L., 2004. The Northern Cordilleran mid-Cretaceous plutonic province: Ilmenite/magnetite-series granitoids and intrusion-related mineralisation. Resource Geology, vol. 54, p. 253–280.

Kingston, S., Mortensen, J.K., Dumala, M. and Gabites, J., 2010. Ar-Ar geochronology and Pb isotopic constraints on the origin of the Rau gold-rich carbonate replacement deposit, central Yukon. *In:* Yukon Exploration and Geology 2009, K.E. MacFarlane, L.H. Weston, and L.R. Blackburn (eds.), Yukon Geological Survey, p. 213–222.

Kiss, F., 2020. Aeromagnetic Survey of the Nash Creek Area, Yukon, Parts of NTS 105-M, N, 106-C, D, 115-P and 116-A. Geological Survey of Canada, Open File 8728; Yukon Geological Survey, Open File 2020-7, scale 1:100 000, https://doi.org/10.4095/326147.

Mair, J.L., Hart, C.J.R. and Stephens, J.R., 2006. Deformation history of the northwestern Selwyn Basin, Yukon, Canada: Implications for orogen evolution and mid-Cretaceous magmatism. GSA Bulletin, vol. 118, p. 304–323.

Moynihan, D., 2014. Bedrock Geology of NTS 106B/04, Eastern Rackla Belt. *In:* Yukon Exploration and Geology 2013, K.E. MacFarlane, M.G. Nordling and P.J. Sack (eds.), Yukon Geological Survey, p.147–167.

Moynihan, D., 2016a. Bedrock geology compilation of the eastern Rackla belt, NTS 105N/15, 105N/16, 105O/13, 106B/4, 106C/1, 106C/2, east-central Yukon. Yukon Geological Survey, Open File 2016-2, scale 1:75 000, 2 sheets.

Moynihan, D., 2016b. Stratigraphy and structural geology of the upper Hyland River area (parts of 105H/8, 105H/9), southeast Yukon. *In:* Yukon Exploration and Geology 2015, K.E., MacFarlane and M.G. Nordling (eds.), Yukon Geological Survey, p. 187–206.

Murphy, D.C., 1997. Geology of the McQuesten River Region, Northern McQuesten and Mayo Map Area, Yukon Territory (115P/14, 15, 16; 105M/13, 14). Exploration and Geological Services Division, Yukon Region, Indian and Northern Affairs Canada, Bulletin 6, 122 p.

Pearce, J.A., 1996. A user's guide to basalt discrimination diagrams. *In:* Trace Element Geochemistry of Volcanic Rocks: Applications for Massive Sulphide Exploration, D.A. Wyman (ed.), Geological Association of Canada, Short Course Notes, vol. 12, p. 79–113.

Read, P.B., Woodsworth, G.J., Greenwood, H.J., Ghent, E.D. and Evenchick, C.A., 1991. Metamorphic Map of the Canadian Cordillera. Geological Survey of Canada, Map 1714A, scale 1:2 000 000.

Roots, C.F., 1988. Cambro-Ordovician volcanic rocks in eastern Dawson map area, Ogilvie Mountains, Yukon. *In:* Yukon Geology, volume 2, G. Abbott (ed.), Exploration and Geological Services Division, Yukon, Indian and Northern Affairs Canada, p. 81–87.

Roots, C.F., 1997. Geology of the Mayo Map Area, Yukon Territory (105M). Exploration and Geological Services Division, Yukon Region, Indian and Northern Affairs Canada, Bulletin 7, 82 p.

Spear, F.S., 1993. Metamorphic Phase Equilibria and Pressure-Temperature-Time Paths. Mineralogical Society of America, Monograph 1, 799 p.

Sun, S.S. and McDonough, W.F., 1989. Chemical and isotopic systematics of oceanic basalts; implications for mantle composition and processes. Geological Society Special Publications, vol. 42, p. 313–345.

Tempelman-Kluit, D.J., 1970. Stratigraphy and structure of the Keno Hill quartzite in Tombstone River-Upper Klondike River map areas, Yukon Territory (116B/7, B/8). Geological Survey of Canada, Bulletin 180, 102 p. and maps.

Thompson, R.I., Roots, C.F. and Mustard, P.S., 1990. Repeated Proterozoic passive margin extension influences Late Cretaceous folding and thrusting in southern Ogilvie Mountains, Yukon. Geological Association of Canada, Program with Abstracts, vol. 15, p. 131.

Vernon, R.H., 2004. A Practical Guide to Rock Microstructure. Cambridge University Press, New York, USA, 594 p.

Yukon Geological Survey, 2020a. Yukon Digital Bedrock Geology. Yukon Geological Survey, http://data.geology.gov.yk.ca/Compilation/3#InfoTab, [accessed November 6, 2020].

Yukon Geological Survey, 2020b. Yukon Lithogeochemistry data set: Yukon Geological Survey, http://data.geology.gov.yk.ca/Compilation/35#InfoTab, [accessed October 20, 2020].

Update on the bedrock geology of the Rusty Mountain area, southern Wernecke Mountains, Yukon (parts of NTS 106C/4, 5, 12 and 106D/1, 8)

Tyler Ambrose
Yukon Geological Survey

Ambrose, T., 2021. Update on the bedrock geology of the Rusty Mountain area, southern Wernecke Mountains, Yukon (parts of NTS 106C/4, 5, 12 and 106D/1, 8). *In:* Yukon Exploration and Geology 2020, K.E. MacFarlane (ed.), Yukon Geological Survey, p. 95–113.

Abstract

The Rusty Mountain area is underlain by sedimentary strata of the Paleoproterozoic Wernecke Supergroup, Mesoproterozoic Pinguicula Group, Neoproterozoic Hematite Creek Group and Windermere Supergroup, and Paleozoic Bouvette Formation. Three suites of intrusions are documented: (1) 10–200 m thick, subalkaline, mafic sills and dikes of the *ca.* 1380 Ma Hart River suite intrude the Wernecke Supergroup; (2) 2–3 m wide, vertical, east-west striking, alkaline, mafic dikes that are geochemically distinct from the Hart River suite intrude the Wernecke Supergroup; and (3) a 30 cm thick, mafic, porphyritic dike intrudes the Wernecke Supergroup at one locality. The main structures in the Wernecke Supergroup are northwest-verging folding and thrusting and a steeply dipping axial-planar cleavage. This deformation affected the Hart River sills, but not the east-west striking dikes. The main structures in the Pinguicula Group and younger strata are northwest-southeast trending gentle folds and a steeply dipping axial-planar cleavage.

* *tyler.ambrose@yukon.ca*

Introduction

This paper presents an update on the bedrock geology and stratigraphy in the Rusty Mountain area following the completion of a second field season of 1:50 000-scale mapping. The new map area covers approximately 200 km^2 to the north of, and contiguous with, the previous map of Ambrose (2020), and includes the northern part of NTS 106C/5 (Rusty Mountain) and the southern extent of 106C/4 (Gillespie Creek).

The map area is located in the southern Wernecke Mountains, ~120 km NE of Mayo (Figs. 1 and 2). Access is by fixed-wing plane from Mayo to the Rackla airstrip (64.22°N, 133.21°W) and helicopter from that point. The map area is located at the southeast margin of the Wernecke Inlier (Fig. 2). The Wernecke Inlier is the largest of several Proterozoic inliers along the southern margin of the Yukon stable block, a triangular region of relatively thick lithosphere (Jeletsky, 1962; Estève et *al.*, 2020) that is bound to the east by the Richardson fault array and by the Dawson fault to the south. This paper focuses on rocks of the Paleoproterozoic Wernecke Supergroup, the oldest stratigraphic unit in the northern Cordillera and the only sedimentary unit exposed in the northern part of the map. These rocks are overlain to the south by Mesoproterozoic and younger rocks previously mapped by Ambrose (2020) and described in Ambrose and Bowie (2020). The new mapping reported here brings revision to the map of Ambrose (2020) to the south.

Previous work

Blusson (1974a) previously mapped the area as part of a series of five 1:250 000-scale maps of east-central Yukon. Blusson (1974b) mapped parts of the region east of the current study area (NTS 106C/6, 7, 10, 11, 13, 15)

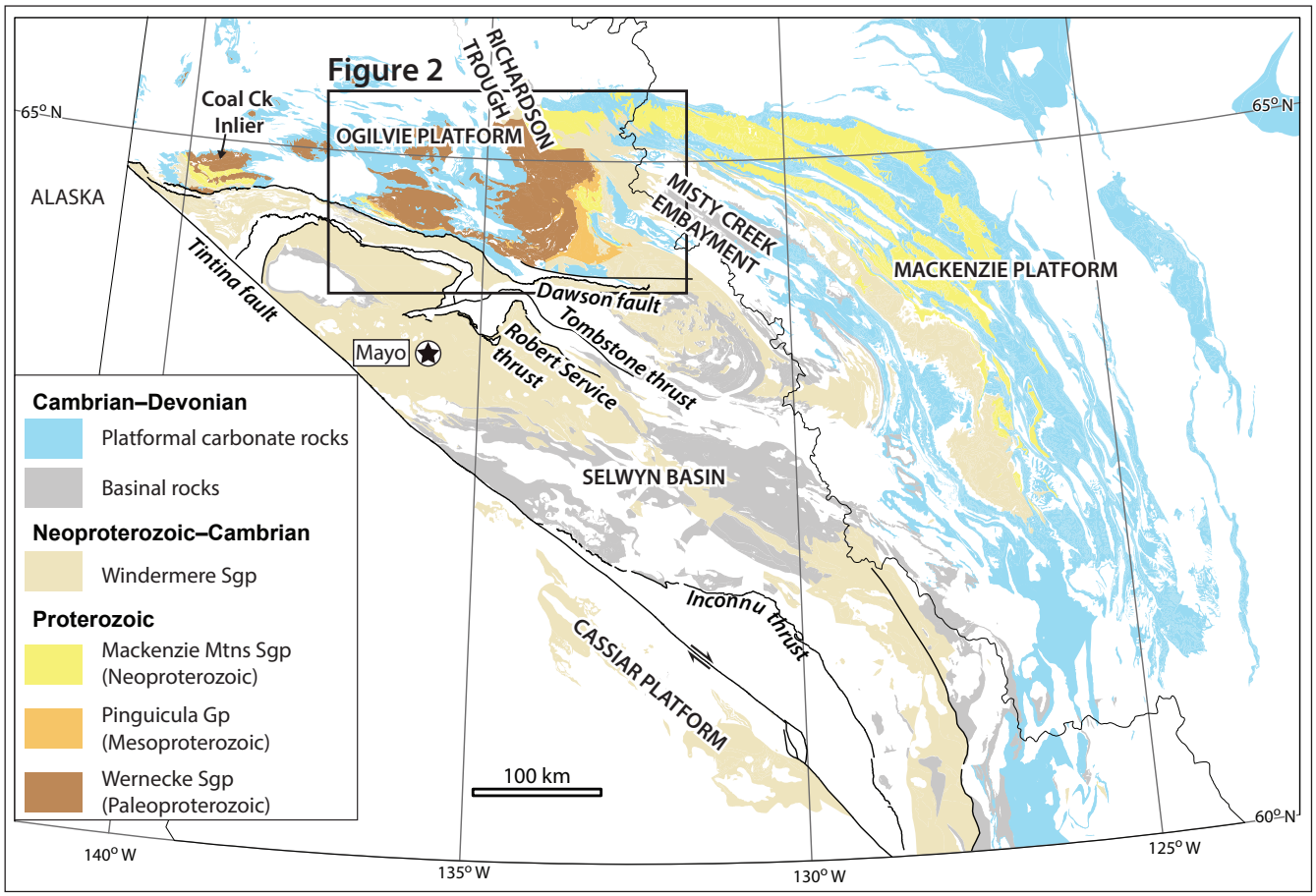

Figure 1. *Simplified geological map showing the distribution of Proterozoic through to Devonian assemblages in Yukon and NWT (after Moynihan et al., 2019). The study area is located within the Wernecke Inlier, the farthest east, and largest of several erosional windows that expose Paleoproterozoic and Mesoproterozoic rocks.*

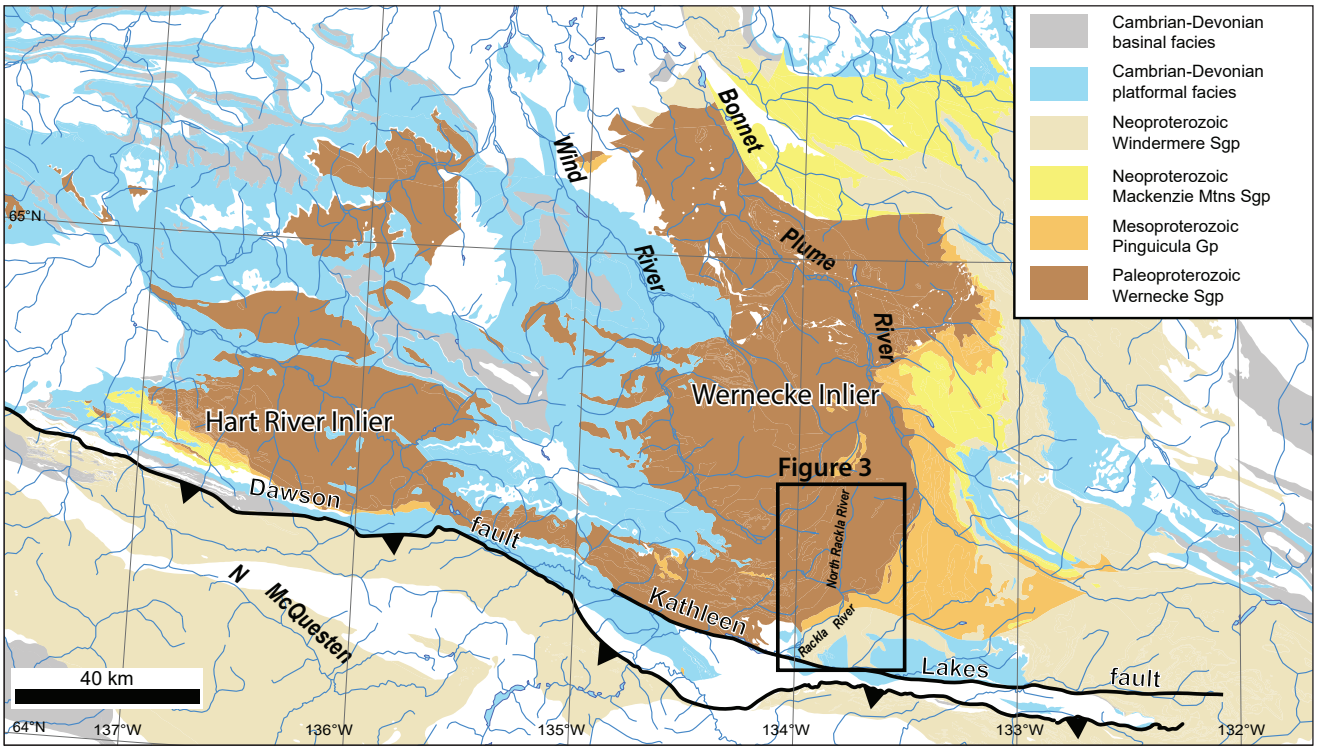

Figure 2. *Simplified geological map of the Wernecke and Hart River inliers. White areas are Late Devonian and younger rocks. Location is shown in Figure 1. The map area (outlined) is located north of the Dawson and Kathleen Lakes faults and across the southern margin of the Wernecke Inlier. Geology from Colpron et al. (2016).*

at the more detailed 1:50 000 scale. Abbott (1997) and Thorkelson (2000) mapped Proterozoic stratigraphy in the Hart River (116A/10, 11) and northern Wernecke (106D/16, 106C/13–14) inliers, respectively. Roots (1990a,b) mapped the adjacent, 1:50 000-scale sheets to the west (eastern half of NTS 106D/7, 8) of the current map area.

Delaney (1981) described and subdivided the Wernecke Supergroup into the Fairchild Lake, Quartet, and Gillespie Lake groups. Furlanetto *et al.* (2013) used detrital zircon and Lu-Hf garnet geochronology to show that the Wernecke Supergroup was deposited after 1640 Ma and metamorphosed at *ca.* 1600 Ma and 1370 Ma. Abbott (1997) and Verbaas *et al.* (2018) provide descriptions, geochemical analyses, and geochronology of the Hart River sills from the Hart River and Wernecke inliers. Eisbacher (1981) described the Pinguicula Group and divided it into units A–F. Thorkelson (2000) documented an unconformity between Pinguicula C and D, and reassigned units D–F of the Pinguicula Group into the newly defined Hematite Creek Group. Turner (2011) formalized the Hematite Creek Group and assigned it to the Mackenzie Mountain Supergroup. Medig *et al.* (2016) formalized formations in the Pinguicula Group and described type sections for them. Medig (2016) presented a detrital zircon study of the Pinguicula Group to constrain a maximum depositional age of 1322 Ma.

Stratigraphy

Only the upper two units of the Wernecke Supergroup are present in the map area and described below. Descriptions of the Pinguicula Group are also given below as the new mapping brings revisions to previous work by Ambrose (2020) and Ambrose and Bowie (2020).

Quartet Group

The Paleoproterozoic Quartet Group is the middle unit of the Wernecke Supergroup and oldest unit exposed in the map area (Figs. 3 and 4). The Quartet Group

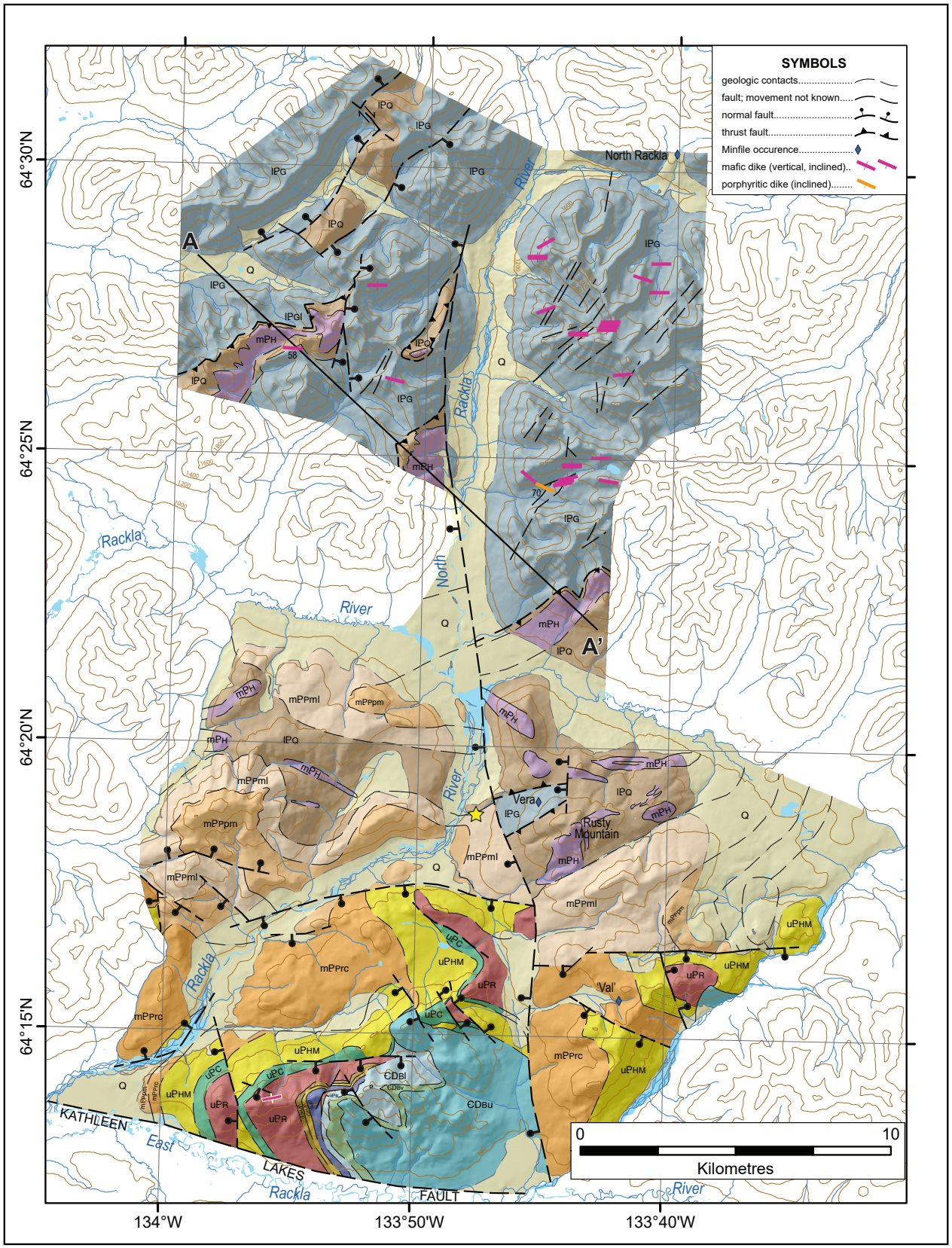

Figure 3. *Simplified geological map of the Rusty Mountain area. Yellow star to the west of Rusty Mountain marks the location of interbedded conglomerate and sandstone at the base of the Mount Landreville Formation (see text for discussion).*

QUATERNARY

Q — unconsolidated alluvial, colluvial, fluvial, and glacial deposits

CAMBRIAN TO DEVONIAN

BOUVETTE FORMATION

ЄDBu — UPPER MEMBER: light to medium grey weathering dolostone; commonly thickly bedded; locally fossiliferous

ЄDBv — VOLCANICLASTIC MEMBER: grey, green and orange weathering volcaniclastic sandstone and conglomerate; locally fossiliferous

ЄDBl — LOWER MEMBER: light to medium grey weathering sugary dolostone

EDIACARAN

RACKLA GROUP

uPB — BLUEFLOWER FORMATION: brown weathering shale and siltstone

uPG — GAMETRAIL FORMATION: Well bedded and laminated grey, buff, maroon, yellow-orange, and green weathering silty lime and dolo-mudstone

CRYOGENIAN–EDIACARAN

HAY CREEK GROUP

uPHCr — RAVENSTHROAT FORMATION: grey and cream weathering dolostone, grey and black chert; local chaotic bedding and tepee structures

uPHCp — MOUNT PROFEIT DOLOSTONE/ICE BROOK FORMATION: grey and cream weathering dolostone; light-grey weathered carbonate-clast diamictite

CRYOGENIAN

RAPITAN GROUP

uPR — orange, maroon, and brown weathering clast to matrix-supported diamictite; maroon and green shale, siltstone and sandstone intervals

TONIAN

CALLISON LAKE FORMATION

uPC — light to medium grey weathering dolostone with irregular chert layers; commonly laminated; locally silica replaced oolitic grainstone; locally hematite-cement conglomerate

NEOPROTEROZOIC

HEMATITE CREEK GROUP

uPHM — laminated, medium to very thickly bedded grey, purple, and orange weathering sandstone, with subordinate shale, siltstone, limestone, red-weathering stromatolitic dolostone, and orange-weathering dolostone and dolomitic siltstone

MESOPROTEROZOIC

PINGUICULA GROUP

mPPrc — RUBBLE CREEK FORMATION: dark and light grey laminated dolostone with local zebra textures

mPPpm — PASS MOUNTAIN FORMATION: well bedded, laminated, grey and orange weathering dolomitic limestone; commonly cross-laminated; minor dolomitic/calcareous shale at base

mPPml — MOUNT LANDREVILLE FORMATION: blue, brown and green-grey weathering shale, mudstone, siltstone and fine-grained sandstone; basal polymictic conglomerate

HART RIVER SILLS

mPH — grey weathering, fine to medium-grained, greenish-grey gabbro sills and dikes

PALEOPROTEROZOIC

GILLESPIE LAKE GROUP

lPG — resistant, thin to thick bedded, orange, red, and grey weathering dolostone and silty dolostone; recessive, cream, orange, and grey weathered siltstone, dolomitic silstone, silty dolostone, and lime mudstone

QUARTET GROUP

lPQ — grey, brown, black, and terracotta-weathered shale, siltstone and fine-grained sandstone; locally phyllitic and slatey

Figure 3 continued. *Legend for simplified geological map of the Rusty Mountain area.*

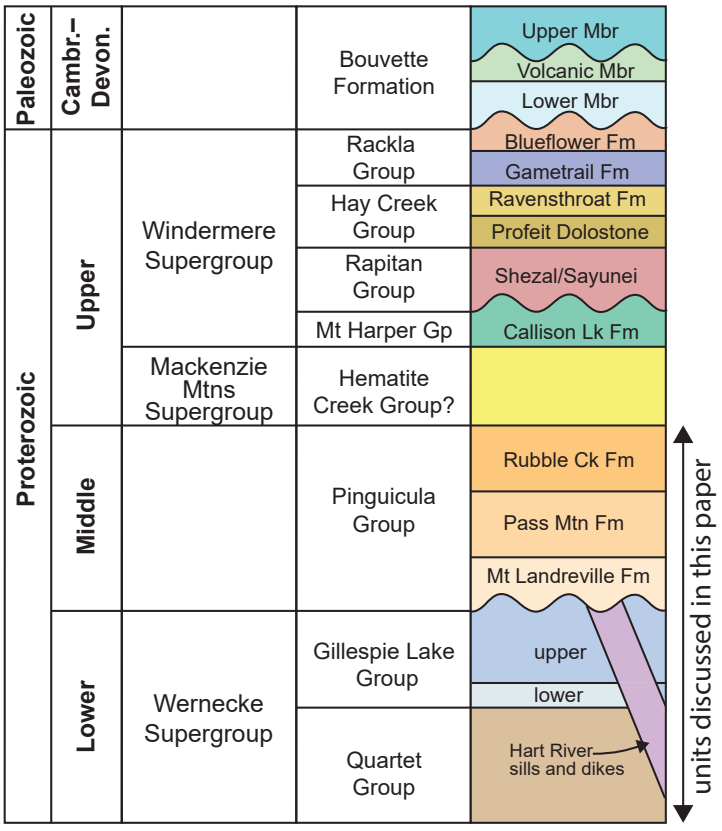

Figure 4. *Schematic lithostratigraphic column of units exposed in the map area.*

comprises black, grey and brown weathering, planar-parallel laminated mudstone, shale and siltstone with less common sandstone and carbonate (Fig. 5). The basal stratigraphic contact with the underlying Fairchild Lake Group (oldest unit of the Wernecke Supergroup) is not exposed in the map area. Unlike the Fairchild Lake Group, which is locally metamorphosed to greenschist facies, the Quartet Group is unmetamorphosed. Towards the contact with the overlying Gillespie Lake Group, the Quartet Group becomes increasingly dolomitic and calcareous (Fig. 5c,d). This increase in carbonate content is reflected by a colour change, from dark weathering typical of the Quartet Group into tan weathering near the contact with the overlying Gillespie Lake Group (Fig. 6). To the north, Delaney (1981) estimated the Quartet Group to be >5 km thick and Thorkelson (2000) estimated it to be >3.4 km thick from a section with a faulted basal contact.

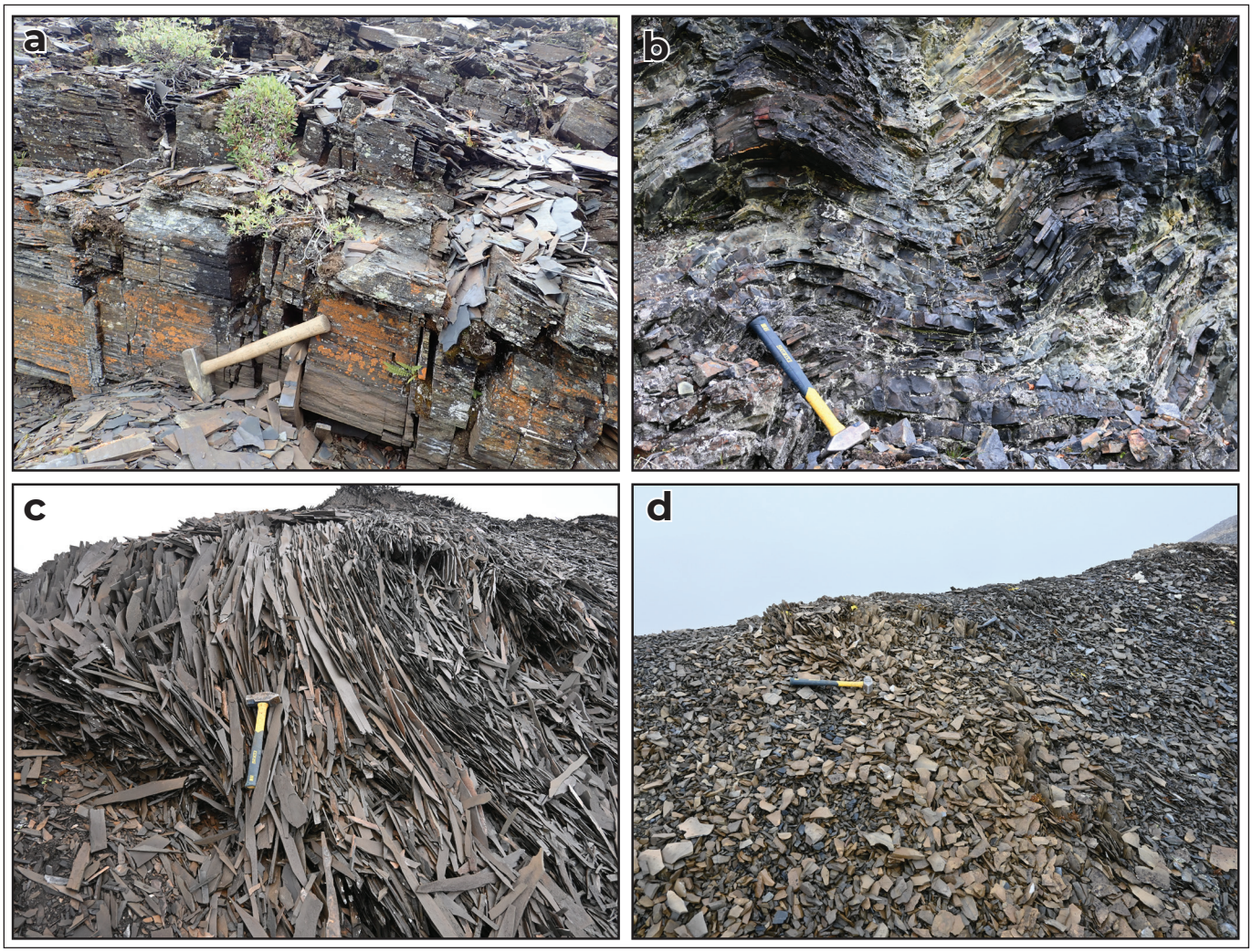

Figure 5. *Representative field photos of the Quartet Group.* ***(a)*** *Brown weathering siltstone.* ***(b)*** *Gently folded dark weathering siltstone.* ***(c-d)*** *Cream-grey weathering dolomitic and calcareous siltstone near the top of the Quartet where it transitions into the Gillespie Lake Group.*

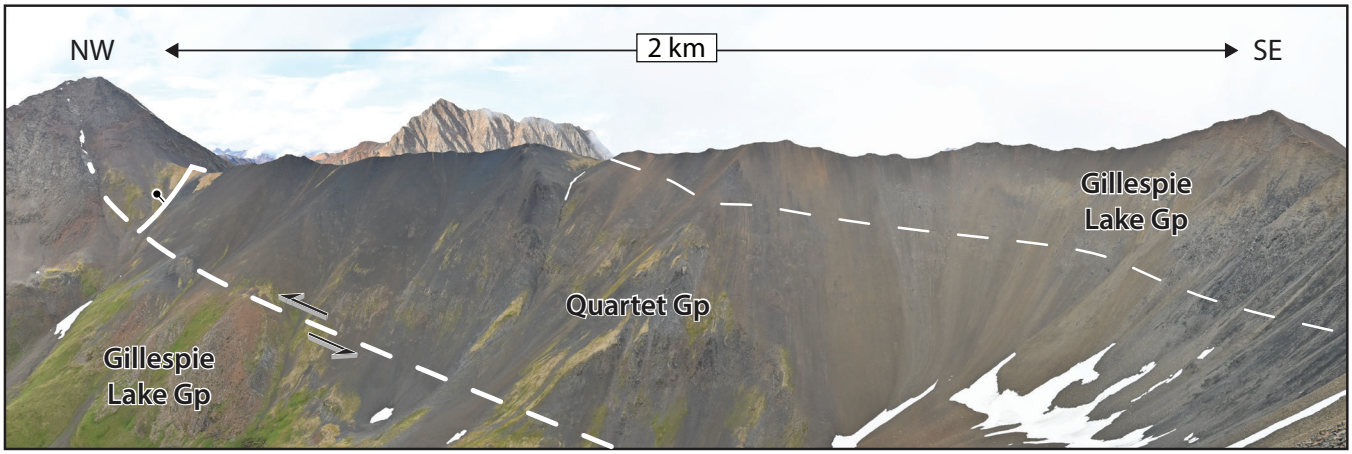

Figure 6. *Gradational contact between the dark weathering siltstones of the Quartet Group, and the cream-weathering dolomitic siltstones and silty dolostones of the lower Gillespie Lake Group. Thin dashed white line marks the stratigraphic contact between the Quartet and Gillespie Lake groups. Thick dashed line marks a sinistral strike-slip fault.*

Gillespie Lake Group

The Paleoproterozoic Gillespie Lake Group is the uppermost unit of the Wernecke Supergroup and consists of orange, red, buff and grey weathering dolostone and silty dolostone with less common dolomitic siltstone, dark-weathering siltstone, and grey limestone (Fig. 4). The contact with the underlying Quartet Group is gradational (Fig. 6). The base of the Gillespie Lake Group, as defined by Delaney (1981), is marked by the first appearance of orange-weathering silty dolostone (Fig. 7a).

The basal several hundred metres of the Gillespie Lake Group typically comprises recessive, thin to medium bedded, grey, cream, orange and black weathering dolomudstone, silty dolostone, dolomitic siltstone, and siltstone (Fig. 7). Intervals of well-bedded, variably dolomitic, grey to orange-weathering lime mudstone are also common in the basal Gillespie Lake Group. Cross-lamination, often lenticular, is abundant in some beds. The remainder of the Gillespie Lake Group comprises resistant, cliff forming, thin to thick-bedded, typically orange and red, and less commonly buff and grey weathering, variably silty dolomudstone and dolograinstone, and dolomitic siltstone (Fig. 8). Above the basal interval, the Gillespie Lake Group contains abundant stromatolites and microbially laminated dolostone (Fig. 8b,c). Coarsening and thickening upwards sequences that, in general, pass from thinly bedded, fine-grained, silty dolomudstone at the base (Fig. 8d–e) to thicker bedded silty dolowackestone–grainstone (Fig. 8f), microbially laminated dolostone (Fig. 8b), and stromatolitic dolostone (Fig. 8c) at the top, are common. Well developed sequences are up to 10 m thick, though they are often incomplete and only 10s of cm thick. Medium to thickly bedded nodular limestone and dolostone occur as intervals up to ~100 m thick.

At the outcrop scale there is a textural continuum from planar-parallel, mechanical laminations (Fig. 8d), through to crinkly, irregular, microbial laminations (Fig. 8b). In places, microbially-laminated dolostone passes along the same bed into stromatolites (Fig. 8c). Silicified oolitic grainstone (Fig. 8f) and, rarely, chert occur as thin beds. As seen in Figure 8b and e, silicification results in a distinct relief on weathered surfaces, with the darker, finer grained, more silicified layers being more resistant than coarser grained orange weathering dolowackestone–grainstone.

The Gillespie Lake Group contains conspicuous intervals of grey-weathering dolomitic mudstone and siltstone (Fig. 9a). These rocks are typically planar-parallel laminated, weather blue, brown and green-grey (Fig. 9b,c), and consist of clay minerals, quartz,

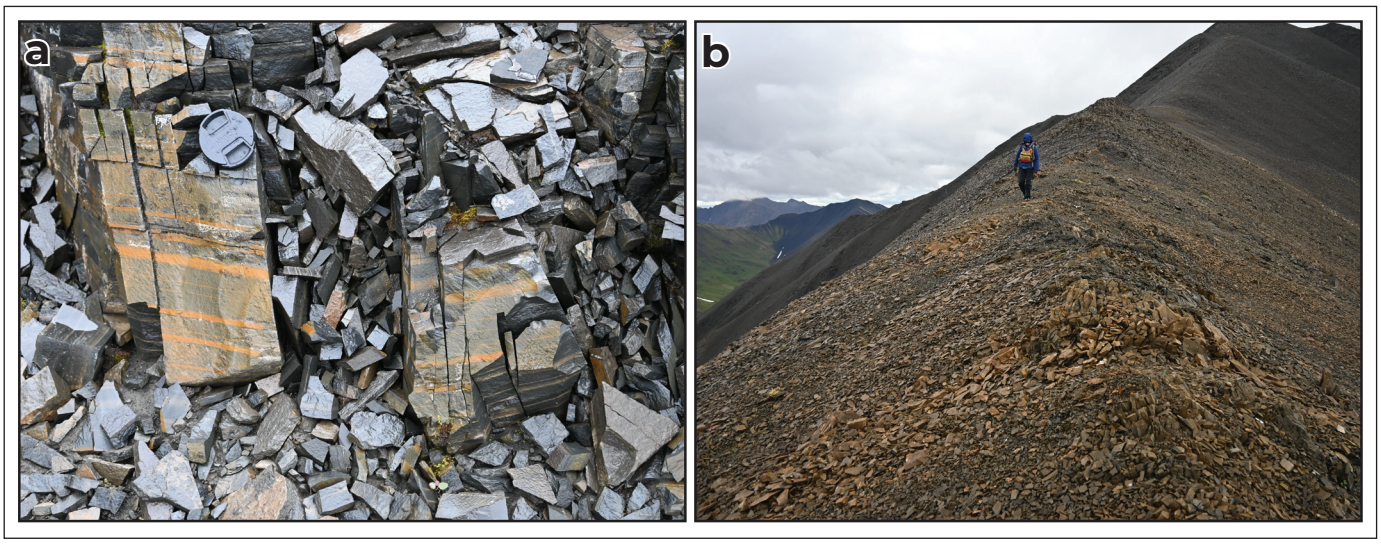

Figure 7. *Field photographs of the lowermost Gillespie Lake Group.* ***(a)*** *Thin beds of orange weathering dolostone that marks the base of the Gillespie Lake Group.* ***(b)*** *Orange weathering dolomitic siltstone and silty dolostone from the base of the Gillespie Lake Group.*

Figure 8. *Field photographs illustrating common features of the Gillespie Lake Group.* ***(a)*** *Well bedded silty dolostone. Hammer for scale.* ***(b)*** *Crinkly, microbially laminated, orange weathering, silty dolograinstone and silty, dark grey weathering dolomudstone.* ***(c)*** *Stromatolitic dolostone.* ***(d)*** *Thinly interbedded, dark weathering, resistant dolomudstone, and orange weathering dolograinstone–wackestone.* ***(e)*** *Nodular to thinly interbedded, resistant, dark grey weathing dolomudstone and orange weathering dolograinstone–wackestone.* ***(f)*** *Silicified, oolitic grainstone.*

and carbonate grains. Depositional contacts between these intervals and the dolostone more typical of the Gillespie Lake Group are gradational. As highlighted by Figure 9a, these intervals act as local marker beds that allow for the recognition of vertical faults (Fig. 3).

The basal stratigraphic contact with the Gillespie Lake Group is exposed along several ridges in the northwestern part of the map area, but its top is truncated by faults (Fig. 3). The stratigraphic thickness of Gillespie Lake Group is estimated to be at least 2 km in the map area. In the type area to the north, Delaney (1981) estimated the thickness to be more than 4 km. Based on three incomplete sections to the west of the map area (106D/7, 8), Mustard et *al.* (1990) estimated a thickness of ~1.2 km. In the Fairchild Lake area (106C/13), Thorkelson (2000) estimated the Gillespie Lake Group to be up to 4.7 km thick.

Pinguicula Group

Mount Landreville Formation

The Mount Landreville Formation (Pinguicula A of Eisbacher, 1978) is the oldest unit of the Mesoproterozoic Pinguicula Group (Fig. 4). It consists of mudstone, shale, siltstone and fine-grained sandstone (Medig et *al.*, 2016). North of the present study area, the Mount Landreville Formation weathers conspicuous green and maroon colours (*e.g.*, see Figure 5 of Medig et *al.*, 2012). In the Rusty Mountain area, the fine-grained siliciclastic rocks of the Mount Landreville Formation are difficult to distinguish from the Quartet Group as both units weather to variable shades of greenish, blueish and brownish grey. Thorkelson (2000) and Medig et *al.* (2016) described the local occurrence of up to 20 m of interbedded sandstone and polymictic conglomerate

Figure 9. (a) *Panorama of red-weathering silty Gillespie Lake Group dolostone with intervals of grey-weathering dolomitic siltstone. Thin dashed lines indicate bedding. Thick solid lines indicate faults.* ***(b–c)*** *Planar laminated siltstone and dolomitic siltstone from intervals within the Gillespie Lake Group.*

at the base of the Pinguicula Group. Ambrose and Bowie (2020) described a thin interval of interbedded sandstone and polymictic conglomerate at one locality to the southwest of Rusty Mountain (see yellow star on Fig. 3). These coarse-grained rocks were assigned to their "lower siliciclastic unit" and tentatively correlated with the Quartet Group. This conglomerate is now interpreted to mark the base of the Mount Landreville Formation.

Pass Mountain Formation

The Pass Mountain Formation (Pinguicula B of Eisbacher, 1978) is the middle unit of the Pinguicula Group (Fig. 4). It gradationally overlies the Mount Landreville Formation and comprises orange weathering, variably silty, dolomitic, thin to medium bedded, platy limestone (see Ambrose and Bowie, 2020). Ambrose and Bowie (2020) assigned these rocks to their "lower carbonate unit" and correlated them with the Gillespie Lake Group. Mapping to the north shows that the "lower carbonate unit" is distinct from the Gillespie Lake Group and is reassigned here to the Pass Mountain Formation.

Red and orange weathering, stromatolitic dolostone northwest of Rusty Mountain that was assigned to the "lower carbonate unit" of Ambrose and Bowie (2020) is probably still correlative with the Gillespie Lake Group. These rocks occupy a low structural level beneath fine-grained siliciclastic rocks of the Quartet Group intruded by Hart River sills and may be exposed within a thrust window (Fig. 3).

Rubble Creek Formation

The Rubble Creek Formation (Pinguicula C of Eisbacher, 1978) gradationally overlies the Pass Mountain Formation and is the uppermost unit of the Pinguicula Group (Fig. 5). Ambrose and Bowie (2020) correlated their "Val dolostone" with the Rubble Creek Formation, a correlation reinforced by the stratigraphic adjustments proposed above. Ambrose and Bowie (2020) provide a more detailed description of the Rubble Creek Formation.

Intrusive Rocks

Hart River Sills

The ca. 1380 Ma Hart River sills and dikes consist of resistant, greenish, medium to dark grey weathering gabbro and diorite (Figs. 10 and 11). The primary igneous mineralogy is dominated by plagioclase and clinopyroxene, with minor quartz and opaque minerals (Fig. 10). Plagioclase grains have been variably altered to saussurite (albite + clinozoisite) and sericite. Clinopyroxene is variably replaced by chlorite. Quartet Group rocks are commonly pyritic and orange-weathering along the margins of Hart River sills and dikes (Fig. 11). The sills and dikes, which range from 10 to ~200 m thick, commonly occur in the hanging wall of, but do not cut, northwest-verging thrust faults (Figs. 3 and 11), suggesting that faulting postdates emplacement. The gabbro is always separated from the thrust fault by tens of metres of Quartet Group siltstone (Figs. 3 and 11).

East–west striking dikes

The Wernecke Supergroup is also intruded by dark grey weathering, relatively magnetic (compared to Hart River sills), nearly vertical, east–west striking, 2–3 m wide mafic dikes (Fig. 12). The colour contrast with the Gillespie Lake Group make them conspicuous and easy to identify in cliff faces (Fig. 12a,b). In hand sample, the east-west striking dikes are generally finer grained, but

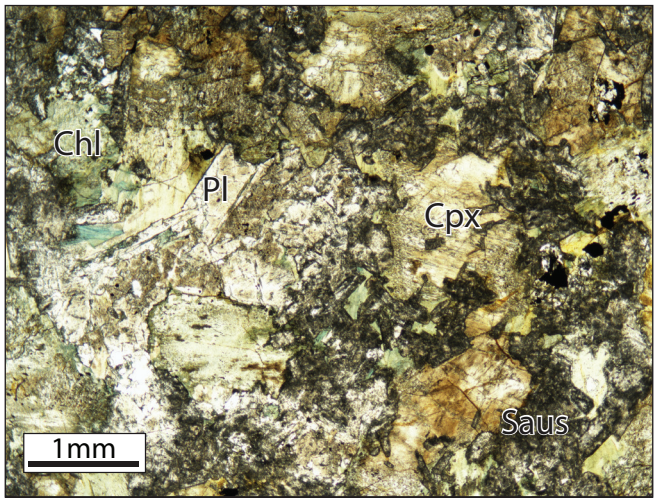

Figure 10. *Photomicrograph of Hart River gabbro showing clinopyroxene (Cpx), plagioclase (Pl), chlorite (Chl), and saussurite (Saus). Plain-polarized light (PPL).*

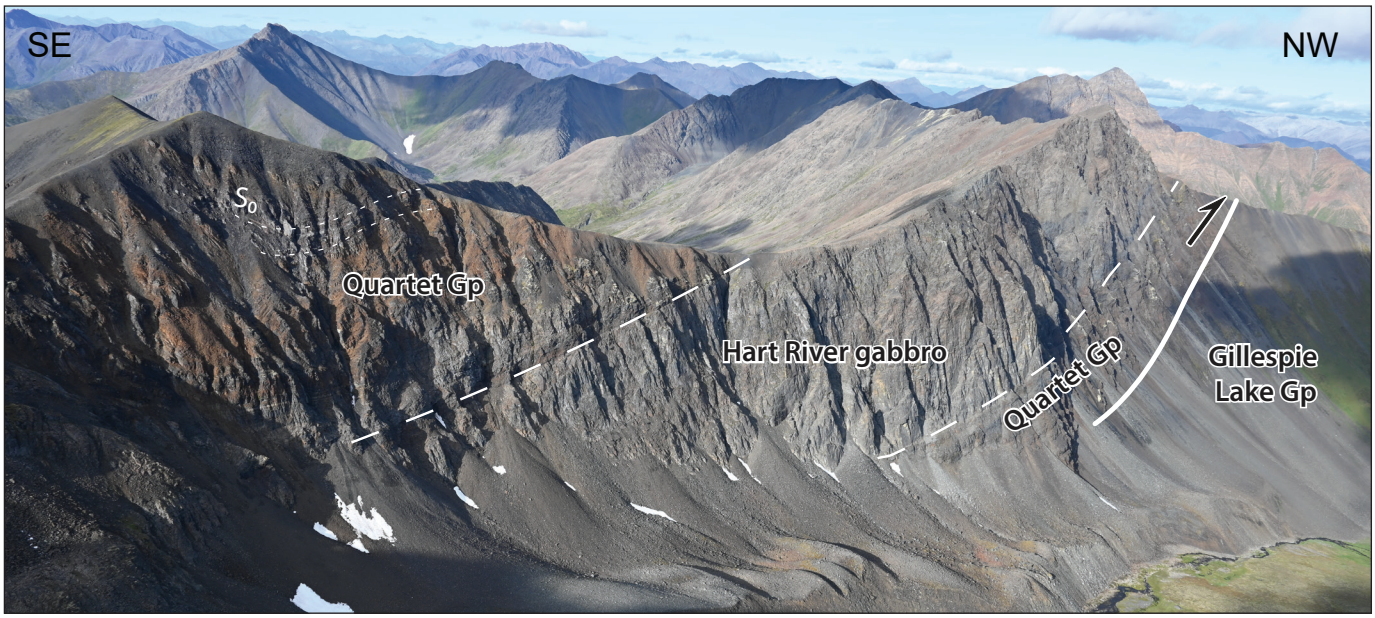

Figure 11. *Quartet Group intruded by Hart River gabbro and thrust faulted over the Gillespie Lake Group. Photo taken in the northwest part of the map area. Solid line indicates thrust fault. Thick dashed line indicates intrusive contact. Thin dashed line in Quartet Group indicates bedding.*

otherwise appear similar to the Hart River sills. The original igneous mineralogy of the dikes is dominated by plagioclase with lesser amounts of clinopyroxene, olivine and opaque minerals (Fig. 12c). Clinopyroxene has been replaced by chlorite and plagioclase has been altered to saussurite and sericite (Fig. 12c). A subset of dikes of dikes are plotted on Figure 3. Many of the dikes occur in cliff faces and thus their orientation is approximate. The precise age of the dikes is unknown; they are only constrained to be younger than the <1640 Ma Wernecke Supergroup rocks that they intrude (Furlanetto et *al.*, 2013). The consistent orientation (Fig. 3) and lack of evidence of folding (Fig. 12b) and thrusting suggests the dikes postdate the dominant phase of deformation of the Wernecke Supergroup. A single dike mapped by Ambrose (2020) to the south has similar composition and orientation and intrudes the Rapitan Group. If this dike is related to the east-west striking dikes mapped north of Rusty Mountain, then these dikes may be Neoproterozoic or younger.

Porphyritic dike

A 30 cm wide, medium-grey weathering, porphyritic dike was observed at one locality to the east of the North Rackla River (Figs. 3 and 13). Pervasive carbonate alteration makes determining the primary mineralogy of this dike difficult. It consist of a fine-grained spongy matrix and phenocrysts or xenocrysts up to ~5 mm across that are replaced by carbonate (Fig. 13b). This dike is petrographically distinct from the Hart River sills and the east–west dikes.

Geochemistry of Intrusive Rocks

Thirteen mafic intrusive samples collected over two field seasons were selected for geochemical analyses (Table 1). Two samples were filtered out due to alteration (LOI >5%). Of the remaining samples, 5 are from Hart River sills and 6 are from the east–west striking mafic dikes.

Results for our Hart River samples are compared with those of Verbaas et *al.* (2018; grey triangles) on the modified Zr/Ti *vs.* Nb/Y diagram of Pearce (1996; after Winchester and Floyd, 1977; Fig. 14a). All samples plot in the basalt field and overlap with those published by Verbaas et *al.* (2018). In contrast, most samples of the east-west striking dikes plot within the alkali basalt field, with the exception of sample 20TA005 which plots in the basalt field.

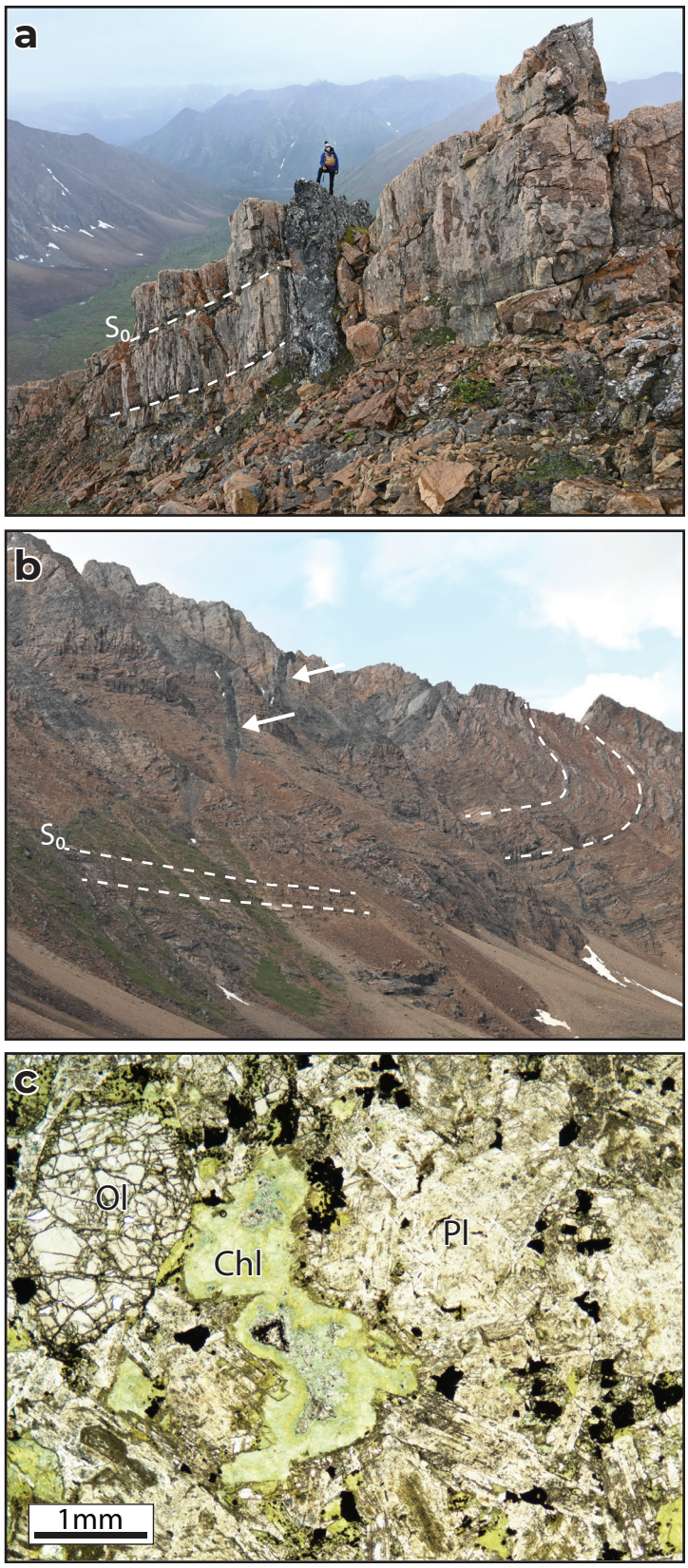

Spider plots presented in Figure 14b further illustrate the geochemical distinction between the Hart River gabbro and the east-west striking dikes. The Hart River sills are characterized by flat trace-element profiles that are similar to mid-ocean ridge basalt. Sample 20TA106-2 has a distinct, more enriched trace element profile with slight positive Nb and Ti anomalies compared to the other Hart River samples. Overall, the trace-element patterns of Hart River samples compare well with those of Verbaas et *al.* (2018).

In contrast, the east-west striking dikes have trace-element signatures similar to ocean island basalt (OIB), with negative slopes, generally slightly positive Nb anomaly, and a slight negative Ti anomaly (Fig. 13b). Sample 20TA005 is distinct with a slightly more depleted trace-element pattern and a negative Nb anomaly.

Structure

The dominant structures in the Wernecke Supergroup are oriented approximately perpendicular to structures in younger strata (Fig. 15). As mentioned above, Wernecke Supergroup strata are primarily exposed in the northern part of the map, whereas younger rocks are exposed in the south. Thus, the distinct orientation of structures may reflect either spatial domains or multiple phases of deformation.

Figure 12. *Field photographs and photomicrograph of east-west striking dikes.* ***(a)*** *Thin (~2 m wide) mafic dike intruded into thick-bedded silty dolostone of the Gillespie Lake Group. Looking east.* ***(b)****Thin mafic dike (white arrows) cutting folded Gillespie Lake dolostone. Dashed white lines mark bedding.* ***(c)*** *Plain-polarized photomicrograph showing olivine (Ol), chlorite (Chl), plagioclase (Pl) and opaque minerals.*

Table 1. *Geochemical analyses for intrusive rocks from the Rusty Mountain area.*

	Hart River sills and dikes					east-west striking dikes					
Sample Number	19TA039-2	19TA053-1	19TA211	20TA106-2	20TA019-1	20TA004	20TA005	20TA010	20TA029-2	20TA137-1	20TA151
Lat.	64.317	64.342	64.327	64.458	64.379	64.411	64.415	64.417	64.453	64.439	64.448
Long.	-133.675	-133.761	-133.914	-133.892	-133.738	-133.713	-133.739	-133.720	-133.735	-133.859	-133.919
SiO_2	49	48.49	48.21	47.87	47.84	45.77	49.88	45.38	47.44	44.69	44.81
Al_2O_3	13.94	13	14.32	11.68	14.92	14	12.84	15.22	15.08	14.8	14.27
Fe_2O_3	14.83	12.58	9.65	21.96	9.67	15.06	15.82	14.59	13.64	10.43	14.26
MnO	0.31	0.19	0.15	0.31	0.19	0.25	0.2	0.05	0.16	0.17	0.16
MgO	6.3	7.89	8.53	2.91	7.64	4.86	4.64	5.63	5.44	5.74	4.72
CaO	7.16	10.5	11.75	4.86	14.15	8.49	6.97	4.53	5.2	11.15	10.05
Na_2O	3.01	2.12	2.21	3.39	1.61	3.28	3.48	3.03	2.82	2.98	1.83
K_2O	1.14	1.42	1.04	0.42	0.8	1.68	1.52	4.19	3.21	1.62	2.04
TiO_2	1.28	1.04	0.66	3.74	0.77	2.41	2.73	2.45	2.61	2.03	2.57
LOI	2.15	1.8	2.22	2.02	1.61	2.97	1.49	3.68	3.11	4.55	4.11
TOTAL	99.52	99.72	99.09	100.95	99.52	99.99	100.3	100.3	100.3	99.39	100.05
Th	0.48	0.46	0.28	1.16	0.34	7.47	4.39	7.53	8.08	6.16	8.42
Nb	3.8	2.7	1.6	11.5	2.5	65.1	13.4	68	64.2	59.5	80.5
La	4.1	3.1	2.2	8.8	2.9	58.5	17.6	60.2	61.7	49.6	64.4
Ce	10.8	8.6	5.8	23.2	7.2	116	41.2	119	122.5	96.4	126
Pr	1.52	1.22	0.86	3.41	1.1	13.55	5.51	13.55	14.1	11	14.4
Nd	7.4	6.2	4.3	17.3	5.5	52.5	24.8	52.2	55.1	42.5	56.1
Sm	2.32	2.1	1.52	5.34	1.63	9.95	6.41	9.96	10.1	8.16	10.5
Zr	62	50	32	153	40	228	210	218	243	190	257
Hf	1.7	1.4	0.9	4.2	1.1	5.5	5.7	4.8	5.6	4.3	5.7
Eu	0.87	0.88	0.53	1.93	0.68	2.79	1.78	2.82	2.99	2.24	2.7
Gd	3.17	3.09	2.03	6.37	2.3	8.79	7.48	7.99	8.83	6.9	9.02
Tb	0.55	0.48	0.33	1.12	0.4	1.29	1.3	1.21	1.21	1.04	1.31
Dy	3.18	3.05	2.17	7.15	2.82	7.8	8.54	6.6	7.07	6.17	7.65
Y	18.8	17.5	12.5	37.7	13.3	37.1	44.3	32.7	33.1	28.9	37.3
Er	2.08	2.01	1.44	4.11	1.61	3.96	4.96	3.43	3.69	3.28	3.96
Yb	1.84	1.91	1.27	3.92	1.4	3.55	4.41	2.95	3.05	2.74	3.47
Lu	0.26	0.27	0.19	0.6	0.19	0.51	0.7	0.41	0.43	0.42	0.47

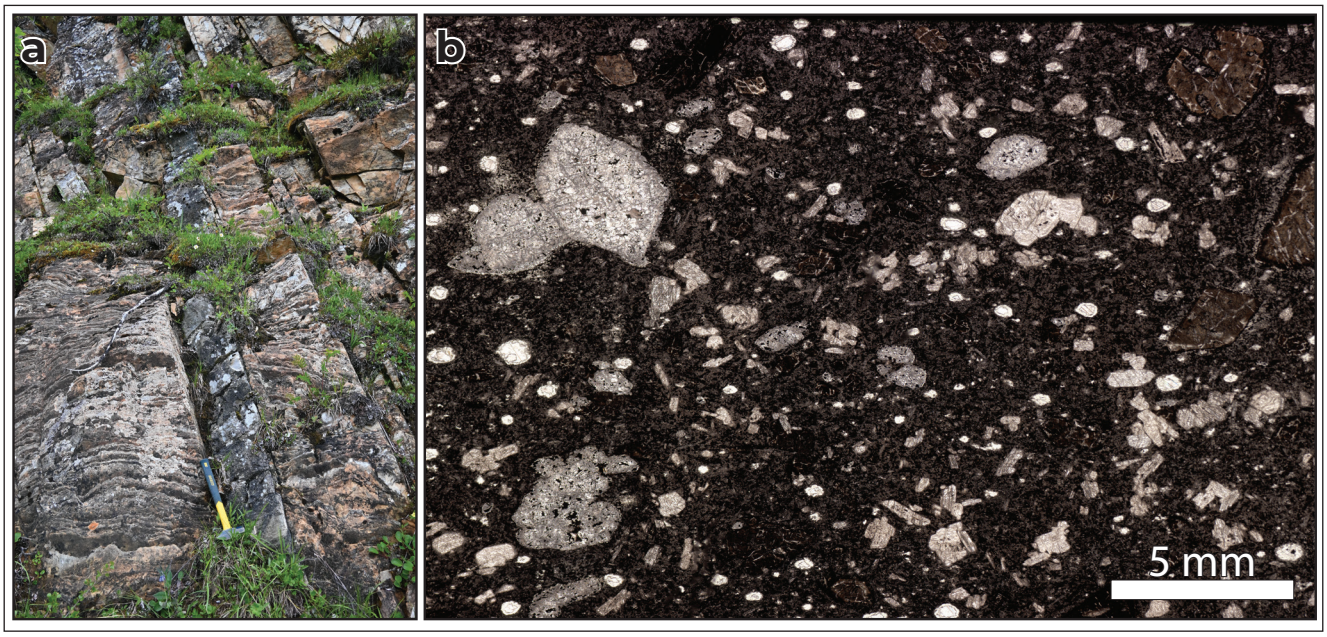

Figure 13. (a) *Field photograph and* **(b)** *thin section slide scan (PPL) of a medium-grey, 30 cm thick, intensely carbonate altered, porphyritic dike cutting Gillespie Lake Group dolostone.*

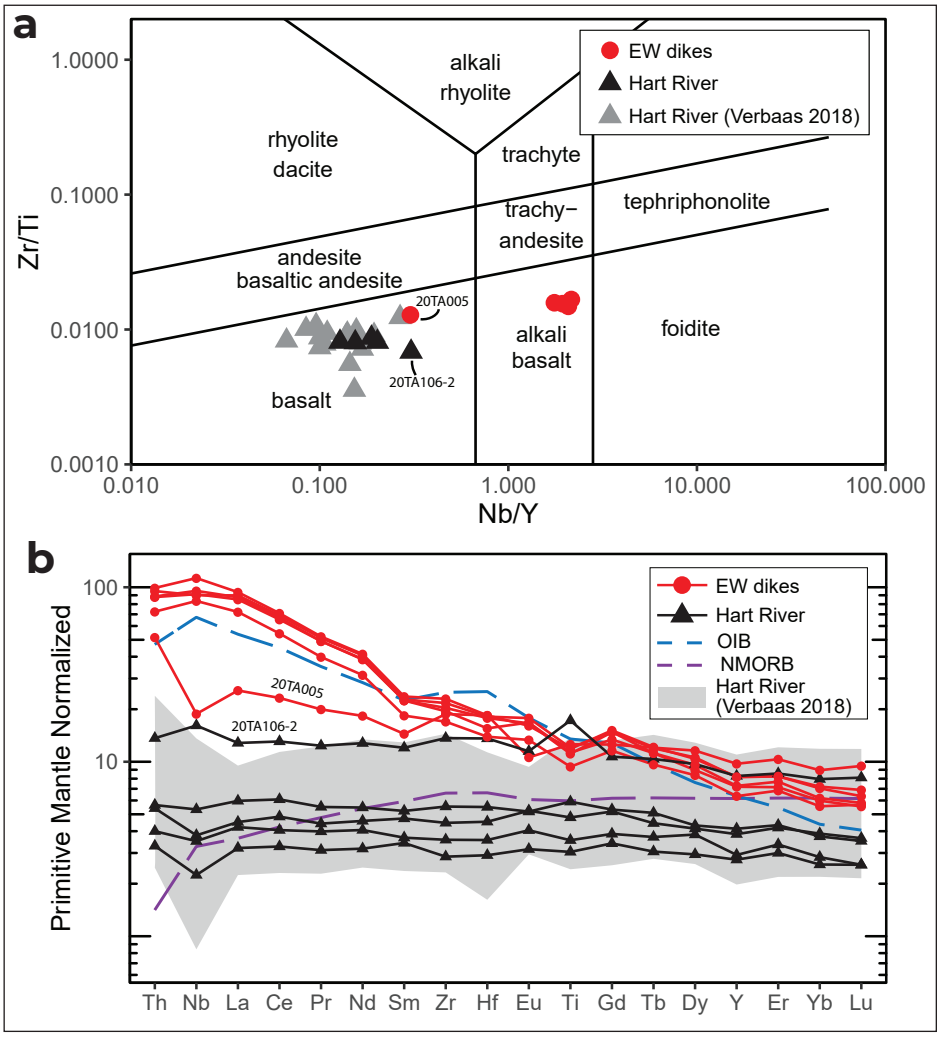

Figure 14. *Trace-element geochemical diagrams for Hart River sills and east-west striking dikes.* ***(a)*** *Modified Winchester and Floyd (1977) diagram of Pearce (1996). For comparison, samples from Verbaas et al. (2018) are plotted as grey triangles.* ***(b)*** *Immobile trace-element patterns normalized to primitive mantle values (Sun and McDonough, 1989). See text for discussion on samples 20TA005 and 20TA106-2 (labelled). The range of compositions of Hart River samples from Verbaas et al. (2018) is shown in grey. Values for ocean island basalt (OIB) and normal mid-ocean ridge basalt (N-MORB) are from Sun and McDonough (1989).*

Northwest-verging folding and thrusting

The dominant structures in the Wernecke Supergroup are oriented southwest-northeast (Fig. 15). Folds range from gentle to close and are generally upright, but locally inclined (Figs. 9a, 12b and 16). Folds are typically shallowly plunging and have steeply dipping axial planes (Fig. 15). Outcrop-scale folds are locally abundant, but generally uncommon in Wernecke Supergroup rocks (Fig. 15). A steeply dipping, northeast-southwest striking, penetrative cleavage is variably developed within the Quartet Group and silty intervals of the Gillespie Lake Group. Sedimentary structures, which are common in the Gillespie Lake Group, show that bedding is generally right way up and rarely overturned on the short limb of asymmetric folds.

The Wernecke Supergroup is imbricated by northwest-verging thrust faults (Figs. 3, 11, 16 and 17), consistent with fold orientations (Fig. 15). These thrusts place dark-weathering siliciclastic rocks of the Quartet Group over recessive carbonate and siliciclastic rocks of the Gillespie Lake Group (Figs. 11 and 17). Where exposed, the thrusts are bedding parallel and only evident from the repetition of stratigraphy. In each instance, a sill of Hart River gabbro intrudes the Quartet Group rocks 100–200 m above the thrust (Figs. 10, 15 and 17). As also demonstrated by Roots (1990) to the west, the Hart River sills do not cut the thrusts, suggesting that thrusting post dates the ca. 1380 Ma intrusions.

Northeast-southwest folding

The dominant structures in Pinguicula Group and younger rocks are oriented southeast-northwest (Fig. 15). A steeply dipping penetrative cleavage is variably developed in the Mount Landreville and Pass Mountain formations and Rapitan Group. Outcrop-scale folds are rare in Pinguicula Group rocks and not observed in younger rocks (Fig. 15; Ambrose and Bowie, 2020). Folds are typically gentle and upright, with a

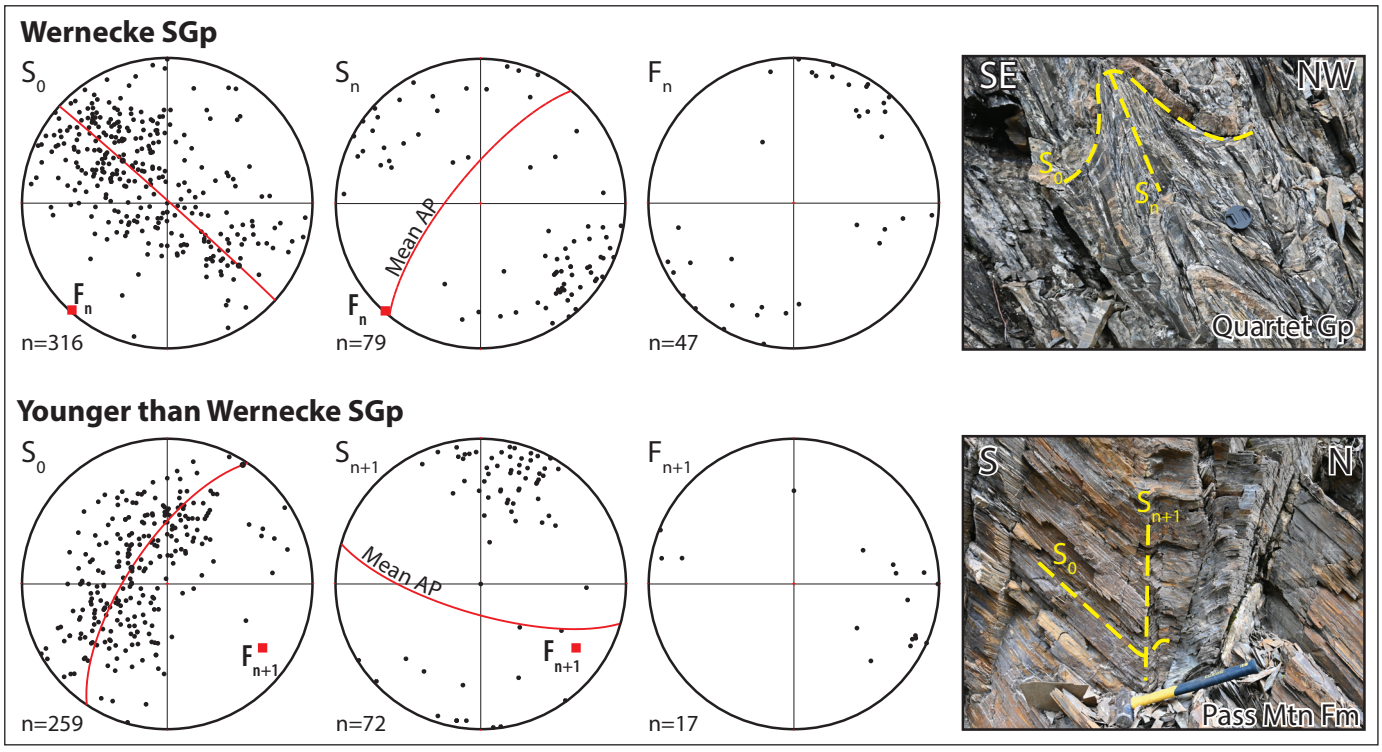

Figure 15. *Structural data plotted on lower hemisphere, equal area stereonets and examples of small-scale folds. Measurements and photo are split into two groups: Wernecke Supergroup and younger than Wernecke Supergroup. Top photograph is of Quartet Group siltstone, and bottom is of Pass Mountain Formation dolomitic limestone.*

mean fold axis that plunges gently to the southeast, and a mean axial plane that dips steeply to the southwest (Fig. 14), consistent with northeast-southwest directed shortening that is approximately perpendicular to the orientation of folding and thrusting in the older units (Fig. 14).

Late faulting

The map area is also cut by late, steeply dipping, strike-slip and normal faults (Fig. 3). A major, north-south striking, normal fault runs through the centre of the map area for ~30 km. In the south, this separates Mesoproterozoic Pinguicula Group rocks to the east from Neoproterozoic and Paleozoic rocks to the west. In the central part of the map area, near Rusty Mountain, the fault coincides with the Rackla River and separates the Wernecke Supergroup to the east from Pinguicula and Quartet group rocks to the west. In the northern part of the map area, where it roughly coincides with the North Rackla River, the fault separates the Gillespie Lake Group in the east from thrust imbricated Quartet Group, Gillespie Lake Group and Hart River suite rocks

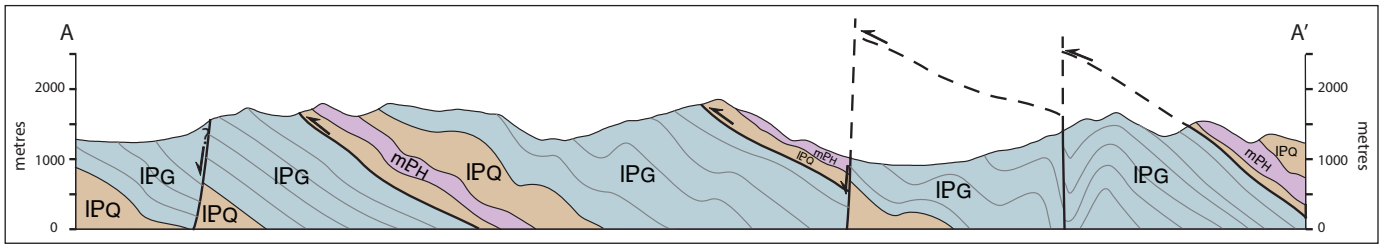

Figure 16. *Cross section illustrating structural and stratigraphic relationships. Location is indicated on Figure 3. See Figure 3 for legend.*

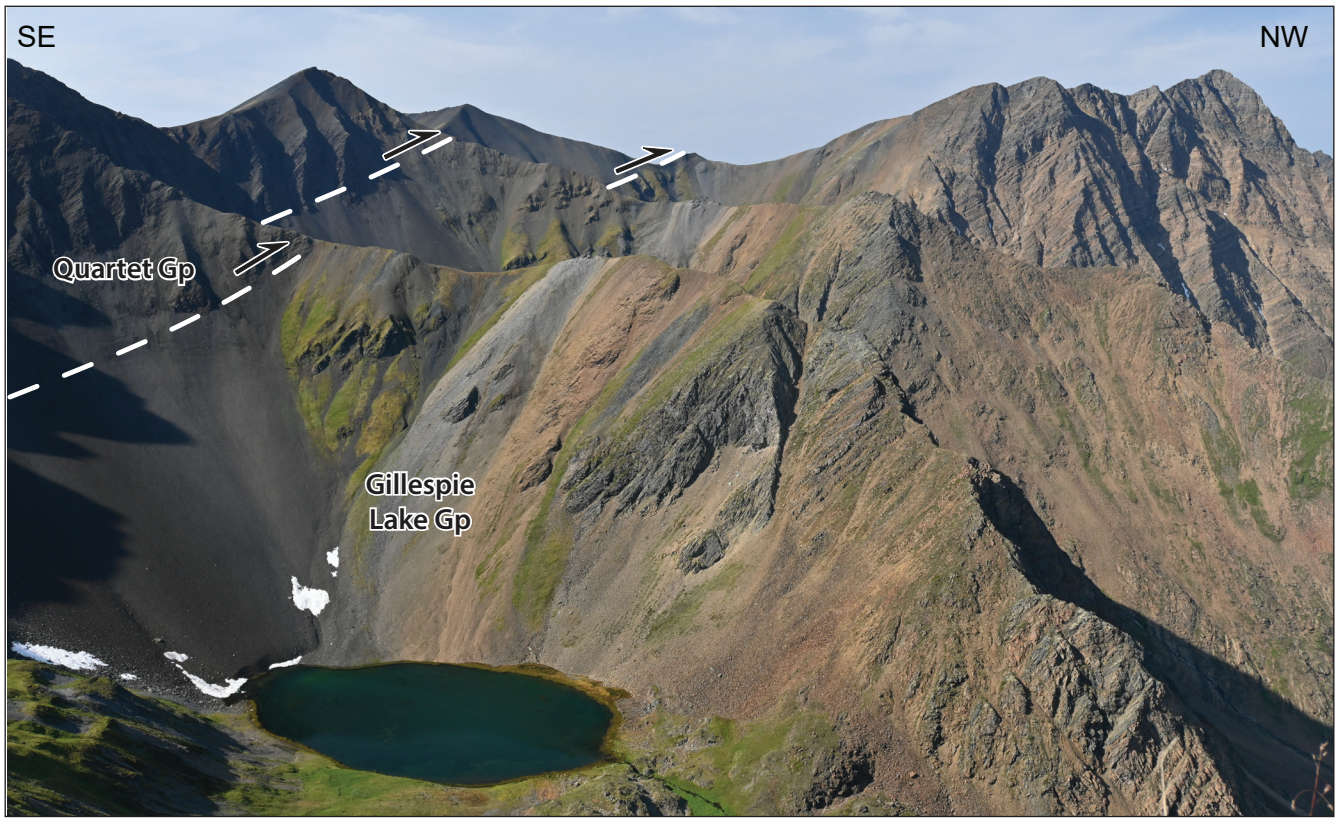

Figure 17. *Field photograph illustrating structural relationships in the northwest part of the map area. Quartet Group siliciclastic rocks thrust over recessive, mixed dolostone and siliciclastic rocks of the Gillespie Lake Group silty.*

to the west. Another major fault that runs east–west through the southern part of the map area separates the Mount Landreville and Pass Mountain formations to the north from younger rocks to the south.

Steeply dipping, northeast-southwest striking faults are common within the Gillespie Lake Group in the northeastern part of the map area (Fig. 3). The faults are highlighted by discrete breaks in bedding orientation and the offset of grey weathering intervals of siliciclastic rocks (Fig. 9a). These faults have a similar strike to the northwest-verging structures mapped west of the North Rackla River (Fig. 3).

Mineralization

The map area contains several notable mineral occurrences. The most significant mineralization is centred on the Vera (Yukon MINFILE 106C 083, 114 and 137–148), North Rackla (Yukon MINFILE 106C 088, 108 and 110–113), and "Val" (Yukon MINFILE 106C 085, 115–119, 131, 133–136, 149 and 150) occurrences (Fig. 3).

The main Vera occurrences comprise Pb-Zn-Ag mineralization hosted in red weathering, brecciated, stromatolitic and microbially laminated dolostone of the Gillespie Lake Group. Mineralization includes quartz-carbonate veins that contain massive and disseminated sphalerite, galena, chalcopyrite and tetrahedrite (Sivertz, 1985). Veins with Pb-Zn-Ag mineralization also occur within and adjacent to Hart River sills that intrude siliciclastic rocks of the Quartet Group (Kammerer and Eaton, 2011). Vera has a historical resource estimate of 392 667 t at 607.0 g/t Ag, 3.18% Pb and 3.47% Zn (Casselman, 2018).

As with the Vera occurrences, the most significant Pb-Zn-Ag mineralization at North Rackla occurs within the Gillespie Lake Group. Mineralization consists of a steeply dipping zone of massive sphalerite and galena within red-weathering stromatolitic and microbially laminated dolostone. The mineralized zone is adjacent to an interval of darker weathering dolomitic siltstones and mudstones, such as those shown in Fig. 9a.

A collection of Pb-Zn-Ag occurrences, commonly referred to as Val, lie to the south of Rusty Mountain (Fig. 3). Mineralization at the main group of Val occurrences (near the Big Red zone; Yukon MINFILE 106C 115) consists primarily of massive and disseminated sphalerite, galena and tetrahedrite within breccia zones and sparry dolomite veins of the Rubble Creek Formation (Sivertz, 1980; Kammerer and Eaton, 2011). To the north, at the Siltstone occurrence (Yukon MINFILE 106C 135), sphalerite, galena, tetrahedrite and chalcopyrite occur within quartz-carbonate veins that cut fine-grained siliciclastic rocks of the Mount Landreville Formation. Val has a historical resource estimate of 19 964 t at 1029 g/t Ag, 26.7% Pb and 7.3% Zn (Casselman, 2018).

Acknowledgements

Thanks to Amanda O'Connor and Sarah Bowie for assistance in the field, and David Moynihan and Maurice Colpron for insightful discussion. A thorough review by Maurice Colpron substantially improved the manuscript. Thanks to Horizon Helicopters and Alkan Air for transport to the field, and Cantex for logistical support.

References

Abbott, J.G., 1997. Geology of the Upper Hart River Area, Eastern Ogilvie Mountains, Yukon Territory (116A/10, 116A/11). Exploration and Geological Services Division, Yukon Region, Indian and Northern Affairs Canada, Bulletin 9, 92 p.

Ambrose, T., 2020. Preliminary bedrock geology map of the southern Rusty Mountain area, southern Wernecke Mountains, Yukon (parts of NTS 106C/4, 5 and 106D/1, 8). Yukon Geological Survey, Open File 2020-2, scale 1:50 000.

Ambrose, T. and Bowie, S., 2020. Preliminary report on the bedrock geology of the Rackla River area, southern Wernecke Mountains, Yukon (parts of NTS 106C/4, 5 and 106D/1, 8). *In*: Yukon Exploration and Geology 2019, K.E. MacFarlane (ed.), Yukon Geological Survey, p. 1–21.

Blusson, S.L., 1974a. Five geological maps of northern Selwyn Basin (Operation Stewart), Yukon Territory and District of Mackenzie (105N, O; 106A, B, C). Geological Survey of Canada, Open File 205, scale 1:250 000.

Blusson, S.L., 1794b. Six geological maps of Nadaleen River map-area, Yukon Territory and District of Mackenzie, N.W.T. (106C/06; 106C/07; 106C/10; 106C/11; 106C/13; 106C/15). Geological Survey of Canada, Open File 206, scale 1:50 000.

Casselman, S. (compiler), 2018. Yukon Mineral Deposits Summary 2018. Yukon Geological Survey, 30 p.

Colpron, M., Israel, S., Murphy, D., Pigage, L. and Moynihan, D., 2016. Yukon bedrock geology map. Yukon Geological Survey, Open File 2016-1, scale 1:1 000 000.

Delaney, G.D., 1981. The mid-Proterozoic Wernecke Supergroup, Wernecke Mountains, Yukon Territory. *In*: Proterozoic Basins of Canada, F.H.A. Campbell (eds.), Geological Survey of Canada, Paper 81-10, p. 1–23.

Eisbacher, G.H., 1978. Two major Proterozoic unconformities, northern Cordillera. Geological Survey of Canada, Current Research Part A, Paper 78-1A, p. 53–58.

Eisbacher, G.H., 1981. Sedimentary tectonics and glacial record in the Windermere Supergroup, Mackenzie Mountains, northwestern Canada. Geological Survey of Canada, Paper 80–27, 40 p., https://doi.org/10.4095/119453.

Estève, C., Audet, P., Schaeffer, A.J., Schutt, D., Aster, R.C. and Cubley, J., 2020. The upper mantle structure of Northwestern Canada from teleseismic body wave tomography. Journal of Geophysical Research, Solid Earth, vol. 125, https://doi.org/10.1029/2019JB018837.

Furlanetto, F., Thorkelson, D.J., Daniel Gibson, H., Marshall, D.D., Rainbird, R.H., Davis, W.J., Crowley, J.L. and Vervoort, J.D., 2013. Late Paleoproterozoic terrane accretion in northwestern Canada and the case for circum-Columbian orogenesis. Precambrian Research, vol. 224, p. 512–528, https://doi.org/10.1016/j.precamres.2012.10.010.

Jeletsky, J.A., 1962. Pre-Cretaceous Richardson Mountains Trough – its place in the tectonic framework of Arctic Canada and its bearing on some geosynclinals concepts. Transactions of the Royal Society of Canada, vol. 56, p. 55–84.

Kammerer, M. and Eaton, W.D., 2011. Geological mapping, prospecting and geochemical sampling at the Rusty Property. Yukon Energy, Mines and Resources Assessment Report 95720.

Medig, K., 2016. Sedimentology, Geochemistry, and Geochronology of unit PR1 of the lower Fifteenmile group and the Pinguicula Group, Wernecke and Ogilvie Mountains, Yukon, Canada: Mesoproterozoic environments and paleocontinental reconstructions. Unpublished PhD thesis, Simon Fraser University, Vancouver, British Columbia, Canada.

Medig, K.P.R., Thorkelson, D.J., Turner, E.C., Davis, W.J., Gibson, H.D., Rainbird, R.H. and Marshall, D.D., 2012. The Proterozoic Pinguicula Group, Wernecke Mountains, Yukon: A siliciclastic and carbonate slope to basin succession with local and exotic sediment provenance. *In*: Yukon Exploration and Geology 2011, K.E. MacFarlane and P.J. Sack (eds.), Yukon Geological Survey, p. 129–149.

Medig, K.P.R., Turner, E.C., Thorkelson, D.J. and Rainbird, R.H., 2016. Rifting of Columbia to form a deep-water siliciclastic to carbonate succession: The Mesoproterozoic Pinguicula Group of northern Yukon, Canada. Precambrian Research, vol. 278, p. 179–206, https://doi.org/10.1016/j.precamres.2016.03.021.

Moynihan, D.P., Strauss, J.V., Nelson, L.L. and Padget, C.D., 2019. Upper Windermere Supergroup and the transition from rifting to continent-margin sedimentation, Nadaleen River area, northern Canadian Cordillera. GSA Bulletin, vol. 131, issue 9–10, https://doi.org/10.1130/B32039.1.

Mustard, P.S., Roots, C.F. and Donaldson, J.A., 1990. Stratigraphy of the middle Proterozoic Gillespie Lake Group in the southern Wernecke Mountains, Yukon. Geological Survey of Canada, Current Research Part E, Paper 90-1E.

Pearce, J.A., 1996. A user's guide to basalt discrimination diagrams. *In:* Trace Element Geochemistry of Volcanic Rocks: Applications for Massive Sulphide Exploration, D.A. Wyman (ed.), Geological Association of Canada, Short Course Notes, vol. 12, p. 79–113.

Roots, C.F., 1990a. Geology of 106D/8 and 7 (East half) map areas. Yukon Geological Survey, Open File 1990-3, scale 1:50 000.

Roots, C. F., 1990b. New geological maps for the southern Wernecke Mountains, Yukon. Geological Survey of Canada, Current Research Part E, Paper 90-IE, p. 5–13.

Sivertz, G.W., 1980. Assessment Report on Geology, Geochemistry and Drilling at Val 1-318 Claims. Yukon Energy, Mines and Resources Assessment Report 090511.

Sivertz, G.W., 1985. Summary Report on the Val-Vera Property, Kathleen Lakes Area, Yukon Territory. Yukon Energy, Mines and Resources Assessment Report 062208.

Sun, S.-S. and McDonough, W.F., 1989. Chemical and isotopic systematics of oceanic basalts: implications for mantle composition and processes. Geological Society, London, Special Publications, vol. 42, p. 313–345, https://doi.org/10.1144/GSL.SP.1989.042.01.19.

Thorkelson, D., 2000. Geology and Mineral Occurrences of Slats Creek, Fairchild Lake and "Dolores Creek" Areas, Wernecke Mountains (106D/16, 106C/13, 106C/14), Yukon Territory. Exploration and Geological Services Division, Yukon, Indian and Northern Affairs Canada, Bulletin 10, 73 p.

Turner, E.C., 2011. Stratigraphy of the Mackenzie Mountains Supergroup in the Wernecke Mountains, Yukon. *In*: Yukon Exploration and Geology 2010, K.E. MacFarlane, L.H. Weston and C. Relf (eds.), Yukon Geological Survey, p. 207–231.

Verbaas, J., Thorkelson, D.J., Milidragovic, D., Crowley, J.L., Foster, D., Daniel Gibson, H. and Marshall, D.D., 2018. Rifting of western Laurentia at 1.38 Ga: The Hart River sills of Yukon, Canada. Lithos, vol. 316–317, p. 243–260, https://doi.org/10.1016/j.lithos.2018.06.018.

Winchester, J.A. and Floyd, P.A., 1977. Geochemical discrimination of different magma series and their differentiation products using immobile elements. Chemical Geology, vol. 20, p. 325–343.

Yukon MINFILE, 2019. Yukon MINFILE – A database of mineral occurrences. Yukon Geological Survey, https://data.geology.gov.yk.ca, [accessed November 2019].

Preliminary investigation of geological controls on radon concentration in surficial sediment in Whitehorse, Yukon (NTS 105D/11, 14)

Michael J. Kishchuk* and John C. Gosse
Department of Earth and Environmental Sciences, Dalhousie University

Panya S. Lipovsky and Jeffrey D. Bond
Yukon Geological Survey

Kishchuk, M.J., Lipovsky, P.S., Bond, J.D. and Gosse, J.C., 2021. Preliminary investigation of geological controls on radon concentration in surficial sediment in Whitehorse, Yukon (NTS 105D/11, 14). *In:* Yukon Exploration and Geology 2020, K.E. MacFarlane (ed.), Yukon Geological Survey, p. 115–135.

Abstract

Although the presence of radon has been reported in Yukon, the controls on radon soil gas fluxes in Yukon have not been studied. Here we report 328 radon concentration measurements collected in surficial sediment at 30 sites throughout Whitehorse during the summer of 2020 for the purpose of examining the controlling factors. The sediment types include till, glaciofluvial sand and gravel, glaciolacustrine silt, fluvial sand and gravel, and eolian sand. Average radon concentrations were compared to bedrock lithology, thickness of surficial sediment, surficial sediment type, surficial sediment grain size distribution, sorting, sediment maturity, and soil moisture to determine the first-order geological controls. Pronounced interseasonal variation was observed, but intraseasonal summer readings were relatively consistent. Positive correlation is apparent between radon concentration and grain size distribution, as well as between radon concentration and soil moisture. Negative correlation is observed between radon concentration and sediment maturity, with till and weathered bedrock displaying the highest concentrations of radon. No appreciable correlation was observed with depth to bedrock or with bedrock type. Additional data are being collected to complete the analyses in order to establish which geological and environmental factors are primary controls on radon concentration in near surface sediments.

* *mc723665@dal.ca*

Introduction

Radon is a colourless, odourless carcinogenic gas which occurs naturally in soil and rock, and which may enter homes via openings and cracks in foundations. While not dangerous in outdoor settings where it quickly dissipates, radon poses a major public health hazard when it accumulates in poorly ventilated basements. As of 2018, nearly 4400 Yukon homes have been tested for indoor radon, with more than 3300 measurements in the greater Whitehorse area (Yukon Housing Corporation, 2018). Of these, some 17 of 44 subdivisions (Fig. 1) have average indoor concentrations of radon gas higher than Health Canada's guideline of 200 Bq m^{-3} (Government of Canada, 2020). World Health Organization (WHO) guidelines are even lower, recommending mitigation if indoor radon concentration exceeds 100 Bq m^{-3}.

While many international studies accept that bedrock uranium concentration is the strongest control on radon concentration in urban regions (e.g., Stanley *et al.*, 2019; Cinelli *et al.*, 2015), attention must also be given to the overlying surficial sediment. This is particularly important in areas where sediment cover is thicker than the diffusion distance of radon over its radioactive lifetime (the half-life of ^{222}Rn is 3.8 days, (Marin, 1956)). In these areas, the physical and chemical properties of the surficial cover could potentially be significant controls on radon flux. Additionally, while uranium concentration in the Whitehorse suite of granitoid rocks is generally low (Yukon Geological Survey, 2020b), high indoor radon values have been measured, potentially indicating non-granitoid radon sources.

This study aims to compare the effect of several geological and meteorological controls on spatial and temporal variability in the flux of soil radon gas, with a long-term goal of understanding how to better predict and mitigate risks associated with radon. In Canada, radon is considered a carcinogen (Government of Canada, 2020) and, after inhalation, its pulmonary effect is compounded when the decay of gaseous ^{222}Rn produces heavy metals ^{210}Po, ^{214}Pb, ^{214}Bi and ^{214}Po. These heavy metals adhere to aerosols and accumulate in the lungs where in turn they produce alpha, beta and gamma radiation (Porstendorfer, 1994). Knowledge of radon source and distribution is necessary to inform public health policy, such as building codes and workplace conditions. By measuring radon in different representative undisturbed natural sediment types, and by documenting which factors have first-order control on soil radon flux variability, we can establish where and when radon exceeds concentration guidelines, and can more accurately predict radon concentration in untested regions of the territory.

The Yukon Geological Survey (YGS) is working to better understand the distribution of radon in surficial materials. The objective of this study is to determine if there is temporal or spatial variability of radon concentration at sites undisturbed by anthropogenic modification and if so, what factors control that variability. Our preliminary results reveal that temporal variation occurs seasonally, and that spatial variation is at least partly controlled by sediment grain-size distribution and maturity. Since the composition and thickness of surficial deposits throughout Yukon are non-uniform, these findings may warrant consideration in future building codes and health policies regarding radon gas.

Background

Geologic setting

Bedrock geology

Four major bedrock lithologic units underlie the Whitehorse area (Hart and Radloff, 1990; Colpron, 2011; and Yukon Geological Survey, 2020a): the limestone Hancock member and the clastic sedimentary Mandanna member of the Aksala formation; Whitehorse pluton granitic rocks; and the Miles Canyon Basalt (Fig. 2). The Hancock and Mandanna members of the Aksala formation were deposited during the upper Triassic in a coastal fluvial setting. The Hancock member is composed of massive and thickly bedded limestone with some dolostone, limestone debris flow conglomerate, and minor chert. The Mandanna member is composed of sandstone and polymictic conglomerate, along with mudstone and minor bioturbated sandstone. The Whitehorse batholith intruded these Triassic units in the mid-Cretaceous, between 112 and 105 Ma. In the study area, these rocks are characterized as medium to coarse-grained granodiorite and diorite. Uranium concentration in the Whitehorse suite varies

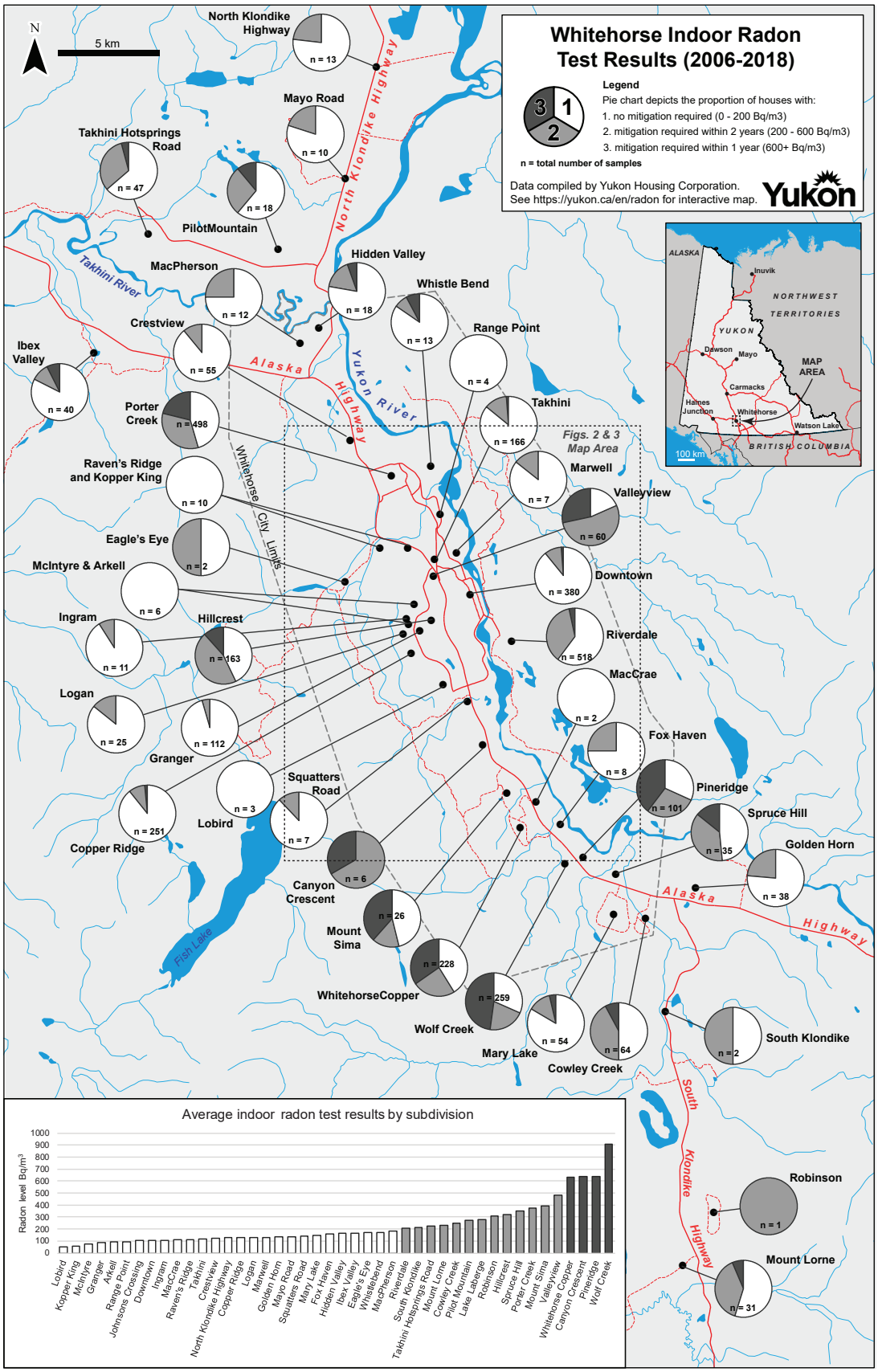

Figure 1. *Distribution and results of indoor radon tests compiled by Yukon Housing Corporation (Yukon Housing Corp., 2018). Sites in this study are located in Whistle Bend, Porter Creek, Raven's Ridge, Takhini, Granger, Copper Ridge, Riverdale, Squatters Road, Mount Sima, and Wolf Creek.*

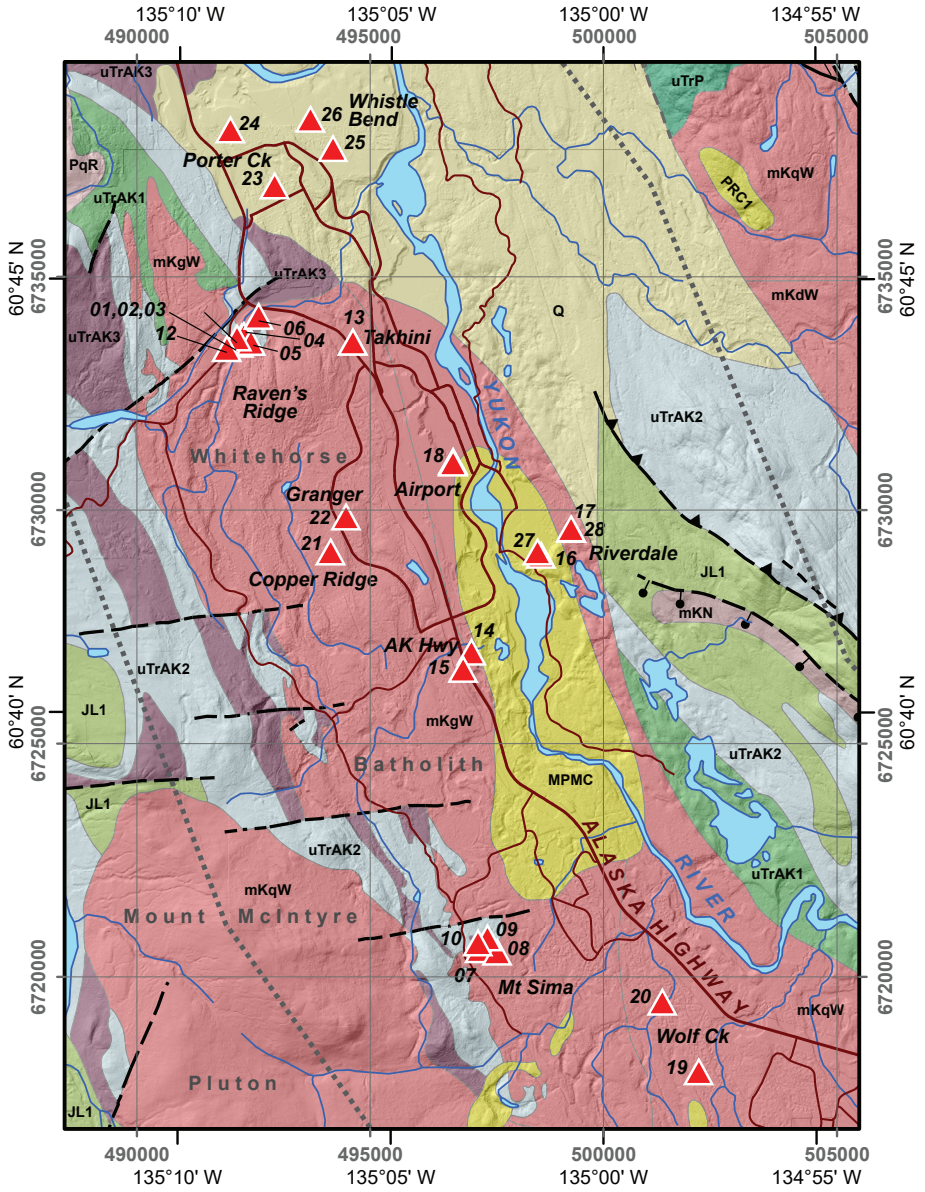

N

LEGEND

- Radon study sites
- Highway
- Primary Road
- Local Road
- Whitehorse city limits
- Watercourse
- Waterbody

FAULTS

- defined
- approximate
- inferred
- covered
- normal fault
- thrust fault

UTM NAD 83 Zone 8 Grid

0 1:150 000 scale 10 km

BEDROCK GEOLOGY (Yukon Geological Survey, 2020)

QUATERNARY
- Q: unconsolidated glacial deposits

MIOCENE TO PLIOCENE (LATE TERTIARY)
- MPMC: Miles Canyon basalt

PALEOCENE (EARLY TERTIARY)
- PRC1: Rhyolite Creek rhyolite and dacite
- PqR: Ruby Range Suite granite

MID-CRETACEOUS
- mKqW: Whitehorse Suite monzonite, granite and leucogranite
- mKgW: Whitehorse Suite granodiorite and diorite
- mKdW: Whitehorse Suite diorite
- mKN: Mount Nansen andesite to dacite

UPPER TRIASSIC
- uTrAK1: Casca shale, siltstone, sandstone, limestone
- uTrAK2: Hancock limestone
- uTrAK3: Mandanna sandstone, pebble conglomerate, mudstone
- uTrP: Povoas andesitic basalt flows, breccia, tuff, sandstone, argillite

LOWER AND MIDDLE JURASSIC
- JL1: Richtofen sandstone, siltstone, mudstone, conglomerate

Figure 2. *Bedrock geology of the Whitehorse area (Yukon Geological Survey, 2020a).*

from 2.4 to 5.2 ppm and thorium concentration varies from 10.2 to 16.2 ppm (Yukon Geological Survey, 2020b). During the Miocene and Pliocene, the Miles Canyon Basalt flowed northward from a vent near Mount Sima (Pearson *et al.*, 2001).

Surficial geology

The surficial geology of the Whitehorse area records a complex history of deposition by ice, water, and wind (Fig. 3). The McConnell Glaciation, which occurred from roughly 23.9 to 10.7 ka, was the most recent glaciation of the Whitehorse area (Bond, 2004). Ice flowed northward from the Coast Mountain and Cassiar lobes of the Cordilleran Ice Sheet and reached a glacial maximum by at least 18 ka BP. At this time, the Whitehorse valley was completely covered by ice. During deglaciation the ice underwent a fluctuating recession characterized by periods of stagnation and readvance. During periods of stagnation, several large glacial lakes formed in the Whitehorse area (Bond, 2004).

Five types of sediment were sampled in this study and classified according to their genetic origin (Bond *et al.*, 2005a–c): till, glaciofluvial sand and gravel, fine-grained glaciolacustrine sediment (sand, silt and clay), post-glacial fluvial sand and gravel, and eolian sand. Till deposits in the Whitehorse area are mostly lodgement tills, typically composed of a dense, unsorted matrix-supported diamicton deposited directly by ice, with most clasts derived from glacially-eroded bedrock, and a matrix that is predominantly sandy silt. Glaciofluvial gravels were deposited in terraces, kettled ice-contact complexes, and outwash channels as the ice receded, and typically comprise moderately sorted rounded pebbles and cobbles with a sandy matrix. A thick package of glaciolacustrine sand, silt and clay was deposited at the bottom of Glacial Lake Laberge. Dammed by ice to the south and a recessional moraine at the north end of Lake Laberge, this glacial lake occupied the Whitehorse area valley bottom during deglaciation (Brideau *et al.*, 2011). Shoreline deposits tend to be coarser and the lake sediments fine upward, reflecting the recession of the ice sheet and associated melt-water input. As Glacial Lake Laberge drained, the Yukon River delta migrated north with the shrinking shoreline, depositing a veneer of glaciofluvial sand on top of the lacustrine sediment. Winds reworked exposed riverbed sand and re-deposited it subaerially as dunes (Wolfe *et al.*, 2011). A veneer of fine-grained sandy silt loess, derived from deflation of the paraglacial surface, was also deposited over much of the study area. These deposits range from 10 to 50 cm thick. The Yukon River incised the thick glaciolacustrine deposits during the Holocene, forming sand and gravel terraces adjacent to the modern floodplain.

Radon

Sources of soil radon

Radon is a radioactive noble gas produced by the decay of radium, itself a decay product of uranium. Uranium occurs naturally, especially in granitic rocks, enriched veins, and ores such as pitchblende. Uranium-bearing rocks and minerals in surficial sediment provide a near-surface source for radon. The natural decay of uranium produces a steady supply of radon via diffusion through crystals and ejection from crystals by decay. Radon has a half-life of 3.8 days (Marin, 1956), and decays to the solid element polonium. Radon is mobile in both air and water, and can be transported to the surface through advection, dissolution in groundwater, diffusion, and passage through faults and fractured bedrock. At the surface, radon quickly dissipates in the atmosphere, and is therefore not hazardous in outdoor spaces.

Radon gas as a hazard

Radon is a recognized public health hazard (WHO 2009, Stanley *et al.* 2019) and is the second-leading cause of lung cancer in Canada. It is the leading cause of lung cancer among non-smokers, and the danger of radon lies in long-term exposure. The health risk is attributed to the radioactivity of ^{222}Rn and its radioactive daughters, which are inhaled and damage lung tissue when they decay. Health Canada recommends that remedial measures be taken to reduce radon in any dwelling to a concentration of 200 Bq m^{-3} or less (Government of Canada, 2020).

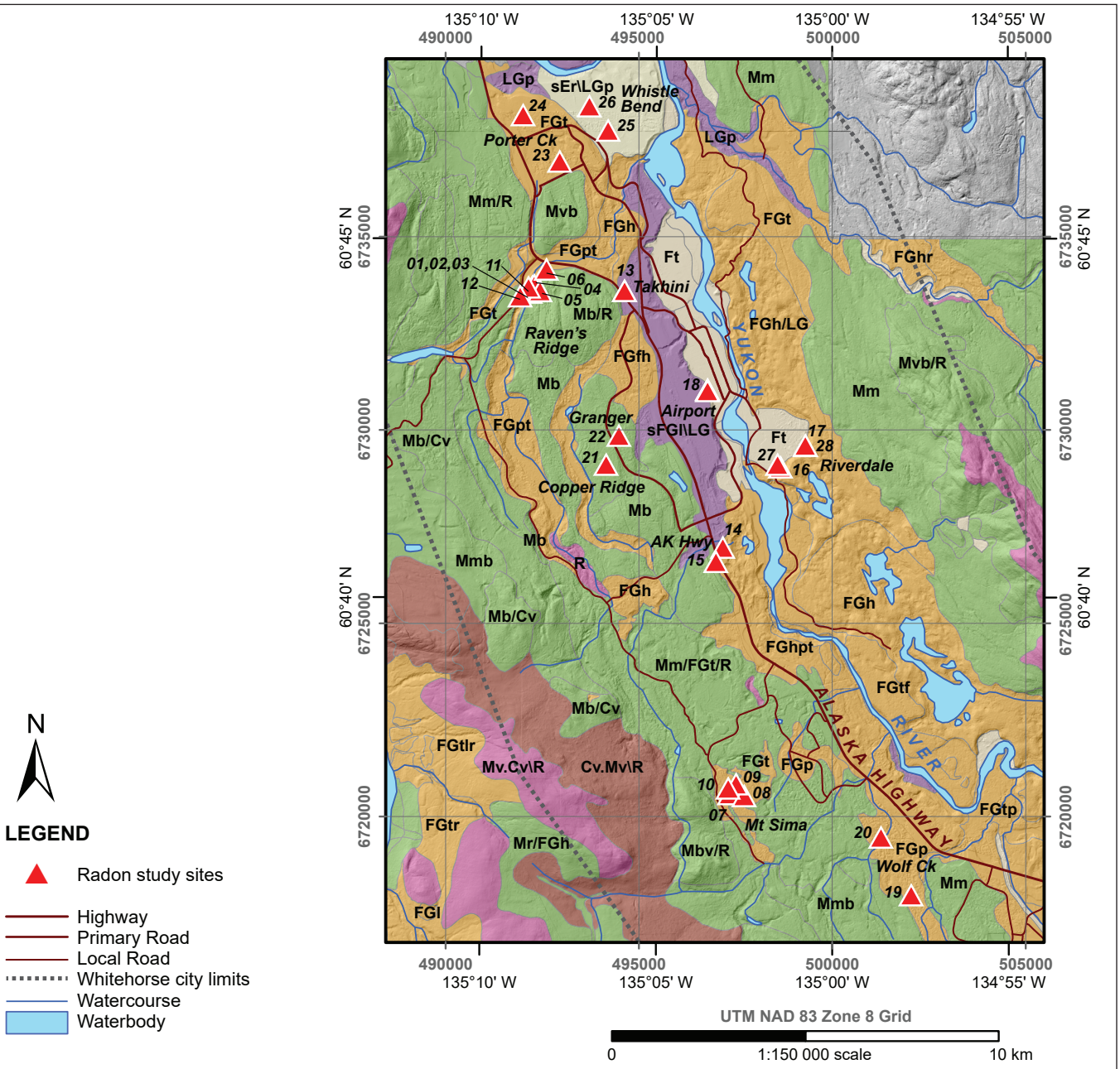

N

LEGEND

- Radon study sites
- Highway
- Primary Road
- Local Road
- Whitehorse city limits
- Watercourse
- Waterbody

SIMPLIFIED SURFICIAL GEOLOGY (modified from Bond, Morison & McKenna, 2005a,b,c)

- F: Fluvial: floodplains (Fp), terraces (Ft), fans (Ff)
- O: Organic
- E: Eolian: sand dunes (sEr), loess (zEv)
- C: Colluvial: veneer (Cv), apron (Ca)
- FG: Glaciofluvial: plain (FGp); terrace (FGt); delta (FGl)
- LG: Glaciolacustrine: plain (LGp)
- M: Moraine (Till): blanket (Mb), veneer (Mv), streamlined (Mm), ridged (Mr)
- R: Bedrock

Figure 3. *Surficial geology of the Whitehorse area (Bond et al., 2005a,b,c).*

Previous radon studies in Yukon

The YGS undertook preliminary sampling of radon concentration in sediment at three control sites (20MK-013, 014, and 015) from fall 2019 to spring 2020. The present study incorporates these results. In addition to those soil radon measurements, Yukon Housing Corporation has compiled extensive indoor radon testing results from homes in Whitehorse and other Yukon communities for the 2006–2018 period (Fig. 1; Government of Yukon, 2020). Based on data compiled for the Whitehorse area, the highest concentrations of indoor radon occur in the Wolf Creek, Canyon Crescent, Pine Ridge and Whitehorse Copper subdivisions. Moderate indoor concentrations (still exceeding the Canadian guideline) are reported in several subdivisions, including Mount Sima, Porter Creek, and Riverdale. The Yukon government has also tested schools throughout Yukon and found that radon levels exceed the recommended level in three schools (Government of Yukon, 2018). In collaboration with the Yukon Lung Association and Yukon Housing Corporation, Angela Sabo has conducted indoor winter testing in neighborhoods with high concentrations and in First Nations housing; these data have not yet been published.

Field and analytical methods

Site selection

Sample sites were selected based on the presence of unambiguous uniform bedrock and surficial sediment type, known sediment thickness, and well-constrained surficial stratigraphy (from nearby water well or borehole logs). To achieve uniform bedrock controls, best attempts were made to cluster sample sites away from unit boundaries or known faults. Sites were chosen in representative, well-defined units so that results can be transferred to other areas in Yukon, and were placed in areas with little or no anthropogenic disturbance.

Sampling protocol

The Geological Survey of Canada protocol for measuring radon in soils (Friske *et al.*, 2010) was closely followed (Fig. 4). In particular, soil gas radon concentration was measured at five subsite locations within a 10 × 10 m area (Fig. 5) and revisited at least once, for a minimum of ten measurements per site during the summer season. Revisits were separated by at least one day. Radon results averaged for each site therefore provide an average concentration over both time and space. An example of a sampling site is provided in Figure 6.

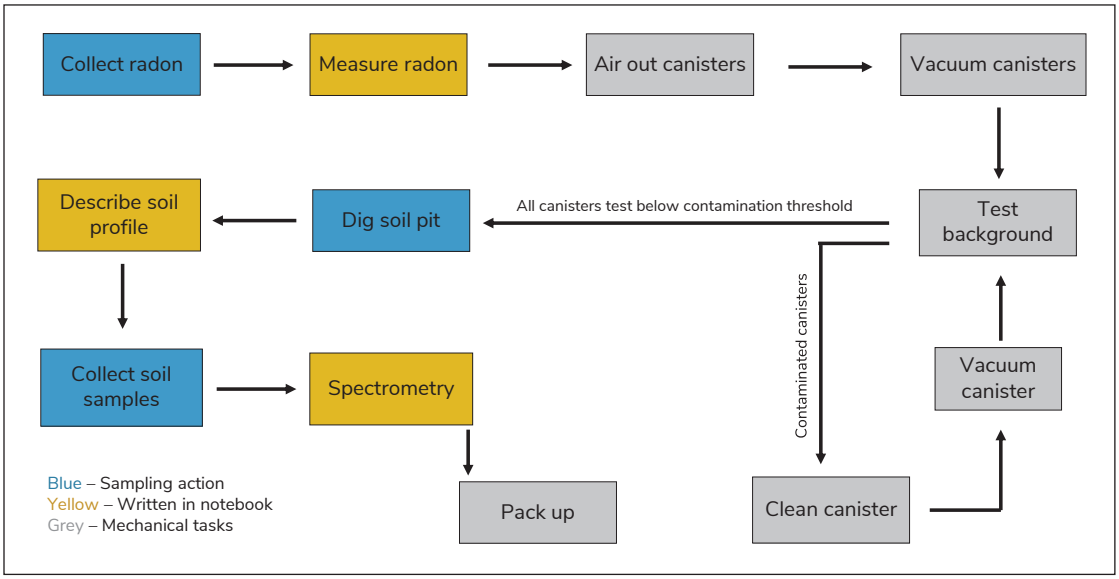

Figure 4. *Flowchart of sampling tasks during first visit to site. Based on protocol from Friske et al., 2010.*

The three control sites (20MK-013, 20MK-014, and 20MK-015) were sampled monthly for nine months and their data are incorporated into this study. Measured radon concentration in sediment, combined with clast lithology, geochemistry, grain size and soil moisture from each site, informed the analysis of suspected controls on radon concentration: bedrock composition, surficial sediment composition, depth to bedrock, surficial sediment grain size distribution, sediment maturity, and soil moisture.

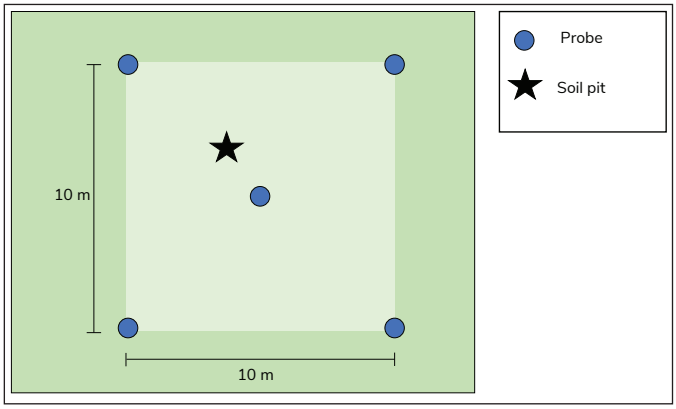

Figure 5. *Typical geometry of a sample site, with probes in corners and center of 10 × 10 m grid, and soil pit near the center probe. Exact placement of soil pit varied depending on position of trees, boulders, and other obstructions.*

Figure 6. *Photograph of sampling site 20MK-010 on June 18, 2020. Glaciofluvial gravel overlying Mandanna member of the Aksala Formation (sandstone and conglomerate). Three bags of sediment, from left to right, for clast lithology/geochemical analysis, matrix geochemistry, and grain size distribution. The spectrometer case is visible in top right and a probe flagged with orange tape can be seen in the top left.*

Radon collection

To ensure consistency with methodology used elsewhere in Canada, we followed the sampling protocols outlined by Friske et *al.* (2010), and used the same equipment and instruments described therein. Soil gas was collected from each site by inserting a piece of narrow metal pipe (hereafter referred to as a "probe") to a depth of 60 cm. A sharp steel point was placed at the groundward end of the probe, which was then hammered into the sediment with a mallet. A "punch rod," thinner and longer than the probe, was then tapped through the probe, pushing the tip roughly 5 cm deeper and creating an air cavity at the end of the probe. A 150 ml syringe was used to extract soil gas (Fig. 7). The first 150 ml of gas were purged to clear the probe of any atmospheric air, and the second volume was used to fill an evacuated ionization chamber (Fig. 8). Uncertainty in volume is estimated to be ± 10 ml (1σ). Concentrations were measured in situ using an ERM-3 Soil Radon Meter manufactured by Radon v.o.s. of Prague, using the protocol in the accompanying manual (included in Friske et *al.*, 2010). Some canisters did not fill completely, due either to low soil permeability and incomplete syringe fill, or to insufficient vacuum in the canister. In these cases the following error correction was applied according to the ERM-3 radon meter manual: $C_{cor} = C_{meas} \times \frac{150}{V_{in}}$, where C_{cor} is the corrected concentration measurement in kBq m^{-3}, C_{meas} is the concentration reported by the radon meter in kBq m^{-3}, and V_{in} is volume of soil gas extracted via syringe in ml.

Collection of other data

Additional geologic and environmental information relevant to radon concentration was also collected from each site. A >60 cm soil pit was hand dug and four sediment samples were collected from a depth of 60 cm (same depth as probe tips) for the following analysis: geochemistry of the matrix and representative clasts, sediment grain size, clast lithology on 50–100 pebbles, and soil moisture on 250 ml of sediment. If fewer than 50 clasts were available in the sediment, we collected as many as possible. The following sites had no clasts present: 20MK-006, 007, 11, 012, 013, 018, 025, 026 and 027. Gamma ray spectrometry was

conducted at each probe and soil pit to measure dose rate, potassium, equivalent uranium, and equivalent thorium. A wandering gamma ray survey of the site ensured that no areas produced anomalous levels of radioactivity (e.g., due to a granite boulder). The soil profile was described (horizon thickness, surficial sediment classification and evidence of disturbance), as well as local meteorological conditions (pressure, air temperature, humidity and wind), and a general description of the site was taken including topography and vegetation. Where accessible, bedrock samples for geochemical analyses were collected as close to the site location as possible.

Figure 7. *Soil gas extraction using 150 ml syringe. Red rubber tube connects directly to valve on ionization chamber. Probe flagged with orange tape.*

Figure 8. *IK-250 ionization chamber for radon concentration measurement, 250 ml capacity. Serial number is red, electrodes are brass pin at left and in central cylinder. Valve at right (knob above protruding tube).*

Analytical methods

Grain Size Distribution and Sorting

Approximately 1 kg of matrix sample was collected from each soil pit to determine grain size distribution. Clasts larger than 5 cm were removed by hand, as they are not considered part of the matrix. Grain size distribution was determined by Pacific Soil Analysis Inc. (Richmond, British Columbia) using sieve separation and a hydrometer. Two sets of sieve sizes were used: 3 inches, 19 mm, 8 mm, 4 mm, and 2 mm; and #10, #18, #35, #60, #140, 53 µm, and 2 µm. GRADISTAT Excel software (Blott and Pye, 2001) calculated sorting based on sieving data. This software returns arithmetic, geometric and logarithmic sorting statistics, as well as textural description based on the Folk and Ward classification. The sorting statistics reported here are all geometric.

Geochemistry

Approximately 0.5 kg of sediment matrix and representative pebble-sized clasts from each site pit were analyzed for major, minor, and other selected elements, and for loss on ignition. Whole rock geochemistry was completed at ALS Global (North Vancouver, British Columbia) using their complete characterization package. This included sample preparation and screening of the samples to 180 µm and the following analytical suite: whole rock by fusion/XRF, base metal by 4-acid digestion, loss on ignition for XRF, lithium borate fusion ICP-MS, and up to 34 elements by ICP-MS, as well as total carbon and total sulphur by IR spectroscopy. Results from the geochemical work are pending and therefore not presented in this paper.

Soil Moisture

Immediately before the radon gas measurement, soil moisture was determined by collecting a representative sample (roughly 0.5 kg of sediment) in a waterproof container from a depth of 60 cm in the soil pit. The sample was collected as soon as this depth was reached, to minimize evaporation upon exposure to the atmosphere. The sediment was weighed in the field (m_w) using a Starfrit High Precision Pocket Scale.

The same day, samples were baked at 100°C for one hour, cooled, and reweighed (m_d), and the difference in mass was used to estimate soil moisture (SM, %) according to $SM = \frac{m_w - m_d}{m_w} \times 100$.

Radon Gas Concentration

All measured data are reported, including any perceived anomalies. Mean radon concentration was calculated by first taking the average and standard deviation of all samples at a site, then removing measurements one standard deviation or greater from the mean (these are considered outliers) to determine if the standard deviation improved significantly, and finally recalculating mean and standard deviation of radon concentration with outliers removed. Weighted means were calculated according to the following formula: $W = \frac{\sum_{i=1}^{n} w_i x_i}{\sum_{i=1}^{n} w_i}$ where W is the weighted mean, x is a mean calculated by the above method, and $w = (1\text{-}COV).COV$ is the coefficient of variation (standard deviation divided by mean).

Results

Soil radon gas measurements

During the 2020 field season, 328 soil gas samples from 30 sites throughout the Whitehorse area were tested for radon concentration. Individual radon concentrations ranged from 0 to 68.1 kBq m^{-3}. Appendix 1 provides detailed characterization of each site based on field observations and borehole data. As shown in Figures 2 and 10, and in Appendix 1, the majority of sites (17 of 30) overlie granodiorite, while 6 overlie limestone, 3 overlie clastic sedimentary rocks, 2 overlie basalt, and 2 overlie unmapped bedrock. Depth to bedrock ranges from 1.5 m to greater than 100 m (the deepest being in Whistle Bend where glaciogenic sediments have not been drilled to bedrock). Twelve of the 30 sites are in glaciofluvial deposits, while 6 are in till, 5 are in fluvial sediments, 2 are in glaciolacustrine deposits, 1 is in eolian sediment, and 2 sample bedrock directly. Two sites are in sediment that was remobilized downhill from a till deposit onto a terrace, and are considered colluviated till. The grain size distribution of these samples is expected to be different from other till samples, but the clast lithology will be similar. Soil moisture varies from 2 to 14% by weight. Coefficients of variation range from 2 to 86%, with an average coefficient of variation of 27%. Variation is highest in silt and gravel units (average 62 and 29% respectively) and lowest in till and sand units (average 19 and 17%, respectively). The weighted means of each of the three major sediment types sampled in this study, weighted according to coefficient of variation, are 7.4 kBq m^{-3} for sand, 8.3 kBq m^{-3} for gravel and 16.0 kBq m^{-3} for till.

Seasonality

To determine if soil radon concentration varies seasonally, three sites (20MK-013, 20MK-014, and 20MK-015) were monitored monthly from August 2019 to August 2020, with a gap from February to April (Fig. 9). These were chosen as representative of sand, gravel, and diamict respectively. In diamict, the mean soil radon concentration is higher during the summer months, while in gravel the radon concentration is measurably lower in summer. Seasonal variation is less obvious in sand; however, December and January had the highest measured concentrations, suggesting a trend similar to that observed in gravel. Mean concentration is relatively consistent in all three sediment types during June, July and August.

Bedrock and surficial sediment type

We grouped mean radon concentration at each site according to the site's bedrock and surficial sediment type, and compared with depth to bedrock (Fig. 10). Within these groups, we calculated weighted means (according to coefficient of variation) for each bedrock and sediment type. No clear relationship between depth to bedrock and radon concentration is observed. The weighted means for sites overlying basalt and granodiorite are nearly identical (9.9 and 9.4 kBq m^{-3} respectively), and slightly higher for sites overlying limestone (13.5 kBq m^{-3}). Of the three parameters, the most influential control on radon concentration is surficial sediment texture. Diamicton has relatively high radon concentration, while sand is generally low and gravel is intermediate. The weighted mean for till is 16.0 kBq m^{-3}, while gravel and sand have similar weighted means with 8.3 kBq m^{-3} in gravel and 7.4 kBq m^{-3} in sand. There is a possible bimodality in gravel concentration, which may be related to sorting or to clast proportion.

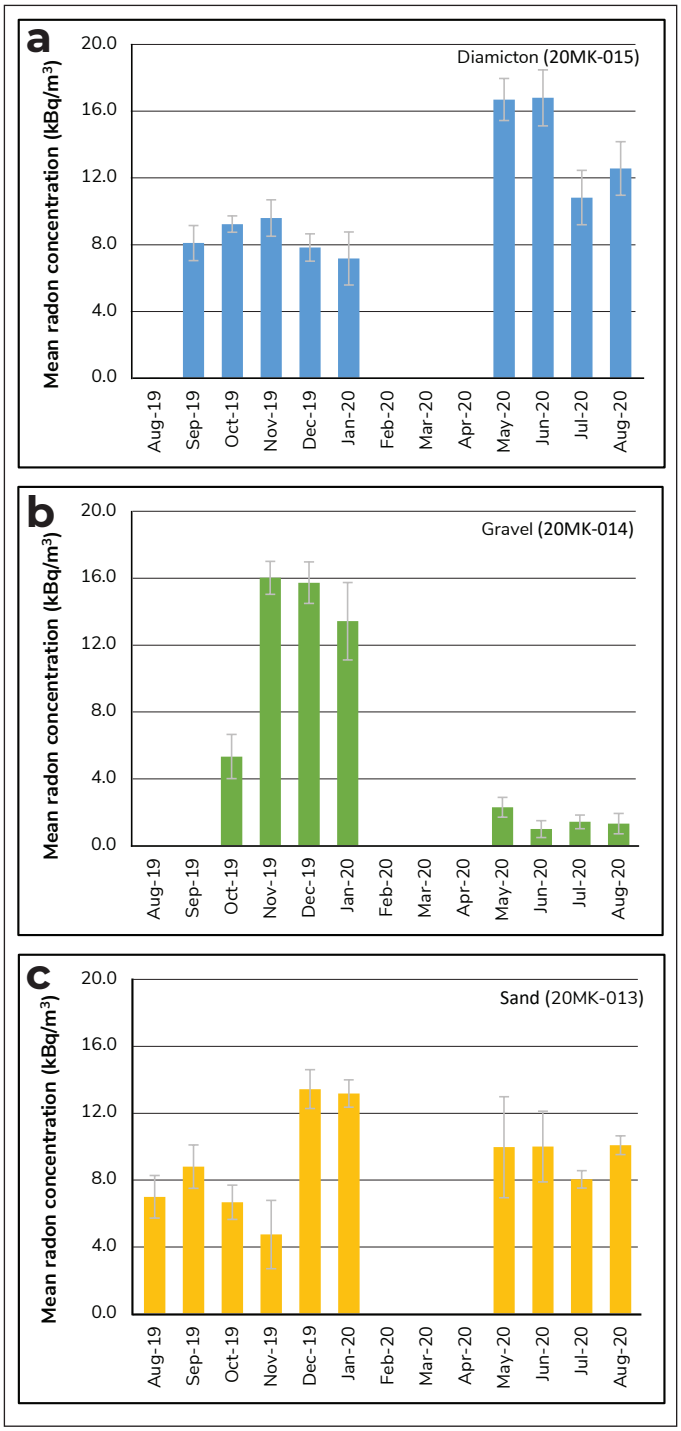

Figure 9. *Mean soil gas radon concentration at three long-term monitoring control sites. Data from* **(a)** *lodgement till,* **(b)** *glaciofluvial gravel, and* **(c)** *fluvial sand are plotted individually. Error bars are 1σ. Note that data are missing from February through April due to adverse winter sampling conditions and onset of global pandemic.*

Grain Size Distribution

In order to determine if there is a relationship between grain size distribution and radon concentration, we compared the mean radon concentration from each site to the fraction of matrix that is less than 53 µm in diameter (*i.e.*, silt and clay; Fig. 11). The tills (classified texturally as diamicton), along with reworked till that was reworked and deposited on a terrace, show the highest fraction of silt and clay in the matrix. The moderately sorted to very poorly sorted gravels consistently have relatively low abundances of fines, while sand displays a bimodal distribution of matrix grain size that is related to eolian versus fluvial/glaciofluvial origins. Results of the grain size analyses suggest a positive correlation between fraction of the matrix that is <53 µm diameter and radon concentration, with a coefficient of determination $R^2 = 0.59$.

Sorting

We also compared mean radon concentration at each site to the sorting of the matrix from the soil pit sample (Fig. 12). No obvious relationship was observed between radon concentration and matrix sorting. Since only the grain size distribution of matrix sample was analyzed, the sorting reported here does not reflect the overall sorting of the sediment. For example, till is typically more poorly sorted than gravel; however, some till samples had relatively well-sorted matrices. Descriptive classifications of the matrix, based on the schema of both Wentworth and Folk and Ward, are reported in Table 1. Although it does not represent the overall sorting of the sediment, matrix sorting may be used as a rough proxy for permeability, since uniform grain size increases permeability (see the section on Moisture).

Maturity

Maturity, or derivative degree of bedrock, may be a control on radon concentration. We therefore classified sediments, in order from least to most mature, as till, glaciofluvial sand and gravel, fluvial gravel and sand, glaciolacustrine silt, and eolian sand, then took a weighted mean for each sediment maturity level (weighted by the coefficient of variation), and compared these to radon concentration. Mean radon

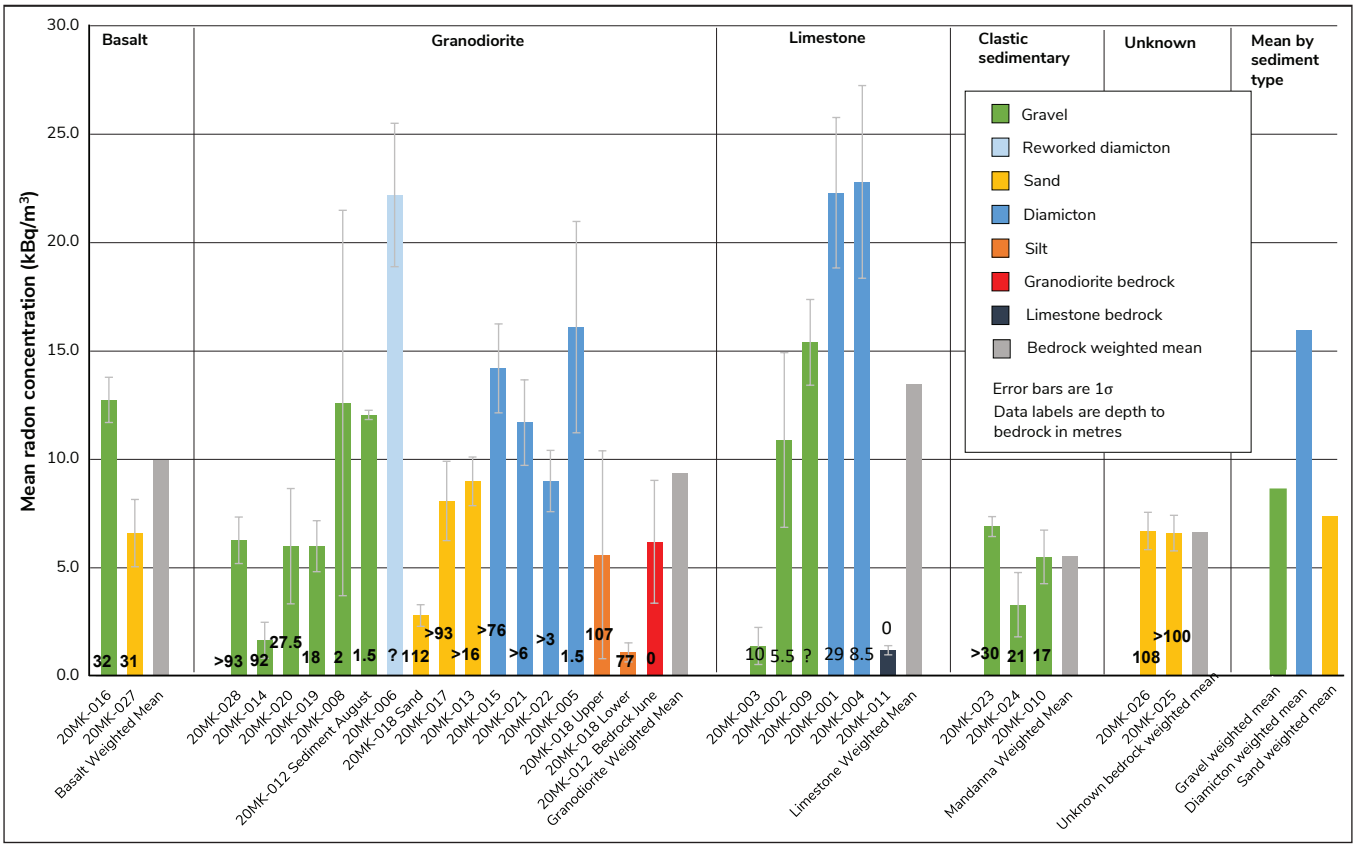

***Figure 10**. Mean soil gas radon concentration (min. 10 measurements) sorted by surficial material and bedrock characteristics. Concentration grouped by underlying bedrock type, and coloured according to overburden texture. Within each bedrock-surficial sediment class, concentrations are sorted by depth to bedrock (represented as data labels, in metres). Means weighted by coefficient of variation also calculated for each bedrock type (grey bars) and major surficial sediment texture (3 bars at far right).*

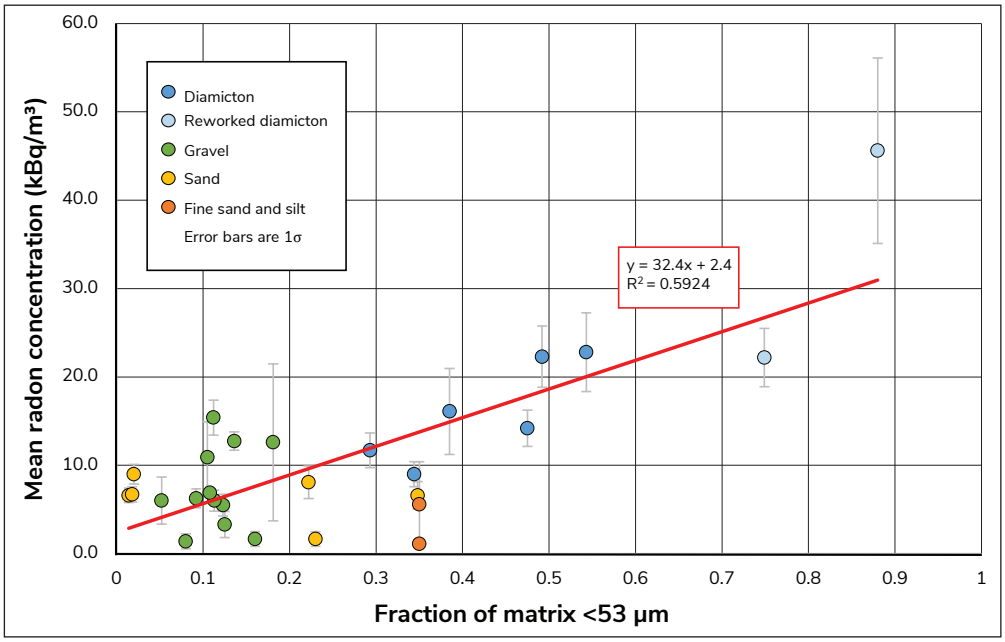

***Figure 11.** Mean radon concentration compared to the fraction of silt and clay in the sediment matrix. Data points are coloured according to surficial sediment type. Error bars are 1σ. Glaciolacustrine matrix samples were not collected so grain size distribution from Brideau et al. (2011) at a nearby sample location is used as a proxy for the two silt samples (orange).*

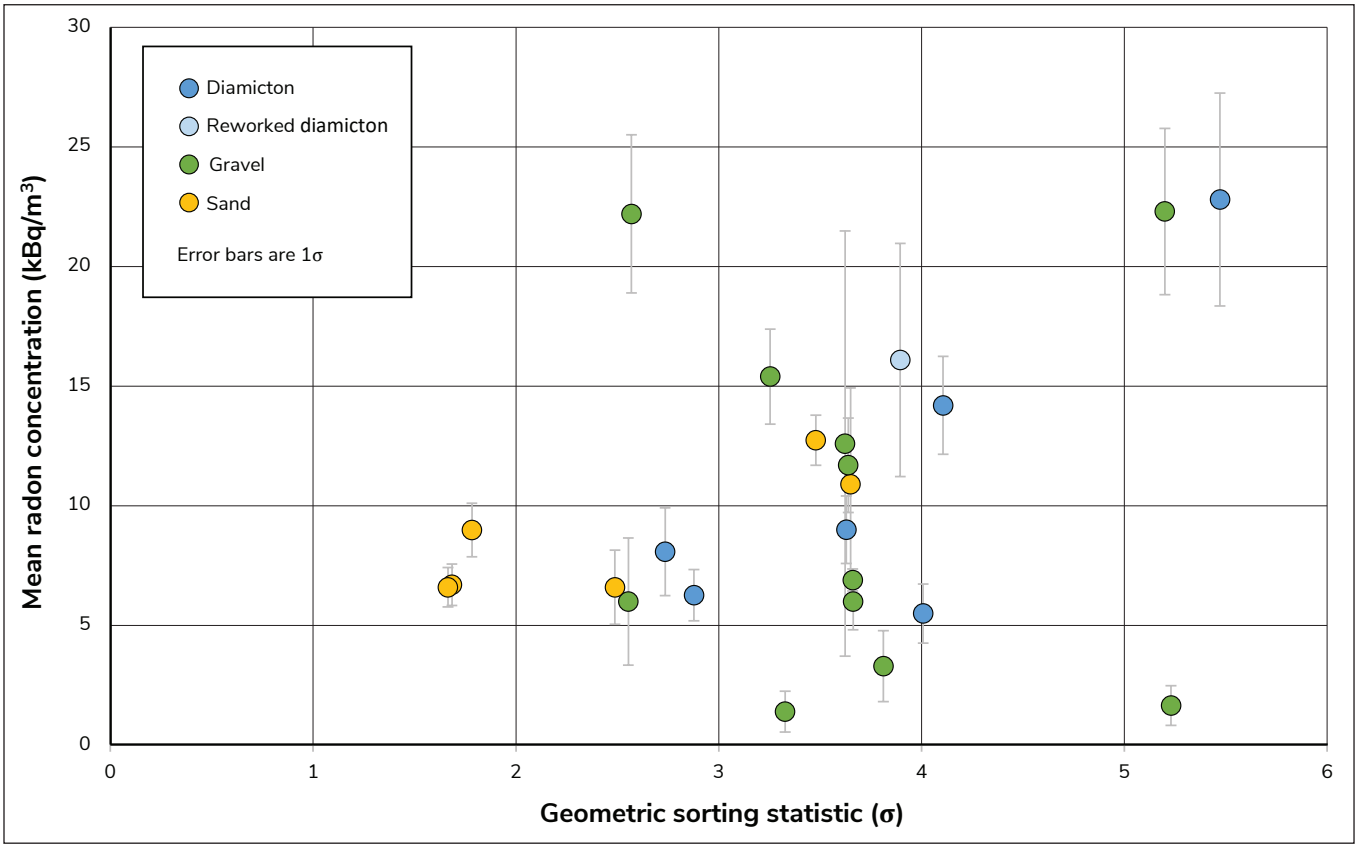

Figure 12. *Mean radon concentration compared to matrix sorting statistic as calculated by GRADISTAT Excel package (Blott and Pye, 2001). Greater values of geometric sorting statistic indicate poorer sorting of the matrix.*

concentration decreases with inferred sediment maturity, however not uniformly (Fig. 13). The coefficient of determination for linear best fit through the weighted means of each sediment type is $R^2 = 0.70$. This high coefficient of determination suggests that maturity is a strong negative control on radon concentration in sediment. It is a somewhat artificial measure; however, since the horizontal distribution of the groups is controlled only by the number of samples collected and is not directly related to the relative maturity of the sediment. Further work will include a more accurate estimation of maturity based on geochemistry.

Moisture

To determine the effect of sediment water content on radon concentration, we compared moisture measured in the soil pit with radon concentration from that site. A positive correlation between moisture and mean radon concentration is observed with a coefficient of determination $R^2 = 0.39$ (Fig. 14a). A positive overall trend also exists within each sediment type (Fig. 14b). Sand follows this trend the closest, with a coefficient of determination $R^2 = 0.99$; however, the dependence of concentration on moisture is also the lowest (shallowest slope). Gravel is the most scattered, and has the steepest trendline, with a coefficient of determination $R^2 = 0.29$ (Fig. 14b). Till has a coefficient of determination $R^2 = 0.44$. Sediment moisture depends on recent rainfall, and therefore sample timing; however, it may also illustrate the holding capacity of a sediment. Sediments with more silt and clay may hold more water than more permeable sands and gravels (see Fig. 15), and this may affect radon concentration. Note that the trendlines in Figure 14 do not take into account the uncertainties of each measurement, and are in some cases heavily affected by a single data point (e.g., rightmost point in Fig. 14a). The actual trends may therefore be less pronounced than those here represented.

Dominant controls

Of the controls compared in this study, maturity, moisture and silt/clay content of matrix appear to have the strongest correlations with mean radon concentration. Principal component analysis is required to determine properly which of these factors is the dominant control. For this preliminary study, we plotted moisture against silt and clay content to determine whether any correlation exists. We then compared these results to sediment maturity and radon concentration (Fig. 15). A positive correlation between moisture and matrix content is possible; however, a linear trendline has a relatively low coefficient of determination $R^2 = 0.19$. Radon concentration appears to increase both with increasing clay and silt content and with increasing moisture.

Table 1. *Description of matrix grain size, by textural group (based on Wentworth, 1922), geometric sorting statistic, and Folk and Ward (1957) classification. Note that grains 2–4 mm are considered "very fine gravel" by the Wentworth scale, and therefore several fine-grained sites (e.g., 20MK-006, 20MK-025 and 20MK-027) are described as "gravelly" in the second column.*

Site	Textural Group	Sigma (geo.)	Folk & Ward Mean	Folk & Ward Sorting
20MK-001	Gravelly Muddy Sand (diamicton)	5.2	Fine Sand	Very Poorly Sorted
20MK-002	Gravelly Sand	3.65	Very Coarse Sand	Poorly Sorted
20MK-003	Sandy Gravel	3.33	Very Coarse Sand	Poorly Sorted
20MK-004	Slightly Gravelly Muddy Sand (diamicton)	5.47	Very Fine Sand	Very Poorly Sorted
20MK-005	Gravelly Muddy Sand (diamicton)	3.89	Fine Sand	Poorly Sorted
20MK-006	Slightly Gravelly Muddy Sand	2.57	Very Fine Sand	Poorly Sorted
20MK-007	Slightly Gravelly Muddy Sand	2.14	Very Fine Sand	Moderately Sorted
20MK-008	Gravelly Sand	3.62	Medium Sand	Poorly Sorted
20MK-009	Gravelly Sand	3.25	Coarse Sand	Poorly Sorted
20MK-010	Sandy Gravel	4.01	Very Coarse Sand	Poorly Sorted
20MK-013	Sand	1.78	Medium Sand	Moderately Sorted
20MK-014	Gravelly Muddy Sand	5.23	Coarse Sand	Very Poorly Sorted
20MK-015	Slightly Gravelly Muddy Sand (diamicton)	4.11	Fine Sand	Very Poorly Sorted
20MK-016	Gravelly Sand	3.48	Medium Sand	Poorly Sorted
20MK-017	Slightly Gravelly Muddy Sand	2.74	Fine Sand	Poorly Sorted
20MK-019	Gravelly Sand	3.66	Very Coarse Sand	Poorly Sorted
20MK-020	Gravelly Sand	2.55	Coarse Sand	Poorly Sorted
20MK-021	Gravelly Muddy Sand (diamicton)	3.64	Medium Sand	Poorly Sorted
20MK-022	Gravelly Muddy Sand (diamicton)	3.63	Medium Sand	Poorly Sorted
20MK-023	Gravelly Sand	3.66	Very Coarse Sand	Poorly Sorted
20MK-024	Gravelly Sand	3.81	Coarse Sand	Poorly Sorted
20MK-025	Slightly Gravelly Sand	1.66	Coarse Sand	Moderately Well Sorted
20MK-026	Sand	1.68	Coarse Sand	Moderately Well Sorted
20MK-027	Slightly Gravelly Muddy Sand	2.49	Fine Sand	Poorly Sorted
20MK-028	Slightly Gravelly Sand	2.88	Coarse Sand	Poorly Sorted

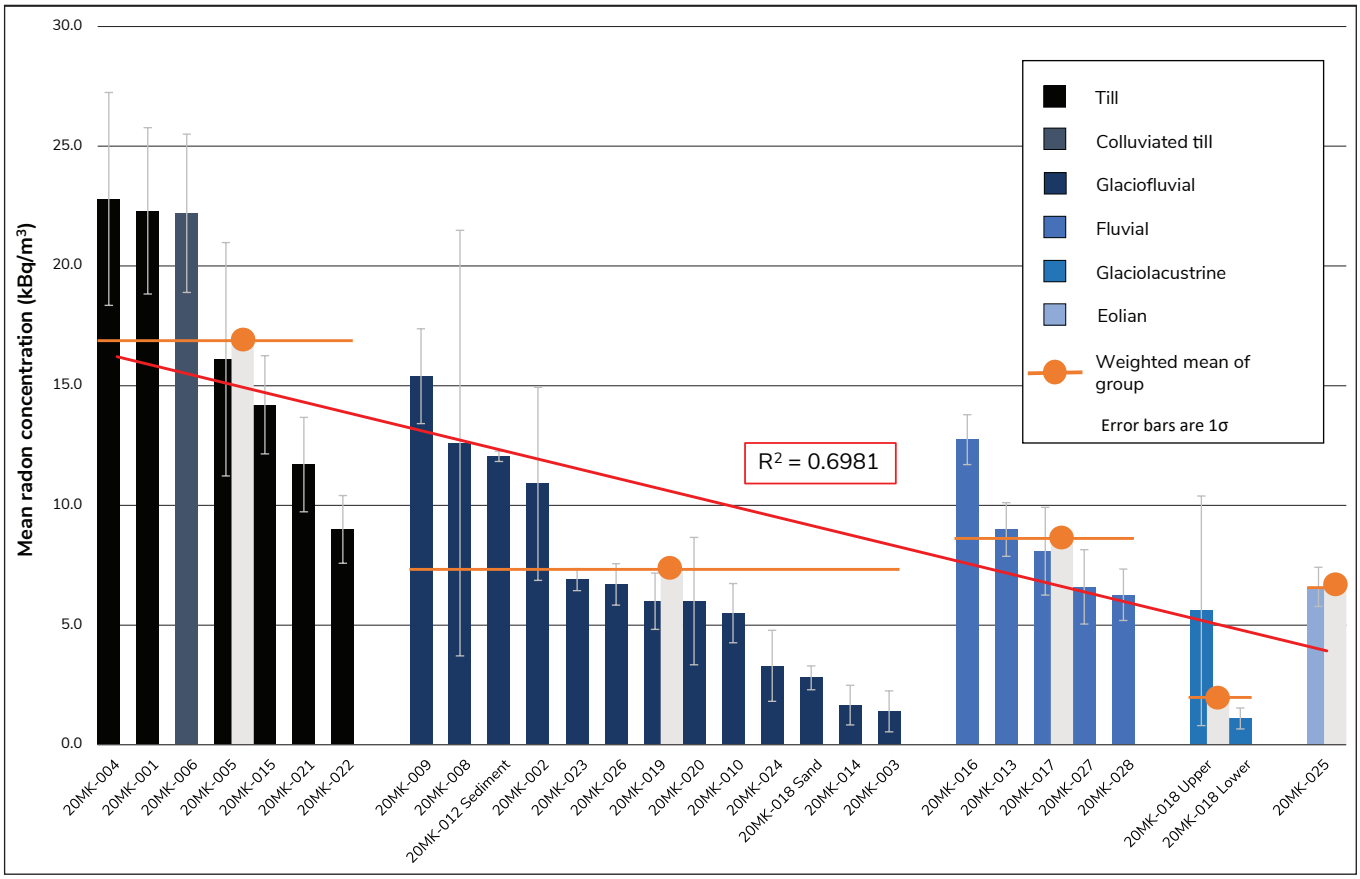

Figure 13. *Surficial sediment classified by maturity, or amount of modification from protolith. Since till is the most directly derived from bedrock, it is at the far left, followed by glaciofluvial, fluvial, glaciolacustrine, and eolian sediments. Note the colluviated till sample third from the left and that reworking (i.e., increase of maturity) has not had any appreciable effect on radon concentration. The average of each group is plotted as a flat line (orange), with a linear trendline in red. Not included in the graph to avoid skewing is 20MK-012, a grus site with mean radon concentration of 55 kBq m^{-3}. Since grus is more proximate to bedrock than till, this sample supports the overall trend of decreasing radon concentration with increasing maturity.*

Discussion and Implications

Seasonality appears to be an important non-geologic control on soil radon concentration in the region of Whitehorse, Yukon. While relatively consistent from May to August and from December to January, measured concentrations from 2019 and 2020 differ significantly between the two periods. Seasonal variability has been widely observed in outdoor and indoor studies (e.g., Siino et al., 2019, Yang et al., 2017, Barazza et al., 2015). However, not all sediment types in the Whitehorse region display consistent variation, as two sediment types exhibit higher and one sediment type lower radon concentrations in the summer (Fig. 9). A particular consideration for seasonal variation in Whitehorse is the seasonal freezing and thawing of ground, possibly creating a frozen cap which traps radon below the surface. Due to lower permeability in the silt-rich till (20MK-15), the retention of soil moisture as ice in the winter months may have reduced soil radon flux in the till more substantially.

The anti-phasing of the seasonal variation in radon concentration in different sediments motivated an analysis of the potential causes of non-seasonal variability in Yukon soil radon flux. Of the parameters evaluated—bedrock lithology, thickness of surficial cover, surficial sediment type, grain size distribution, sorting, sediment maturity, and soil moisture—silt and clay content of the matrix and sediment maturity appear to be the strongest geological controls on soil radon concentration in sediment.

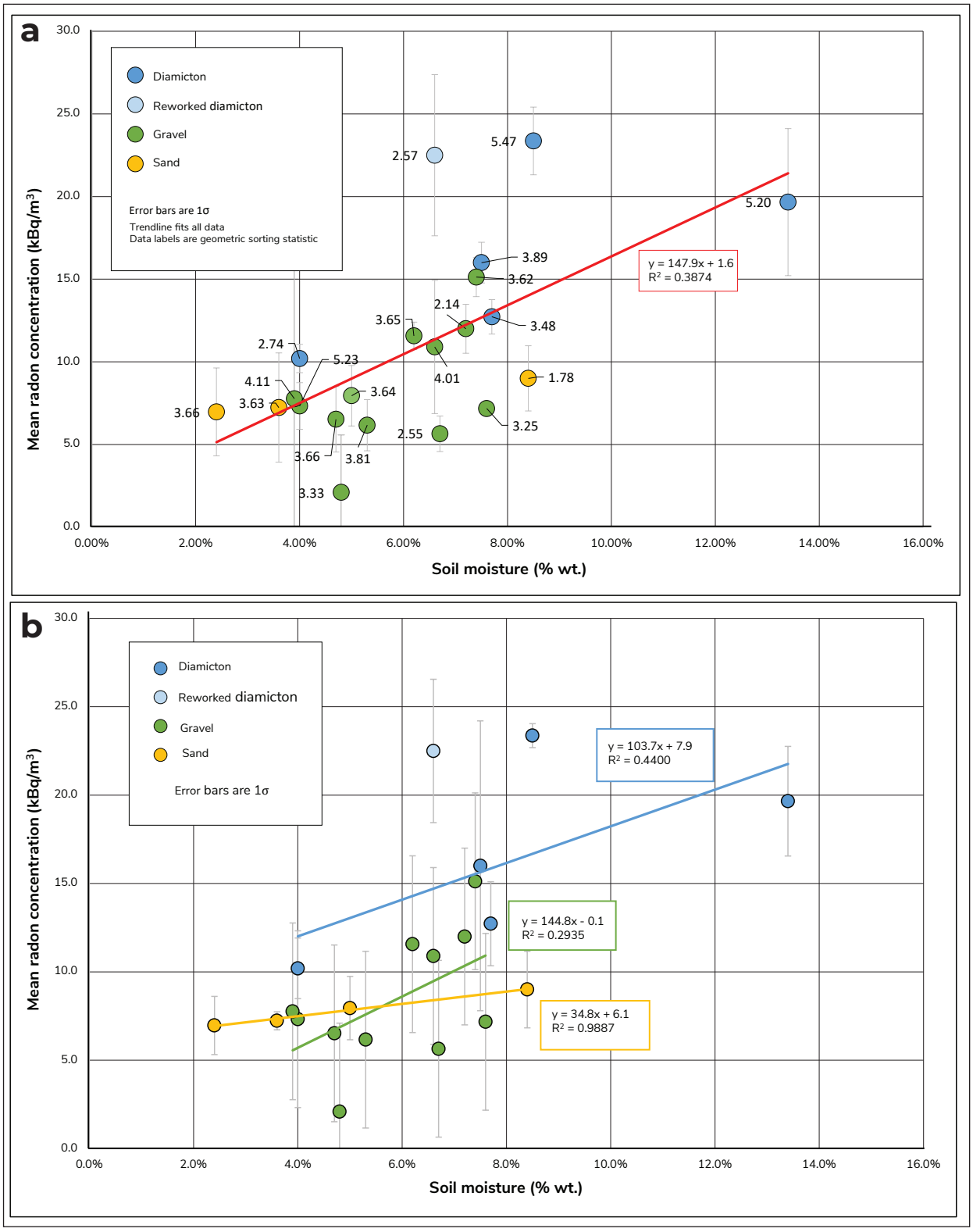

Figure 14. *Mean radon concentration compared to moisture at 60 cm depth. Trendlines calculated for* ***(a)*** *all samples and* ***(b)*** *each major sediment type. Data labels correspond to geometric sorting statistic of the matrix. Moisture is calculated as fraction of water by mass and was measured by mass difference of sediment from soil pit before and after heat treatment. All means were calculated only from measurements on the day a soil pit was dug (five measurements instead of ten).*

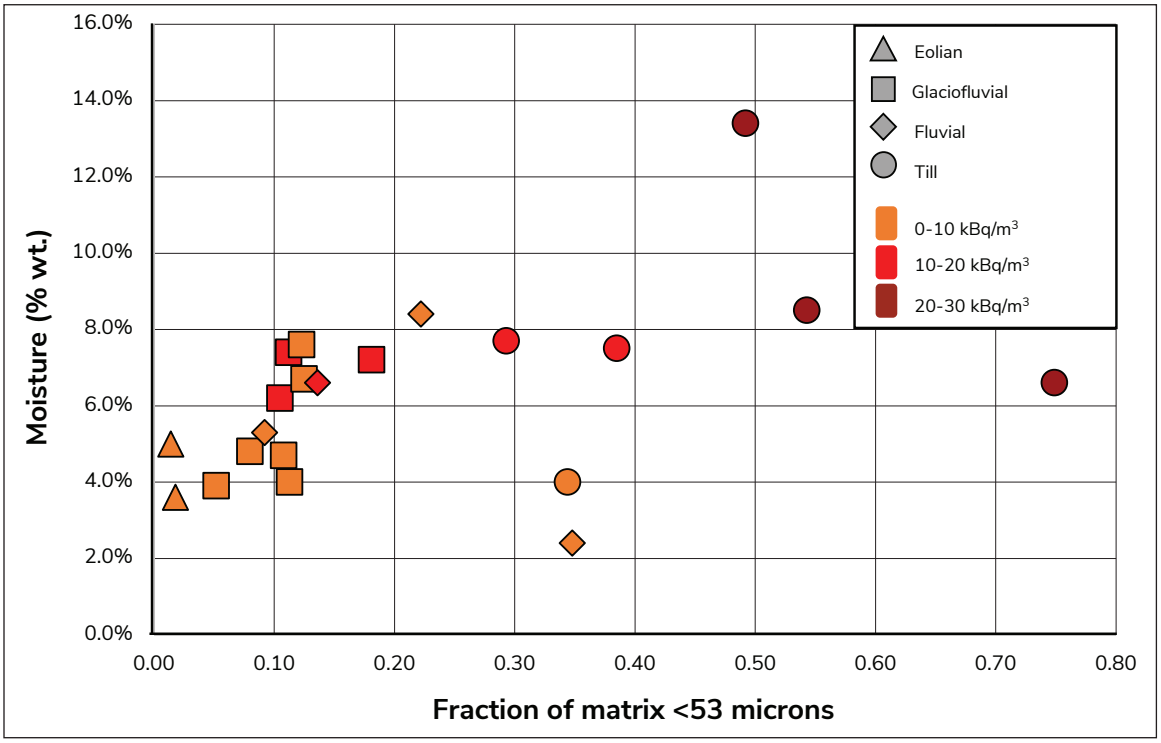

Figure 15. *Moisture at 60 cm depth compared to silt and clay content of matrix. Shapes correspond to genetic origin of sediment and colour corresponds to mean radon concentration. Trendline is not included due to low coefficient of determination.*

A grain size control in the study area is most evident from the positive correlation of radon concentration and quantity of silt and clay in the surficial sediment (Fig. 11). The observed seasonal anti-phasing seems to correspond with local differences in texture, where sites 20MK-013 and 20MK-014 have dominantly sandy matrices and overall textures of sand or gravelly muddy sand, whereas site 20MK-015 is a glacial diamicton with a greater silt component and therefore relatively lower permeability.

Grain size has previously been attributed as a first order control on radon flux (Saad *et al.*, 2018; Sakoda *et al.*, 2010; Markannen and Arvela, 1992). Fine-grained glaciolacustrine sediments examined in this study do not display high concentrations of radon however. This suggests that sediment maturity may also control radon concentration. For example, tills, which are relatively recently derived from bedrock and have sandy silt matrices, tend to contain high levels of radon compared to similarly fine-grained glaciolacustrine sediments. It is possible that as the glaciolacustrine sands and silts are reworked, the uranium-bearing minerals, *i.e.*, the radon sources, are weathered and destroyed. Overall, radon concentration tends to decrease with sediment maturity (Fig. 13).

A positive correlation is observed between radon concentration and moisture (Fig. 14), and this may reflect both average grain size and porosity of these sediments. Water may also facilitate the transport of radon by dissolution. To test the hypothesis that grain size and sediment maturity are the dominant controls of both spatial and temporal variability in soil radon, a principal component analysis should be conducted, and sediment mineral uranium concentrations need to be evaluated.

Depth to bedrock does not appear to be a first-order control on radon concentration, at least in areas where surficial material thickness is greater than 1 m (as is the case for the current study). A site in 1.5 m of sediment of overlying grus displays high concentrations of radon, suggesting that bedrock contributions may be important in areas of very shallow surficial cover.

In general, it seems that diffusion and emanation from bedrock minerals is not the sole source of radon nor is it a first-order control of spatial and temporal variability. Previous studies (e.g., O'Brien *et al.*, 2011) seem to support this observation, where bedrock-to-surface transport time exceeded the lifetime of ^{222}Rn. Variable isotopic composition of the different Quaternary sediment types overlying a single bedrock type could help further explain the source of variation in radon concentration.

In addition to our own and previous observations of the relationship between silt and clay content and soil radon concentration, it may be worthwhile to explore the escape of ^{222}Rn from uranium-bearing crystals. Emanation of ^{222}Rn is controlled by its recoil distance from the alpha decay of ^{226}Ra, which must therefore be within tens of micrometres of the grain surface for ejection to occur. The short half-life of ^{222}Rn and the low diffusivity at surface temperatures would suggest that diffusion of ^{222}Rn requires internal defects such as fission tracks that intersect with the grain surface. Therefore, sediments with finer grain sizes and higher surface area-to-volume ratio may have a larger contribution to soil gas radon, particularly if the fine fraction is a close derivative of bedrock. Furthermore, the fate of the ^{222}Rn after it escapes the grain may also be controlled by grain size, permeability, sorting, and moisture content. Sakoda *et al.* (2010) have considered some of these possible controls through numerical modeling, and their approach merits further analysis based on the available data from our study.

Almost all of the measured soil radon concentrations were above the Canadian recommended limit for indoor radon exposure of 0.2 kBq m^{-3}. An analysis of the link between soil radon concentration and indoor radon concentration is highly recommended in order to assess how surficial geology and architecture contribute to risks of radon exposure in Yukon.

In summary, our preliminary analysis of the 2020 soil radon data indicates that bedrock is not the single nor the most important source or control of near-surface soil radon concentration in the Whitehorse area. Of the surficial sediment parameters measured, silt and clay content of the soil matrix is the most closely correlated to radon concentration. Sediment maturity also appears to be a strong control on radon concentration, and this connection warrants geochemical analysis. Several meteorological factors, such as moisture and season, impart appreciable temporal variability on soil radon concentration among different sediment types. Future field programs targeting the source of variability should include more long-term continuous sampling at selected sites to evaluate the strength and reproducibility of the apparent seasonality, and additional sites in eolian and glaciolacustrine units are needed for a more representative characterization of the regional soil radon flux. We also recommend an overall increase in the number of sample sites to strengthen the statistics. Principal component analysis and investigation of ^{222}Rn diffusion will be completed once all geochemical data become available and will reported in a thesis by the lead author (Kishchuk, 2021).

Conclusions

Radon concentration was measured in sediment at 30 sites throughout the Whitehorse area. These sites represent till, glaciofluvial sand and gravel, fluvial sand and gravel, glaciolacustrine silt, and eolian sand. They overlie granodiorite, limestone, clastic sedimentary and basalt bedrock in various combinations. Almost all sites are in undisturbed sediment. A variety of geological controls (bedrock and sediment type, surficial cover thickness, grain size distribution, sorting, sediment maturity, soil moisture) and meteorological factors (rainfall, air pressure, wind, temperature) were compared to soil radon concentration. Conclusions reported here are preliminary as data collection and analysis are ongoing.

A notable seasonal shift in soil gas radon concentrations was observed at three long-term monitoring sites representing fluvial sand, glaciofluvial gravel and lodgement till. In the gravel site, radon concentration was at its lowest from May to August, while concentration in the diamict site was highest during these months. Relative to the seasonal variation, soil radon concentration was consistent during the summer months when most of this study was undertaken, and so intraseasonal variability likely had little effect on the results reported here.

Radon concentration is found to be independent of depth to bedrock, and shows no clear correlation with bedrock type. However, geochemical analyses of the sediments and bedrock are still pending, so a complete assessment of the importance of the underlying bedrock is not currently possible. Grain size distribution and sediment genesis appear to be the strongest geological controls on radon concentration in the surficial cover. It also appears that soil radon concentration correlates positively with soil moisture and negatively with sediment maturity.

Further analyses, including matrix geochemistry, clast lithology, and principal component analysis, will be undertaken next to confirm these results. Further work is also recommended to compare indoor radon concentration to radon concentration in sediment.

Acknowledgements

This project took place on the traditional territory of the Kwanlin Dün and Ta'an Kwäch'än First Nations. Thanks to Derek Cronmiller for reviewing this manuscript, and to staff at YGS this summer for their interest and input in this project. Brad Harvey (Geological Survey of Canada) kindly provided access to radon sampling equipment. YGS provided funding for the analyses and fieldwork. Funding to Michael Kishchuk was provided jointly by YGS and an NSERC Undergraduate Student Research Award at Dalhousie University. Special thanks to Paul Kishchuk and Kristina Craig of Whitehorse for providing a truck for fieldwork. Brett Elliot, of the YGS, produced Figure 1. Finally, we appreciate the generosity of landowners who let us sample on their property.

References

Barazza, F., Gfeller, W., Palacios, M. and Murith, C., 2015. An investigation of the potential causes for the seasonal and annual variations in indoor radon concentrations. Radiation Protection Dosimetry, vol. 167, p. 75–81.

Blott, S.J. and Pye, K., 2001. GRADISTAT: a grain size distribution and statistics package for the analysis of unconsolidated sediments. *Earth Surface Processes and Landforms*, vol. 26, p. 1237–1248.

Bond, J.D., 2004. Late Wisconsinan McConnell glaciation of the Whitehorse map area (105D), Yukon. In: Yukon Exploration and Geology 2003, D.S. Emond and L.L. Lewis (eds.), Yukon Geological Survey, p. 73–88.

Bond, J., Morison, S. and McKenna, K., 2005a. Surficial Geology of MacRae (NTS 105D/10), Yukon (scale 1:50 000). Yukon Geological Survey, Geoscience Map 2005-6.

Bond, J., Morison, S. and McKenna, K., 2005b. Surficial Geology of Whitehorse (NTS 105D/11), Yukon (scale 1:50 000). Yukon Geological Survey, Geoscience Map 2005-7.

Bond, J., Morison, S. and McKenna, K., 2005c. Surficial Geology of Upper Laberge (NTS 105D/14), Yukon (scale 1:50 000). Yukon Geological Survey, Geoscience Map 2005-8.

Brideau, M.-A., Stead, D., Bond, J.D, Lipovsky, P.S. and Ward, B.C., 2011. Preliminary stratigraphic and geotechnical investigations of the glaciolacustrine and loess deposits around the city of Whitehorse (NTS 105D/11), Yukon. *In:* Yukon Exploration and Geology 2010, K.E. MacFarlane, L.H. Weston, and C. Relf (eds.), Yukon Geological Survey, p. 33–53.

Cinelli, G., Tositti, L., Capaccioni, B., Brattich, E., and Mostacci, D., 2015. Soil gas radon assessment and development of a radon risk map in Bolsena, Central Italy. Environmental Geochemistry and Health, vol. 37, p. 305–319.

Colpron, M. (comp.), 2011. Geological compilation of Whitehorse trough – Whitehorse (105D), Lake Laberge (105E), and part of Carmacks (115I), Glenlyon (105L), Aishihik Lake (115H), Quiet Lake (105F) and Teslin (105C). Yukon Geological Survey, Geoscience Map 2011-1, 3 maps, scale 1:250 000, legend and appendices.

Folk, R.L. and Ward, W.C., 1957. Brazos River bar: a study in the significance of grain size parameters. Journal of Sedimentary Petrology, vol. 27, p. 3–26.

Friske, P.W.B., Kettles, I.M., McCurdy, M.W., McNeil, R.J. and Harvey, B.A., 2010. North American Soil Geochemical Landscapes Project: Canadian field protocols for collecting mineral soils and measuring soil gas radon and natural radioactivity. Geological Survey of Canada, Open File 6282, 177 p.

Government of Canada, 2020. Radon – What you need to know. Health Canada, https://www.canada.ca/en/health-canada/services/environmental-workplace-health/reports-publications/radon-what-you-need-to-know.html, [accessed December 10, 2020].

Government of Yukon, 2018. Radon testing in Yukon schools, https://yukon.ca/en/learn-about-radon-testing-yukon-schools#radon-testing-in-yukon-schools, [accessed November 30, 2020].

Government of Yukon, 2020. Radon Information, https://yukon.maps.arcgis.com/apps/MapSeries/index.html?appid, [accessed November 30, 2020].

Hart, C.J.R. and Radloff, J.K., 1990. Geology of Whitehorse, Alligator Lake, Fenwick Creek, Carcross and Part of Robinson Map Areas (105D/11, 6, 3, 2 and 7). Yukon Geological Survey, Open File 1990-4(G).

Kishchuk, M.J., 2021 (in prep.). Geological controls on radon concentration in surficial sediment in Whitehorse, Yukon. Unpublished honours thesis, Dalhousie University, Nova Scotia, Canada.

Marin, P.C., 1956. Measurement of the half-life of radon with a Curie-type ionization chamber. British Journal of Applied Physics, vol. 7, p. 188–190.

Markannen, M. and Arvela, H, 1992. Radon emanation from soils. Radiation Protection Dosimetry, vol. 45, p. 269–272.

O'Brien, K.E., Goodwin, T.A. and Risk, D., 2011. Radon soil gas in the Halifax Regional Municipality, Nova Scotia, Canada. Atlantic Geology, vol. 47, p. 112–124.

Pearson, F.K., Hart, C.J.R. and Power, M., 2001. Distribution of Miles Canyon basalt in the Whitehorse area and implications for groundwater resources. *In:* Yukon Exploration and Geology 2000, D.S. Emond and L.H. Weston (eds.), Exploration and Geological Sciences Division, Yukon Region, Indian and Northern Affairs Canada, p. 235–245.

Porstendorfer, J., 1994. Properties and behavior of radon and thoron and their decay products in the air. Journal of Aerosol Science, vol. 25, p. 219–263.

Saad, A.F., Abdallah, R.M. and Hussein, N.A., 2018. Physical and geometrical parameters controlling measurements of radon emanation and exhalation from soil. Applied Radiation and Isotopes, vol. 137, p. 273–279.

Sakoda, A., Ishimori, Y., Hanamoto, K., Kataoka, T., Kawabe, A. and Tamaoka, K., 2010. Experimental and modeling studies of grain size and moisture content effects on radon emanation. Radiation Measurements, vol. 45, p. 204–210.

Siino, M., Scudero, S., Cannelli, V., Piersanti, A. and D'Alessandro, A., 2019. Multiple seasonality in soil radon time series. Scientific Reports, vol. 9, 13 p.

Stanley, F. K. T., Irvine, J.L., Jacques, W.R., Salgia, S.R., Innes, D.G., Winquist, B.D., Torr, D., Brenner, D.R. and Goodarzi, A.A., 2019. Radon exposure is rising steadily within the modern North American residential environment, and is increasingly uniform across seasons. Scientific Reports, vol. 9, 17 p.

Wentworth, C. K., 1922. A Scale of Grade and Class Terms for Clastic Sediments. The Journal of Geology, vol. 30, p. 377-392.

West, K. and Donaldson, A., 2007. White River Ash, Yukon. Yukon Geological Survey, YGS Brochure 2007-1.

Wolfe, S., Bond, J. and Lamothe, M., 2011. Dune stabilization in central and southern Yukon in relation to early Holocene environmental change, northwestern North America. Quaternary Science Reviews, vol. 30, p. 324–334.

World Health Organization, 2009. WHO handbook on indoor radon: a public health perspective. WHO Press, Geneva, 94 p.

Yang, J., Buchsteiner, M., Salvamoser, J., Irlinger, J., Guo, Q. and Tschiersch, J., 2017. Radon exhalation from soil and its dependence on environmental parameters. Radiation Protection Dosimetry, vol. 177, p. 21–25.

Yukon Geological Survey, 2020a. Yukon digital bedrock geology. Yukon Geological Survey, http://data.geology.gov.yk.ca/Compilation/3#InfoTab, [accessed November 30, 2020].

Yukon Geological Survey, 2020b. Yukon Lithogeochemistry data set. Yukon Geological Survey, http://data.geology.gov.yk.ca/Compilation/35#InfoTab, [accessed December 1, 2020].

Yukon Housing Corporation, 2018. Whitehorse Indoor Radon Test Results 2006-2018. Yukon Housing Corporation, https://yukon.ca/en/radon, [accessed November 26, 2020].

Appendix 1 (digital only)

Sample site characteristics. Bedrock type, depth to bedrock, and soil pit profile are reported for each site, as well as elevation, geographic coordinates, vegetation type, estimates of drainage, and disturbance indicators. Drainage estimates are based on vegetation and underlying sediment type, while disturbance indicators are field observations such as tire-ruts, dug holes, and the presence of White River Ash in the soil pit. White River Ash was deposited roughly 1200 years ago following the eruption of Mt. Churchill in Alaska (West and Donaldson, 2007), and continuous tephra is taken to indicate an intact, undisturbed soil.

The geometry and kinematic history of Cordilleran deformation at the Howard's Pass shale-hosted massive sulphide deposit, Yukon: 1st year progress report

Darius Kamal* and Kenneth A. Hickey
University of British Columbia

Kamal, D. and Hickey, K.A., 2021. The geometry and kinematic history of Cordilleran deformation at the Howard's Pass shale-hosted massive sulphide deposit, Yukon: 1st year progress report. *In:* Yukon Exploration and Geology 2020, K.E. MacFarlane (ed.), Yukon Geological Survey, p. 137–156.

Abstract

The shale-hosted massive sulphide Zn-Pb deposits of Howard's Pass were deposited during the Silurian and subsequently deformed during the Cretaceous Cordilleran orogeny. A recent model proposes that the deposits are hosted within a regional thrust duplex with strong transposition of bedding. This study aims to test this model and is focused on the XY group of deposits. Lithostratigraphic mapping and structural observations indicate one main phase of folding, F_1, and the XY group of deposits is located on the southern limb of a macroscopic F_1 syncline. F_1 folds are steeply inclined and gently plunging to the WNW–NW. A regionally developed, steep, NE dipping, cleavage, S_1, is axial planar to the F_1 folds across Howard's Pass. S_1 manifests as a slaty cleavage comprising pervasively developed dissolution seams. WNW and NNE striking extensional faults overprint F_1 folds. No shear fabrics or evidence for transposition of bedding were identified.

* *dkamal@eoas.ubc.ca*

Introduction

Shale-hosted massive sulphide (SHMS) Zn-Pb-Ag deposits account for 40% of Zn and 60% of Pb reserves globally (Goodfellow, 2004; Hoggard et *al*., 2020). They also supply more than 25% of global production of these metals. In the past, SHMS deposits have been more commonly referred to as sedimentary exhalative, SEDEX, deposits. However, at several locations globally, there is evidence that such deposits do not form exclusively by hydrothermal exhalative processes on the seafloor, but can also be a product of replacement by infiltrating hydrothermal fluids in the subsurface during sedimentation, diagenesis, or early basin inversion (e.g., Perkins, 1997; Kelley et *al*., 2004; Leach et *al*., 2010; Magnall et *al*., 2016). They are usually deposited in tabular or lenticular stratiform sulphide bodies containing sphalerite, galena, pyrite, ± barite (McClay, 1991; Goodfellow and Lydon, 2007; Emsbo et *al*., 2016). SHMS deposits form within intracontinental rifts and failed rifts, passive margins, and back-arc basins (Leach et *al*., 2005; Goodfellow and Lydon, 2007). They are typically hosted within reduced sag-phase sedimentary units and form during periods of reactivated extensional faulting or, in some cases, during early basin inversion (Leach et *al*., 2005; Goodfellow and Lydon, 2007; Gibson et *al*., 2017). Sedimentary basins hosting SHMS deposits commonly undergo inversion and internal deformation during subsequent periods of crustal shortening and orogenesis (Bell and Hickey, 1998; De Vera et *al*., 2004; Leach et *al*., 2010; Gibson et *al*., 2017), with many deposits being incorporated into foreland fold and thrust belts (e.g., Red Dog; De Vera et *al*., 2004).

The Selwyn basin, located in the Canadian Cordillera across central Yukon and western Northwest Territories, is host to several world-class Zn-Pb deposits (Fig. 1; Goodfellow, 2004; Goodfellow, 2007). These include the Devonian age Tom and Jason deposits of the Macmillan Pass district, the Cambrian age deposits of the Anvil district (e.g., Faro, Grum, DY), and 15 Silurian age deposits that together comprise the Howard's Pass district in eastern Yukon, adjacent to the border with the Northwest Territories (Fig. 1; Goodfellow, 2004; Goodfellow, 2007). The latter group of deposits represents one of the largest undeveloped Zn-Pb resources in the world with an estimated 400 Mt grading 4.5% Zn and 1.5% Pb (Kirkham et *al*., 2012). The Howard's Pass orebodies comprise bedded sulphide laminae hosted within Ordovician to Silurian siliceous and phosphoritic shales of the Duo Lake Formation (Morganti, 1979; Goodfellow and Jonasson, 1986; Goodfellow, 2007; Slack et *al*., 2017). No vent complexes have been identified, and the deposits are generally considered to be examples of distal exhalative sulphide deposition, where mineralization was emplaced below the sediment–water interface as a dense, acidic, metalliferous brine percolated down into sulphidic muds during early diagenesis (McClay, 1991; Goodfellow, 2007; Gadd et *al*., 2016, 2017; Slack et *al*., 2017). During the Cretaceous Cordilleran orogeny, the rocks of the Selwyn basin underwent regional shortening and were incorporated into a foreland fold and thrust belt

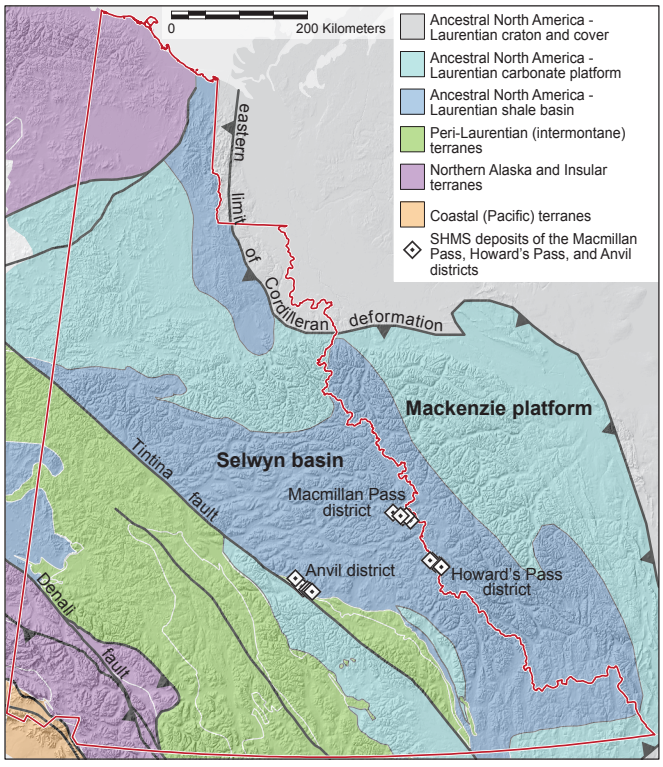

Figure 1. *SHMS Zn-Pb deposits of the Macmillan Pass, Anvil and Howard's Pass districts in the Selwyn basin of central Yukon. Geological terranes of the Canadian cordillera are grouped by paleogeographic affinities as described by Nelson et al. (2013). Geological data from Yukon Geological Survey (2020).*

to the east of the orogenic core (Gordey and Anderson, 1993; Mair *et al.*, 2006; Staples *et al.*, 2016). The region containing the Howard's Pass deposits has been affected by thin-skinned deformation forming relatively tight upright folds within wide, thrust-separated, fault panels (Gordey and Anderson, 1993; Gordey, 2013). The orebodies themselves are folded and have been locally remobilized into dissolution cleavages (McClay, 1991), although the intensity of deformation and the timing of deformation, Silurian *vs.* Cretaceous, have been subject of some debate (Goodfellow and Jonasson, 1986; Jonasson and Goodfellow, 1986; McClay, 1991; Martel, 2017; Slack *et al.*, 2017). Most previous workers agree, however, that the spatial distribution of the ore is largely unaffected by the deformation at the deposit to district scale.

Recently, Hodder *et al.*, (2014) and Martel (2017) proposed that the ore horizons and their host stratigraphy in the Howard's Pass district lie within a regional-scale Cordilleran-age duplex structure with complex internal folding and imbricate thrusting between a mylonitic basal thrust (the Howard's Pass décollement) and an upper roof thrust. The duplex is described as having significant internal ductile deformation within steeply dipping thrust-bounded fault blocks, with Martel (2017) noting that zones of intense foliation development and transposition of bedding alternate with other zones that are only weakly to moderately strained. Hodder *et al.* (2014) and Martel (2017) suggest that the orebodies have been extensively imbricated by thrusting and accompanying tight folding. The sulphide minerals were remobilized and concentrated along pressure solution cleavage that is attributed to high-strain within the duplex rather than regional folding. Contrary to the previous geometric interpretations of Howard's Pass, the duplex model suggests that imbricate thrusting, folding, and bedding transposition rather than stratigraphic position are the main control on the distribution of SHMS ore at the deposit to district scale (Hodder *et al.*, 2014; Martel, 2017). The duplex model is a radical reinterpretation of the geometry and kinematic history of the Howard's Pass SHMS deposits. It has significant implications for the first-order controls on the spatial distribution of ore and the premise of stratigraphic control that underpins exploration for this deposit type (Martel, 2017).

Here we present preliminary results from a structural study of deformation in and around the XY group of deposits at the eastern end of the Howard's Pass district: XY Central (XYC), XY West (XYW), XY Nose (XYN), and the HP deposit (Fig. 2a). The goals of the study are to: (i) test the geometric and kinematic validity of the duplex model presented by Hodder *et al.*, (2014) and Martel (2017); (ii) assess how deformation history of the host rock package affected the sulphide orebodies; and (iii) determine the scale at which the distribution of ore is controlled by deformation. The data presented below represent the results of our initial, 2020, summer field season. The main focus of this field work was 1:10 000 scale lithostratigraphic and structural mapping in the XY area. A new geological map and section based on this mapping is shown in Figure 2. In addition, 1500 m of drill core was logged across 7 holes with 4 holes (XYC-206, XYC-228, XYC-235, XYC-298) located on Cross Section A-A' (Fig. 2b). Within some holes, only the mineralized portion was logged owing to time constraints. Logging focused on checking lithostratigraphic contacts and assessing structure in all lithostratigraphic units. This included documenting bedding-cleavage relationships, microfolding, veins, boudins, concretions, sulphide textures and all their overprinting relationships.

Geologic Setting

The Selwyn basin was initiated in the Neoproterozoic and sedimentation continued into the Mesozoic. The basin fill comprises rift (Neoproterozoic–Cambrian), continental margin (Cambrian to Mid-Devonian and Mississippian to Mesozoic), and backarc basin sediments (Mid-Devonian to Mississippian; Gordey and Anderson, 1993; Nelson *et al.*, 2013). Plate convergence on the northwestern margin of ancestral North America initiated in the Triassic and culminated in the Mid-Cretaceous Cordilleran orogeny (Gordey and Anderson, 1993; Mair *et al.*, 2006; Staples *et al.*, 2016; Monger and Gibson, 2019). During this orogeny the rocks of the Selwyn basin underwent significant shortening and now form a foreland fold-and-thrust belt that is wedged between the Mackenzie foreland fold-and-thrust belt and accreted exotic terranes along

a

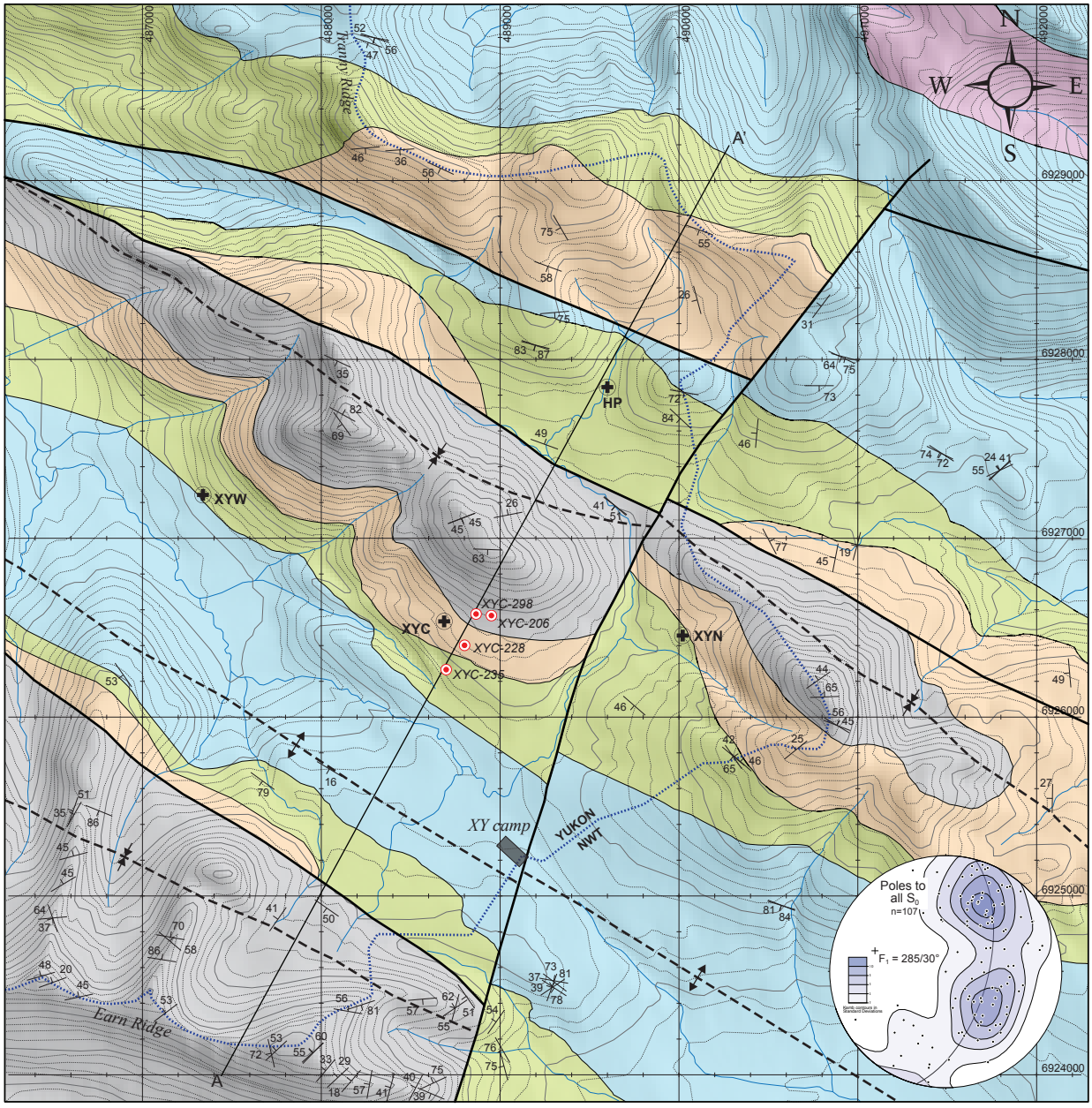

Legend

Devonian

Earn Group
Undifferentiated mudstone and sandstone. Dark to light grey finely laminated mudstone with <5 mm grey-black silty layers. Weathered outcrops show distinct maroon bands. Interbedded with cherty lenses 1-20 cm and silty limestone up to 1 m. Often forms shale when breaking along dense cleavage planes. Mudstone is variably calcareous. Sandstone is fine-grained with small, rounded chert and quartz granules. Matrix is beige-yellow with orange weathering and consists of subrounded chert clasts and lithic fragments. Seen as piles of rubble and not *in situ*. Massive sandstone blocks are cut by large quartz veins. Poorly sorted conglomerate is seen just outside of the field area.

Silurian to Early Devonian

Steel Formation
Medium to dark grey mudstone with strong orange weathering strongly expressed in outcrop and in talus. Small, <1 cm dark grey silty layers show "wispy" texture that does not weather as strongly. Associated with weathered pyrite cubes with quartz-calcite pressure shadows. Contains coarse, crystalline limestone concretions ranging from 1 cm up to 2 m. Concretions exhibit a strong, fetid odor when a fresh surface is exposed.

Early Ordovician to Silurian

Duo Lake Formation
Dark grey to black, recessively weathering, mudstone. Fine-grained, carbonaceous and locally calcareous. Interbedded with thin <1 cm dark grey silty bands, chert lenses up to 1 m and limestone beds from 1 cm to 2 m. Contains 1 cm blue bands of phosphate. Very fissile and forms pencil cleavage in outcrop. Locally graptolitic towards the top. Mineralization is hosted within the "Active Member" and sulphides (sphalerite, galena, pyrite) are seen in sedimentary beds and in spaced, sulphide rich dissolution seams that are axial planar to folds.

Cambrian to Early Ordovician

Rabbitkettle Formation
Dominantly fine-grained, crystalline light grey limestone layers up to 5 cm with a "wavy" texture interbedded in a rusty orange silty, argillaceous matrix with visible quartz and feldspar. Matrix is variably dolomitic. Different varieties show much thinner layers with laminae thickness <1 cm and no dolomite. Local layers of massive crystalline limestone with no internal textures.

Cambrian

Vampire Formation
Recessive weathering, dark grey to brown, mudstone, siltstone and interbedded sandstone. Not mapped as part of this study, but compiled from Gordey and Anderson, (1993)

XYC — Pb-Zn deposit
XYC-228 — Drillhole
84 — Bedding, S_0
Contact
Fault
Trace of S_1 axial plane cleavage (cross section)
F_1 synform
F_1 antiform
AM — Active member of Duo Lake (on cross section)

Universal Transverse Mercator Projection, Zone 9N. North American Datum 1983.

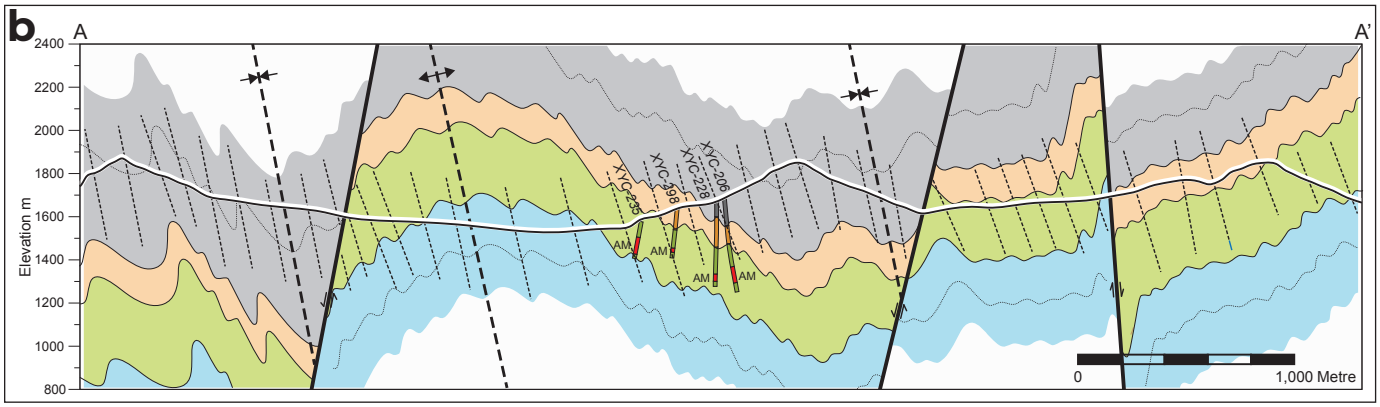

Figure 2. (a) *Geologic map of the 2020 field area with major fold axial traces, faults and cross section line shown. Stereonet of all bedding data collected in mapping area is shown in lower right (lower hemisphere projection, equal area).* ***(b)*** *Cross section A-A' through the XYC Deposit.*

the ancestral North American continental margin (Mair et *al*., 2006; Staples et *al*., 2016). Following regional deformation, the Selwyn basin was intruded by mid-Cretaceous granitoid rocks (Gordey and Anderson, 1993; Mair et *al*., 2006).

The oldest rocks within the Selwyn basin are the sandstone, shale and carbonate rocks of the Hyland Group which underlie the western Selwyn basin (Gordey and Anderson, 1993; Mair et *al*., 2006). These are constrained to the Neoproterozoic to early Cambrian age. The transition from carbonate platform sediments of the Mackenzie platform to basin facies occurs across a series of NW–SE to E–W trending normal faults (Eisbacher, 1981). The Hyland Group is overlain by a thick package of Cambrian to Middle Devonian strata that includes siltstone of the Cambrian Vampire Formation, shale of the Lower to Middle Cambrian Gull Lake Formation, siliceous limestone and calcareous shale of the Late Cambrian to Early Ordovician Rabbitkettle Formation, and carbonaceous shale, chert and mudstone of the Road River group, which comprises the Early Ordovician to Silurian Duo Lake Formation and Silurian to Early Devonian Steel Formation (Gordey and Anderson, 1993; Turner et *al*., 2011). Finally, the Earn Group was deposited during the Early to Middle Devonian and is characterized by a stratigraphically complex package of black siliceous shale, chert, mudstone, quartz-arenite, and conglomerate with unconformities and sharp variations in thickness and facies (Garizone et *al*., 1997). Regional metamorphic grade in the Howard's Pass region is constrained to sub-greenschist facies as estimated by Gordey and Anderson (1993).

The stratiform orebodies at Howard's Pass district comprise 15 separate Zn-Pb deposits distributed along a 40 km-long NW–SE trending corridor adjacent to the Yukon-Northwest Territories border. All the deposits of Howard's Pass are hosted in the Duo Lake Formation, which Morganti (1979) subdivided into four separate members that from bottom to top are: the Pyritic Siliceous Mudstone (PSMS), the Calcareous Mudstone (CCMS), the Active Member (ACTM), and the Upper Siliceous Mudstone (USMS). A Lower Cherty Mudstone was also broken out but is now combined with the CCMS. The Active Member is defined by the presence of fine-scale, bedding parallel, laminae of sphalerite, galena and pyrite and is the host for mineralization. In a recent study, Kelley et *al*., (2017) reported a Re-Os isochron age of 442 ± 14 Ma for 12 pyrite separates from the Don and XYC deposits at Howard's Pass. The textures of the pyrite are interpreted as being indicative of coeval deposition with sphalerite, and mineralization is considered to have occurred during the early Silurian, concurrent with sedimentation or early diagenesis.

Much of the stratiform ore at Howard's Pass exhibits hand specimen-scale tight folding of sulphide laminae with spaced sulphide-rich seams that crosscut the laminae at a high angle (Morganti, 1979; McClay, 1991; Jonasson and Goodfellow, 1986; Kelley *et al.*, 2017; Gadd *et al.*, 2016; Martel., 2017; Slack *et al.*, 2017). Jonasson and Goodfellow (1986) attribute the folding to Silurian tectonic deformation during compaction and dewatering of the sediments. Some of the crosscutting sulphide seams are attributed to dewatering and the formation of sulphide "concretionary pillars", while others are recognized as dissolution cleavage related to folding (Jonasson and Goodfellow, 1986). In the latter case dissolution has removed almost all of the quartz and/or carbonate to leave a very high concentration of sulphide and carbonaceous matter (McClay, 1991). The folding and pressure solution cleavage are now generally considered to be a product of Cordilleran rather than Silurian deformation (McClay, 1991; Gadd *et al.*, 2016, 2017; Martel, 2017).

Lithostratigraphy

The following section provides a brief description of the lithostratigraphic units within the mapped area shown in Figure 2. From oldest to youngest, these are: the Vampire, Rabbitkettle, Duo Lake, and Steel formations, and rocks of the Earn Group. The descriptions combine field observations made during this study with those of previous workers (Gordey and Anderson, 1993; Martel *et al.*, 2011; Gordey, 2013). The Vampire Formation was not mapped during this field season and is not described below.

Rabbitkettle Formation

The Rabbitkettle Formation is a thick package of limestone interbedded with shale that overlies the Vampire Formation around the XY deposits. Rabbitkettle comprises three lithofacies: wavy banded limestone, massive limestone and the transition zone (Fig. 3). The wavy banded limestone is the most common of the lithofacies in the study area. It consists of 1–5 cm thick crystalline limestone beds embedded in a rusty brown-orange, variably dolomitic and argillaceous matrix. Original descriptions by Morganti (1979) describe the "wavy" texture as nodular limestone. Wavy banded limestone outcrops display well-developed mesoscopic folding and good exposures are seen in the valley near the XY Camp. Massive Rabbitkettle limestone was only observed as large talus boulders at Tranny Ridge (Fig. 2a). This unit lacks compositional layering and comprises massive, grey, fine-grained crystalline limestone. The transition zone forms the top of the Rabbitkettle Formation and underlies the Duo Lake Formation. It is similar in composition to the wavy banded limestone but the laminae occur on the <1 cm scale (Fig. 4). The orange-brown layers are fine-grained argillaceous siltstone that contain variable amounts of dolomite.

Pratt (1992) correlated trilobite ages of the Late Cambrian (NTS 105P and NTS 105I). Gordey and Anderson (1993) reported a mid-Ordovician conodont age for the Rabbitkettle Formation in contact with Duo Lake Formation at Howard's Pass. Within the study area it is estimated to have a minimum thickness of between 650 and 700 m.

Duo Lake Formation

The Duo Lake Formation, part of the Road River Group, conformably overlies the Rabbitkettle Formation and is predominantly a dark grey to black, recessively weathering, shale (Fig. 5). The uppermost USMS Member of the Duo Lake is a siliceous, non-calcareous, massive, carbonaceous mudstone interbedded with light grey cherty mudstone and limestone up to 2 m thick. Graptolites are found in the upper 15 m of the unit. The unit shows abundant crystalline limestone concretions up to 1 m in diameter. Zones with cherty texture show strong conchoidal fracturing. Small blue bands <5 cm thick have been interpreted to be phosphatic by Slack *et al.*, (2017). Galena and sphalerite occur locally near the contact with the underlying Active Member, which is host to the mineralization at Howard's Pass. The Active Member is a 20 to 80 m thick repetitive sequence of carbonaceous mudstones, chert, limestone and economically significant Zn-Pb mineralization. Sphalerite and pyrite occur in planar laminae that are <0.5 cm thick. Within the laminae, pyrite is fine-grained and has a framboidal habit. Sphalerite is fine-grained and beige with a dull luster. In the diamond drill core examined in this study,

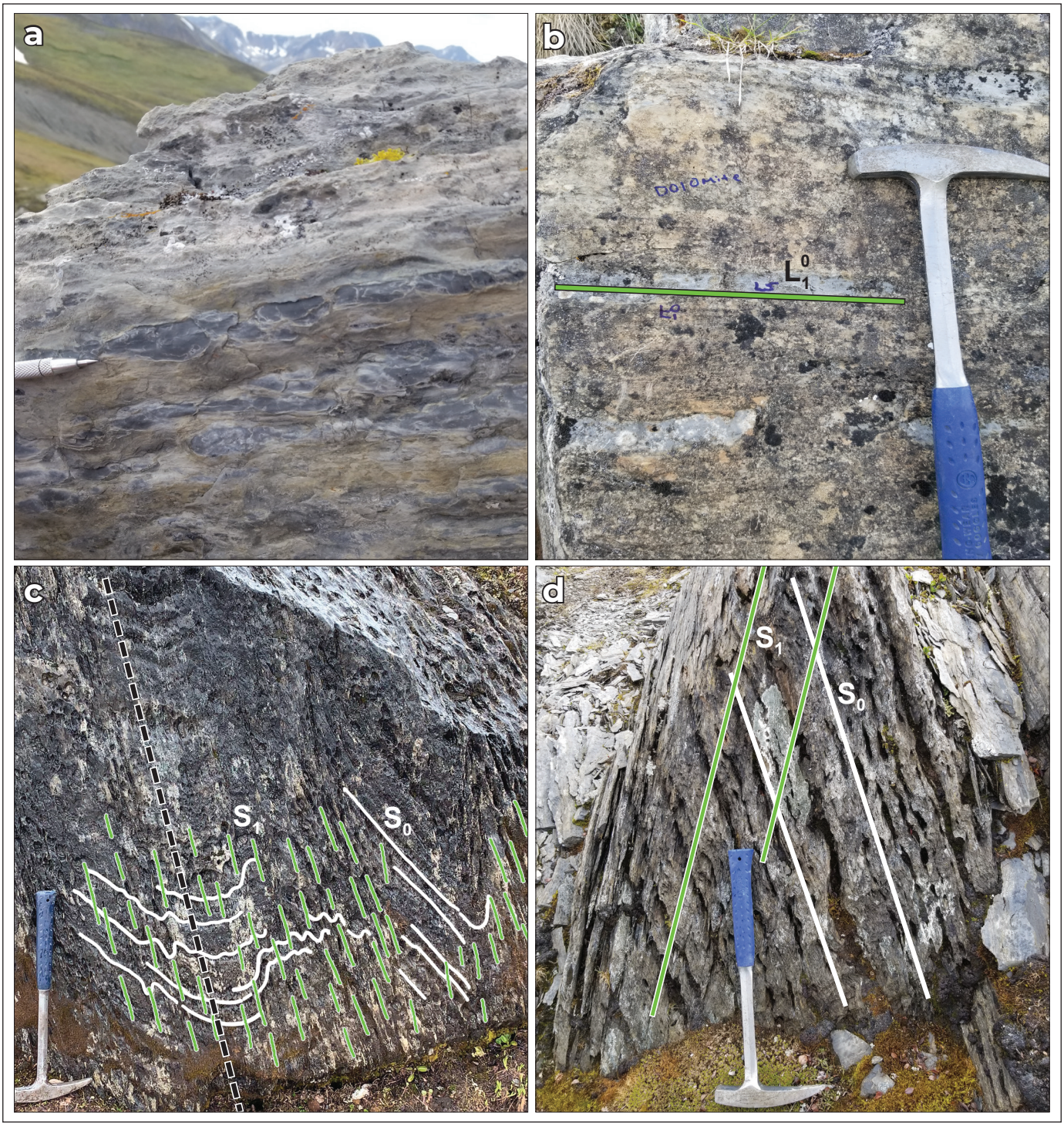

Figure 3. *Rabbitkettle Formation.* ***(a)*** *Wavy banded limestone interbedded with orange weathering silty mudstone.* ***(b)*** *Grey planar limestone beds within thicker dolomitic layers. The exposed face of the outcrop is parallel to* S_1 *and the trace of bedding defines the intersection lineation,* L_1^0 *(green line).* ***(c)*** *Mesoscopic folding within the Rabbitkettle limestone. Axial planar cleavage (*S_1*) shown by short green lines. Folded bedding* S_0 *are highlighted by white lines. The black dashed line defines the axial plane of the synform, 285/76°NE.* ***(d)*** *Rabbitkettle limestone with the* S_1 *cleavage indicated by green line and bedding,* S_0*, by white lines. Asymmetry indicates direction to nearest antiform is to the left of the image. Hammer and scribe for scale.*

galena was rarely observed in sulphide laminae. The CCMS Member is characterized by a lack of Pb and Zn mineralization. It is a massive, calcareous, carbonaceous, dark grey to black mudstone. Calcite occurs as cement within the mudstone or as small, <1 cm concretions. As the unit is massive, primary bedding is hard to identify. The lowermost PSMS Member is a massive, carbonaceous black mudstone with 1 to 10 mm long lenticular pyrite concretions. The PSMS Member is not present everywhere in the stratigraphic sequence and in places the CCMS Member is in conformable contact with the underlying Rabbitkettle Formation.

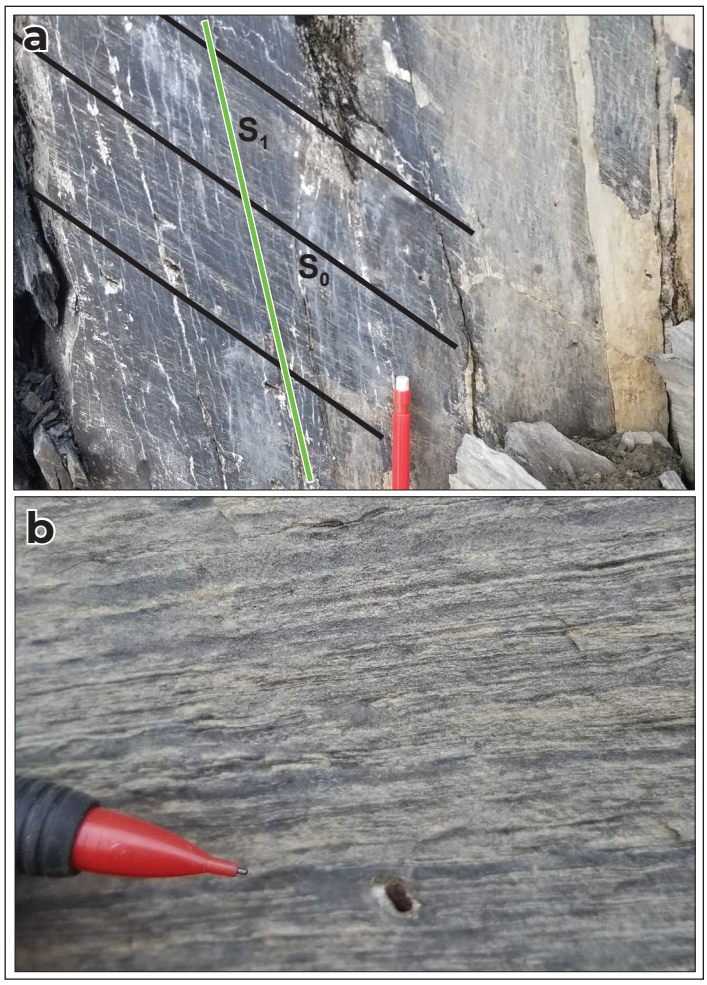

Figure 4. *Rabbitkettle Formation transition zone.* ***(a)*** *Thin (mm-thick) limestone layers (grey) with interbedded mudstone. Black lines highlight bedding, S_0. The green line highlights S_1.* ***(b)*** *Close up of (a) with pencil for scale. Weathered pyrite cube has a narrow calcite pressure shadow.*

Owing to the recessive nature of the Duo Lake members and the predominance of massive, black mudstone, it is hard to identify which members are exposed at surface unless visible sphalerite or galena is present which indicates the Active Member. The formation is well exposed around XYC, XYW, and XYN. It typically weathers grey-orange, but around the XY deposits, it bleaches to a yellow colour along cleavage planes. Conodont and macrofossils constrain the age of the Duo Lake Formation to be mid-Ordovician to Silurian (Cecil, 1982; Kelley *et al.*, 2017). The Duo Lake Formation has a total thickness of up to 300 m.

Steel Formation

The Steel Formation, also part of the Road River Group, overlies the Duo Lake Formation across a sharp, conformable boundary. The Steel Formation is an orange-weathering mudstone whose diagnostic colour provides a useful marker horizon in the district. Outcrops of Steel mudstone are relatively common in the XY area, most notably around the deposits at XYW, XYC, and XYN. Contacts between Steel and other units are well exposed in ridge facies and talus slopes. Fresh rocks of the Steel Formation are a light grey mudstone interbedded with dark grey carbonaceous layers that show a "wispy" texture (Fig. 6). The wispy bedding does not weather orange like the rest of the rock but becomes a light grey. Different workers have attributed wispy bedding to bioturbation by microorganisms (Gordey and Anderson, 1993). Weathered cubic pyrite grains with distinct pressure shadows of quartz and calcite are seen in both core and outcrop. Limestone concretions are abundant and can be up to 2 m in diameter (Fig. 6b). Concretions give off a strong fetid odor when broken. The unit's age is poorly constrained, but conodont assemblages provide a tentative range of Silurian to Upper Devonian (Gordey and Anderson, 1993). The Steel Formation has an estimated thickness of 100 to 150 m in the XY area.

Figure 5. *Duo Lake Formation.* **(a)** *Outcrop of Duo Lake black mudstone with distinct orange weathering from the south side of the XY Nose.* **(b)** *Weathered Duo Lake showing oblong blocks caused by preferential parting along S_1 (subvertical dip to right) and S_0 (gentle dip to left).* **(c)** *Diagnostic black cherty mudstone of Duo Lake Formation (Upper Siliceous Mudstone member). White fracture fill is probably clay minerals. Hammer and notebook for scale.*

Figure 6. *Steel Formation.* ***(a)*** *Outcrop north of XYC (looking 270) with well-developed cleavage-bedding asymmetry. S_1 is 255/79°N and indicated by green line. Bedding, S_0, (white line) is 110/58°S. Cleavage-bedding asymmetry indicates antiform to the right of the image.* ***(b)*** *Fetid limestone concretion. Found from the cm scale up to >1 m. Orange weathering talus that is diagnostic of Steel Formation litters the ground around the concretion.* ***(c)*** *Intersection lineation (L^0_1) of bedding on S_1 cleavage surface (green line). Characteristic bioturbated "wispy" bedding is prominent in this outcrop.* ***(d)*** *Similar to (c), with L^0_1 intersection lineation (green line) of bedding on weathered S_1 cleavage face. Hammer and pencil for scale.*

Earn Group

The Earn Group is the youngest unit exposed in the field area and consists of finely laminated mudstone interbedded with fine-grained sandstone. Just outside the field area in the south and west, large ridges of poorly sorted pebble conglomerate dominate. The Earn mudstone is medium to dark grey, with maroon laminae up to 5 cm thick (Fig. 7). The mudstone is typically interbedded with thin, <1 cm silty layers and cherty beds up to 1 m thick. The unit breaks readily along cleavage planes where they are well-developed in outcrop (Fig. 7a). Bedding is generally planar. The Earn sandstone is fine to medium grained with small, well-rounded chert and quartz grains. It is beige-yellow with orange weathering. Outcrops of sandstone are rare and it is rarely seen *in situ*. Gordey and Anderson (1993) have mapped the Earn Group rocks in the field area as the Portrait Lake Formation and give its age as Early to Late Devonian.

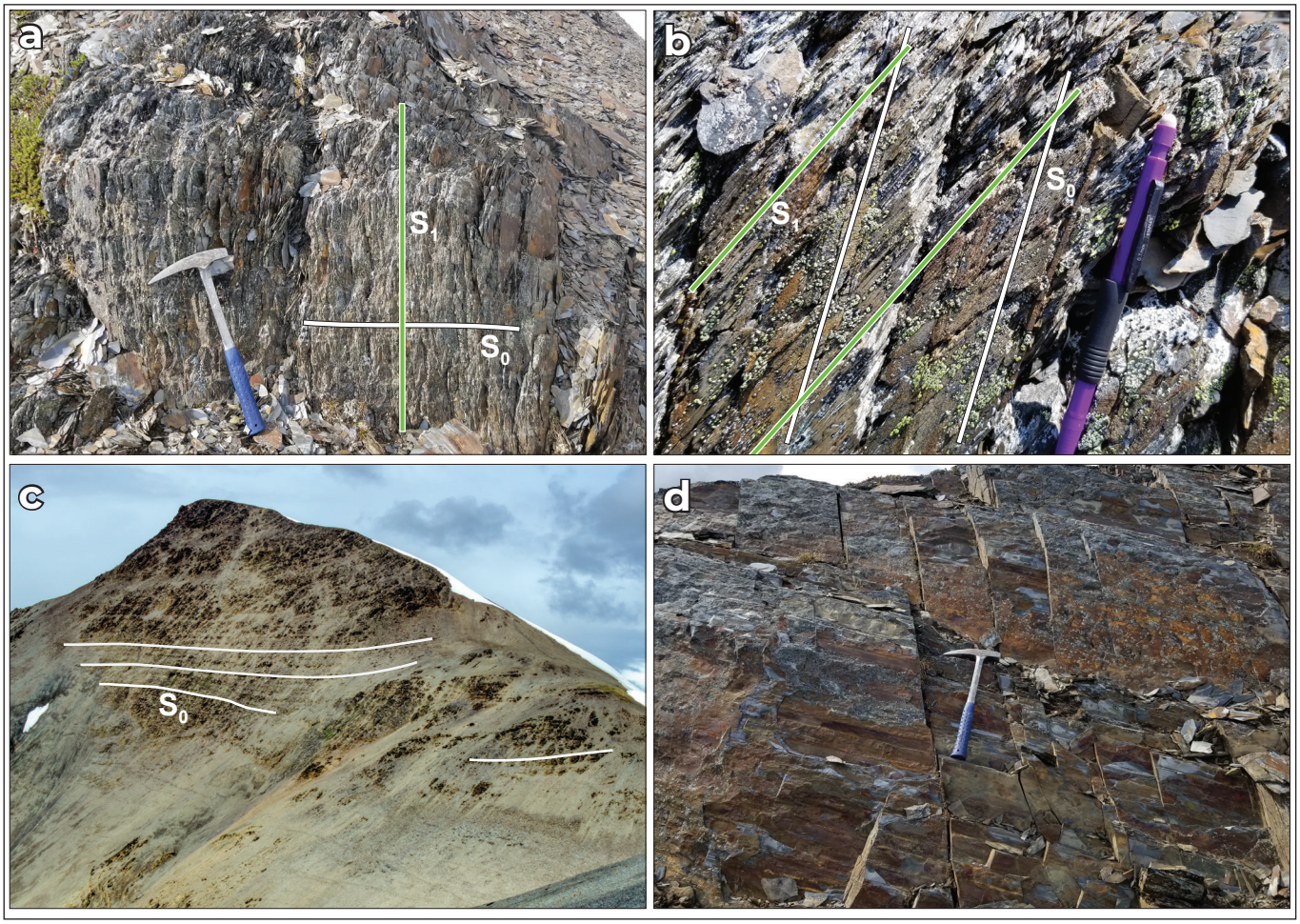

Figure 7. *Earn Group.* ***(a)*** *Highly fissile Earn mudstone with S_1 slaty cleavage (green line) perpendicular to bedding, S_0 (white line) in hinge zone of F_1 fold.* ***(b)*** *Well-developed cleavage-bedding relationship. The S_1 cleavage (green line) is 310/58°NE and bedding, S_0 (white line), is 293/75°NE. Asymmetry indicates antiform to the left of the image.* ***(c)*** *Bedding, S_0, dipping moderately into the ridge face on south limb of the XY Syncline.* ***(d)*** *Blocky Earn Group strata with distinct maroon weathering. Hammer and pencil for scale.*

Structure

Methodology

Structural mapping focused on determining the geometric relationship of primary compositional layering, bedding (S_0), relative to the dominant foliation developed at the hand specimen to outcrop scale. The goal was twofold: firstly, to use bedding-cleavage asymmetry at the mesoscopic scale to determine the direction to antiform (vergence; Figs. 3d, 6a, 7b) and map out the geometry of folds at the macroscopic scale (e.g., Bell and Hickey, 1998; Hickey and Bell, 2001). Secondly, to evaluate the evidence for the transposition of bedding within a duplex structure and any fabrics indicating significant non-coaxial shear attributed to intense ductile deformation by Martel (2017).

Bedding was readily identified in most outcrops across the study area. It is discernable from the hand specimen scale to the macroscopic scale; being evident on mountain sides (Fig. 7c) and in satellite imagery of the whole XY region. In units of the Rabbitkettle Formation, bedding is most commonly manifested as interlayered, variably dolomitized, limestone bands and argillaceous silt layers (Figs. 3a,b and 4). Within Duo Lake Formation mudstones, bedding is defined by thin, <1 cm, bands of siltstone. In the more siliceous sections of the Duo Lake Formation, careful inspection is needed to identify such siltstones in individual outcrops. Bedding in the Steel Formation is evident as bioturbated silt layers (Fig. 6a,c,d). In the Earn Group rocks, bedding is most readily visible as mudstone interbedded with laminae and thin beds of siltstone (Fig. 7a,b). In more massive, coarse-grained, sandstone and conglomeratic units of the Earn Group, bedding planes are less obviously discernable at the outcrop scale.

F_1 Folding

Figure 8 presents a summary of structural data collected across the XY area during the 2020 field season. Our structural mapping is consistent with the XY area having been affected by one main phase of folding, F_1. Folds are developed at all scales with a well-developed axial planar foliation, S_1. The best examples of mesoscopic F_1 folds occur in wavy banded units of the Rabbitkettle Formation (Fig. 3c), but they are developed in all stratigraphic units. F_1 folds are upright (Fig. 2b) and S_1 has a subvertical to steep NNE dip (Fig. 8a). L_1^0 intersection lineations have a horizontal to gentle WNW plunge (Fig. 8b).

S_1–S_0 asymmetry (vergence) identified three macroscopic steep, NNE dipping, F_1 folds in the XY area (Figs. 2 and 8): a synform centered on the Earn Ridge south of the XY Camp with an approximate trend and plunge of 299/30°; an antiform that passes through the area of the XY Camp immediately south of the deposit with a trend and plunge of approximately 300/20°; and another synform along the topographic ridge immediately northeast of XY and XYN with an approximate trend and plunge of 300/20°. Outcrops northeast of the central synform have a consistent S_1–S_0 asymmetry indicating the presence of another macroscopic antiform somewhere to the northeast of the study area (Figs. 2a and 8b). Although F_1 folds at the outcrop scale can be open to close in terms of interlimb angle (Fleuty, 1964), the macroscopic F_1 folds have an open geometry with wavelengths and amplitudes of ~4 km and ~700 m respectively (Fig. 2b). The study area was split into three separate zones (south, central and north) based on the density of data points gathered during the field season. Structural data for each of these zones are presented on stereonets in Figure 8.

S_1 Cleavage

In all lithostratigraphic units except the Active Member of the Duo Lake Formation, S_1 is typically manifested as a well-developed slaty cleavage comprising penetrative dissolution seams that are axial planar to F_1 folds at all scales (Fig. 9). S_1 was the only penetrative foliation observed in the XY area. No evidence was found for an earlier foliation at a low angle or subparallel to S_0, and S_1 was not observed to transpose S_0 to any significant extent. Variable degrees of S_1 refraction across bedding contacts is common in the limbs of mesoscopic F_1 folds (Fig. 10a,b), especially in Rabbitkettle Formation and Earn Group units and this can decrease the cleavage-bedding obliquity in less competent units. However, at the outcrop scale S_0 has an enveloping surface that is always oblique to S_1 and changes in cleavage-bedding asymmetry reflect a switch in vergence across F_1 fold hinges.

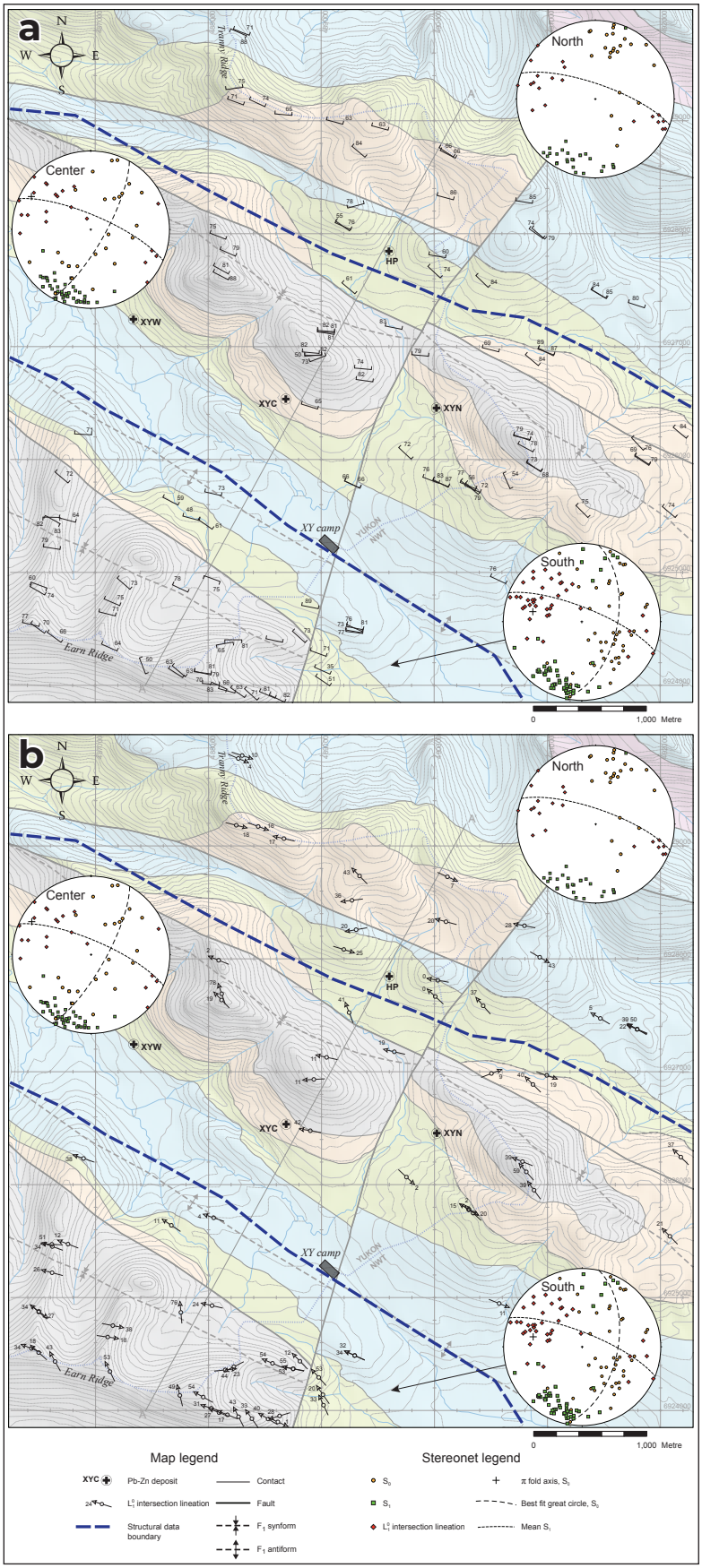

Sulphide Seams

Mineralized laminae intersected in drill core through the Active Member at XYC are commonly crosscut by sulphide-rich seams that are up to 0.5 cm wide (Fig. 9). In areas of high Zn + Pb grade (~30% Zn, 15% Pb) the seams have a spacing of about 1 cm, and are typically at a high angle to bedding laminae. Sphalerite and pyrite are common within the laminae and seams. Where present, galena tends to be concentrated more in the sulphide seams. Pyrite, sphalerite and galena are coarser grained within the seams than the laminae they cut across (Fig. 10c,d). Sulphide grain size is finer on the edge of the seam than the center (coarse grains are up to 3 mm). The sulphide seams also contain a high amount of carbonaceous material. Sphalerite often occurs as inclusions within larger pyrite grains. Sphalerite shows a lighter colour within the sulphide seam and a darker colour in the laminae when viewed in plane polarized light. Locally, sulphide seams transition along their length into spaced dissolution cleavage with a more stylolitic texture in intervening layers of carbonaceous mudstone, chert or limestone. These dissolution cleavages are axial planar to microfolds and are interpreted as being S_1. In the core we have logged to date, no evidence has been found to suggest that the sulphide seams are a different generation to S_1 in the intervening layers (no significant obliquity and no overprinting relationships). Consequently, the sulphide seams are considered to be an expression of S_1 in sulphide-rich laminae.

Figure 8. ***(a)*** *Overlay map of* S_1. ***(b)*** *Overlay map of* L^0_1 *intersection lineation. The mapping area has been subdivided into three structural zones based on data density: North zone (north of the XY deposits); Center zone (centered on the XY deposits); and South zone (south of XY camp). Structural data for each zone is presented on a separate stereonet (lower hemisphere projection, equal area). See Figure 2 for explanation of geological units.*

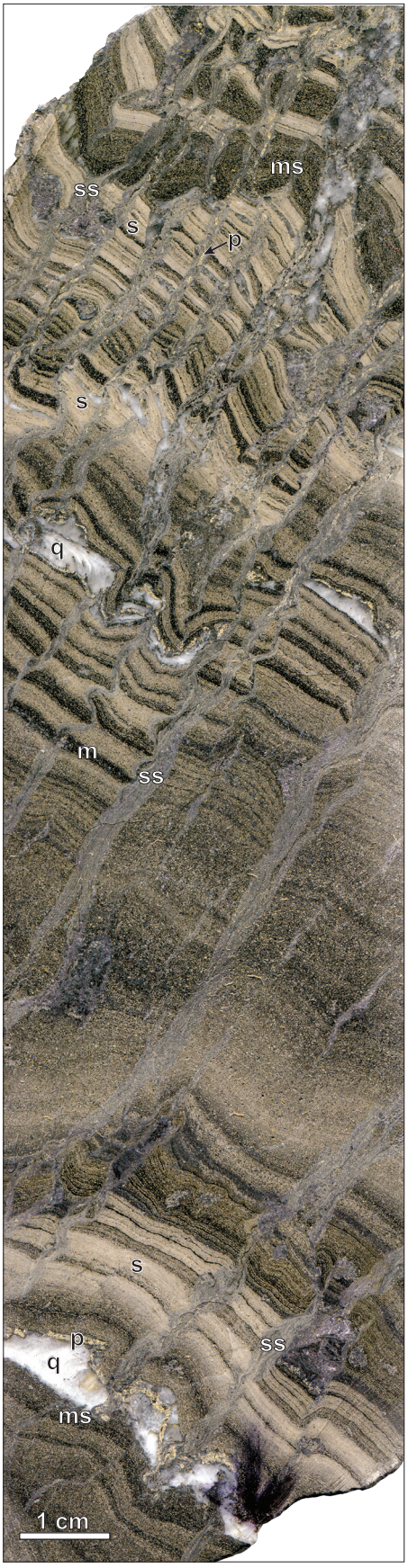

S_k Kinks

A set of kink bands, S_k, that overprint S_0 and S_1 are developed in Earn Group mudstones and Rabbitkettle wavy banded limestone at a limited number of locations across the study area (Fig. 11). The kink bands have moderate to subvertical dip and a NNW to NNE strike. An area with well-developed S_k, is developed in Earn Group rocks spatially adjacent to the trace of a steep, NW–SE striking, fault on the southern limb of the antiform just south of the XY deposits (Fig. 11a), suggesting the kinks may be linked to movement on that structure. This is also exhibited in the northwestern part of the field area where kinks in the Rabbitkettle wavy banded limestone (Fig. 11b) are observed directly adjacent to a NNE–SSW extensional fault.

Faults

Several WNW and NNE striking faults that postdate F_1 folding occur in the study area. Mapping constraints on their trace across topography indicate that they are steeply dipping structures. Relative displacement of folds and stratigraphic contacts suggest predominantly normal dip-slip movement. In the southern part of the mapping area, a steeply SW dipping fault SW of the XY Camp omits a thin layer of Steel Formation and juxtaposes younger Devonian rocks of the Earn Group against the older Silurian Duo Lake Formation. Just north of XYC and XYN, rocks of the Earn Group are juxtaposed against Duo Lake Formation across a steep SW dipping fault. Farther to the east and west, Steel wraps around topography on the northern limb of the synform that hosts the XY deposits. Between the two deposits, there is no Steel Formation exposed and Earn Group is in contact with Duo Lake Formation across the fault, indicating a normal sense of displacement. A NNE–SSW striking extensional fault is mapped down-dropping rocks of the Steel Formation against Rabbitkettle Formation. These faults are not well exposed at surface.

Figure 9. *Drill core through a deformed section of the Active Member at the XYC deposit. Sulphide-rich and mudstone laminae are crosscut at a high angle by sulphide seams. The sulphide-rich laminae and the sulphide seams are largely made up of sphalerite and pyrite. Galena was rarely identified and is concentrated in the seams rather than the laminae. m = mudstone; ms = mudstone with disseminated sulphide; s = sulphide-rich laminae; p = pyrite; ss = sulphide seam; q = extensional quartz veinlets. Core is from XYC-235 at 86.70 m.*

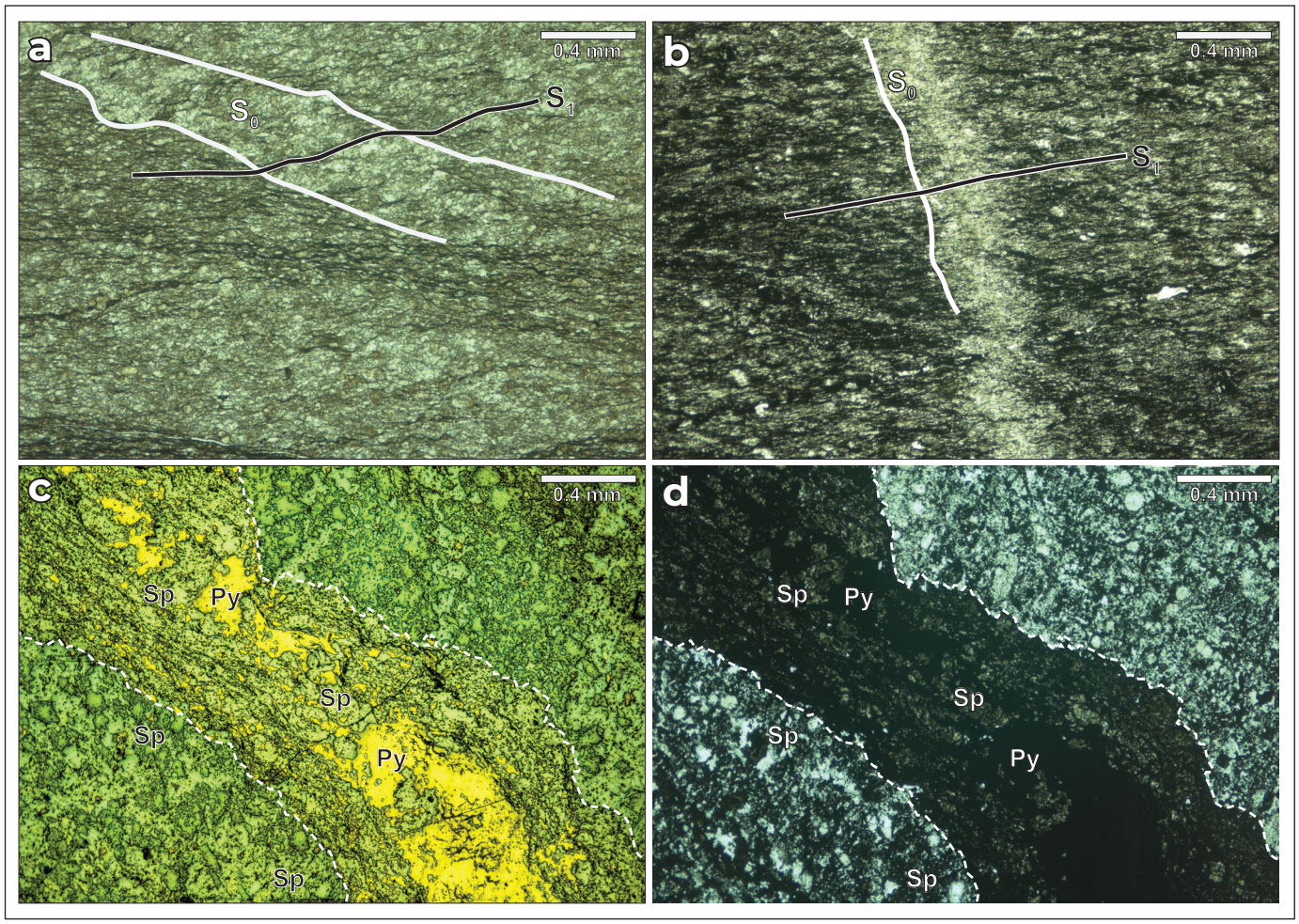

Figure 10. (a) *PPL image of bedding, S_0 (white line), and S_1 slaty cleavage (black line) within Rabbitkettle wavy banded limestone. S_1 refracts slightly across bedding laminae.* ***(b)*** *PPL image of bedding, S_0 (white line), and S_1 slaty cleavage (black line) within the USMS Member of the Duo Lake Formation. S_1 is at a high angle to S_0 indicative of an F_1 hinge zone.* ***(c)*** *Reflected light image from the Active Member of the Duo Lake Formation. Sulphide-rich seam (highlighted by dashed white lines) crosscuts sulphide-rich laminae making up the wall rock. Coarse-grained pyrite fills the center of the sulphide seam. Sphalerite occurs in the sulphide seam and in the surrounding wall rock. Sphalerite is lighter coloured in the seam than in the wall rock.* ***(d)*** *Same image in plane polarized light (PPL). Pyrite is opaque. Sphalerite is slightly anisotropic. Sp = sphalerite; Py = pyrite. Scale bar is 0.4 mm on all images.*

Although most of the faults identified in this study are thought to be normal faults, a steep fault with an apparent backthrust geometry is exposed in Earn Group rocks just W of the SW corner of the mapping area (Fig. 12). Bedding on the south side dips approximately 50° NNW. Across the fault, bedding is rotated to a steeper, subvertical dip.

Discussion

Our first season of mapping indicates that the cluster of XY deposits at Howard's Pass has been affected by one main deformation event that folded the host sedimentary strata into a series of upright to steeply NNE dipping, gently WNW to NW plunging folds (Figs. 2 and 8). These folds are part of a regional Cordilleran fold set that are extensively developed along the northeastern half of the Selwyn basin (Gordey and Anderson, 1993). The axial planar cleavage, S_1, is

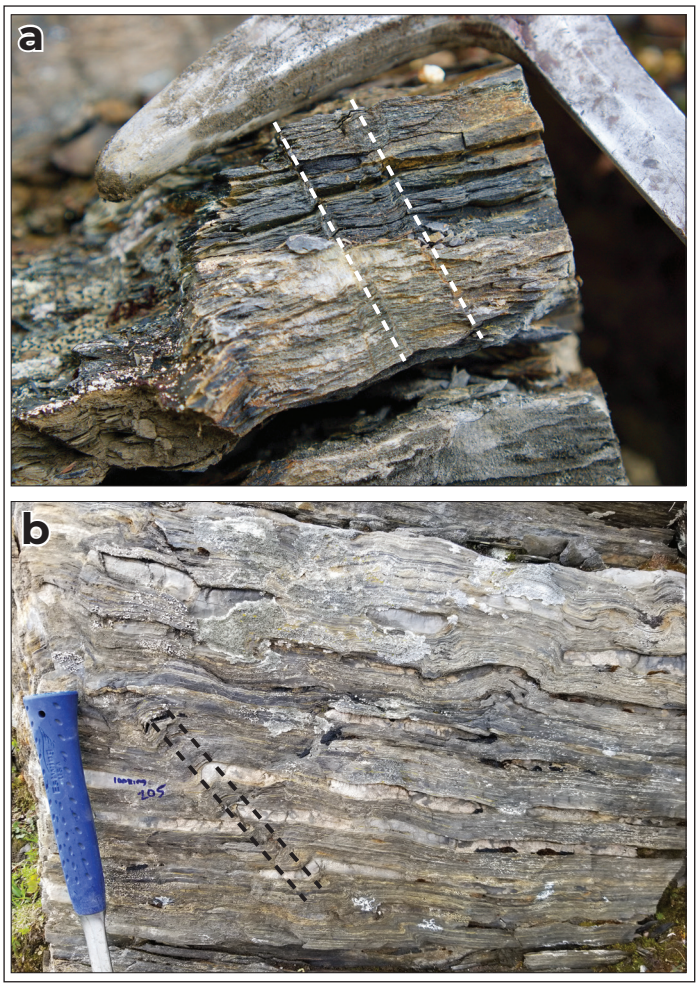

Figure 11. ***(a)*** *Kink banding (white dashed lines) within the Earn Group mudstone in the southern field area (NAD83/UTM9N, 486612 E, 6925420 N).* ***(b)*** *Kink banding (black dashed line) within Rabbitkettle limestone adjacent to normal fault at 490924 E, 6928012 N (NAD83/UTM9N).*

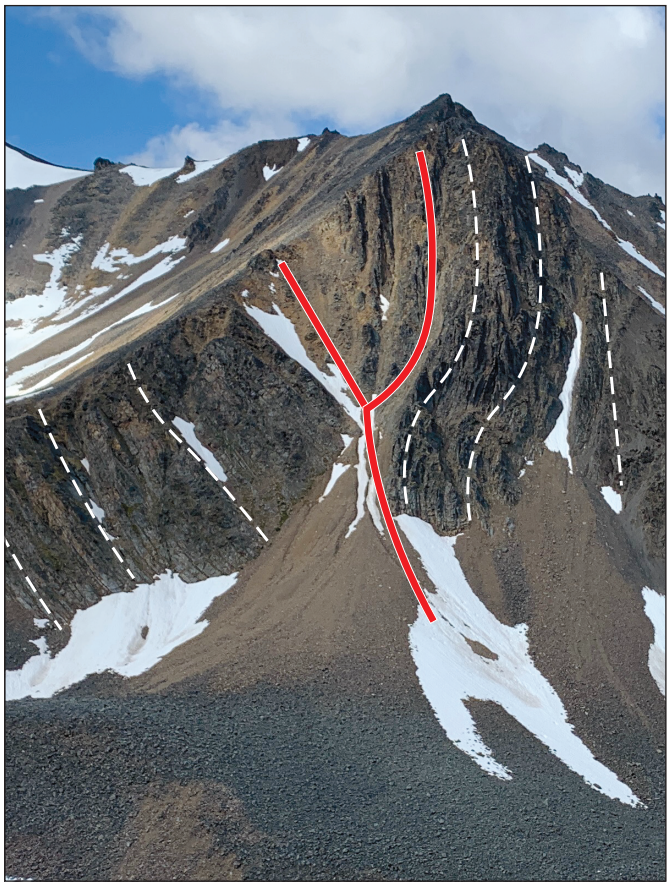

Figure 12. *Backthrust in Earn Group rocks just outside the SW corner of the mapping area (at NAD83/UTM9N, 485625 E, 6924848 N). Bedding appears to be dipping ~50° NW and is rotated to subvertical across the trace of the thrust. White dashed lines highlight bedding. Red lines highlight the thrust trace.*

also regionally developed (McClay, 1991; Gordey and Anderson, 1993). The distribution of host rock units in the XY region and the mapped changes in vergence determined from bedding-cleavage asymmetry and minor fold asymmetry are consistent with a conformable, folded, stratigraphic sequence. There are no mapped stratigraphic relationships identified to date that require the presence of significant thrusts to explain the geometry of mapped lithostratigraphic units. In that respect, our results are at odds with Martel (2017) who suggests that thrusts are needed to explain the geometry of lithostratigraphic units in the Howard's Pass district. Similarly, we did not observe any structural evidence for the thrust duplex proposed by Hodder et al., (2014) and Martel (2017). The steeply dipping S_1 slaty cleavage is well developed in almost every rock type and is kinematically linked to the development of F_1 folds at all scales. No other mylonitic foliation was observed and there is no evidence for extensive transposition of bedding prior to the development of S_1. The transition zone at the top of the Rabbitkettle Formation has been described as a mylonitic basal thrust by Martel (2017), but in outcrops visited as part of this study S_1 is the only foliation present and its angular relationship to S_0 is a function of its relative location across an F_1 fold.

It is possible that there are some thrusts present in the XY area, and one possible backthrust exposed in Earn Group rocks (Fig. 12) is supportive of that possibility. However, it is unlikely that any such thrusts have significant displacement across them. Smaller scale thrusts might be an explanation for multiple intersections of the Active Member of the Duo Lake Formation in several drillholes at XY (Martel, 2017), although tight F_1 folding might be more likely. At the deposit to district scale, our mapping is consistent with the distribution of ore being primarily a stratigraphic control (the Active Member) with local reconcentration of sulphides in dissolution cleavages (the sulphide seams) occurring at the hand specimen to microscopic scale (Figs. 9 and 10c,d).

A post-folding series of steeply dipping, WNW and NNE striking faults overprint the regional F_1 folds, and an observed kink fabric, S_k, may be associated with movement on these structures. As the timing on these faults are poorly constrained, it is possible that they have been reactivated several times in the past and that the current apparent displacement may be a product of more than one period of movement. Although no feeder structures for the mineralization have been identified at Howard's Pass, it is possible that one of the mapped faults might represent a Silurian structure that controlled the upwelling of hydrothermal metalliferous fluid. Cordilleran reactivation of such faults might make it difficult to identify them as feeder structures.

Future Work

The work presented in this report is based on one, initial season of mapping at Howard's Pass. Additional microstructural analysis of oriented samples and of drill core collected as part of that fieldwork will be undertaken to evaluate the kinematic evidence for significant non-coaxial shear as proposed by Martel (2017). Next year, additional mapping around the XY region will be focused on understanding the geometry of the faults mapped this year and evaluate evidence for the sense of slip across them. Detailed mapping of lithofacies on either side of the faults will help determine if any of these faults were active at the time of sedimentation. Additionally, the mapping area will be extended to the south to compare and integrate the regional structure into our interpretation of the geometry at Howard's Pass and see how structural complexity changes across regional structures.

Acknowledgements

This work was conducted as part of Darius Kamal's MSc Thesis at the University of British Columbia and represents the results of the 2020 field season. We would like to thank Gabe Xue for his help and support of the project, Joe Haggett for helping us figure out camp logistics during a very unique summer, and John Xu for his help as a field assistant. Selwyn Chihong Limited is thanked for the financial support of this project. Thank you to Dr. Murray Allan of Teck Resources Ltd. for reviewing this paper prior to submission. This project is funded in part by a Natural Sciences and Engineering Research Council of Canada (NSERC) Discovery Grant (RGPIN-2019-05457) to KAH.

References

Bell, T.H. and Hickey, K.A., 1998. Multiple deformations with successive subvertical and subhorizontal axial planes in the Mount Isa region: Their impact on geometric development and significance for mineralization and exploration. Economic Geology, vol. 93, p. 1369–1389.

Cecile, M.P., 1982. The lower Paleozoic Misty Creek Embayment, Selwyn basin, Yukon and Northwest Territories. Geological Survey of Canada, Bulletin 335, 78 p.

De Vera, J., McClay, K.R. and King, A.R., 2004. Structure of the Red Dog district, western Brooks Range, Alaska. Economic Geology, vol. 99, p. 1415–1434.

Eisbacher, G.H., 1981. Sedimentary tectonics and glacial record in the Windermere Supergroup, Mackenzie Mountains, north-western Canada. Geological Survey of Canada, Paper 80-27, 40 p.

Emsbo, P., Seal, R.R., Breit, G.N., Diehl, S.F. and Shah, A.K., 2016. Sedimentary exhalative (sedex) zinc-lead-silver deposit model. US Geological Survey, Scientific Investigations Report 2010-5070-N, 57 p.

Fleuty, M.J., 1964. The description of folds. Proceedings of the Geologists' Association, vol.75, p. 461–492.

Gadd, M.G., Layton-Matthews, D., Peter, J.M. and Paradis, S.J., 2016. The world-class Howard's Pass SEDEX Zn-Pb district, Selwyn Basin, Yukon. Part I: trace element compositions of pyrite record input of hydrothermal, diagenetic, and metamorphic fluids to mineralization. Mineralium Deposita, vol. 51, p. 319–342.

Gadd, M.G., Layton-Matthews, D., Peter, J.M., Paradis, S. and Jonasson, I.R., 2017. The world-class Howard's Pass SEDEX Zn-Pb district, Selwyn Basin, Yukon. Part II: the roles of thermochemical and bacterial sulfate reduction in metal fixation. Mineralium Deposita, vol. 52, p. 405–419.

Garizone, C.N., Patchett, P.J., Ross, G.M. and Nelson, J., 1997. Provenance of Paleozoic sedimentary rocks in the Canadian Cordilleran miogeocline: A Nd isotopic study. Canadian Journal of Earth Sciences, vol. 34, p. 1603–1618.

Gibson, G.M., Hutton, L.J. and Holzschuh, J., 2017. Basin inversion and supercontinent assembly as drivers of sediment-hosted Pb–Zn mineralization in the Mount Isa region, northern Australia. Journal of the Geological Society, vol. 174, p. 773–786.

Goodfellow, W.D., 2004. Geology, genesis and exploration of SEDEX deposits, with emphasis on the Selwyn Basin, Canada. *In:* Sediment-hosted Lead-Zinc Sulphide Deposits: Attributes and models of some major deposits of India, Australia and Canada, M. Deb and W.D. Goodfellow (eds.), Narosa Publishing House, Delhi, India, p. 24–99.

Goodfellow, W.D., 2007. Base metal metallogeny of the Selwyn Basin, Canada. *In:* Mineral Deposits of Canada: A Synthesis of Major Deposit-types, District Metallogeny, the Evolution of Geological Provinces and Exploration Methods, W.D. Goodfellow (ed.), Geological Association of Canada, Special Publication 5, p. 553–579.

Goodfellow, W.D. and Jonasson, I.R., 1986. Environment of formation of the Howards Pass (XY) Zn-Pb deposit, Selwyn Basin, Yukon. *In:* Mineral deposits of northern Cordillera, J.A. Morin (ed.), Canadian Institute of Mining and Metallurgy, Special Volume 37, p. 19–50.

Goodfellow, W.D. and Lydon, J.W. 2007. Sedimentary exhalative (SEDEX) deposits. *In:* Mineral Deposits of Canada: A Synthesis of Major Deposit-types, District Metallogeny, the Evolution of Geological Provinces and Exploration Methods, W.D. Goodfellow (ed.), Geological Association of Canada Special Publication 5, p. 163–183.

Gordey, S.P., 2013. Evolution of the Selwyn basin region, Sheldon Lake and Tay River map areas, central Yukon. Geological Survey of Canada, Bulletin 599, 176 p.

Gordey, S.P. and Anderson, R.G., 1993. Evolution of the northern Cordilleran miogeocline, Nahanni map area (105I), Yukon and Northwest Territories. Geological Survey of Canada, Memoir 428, 214 p.

Hickey, K.A. and Bell, T.H., 2001. Resolving complexities associated with the timing of macroscopic folds in multiply deformed terrains: The Spring Hill synform, Vermont. Geological Society of America Bulletin, vol. 113, p. 1282–1298.

Hodder, R., Bain, D.J. and Martel, E., 2014. Interpretive structural geology map and cross- sections of the Howard's Pass Pb-Zn district, Yukon and Northwest Territories. Northwest Territories Geoscience Office, NWT Open File 2014–02, 1 sheet, 1:50 000 scale and digital files.

Hoggard, M.J., Czarnota, K., Richards, F.D., Huston, D.L., Jaques, A.L. and Ghelichkhan, S., 2020. Global distribution of sediment-hosted metals controlled by craton edge stability. Nature Geoscience, vol. 13, p. 504–510.

Johnson, C.A., Slack, J.F., Dumoulin, J.A., Kelley, K.D. and Falck, H., 2018. Sulfur isotopes of host strata for Howards Pass (Yukon–Northwest Territories) Zn-Pb deposits implicate anaerobic oxidation of methane, not basin stagnation. Geology, vol. 46, 619–622.

Jonasson, I.R. and Goodfellow, W.D., 1986. Sedimentary and diagenetic textures, and deformation structures within the Sulphide zone of the Howards Pass (XY) Zn-Pb deposit, Yukon and Northwest Territories. *In:* Mineral deposits of northern Cordillera, J.A. Morin (ed.), Canadian Institute of Mining and Metallurgy, Special Volume 37, p. 51–70.

Kelley, K.D., Dumoulin, J.A. and Jennings, S., 2004. The Anarraaq Zn-Pb-Ag and barite deposit, northern Alaska: Evidence for replacement of carbonate by barite and Sulphides. Economic Geology, vol. 99, p. 1577–1591.

Kelley, K.D., Selby, D., Falck, H. and Slack, J.F., 2017. Re-Os systematics and age of pyrite associated with stratiform Zn-Pb mineralization in the Howards Pass district, Yukon and Northwest Territories, Canada. Mineralium Deposita, vol. 52, p. 317–335.

Kirkham G., Dunning J. and Schleiss W., 2012. Update for Don deposit mineral resource estimate, Howard's Pass property, eastern Yukon. Selwyn Resources Ltd., NI 43–101 Technical Report, 145 p.

Leach, D.L., Sangster, D.F., Kelley, K.D., Large Ross, R., Garven, G. and Allen, C.R., 2005. Sediment-hosted Pb-Zn Deposits: a global perspective. *In:* Economic Geology One Hundredth Anniversary Volume, J.W. Hedenquist, J.H.F. Thompson, R.J. Goldfarb and J.P. Richards (eds.), Society of Economic Geologists, p. 561–608.

Leach, D.L., Bradley, D.C., Huston, D., Pisarevsky, S.A., Taylor, R.D. and Gardoll, S.J., 2010. Sediment-Hosted Lead-Zinc Deposits in Earth History. Economic Geology, vol. 105, p. 593–625.

Magnall, J.M., Gleeson, S.A., Stern, R.A., Newton, R.J., Poulton, S.W. and Paradis, S., 2016. Open system sulphate reduction in a diagenetic environment–Isotopic analysis of barite (δ34S and $\delta^{18}O$) and pyrite ($\delta^{34}S$) from the Tom and Jason Late Devonian Zn–Pb–Ba deposits, Selwyn Basin, Canada. Geochimica et Cosmochimica Acta, vol. 180, p. 146–163.

Mair, J.L., Hart, C.J.R. and Stephen, J.R., 2006. Deformation history of the northwestern Selwyn basin, Yukon, Canada: Implications for orogen evolution and mid-Cretaceous magmatism. Geological Society of America Bulletin, vol. 118, p. 304–323.

Martel, E., 2017. The Importance of Structural Mapping in Ore Deposits–A New Perspective on the Howard's Pass Zn-Pb District, Northwest Territories, Canada. Economic Geology, vol. 112, p. 1285–1304.

Martel, E., Turner, E.C. and Fischer, B., 2011. Geology of the central Mackenzie Mountains of the northern Canadian Cordillera, Sekwi Mountain (105P), Mount Eduni (106A) and northwestern Wrigley Lake (95M) map-areas, Northwest Territories. Northwest Territories Geological Survey, NWT Special Volume 1.

McClay, K.R., 1991. Deformation of stratiform Zn-Pb (-barite) deposits in the northern Cordillera. Ore Geology Reviews, vol. 6, p. 435–462.

Monger, J.W. and Gibson, H.D., 2019. Mesozoic–Cenozoic deformation in the Canadian Cordillera: the record of a "Continental Bulldozer"? Tectonophysics, vol. 757, p. 153–169.

Morganti, J.M., 1979. The geology and ore deposits of the Howard's Pass area, Yukon and Northwest Territories: The origin of basinal sedimentary stratiform Sulphide deposits. Unpublished PhD thesis, University of British Columbia, Vancouver, BC, 327 p.

Nelson, J., Colpron, M. and Israel, S., 2013. The Cordillera of British Columbia, Yukon, and Alaska: Tectonics and Metallogeny. Society of Economic Geologists, Special Publication, vol. 17, p. 53–100.

Perkins, W.G, 1997. Mount Isa lead-zinc orebodies: Replacement lodes in a zoned syndeformational copper-lead-zinc system? Ore Geology Reviews, vol. 12, p. 61–110.

Pratt, B.R., 1992. Trilobites of the Marjuman and Steptoean stages (Upper Cambrian), Rabbitkettle Formation, southern Mackenzie Mountains, northwest Canada. Canadian Society of Petroleum Geologists and Geological Association of Canada, Palaeontographica Canadiana no. 9, p. 179.

Slack, J.F., Falck, H., Kelley, K.D. and Xue, G.G., 2017. Geochemistry of host rocks in the Howards Pass district, Yukon-Northwest Territories, Canada: implications for sedimentary environments of Zn-Pb and phosphate mineralization. Mineralium Deposita 52, p. 565–593.

Staples, R.D., Gibson, H.D., Colpron, M. and Ryan, J.J., 2016. An orogenic wedge model for diachronous deformation, metamorphism, and exhumation in the hinterland of the northern Canadian Cordillera. Lithosphere, vol. 8, p. 165–184.

Turner, E.C., Roots, C.F., MacNaughton, R.B., Long, D.G.F., Fischer, B.J.E., Gordey, S.P., Martel, M.E. and Pope, M.C., 2011. Chapter 3. Stratigraphy. In: Geology of the Central Mackenzie Mountains of the Northern Canadian Cordillera, Sekwi Mountain (105P), Mount Eduni (106A), and Northwestern Wrigley Lake (95M) Map-Areas, Northwest Territories, M.E. Martel, E.C. Turner and B.J. Fischer (eds.), Northwest Territories Geological Survey, NWT Special Volume 1, p. 31–192.

Yukon Geological Survey, 2020. Yukon Terranes – A digital atlas of terranes for the northen Cordillera. Yukon Geological Survey, http://data.geology.gov.yk.ca/Compilation/2, [accessed December 12, 2020].

Surficial geological mapping of the central Kluane Ranges (parts of NTS 115G/1, 2, 3, 7 and 115B/15, 16), southwestern Yukon

Crey M Ackerson* and Brent Ward
Simon Fraser University

Kristen Kennedy
Yukon Geological Survey

Ackerson, C.M, Ward, B. and Kennedy, K., 2021. Surficial geological mapping of the central Kluane Ranges (parts of NTS 115G/1, 2, 3, 7 and 115B/15, 16), southwestern Yukon. *In*: Yukon Exploration and Geology 2020, K.E. MacFarlane (ed.), Yukon Geological Survey, p. 157–176.

Abstract

Surficial geological mapping in the central Kluane Ranges was undertaken to better understand the distribution and character of surficial materials. Upland surficial materials in the area are dominated by near-source bedrock derivatives. Valley bottom settings, including Shakwak trench and Duke River valley, are characterized by broad open valleys with thick deposits of Quaternary sediment. Permafrost is discontinuous in the study area and its character is affected by slope and aspect, topography and material texture. Mass wasting processes in the study area include rock fall and avalanches, debris flows and avalanches and active layer detachment slides. The distribution and character of surficial materials has significance for soil geochemical sampling programs and infrastructure and implications for mineral exploration and developments are addressed.

* crey_ackerson@sfu.ca

Introduction

This paper presents preliminary results from 1:50 000-scale surficial geological mapping undertaken in the central Kluane Ranges in 2020 (Fig. 1). Emphasis is placed on describing the character and distribution of surficial materials within the map area. Mapping (currently in progress) will also identify glacial limits that will be placed into the stratigraphic framework of the Kluane Ranges.

The Kluane district has both placer (Kennedy and van Loon, 2017; Bond and van Loon, 2018) and bedrock mineral potential (Israel et *al.*, 2006). In the central Kluane Ranges, placer claims exist along the entirety of Bock's Creek and most of Nines Creek and its largest tributary (Fig. 1). There are also several active aggregate quarries along the Alaska Highway in the study area and there is potential for further aggregate development in fluvial fan deposits.

Bedrock mineral exploration in the Kluane district focuses primarily on nickel-copper-platinum group elements (PEG) in Triassic ultramafic rocks (Israel et *al.*, 2006) with several mineral showings and prospects located within the mapping area (Fig. 1). Porphyry and skarn intrusion-related mineralization exists throughout this region and has been shown to be associated with the Kluane Ranges suite (Kennedy and van Loon, 2017).

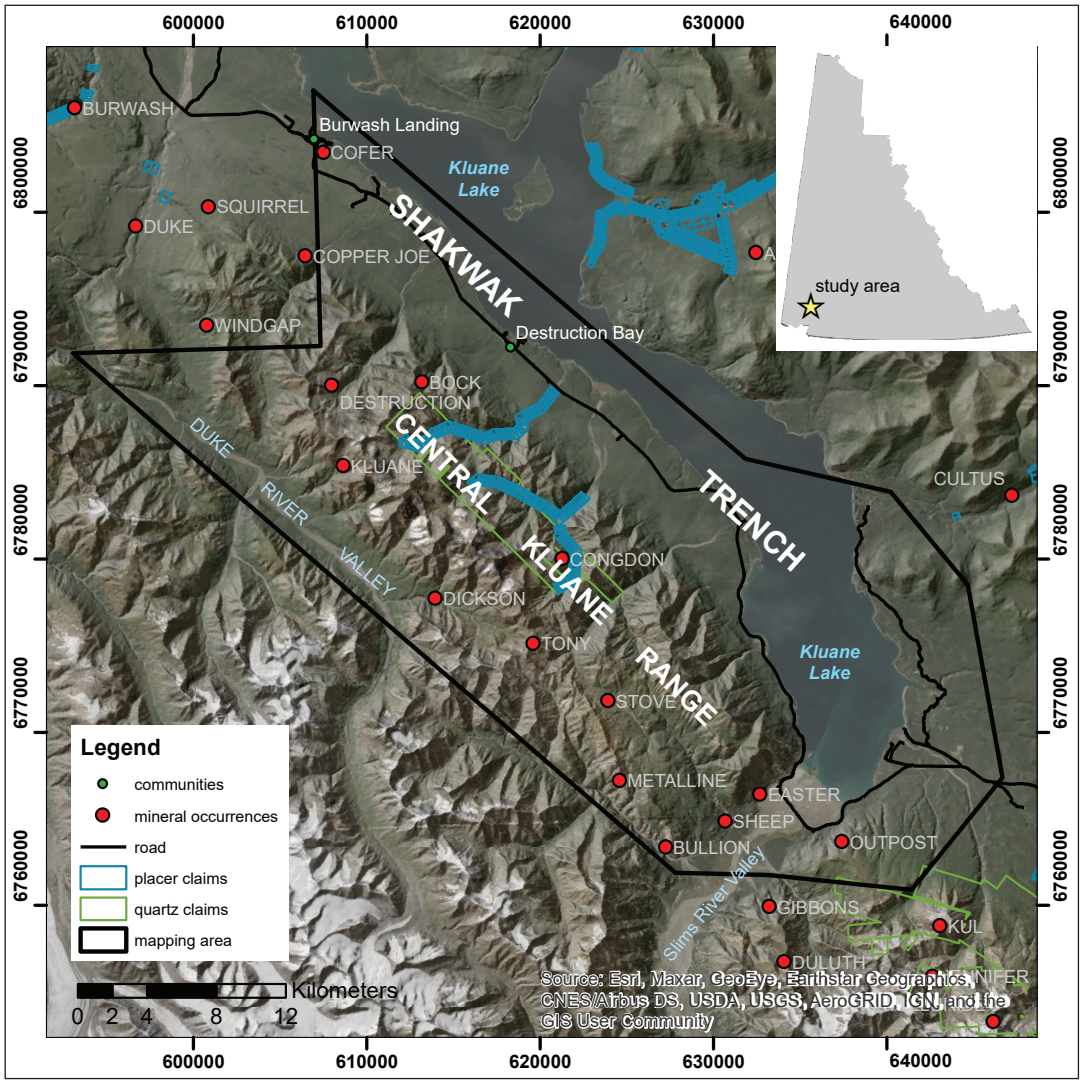

Figure 1. *Location map of the central Kluane Ranges study area and locations of mineral occurrences, placer claims, and quartz claims.*

In addition to the surficial mapping project, work on active layer detachment slides is being undertaken to investigate temporal changes to frequency and magnitude and a possible relation to climate warming. Heavy rainfall in August 2020 triggered landslides that crossed the Alaska Highway south of Ä'äy Chù (Slims River) and resulted in a highway closure. The same precipitation event is also thought to have initiated large active layer detachments at the confluence of Arch Creek and the Donjek River (Fig. 2). Work related to mass wasting is ongoing and will be published at a later date.

Figure 2. *Active layer detachment slides at the confluence of Arch Creek and Donjek River. Helicopter (circled) for scale. The initiation zone is ~150 m vertically above the toe and the track is ~500 m long. These active layer detachment slides are quite large with respect to others seen in this region.*

Physiography and bedrock geology

The Kluane Ranges and the southwestern Kluane Lake area are part of the northeastern Coast Mountain Belt. The Kluane Ranges span 30 km and are part of the front ranges of the St. Elias Mountains, which are some of the highest mountains in North America, with peaks exceeding 5000 m above sea level (a.s.l.). This region is characterized by rapid uplift resulting in steep valley walls sculpted by repeated glaciations. Much of the map area is mountainous terrain with bedrock commonly exposed in canyons, along ridges, summits and upper slopes. Lower slope positions and valley bottoms have thick and more varied deposits of surficial materials. Kluane Lake occupies Shakwak trench, a 10–15 km wide valley that trends northwest-southeast and parallel to the Denali fault. The Duke River fault parallels the Duke River Valley at the western margin of the map area (Fig. 1).

Bedrock in the study area is complex and variable consisting of volcanic, granitic, metamorphic and uplifted oceanic and terrestrial sedimentary rocks (Israel et *al.*, 2006; 2010; Israel and Cobbett, 2008; Colpron et *al.*, 2016). The study area predominantly lies within the Wrangellia Insular terrane which was accreted onto the continent in Early to Middle Jurassic. It is composed of mafic and ultramafic oceanic and island arc rock. Overlapping the Insular terrane rocks are Upper Jurassic to Lower Cretaceous muddy sandstones of the Dezadeash Formation. The Paleocene to Oligocene aged Amphitheater Formation is composed of poorly consolidated conglomerate and sandstone with some interbedded coal seams (Greene et *al.*, 2004; Israel et *al.*, 2006). Andesitic and basaltic volcaniclastic and tuff rocks from the Miocene aged Wrangell volcanic rocks are positioned stratigraphically above and interbedded with the Amphitheater Formation (Israel et *al.*, 2006).

At the southeastern end of the study area bedrock consists of Kluane schist. These metamorphic rocks consist of muscovite, biotite and quartz-rich schist. This schistose rock can also be found under the Ruby Range batholith situated on the east side of Kluane Lake (Israel et *al.*, 2010). The Ruby Range batholith is dominantly composed of quartz-diorite, tonalite and granodiorite and is located east of Kluane Lake in the Ruby and Nisling ranges (Israel et *al.*, 2010).

Glacial history

Yukon was repeatedly glaciated by the northern part of the Cordilleran Ice Sheet during the Quaternary. The northern Cordilleran Ice Sheet consisted of quasi-independent ice lobes rather than a coherent ice sheet (Jackson et *al.*, 1991). The study area was affected by the St. Elias Lobe. Stratigraphic studies have recognized

five glacial advances in southwestern Yukon but there were likely additional unrecognized earlier advances (Turner, 2014; Turner *et al.*, 2016; Cronmiller, 2019). Uplift of the St. Elias Mountains in the Miocene is thought to have created a precipitation barrier east of the St. Elias Mountains in southwestern Yukon (Foster *et al.*, 2010). This is thought to have caused Late Pliocene and Pleistocene ice to initiate in these mountains and flow north-northeast into the Shakwak trench (Fig. 3; Hughes *et al.*, 1969; Duk-Rodkin 1999).

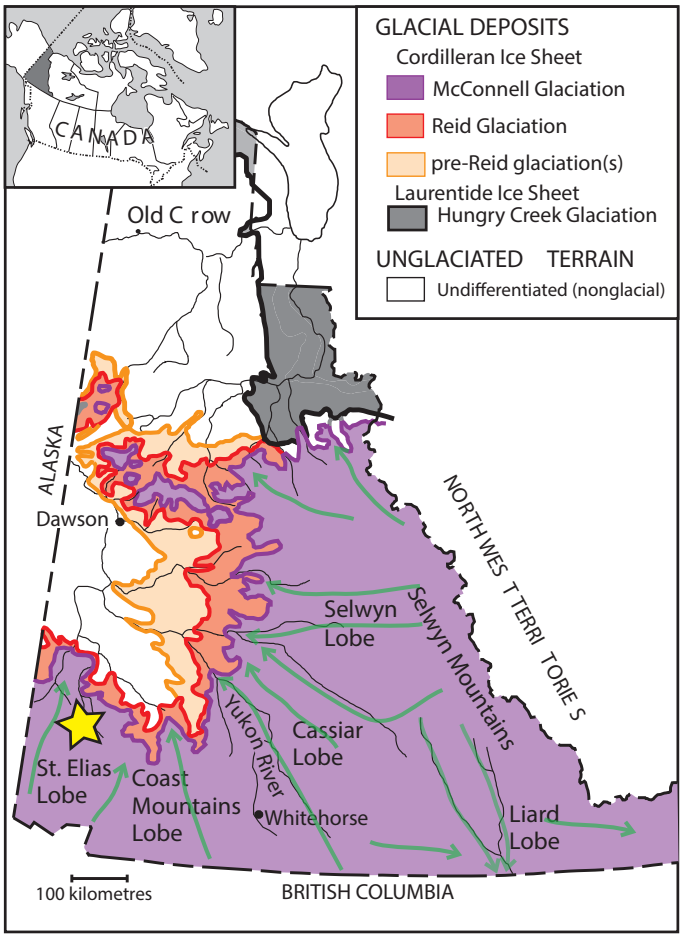

Figure 3. *Map of Yukon showing ice flow directions and approximate extents of glaciations during the Pleistocene. The study area (marked with a yellow star) is approximately 200 km west of Whitehorse. Modified from Ward et al. (2007) after Duk-Rodkin (1999).*

Regional glacial and interglacial terminology exists for southwestern Yukon, but most researchers now place this into the framework developed for central Yukon. Denton and Stuiver (1967) identified and named three glaciations in southwestern Yukon, from oldest to youngest, the Shakwak, Icefield and Kluane; these glaciations are separated by interglacial intervals termed the Silver, Boutellier and Slims interglacials. Turner *et al.*, (2016) confirmed these results and identified two additional glaciations. Evidence for these glaciations was obtained from five units interpreted as till in stratigraphic sections along Silver Creek (Turner *et al.*, 2016). The Boutellier interval, below the Kluane till and above the Icefield till, is dated to Marine Isotope Stage (MIS) 3 (~60–30 ka) (Denton and Stuiver, 1967; Lowdon *et al.*, 1970; Turner *et al.*, 2016). This constrains the Kluane till to MIS 2 which, correlates to the McCauley till (Rampton, 1971) from the Snag-Klutlan area and the McConnell glaciation from central Yukon.

Ages of older tills are not well constrained. The next youngest till in southwestern Yukon is from the Icefield glaciation (Denton and Stuiver, 1967). The Icefield glaciation is correlated to the Mirror Creek (Rampton, 1971) and Gladstone (Ward *et al.*, 2007) glaciations from the Snag-Klutlan and Aishihik areas, respectively. The Gladstone glaciation has been dated to MIS 4 with ^{10}Be on deglacial erratics (Ward *et al.*, 2007). The Shakwak glaciation is correlated to central Yukon's MIS 6 Reid glaciation (Turner *et al.*, 2016). The two oldest tills are considered pre-Reid. A loess unit above the younger of the two tills is dated to at least 320 ka using infrared-stimulated luminescence dating indicating MIS 10 or older deposition (Turner *et al.*, 2016). Only two glacial limits have been mapped in southwestern Yukon, in contrast to other areas where the pre-Reid is much more extensive.

Surficial materials

A combination of foot, truck and helicopter traverses were used to examine the surficial geology of the study area. Texture, surface expression, contacts between surficial materials, and geomorphic processes were described during traverses. Where present, depth to permafrost was noted along with slope position and aspect. These data were used to develop an interpretation of the genesis of the material and to assign terrain polygon labels using a modified version of the Howes and Kenk (1997) Terrain Classification System for British Columbia (YGS, 2020).

Till

Till is material directly deposited by glacier ice without significant modification. Till deposits in the study area are variable but are all matrix supported (Fig. 4a). Clast sizes range from pebble to large boulders (>1 m). Clasts are dominantly subround with fewer subangular and round shapes. Clast content ranges from 10–40% (20–30% is dominant) and clasts are polymictic, representing a broad range of rocks transported by the St. Elias Lobe. The matrix is dominantly sandy silt, but can be clayey silt and silty sand as well. The source area and depositional environment influence the variability. Subglacial till is commonly over-consolidated with subhorizontal fissility.

Till is preserved on gently sloping surfaces and benches on mid to lower slopes both in the central Kluane Ranges and in Shakwak trench. It is also present in section on bluffs along Kluane Lake, where it usually occurs at the base of the stratigraphy. In the central Kluane Ranges, till is commonly overlain by loess and is discontinuous on mid-elevation slopes due to reworking by gravitational processes and surface water.

Glaciofluvial

Glaciofluvial materials are deposited by braided rivers in close proximity to an ice margin. They typically comprise moderately sorted, moderately to well-stratified silty-sandy gravel. Fining-upward grading from boulder dominated to cobble, and even pebble dominated, is common (Fig. 4b). In the canyons and valleys of the central Kluane Ranges, glaciofluvial materials are typically poorly preserved in isolated pockets; there are some glaciofluvial terraces present above Sheep and Bouillon creeks. In Shakwak trench there are extensive glaciofluvial deposits visible in section along the bluffs of Kluane Lake. Clast content is variable but is generally 60–80%. At the south end of Kluane Lake, hummocks, discontinuous ridges and kettle lakes form ice stagnation topography composed primarily of glaciofluvial gravel.

Glaciolacustrine

Glaciolacustrine materials are deposited in or along the margins of glacial lakes and include ice rafted debris. These sediments are observed in sections along the bluffs of Kluane Lake and in the Duke River area. They are dominantly well-stratified, laminated to thinly bedded sand, silt and silty clay. Drop stones (ice rafted debris) and soft sediment deformation structures including faulting are common (Fig. 4e). Sections with diamict containing rip up clasts and pebble gravel layers and lenses were noted along and near Kluane Lake.

Weathered bedrock

Weathered bedrock is the product of *in situ* mechanical and/or chemical weathering of bedrock leading to decomposition or disintegration mainly as a result of strong periglacial processes coupled with weak or faulted bedrock. There is extensive weathered bedrock in the study area, particularly in the northwestern part of the map area and at higher elevations. Deposition of weathered bedrock occurs primarily on flat or gentle slopes. The northwestern part of the mapping area is characterized by poorly consolidated bedrock such as the Wrangell basalt and Amphitheater Formation conglomerate (Fig. 4d), resulting in widespread weathered bedrock. Texture varies with respect to the initial lithologic characteristics and degree of mixing with loess and/or till by periglacial processes, such as cryoturbation and frost heave.

Fluvial

Fluvial sediments are composed of stratified sand and gravel, with a minor silt component. They occur in, and adjacent to, modern drainages including fan settings

Figure 4. *Examples of the surficial materials encountered in the mapping area are:* ***(a)*** *till;* ***(b)*** *glaciofluvial;* ***(c)*** *lacustrine (from pit on Kluane Lake beach);* ***(d)*** *weathered bedrock;* ***(e)*** *glaciolacustrine;* ***(f)*** *loess (eolian);* ***(g)*** *fluvial;* ***(h)*** *colluvium. Measuring tape units are in centimetres and both shovel and pick handles are ~1 m long.*

(Fig. 4g). These deposits are dominantly moderately-sorted, however, lenses and layers of well-sorted sand and gravel are also present. Clast size ranges from pebble to boulder with pebble being dominant. Steep and confined channels are characterized by coarser fluvial deposits. Clasts are dominantly round to subround. However, some fans proximal to source have dominantly subround to subangular clasts. The majority of these deposits are limited to narrow bedrock-constrained channels and small fans. However, in the Duke River valley and Shakwak trench large fans prograde into broad, open valleys.

Lacustrine

Lacustrine sediments are primarily located at the margin of Kluane Lake as raised beaches. Lacustrine sediments are moderate to weakly stratified sand, pebble gravel with a sandy matrix, and openwork pebble gravel (Fig. 4c). Berms of lacustrine beach sediment up to 2 m high can be found several hundred metres inland from the shore. Clast lithology is variable as many clasts have a history of glacial transport, and are dominantly round to subround, although tabular clasts are present.

Colluvium

Colluvium is material transported by gravity-driven processes including rapid processes such as rock fall, debris flows and avalanches, and slow processes such as solifluction and creep. These deposits have variable texture and composition due to the variability in process and sediment source. At higher elevations blocks from rock fall are dominant while finer grained sediments can be found on gentler slopes where slow mass movement processes are prevalent. On lower slopes colluvium is commonly a diamict, deposited by rock avalanches, debris flows and debris avalanches (Fig. 4h) or loose blocky angular fragments from accumulated rock fall. These deposits can be high in silt and/or clay if sourced from sediments with fine-grained matrix, fine-grained glaciolacustrine sediments or if mixed with significant quantities of loess. In areas of Wrangell basalts colluvium typically has a higher content of fines (silt and clay).

Eolian

Although generally too thin to map, loess or windblown silt is the most widespread sediment throughout the study area (Fig. 4f). During glacial and deglacial times loess is generated by katabatic winds blowing over recently deglaciated or unvegetated surfaces, entraining silt and fine sand and depositing it downwind. There are both paleo and modern loess deposits in the central Kluane Ranges. Paleo loess deposits in the study area formed from katabatic winds at the end of the last glaciation. Modern loess deposits are typically confined to the southern part of the map area and originate primarily from katabatic winds blowing down Ä'äy Chù Valley.

Stratigraphy

Stratigraphic sections were divided into units based on material type and texture. Unit descriptions include texture, structures, weathering and contacts between units. With a paucity of well exposed sections, the majority of stratigraphic correlations are based on manual excavations through slopewash sediments. As a result, contacts and units could be unintentionally omitted. This adds uncertainty to the stratigraphy in the study area. For the purpose of stratigraphic correlations, the study area has been divided into three main areas: Shakwak trench, Duke River, and the central Kluane Ranges.

Shakwak trench

Lewis Creek north (CA203201)

This section is located on the upper part of a bluff overlooking Kluane Lake just south of Lewis Creek (Fig. 5). The section is ~22 m high (Fig. 6).

Unit 1 is a stratified, clast supported sandy gravel ≥1 m thick. The lower contact of unit 1 is covered. Bedding is defined by stratification of pebble-cobble gravel and granule-pebble gravel. Beds range from 2–10 cm thick and dip 8–10° to the NW. Finer beds composed of small pebbles are dominantly openwork and clasts have silt and clay coatings. Some medium to very coarse sand matrix partially infills the interstices between

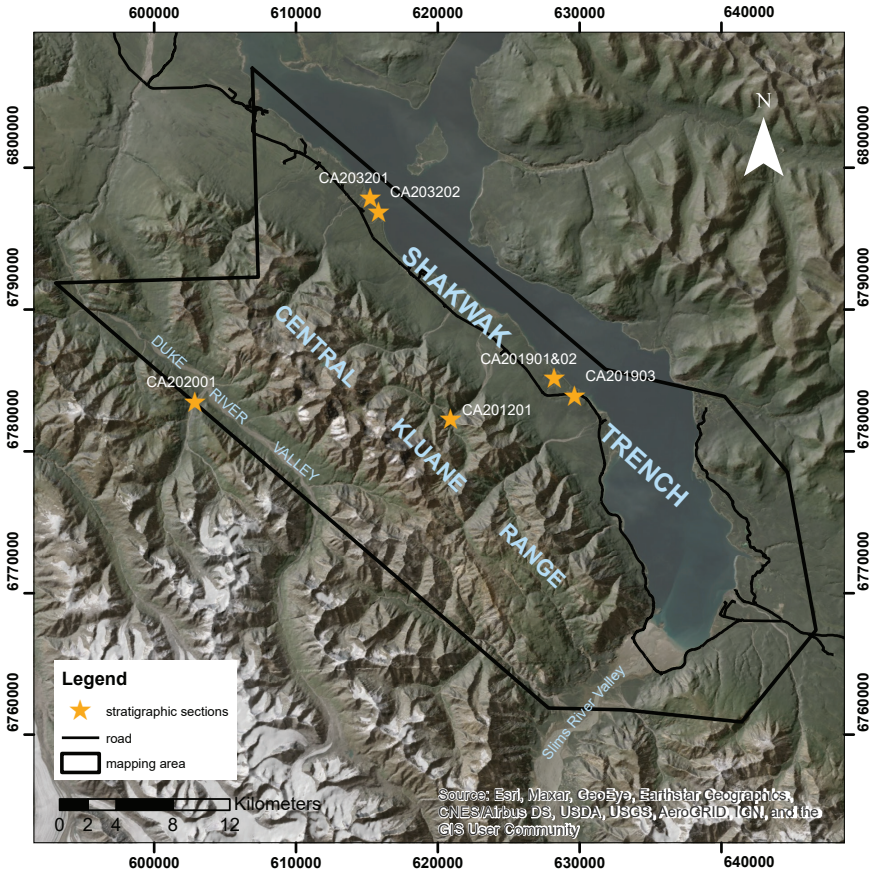

Figure 5. *Location map of stratigraphic sections.*

clasts that are dominantly subround. Clast content in the finer beds is ~90–95%. Coarser beds are matrix supported pebbles and small cobbles with a 70–80% clast content. The matrix in these beds is coarse to very coarse sand. Unit 1 is interpreted as advance outwash as ice moved northwest down Shakwak trench, based on stratigraphic position (below till) and inclined bedding interpreted to represent deposition into water.

Unit 2 is a stratified diamict ≥1.2 m thick, that is fissile and has an abrupt, irregular, inclined, nonconformable lower contact. The two layers observed in this diamict are differentiated by clast content and matrix. However, clast shape and size, and features such as facets and striations are the same between beds. The lower bed is ≥30 cm thick with a fine sandy silt matrix and 30–40% clasts. The upper bed is ≥90 cm thick with a very fine to fine sand matrix and 20–25% clasts. The two beds are separated by an abrupt contact. Clasts are dominantly pebble-sized but range up to 30 cm in diameter and are dominantly subround with abundant faceted and striated clasts. Unit 2 is interpreted as till due to its stratigraphic position, texture, and the presence of striated and faceted clasts. Variation between the upper and lower till layers in this unit could represent till deposited during advance (lower) and retreat (upper) phases of glaciation.

Unit 3 is a laterally discontinuous deposit of silty organic material 0.05–0.08 m thick with a clear subhorizontal, irregular, unconformable lower contact. This unit is dominantly fibric organics with silt and has a medium brown colour when freshly exposed. Unit 3 is interpreted as a paleosol based on the abundance of fibric organics and stratigraphic context. This implies a period of subaerial exposure between Units 2 and 4.

Unit 4 is ≥0.45 m of laminated and finely bedded silt and sand with an abrupt, irregular, inclined (~8° to the NW) lower contact. This unit is composed of fine beds and laminations of medium sand fining upward to very fine sand and is capped by a 2 cm bed of silty

medium sand. Soft sediment deformation structures such as flame structures, convolute bedding, and dish structures are present. Unit 4 is interpreted as a lacustrine deposit based on texture, bedding, and soft sediment deformation. Its stratigraphic position above a paleosol indicates this unit was deposited during a non-glacial period.

Unit 5 comprises massive silt with tephra. The unit is ≥0.8 m thick with a gradational, horizontal lower contact. It has a 3–5 cm thick bed of tephra ~30 cm from its base. This unit is dominantly massive silt with minor very fine sand. The upper 30–40 cm has a well developed soil. The tephra comprises medium to coarse sand sized particles with a black-and-white speckled colour like salt-and-pepper. Unit 5 is interpreted as eolian loess and tephra. The tephra is assumed to be White River Ash deposited approximately 1200 years ago (Jensen *et al.*, 2014). The tephra in the loess indicates significant windblown sediment deposits have occurred in this region in the last 1200 years.

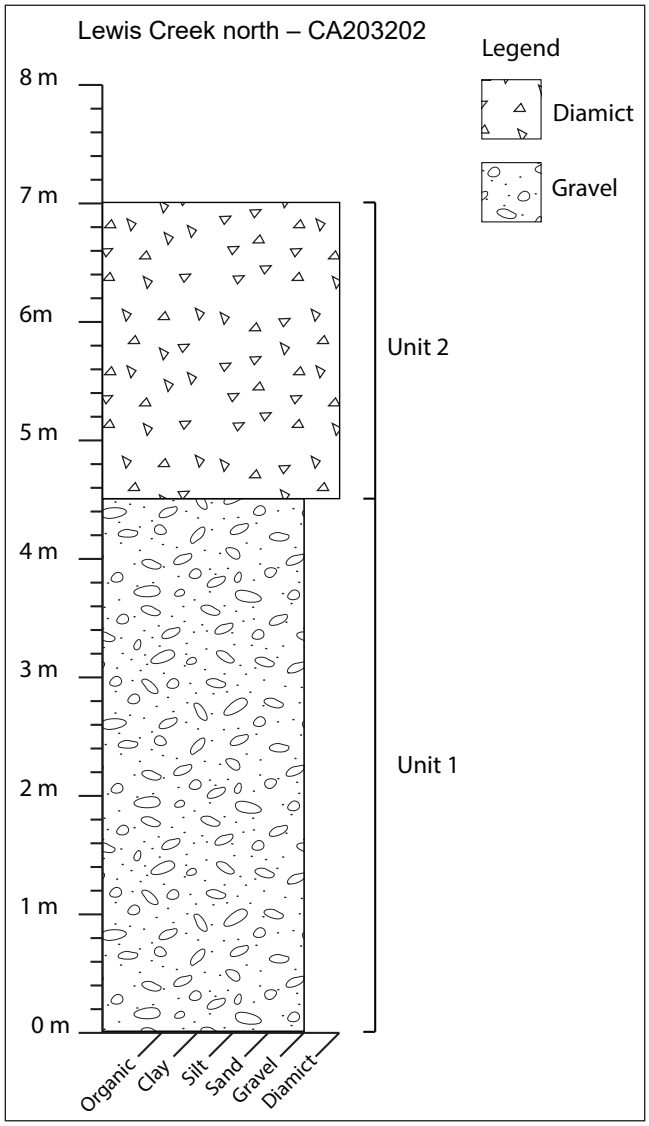

Figure 6. *Stratigraphy of sediments observed in section along bluffs on the western shore of Kluane Lake (Lewis Creek north - CA203201).*

Lewis Creek south (CA203202)

This section is exposed in bluffs along Kluane Lake between Destruction Bay and Lewis Creek (Fig. 5). The section is ~20 m high with two units exposed in the lower 7 m of the section (Fig. 7).

Unit 1 is a ≥4.5 m-thick, moderately consolidated, stratified gravel. Poorly sorted pebble-cobble beds are dominantly matrix-supported with silty medium to very coarse sand, and include some clast-supported lenses and beds. Beds are separated by clear, inclined (~8° to the NW), planar contacts, commonly with laminated silt beds (2–3 cm thick) along bedding planes. Bedding ranges from 15–100 cm thick and matrix supported beds are generally thicker than clast supported beds and lenses. Unit 1 is interpreted as subaqueous outwash deposited in front of a glacier advancing northwest along Shakwak trench. This is based on the unit's stratigraphic position below till, inclined bedding, and interstratified silt representing quiet water deposition.

Unit 2 is a ≥2.5 m thick stratified diamict. The lower contact appears sub-horizontal, although it is poorly exposed. The matrix is dominantly silt with some very fine to medium sand. Clasts comprise 30–40% of the unit, and are dominated by pebbles with lesser amounts of cobbles and boulders. Clasts are commonly faceted, striated, and fractured. Unit 2 is interpreted as till deposited during the last glaciation based on texture, clast features (striations, facets and fractured clasts), and stratigraphic position. Silt partings indicate this may be a flow till deposited at the ice margin.

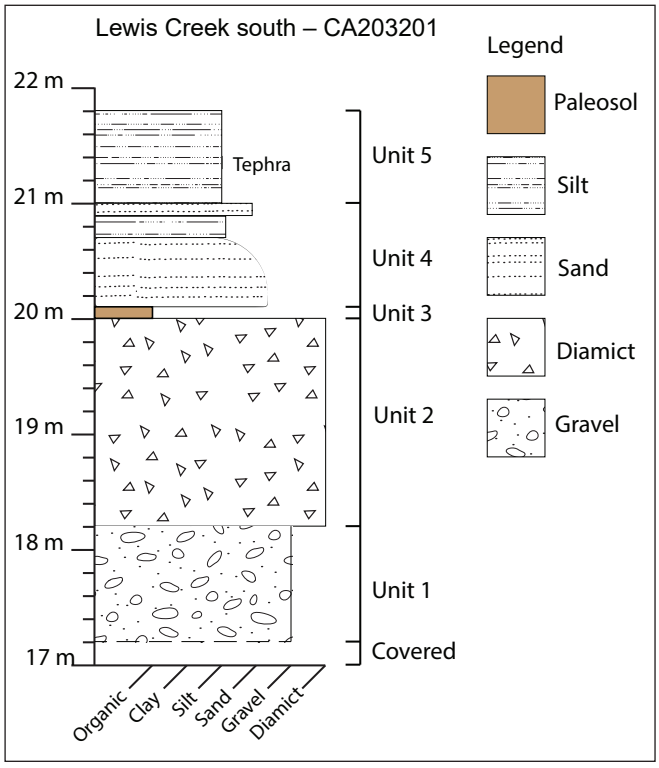

Figure 7. *Stratigraphy of sediments observed in section along bluffs on the western shore of Kluane Lake (Lewis Creek south - CA203202).*

Dutch Harbour (CA201901 & CA201902)

These sections are located on the south side of Dutch Harbour on the west shore of Kluane Lake (Fig. 5). The CA201901 section is ~15 m high with only the upper ~1 m well exposed; thus the majority of descriptions were from manually-excavated exposures. Site CA201902 is located in a small landslide scar several hundred metres south-southwest of site CA201901.

Unit 1 (Fig. 8) is light grey brown, weakly-stratified, unconsolidated diamict with a covered lower contact. There are silt partings less than 1 cm thick separating the layers of diamict that are laterally continuous for at least several metres. Unit 1 has a fine sandy-silt matrix (60–70%) supporting subround, striated, and faceted clasts ranging from pebble (>50%) to boulder (<5%) in size. Elongate and anvil-shaped clasts are present, some with infrequent vertical to subvertical orientations. Clasts are polymictic. This unit has undergone chemical weathering resulting in many disintegrating clasts. Unit 1 is interpreted as flow till deposited in an ice marginal glaciolacustrine environment during deglaciation of Shakwak trench. This is based on stratigraphic context (below glaciofluvial and glaciolacustrine sediment), texture, clast features (striations, facets and anvil-shape), and interbedded silts.

Unit 2 comprises ≥0.8 m of laterally discontinuous sand. The unit displays horizontal planar stratification and a gradational, irregular, horizontal, lower contact. Overall, laminae and beds range from 0.5–5 cm and coarsen upward from very fine sand to very coarse sand and pebbles. Lenses and blebs of Unit 1 are present in the lower 15–20 cm of this unit. Unit 2 is interpreted as a glaciolacustrine deposit from the end of the last glaciation based on horizontal bedding, texture, and stratigraphic context (above till and below glaciofluvial deposits). The reverse grading is interpreted to represent deposition from a sediment flow in a subaqueous environment.

Unit 3 is a stratified sandy gravel that is ≥1.4 m thick with a nonconformable (erosive), sharp, inclined (toward the north-northwest) lower contact at site CA201901 and covered lower contact at site CA201902. Matrix supported beds, 5–20 cm thick, are interbedded by openwork pebble gravel beds with some 5–10 cm diameter cobbles. These beds have an apparent dip of ~5° to the northwest. This unit has a dominantly coarse sand matrix with some medium sand and a clast content of 70–75%. Clasts are dominantly pebbles with some cobbles and have a subround shape. Many elongate clasts display a vertical to subvertical orientation. Unit 3 is interpreted as a glaciofluvial gravel deposited during deglaciation of Shakwak trench based on texture, inclined beds, and an erosive lower contact over till.

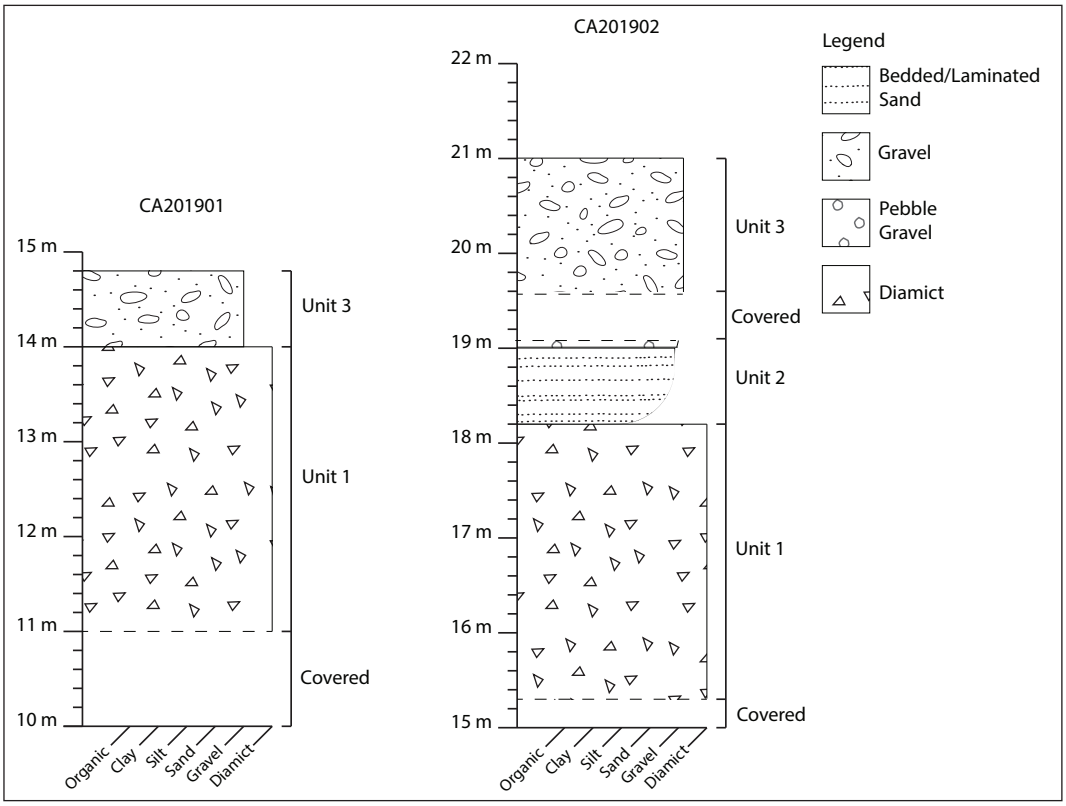

Figure 8. *Stratigraphy of sections at Dutch Harbour (CA201901 and CA201902).*

Goose Bay (CA201903)

This site is located near Goose Bay off the Alaska Highway in a cut for the pipeline (Fig. 5). Three units were observed and are described below (Fig. 9).

Unit 1 is a weakly stratified diamict ≥1.2 m thick that has a covered lower contact. Horizontal to subhorizontal beds are separated by sandy-silt and silt partings with horizontal to subhorizontal fissility. The matrix is a light greyish brown and is dominantly silt with some sand. Clast content is 30–40% and clasts are subangular to subround. Clasts are dominated by pebbles but can be up to 50 cm in diameter and many are faceted and striated. Clasts are polymictic with sedimentary, granitic, porphyritic volcanic and schistose present. Unit 1 is interpreted as a flow till from the margin of an ice sheet in Shakwak trench at the end of the last glaciation due to its texture, faceted and striated clasts, and interbedded silt and sandy silt.

Unit 2 is a ≥0.55 m thick stratified sandy pebble gravel that pinches out to the west (possibly thickening in the opposite direction) with an abrupt, irregular, inclined (apparent strike and dip = 20⁄310°) nonconformable (erosive) lower contact. Beds are dominantly horizontal to subhorizontal openwork gravel interbedded by matrix supported sandy gravel beds up to 10 cm thick. Clasts are dominantly subround fine pebbles. Unit 2 is interpreted as a glaciofluvial outwash gravel deposited during deglaciation of Shakwak trench based on its stratigraphic position (above till) and the presence of an erosive lower contact. The apparent dip of the beds could indicate this unit was deposited in a subaqueous environment.

Unit 3 is interbedded silt and pebbly sand ≥1.7 m thick with an abrupt, conformable lower contact. It is dominated by horizontal to subhorizontal laminations of silt and clayey silt with sand and pebbly sand and sandy pebble gravel laminations, beds, and lenses. Silt and clayey silt laminae are dominantly fine (≤0.5 cm) sandy laminae are coarse (≥0.5 cm and <1 cm) and pebbly sand and pebble gravel with a sandy matrix are dominantly finely bedded (≥1 cm and <5 cm). The frequency of the coarser beds increases toward the top of the unit. Silt and clayey-silt layers contain pebble clasts with laminae and beds draped over them.

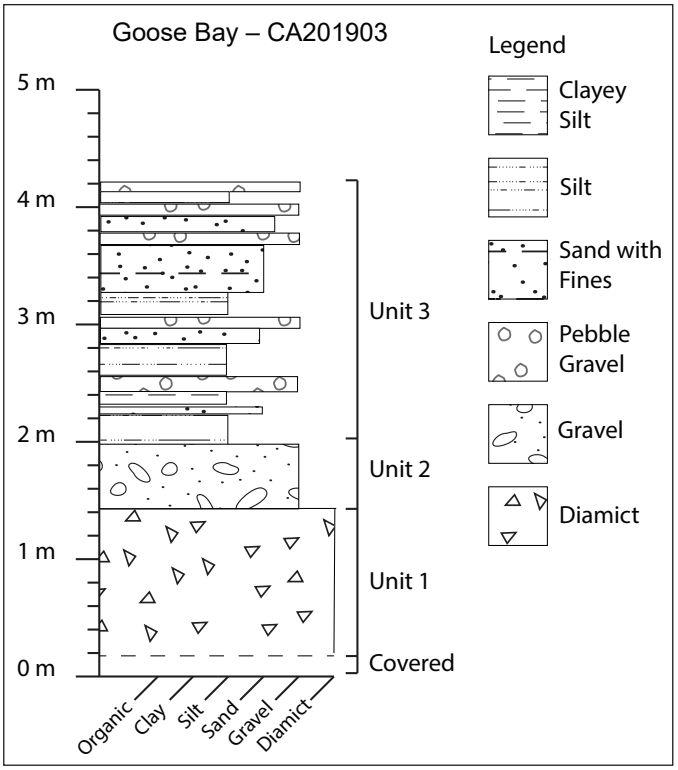

Figure 9. *Stratigraphy of sediment in a pipeline cut off the Alaska Highway near Goose Bay (CA201903).*

Unit 3 is interpreted as a glaciolacustrine deposit based on texture and the presence of drop stones (clasts draped by silt and clayey silt). The coarser beds could be debris melting out of ice or might represent a more proximal position to the ice front.

Duke River

Grizzly Creek (CA202001)

Located ~500 m upstream of the confluence of Grizzly Creek and Duke River (Fig. 5), the Grizzly Creek section comprises 14–16 m of surficial sediments overlying discontinuously exposed bedrock at creek level.

Unit 1 is a matrix-supported stratified diamict ~5.5 m thick (Fig. 10). It is consolidated and fissile with an irregular lower contact with underlying basalt. Comprising 60–65% of the unit, clasts are dominantly subangular to angular greenstone pebbles, with rare subround clasts of amygdaloidal basalt and fine grained sedimentary rocks. Clasts are dominantly pebble sized with a maximum clast diameter of ~1 m. The matrix of Unit 1 is light greenish–grey fine sand (Fig. 4H) with a dark rusty brown horizon in the upper 60 cm of the unit. Unit 1 is interpreted as a colluvial fan deposit based on stratification and the dominant locally-sourced clast composition of the diamict. The rusty brown colour along the upper contact of the unit is interpreted as subaerial oxidation, but could also have resulted from groundwater movement.

Unit 2 is a ~3.8 m-thick unconsolidated, fissile, matrix-supported diamict with a sharp, planar lower contact. Grey sandy–silt matrix supports 30–40% subround, polymictic pebbles and small cobbles. Some clasts are striated and faceted. Unit 2 is interpreted as till based on its texture and the presence of striated and faceted clasts.

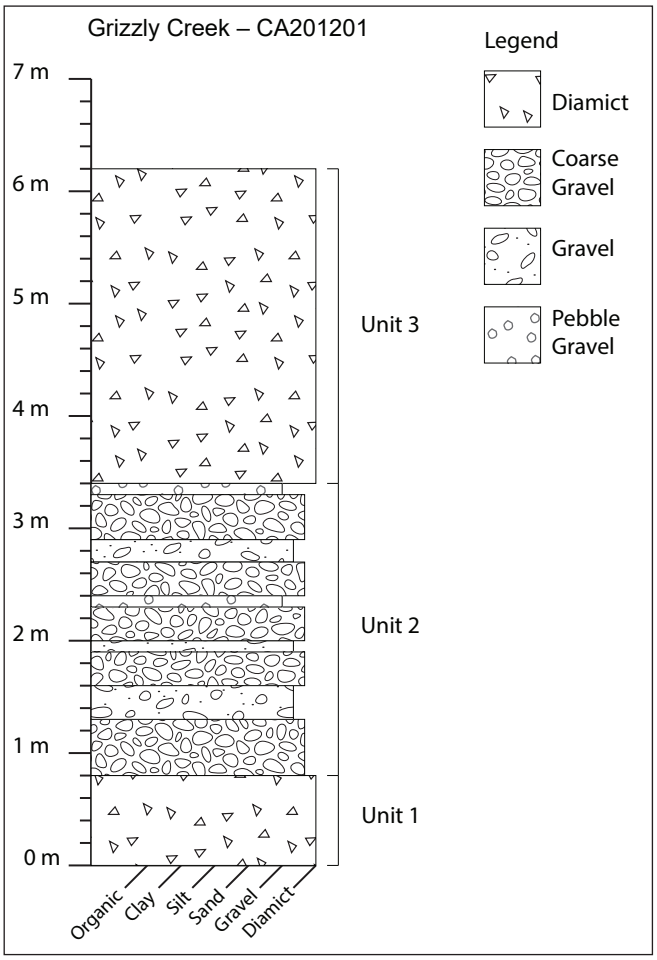

Figure 10. *Stratigraphy of sediments at Grizzly Creek (CA202001).*

Unit 3 is a ~1.7 m thick matrix-rich diamict with a sharp, irregular, horizontal lower contact. It is fissile, unconsolidated, and has a dark grey silt matrix with a clast content of 10–15%. Clasts are commonly striated and faceted and comprise subround pebbles with rare cobbles. Unit 3 is interpreted as till based on its texture and the presence of striated and faceted clasts. The low clast content could indicate a change in glacier source area.

Unit 4 comprises 40 cm of interbedded silt and sand with a sharp, subhorizontal, planar lower contact. Rare (~5%) round to subround pebbles are draped by clayey-silt to silty fine-sand laminae and beds. Laminae and thin beds (<2 cm) thicken upward to a 25 cm-thick bed of dark grey clayey silt at the top of the unit. Unit 4 is interpreted as a glaciolacustrine deposit based on the texture, stratigraphic context and clasts draped by beds and laminae.

Large striated boulders up to 1 m in diameter are present on the recessive, covered surface above the Grizzly Creek section. No clasts of this size and description with striations were found in the lower units. The presence of large striated boulders at the top of the section may indicate a stratigraphically higher till, or that one of the diamict units lower in the stratigraphy has been draped over the section.

Central Kluane Ranges

Nines Creek (CA201201)

The Nines Creek section (Fig. 11) is characteristic of the sections found in the steep narrow valleys of the central Kluane Ranges. Located at the confluence of Nines Creek and its main tributary (Fig. 5), the section comprises 3 units and is ~6 m high with a sloping upper surface.

Unit 1 is a 0.8 m-thick moderately consolidated diamict with a sandy silt matrix and a covered lower contact. Clasts comprise 60–65% of the unit and are dominantly subround pebbles and cobbles with rare boulders. Unit 1 is interpreted as colluvium deposited by a mass wasting event such as a debris flow or avalanche. The high clast content coupled with an abundance of angular clasts indicate a non-glacial origin.

Unit 2 is a 2.6 m-thick moderately sorted, stratified, cobble-pebble gravel with a coarse sandy matrix. Unit 2 has a sharp lower contact and is interpreted as a high energy fluvial deposit based on its texture and position in the bottom of a bedrock canyon.

Unit 3 is a 2.8 m-thick stratified, silty diamict with a clast content of 65–70% and an abrupt lower contact. Clasts are dominantly angular to subangular and range from boulder to pebble. Bedding in this unit is inclined ~12° to the north-northeast, with the entire unit thinning and fining before pinching out in the same direction.

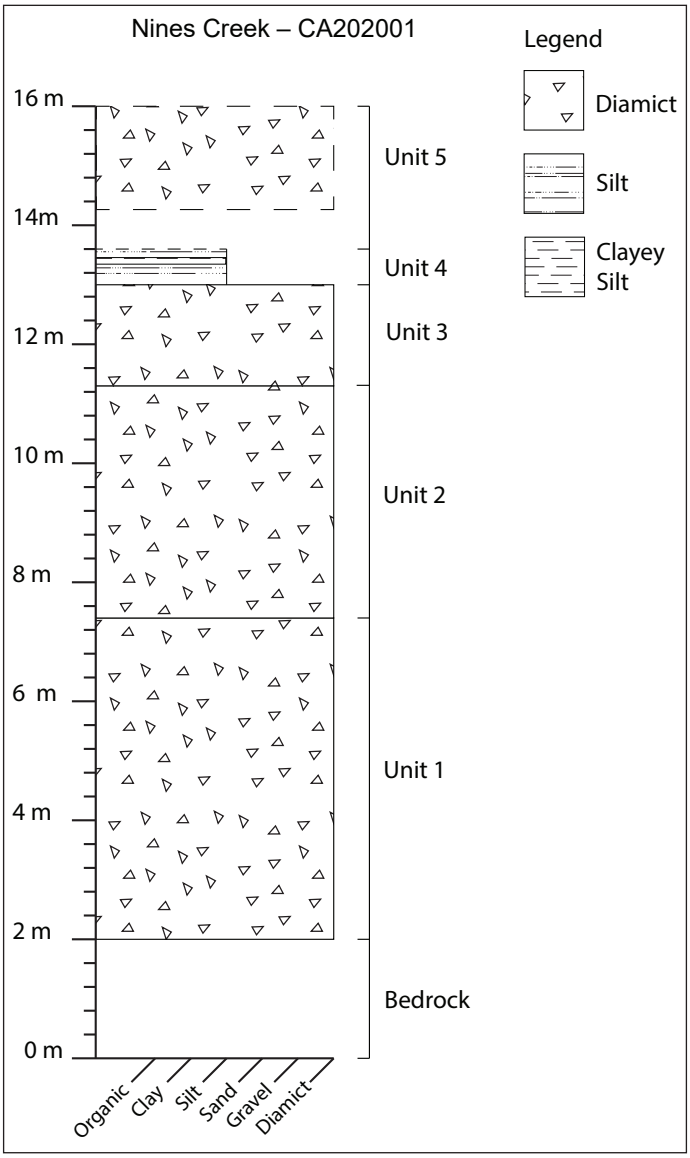

Figure 11. *Stratigraphy of sediments exposed along a river cut on Nines Creek in the central Kluane Ranges (CA201201).*

Unit 3 is interpreted as a colluvial fan deposit based on the high clast content, abundance of angular clasts, and lateral fining. This unit likely formed from successive mass movements originating on the steep slopes above the canyon floor. The lateral fining and thinning of beds in this as the unit pinches out likely indicate a change from proximal to distal position during deposition.

Discussion of regional stratigraphy

The Lewis Creek north section represents ice advancing down Shakwak trench depositing advance outwash sediments. The outwash could have been deposited in a subaqueous environment based on inclined beds but lacks obvious interstratified silt that indicate periods of quiet water deposition to confirm this interpretation. Ice then advances over the site, depositing till. Following deglaciation a paleosol formed and was subsequently buried by lacustrine sediments representing a high stand of Kluane Lake at ~20 m above its current level, which is a higher elevation than previously determined in the Holocene (Clague *et al.*, 2006). Loess and White River ash were deposited over the lacustrine sediments after lake levels dropped.

The Lewis Creek south site represents ice advancing northwest along Shakwak trench depositing advance outwash into a lake. Ice subsequently overruns the site depositing till. Ice advancing out of the St. Elias Mountains or the Ruby Range north of Kluane Lake could have blocked drainage in Shakwak trench to form the lake that ice was advancing into (*cf.* Turner *et al.*, 2016; Cronmiller, 2019).

The Dutch Harbour sections represent ice overrunning the site depositing till during the last glaciation. Then during deglaciation glaciolacustrine sediments were deposited representing a lake occupying Shakwak trench. Finally glaciofluvial outwash gravel was deposited over the glaciolacustrine sediments.

The Goose Bay section represents ice overriding this site depositing till. Outwash gravel documents the initial retreat of ice in Shakwak trench, which is followed by deposition of glaciolacustrine sediments.

The Grizzly Creek section has pre-last glacial sediments (Unit 1 at least) that suggest ice in this area was not erosive enough to remove these sediments. Glaciolacustrine sediment overlying till shows a glacial lake occupied the area during deglaciation. It is possible a readvance occurred depositing another till above the glaciolacustrine sediments but further work is needed to confirm this.

In the central Kluane Ranges during the last glaciation, ice initiated in cirques and expanded and flowed down valley and out into Shakwak trench. During deglaciation ice retreated back up the valleys where glaciers still exist in some high elevation cirques and icefields. The Nines Creek section represents post glacial colluviation and fluvial action.

A composite stratigraphic column was developed to help reconstruct the stratigraphy of Shakwak trench (Fig. 12). It is likely that ice advancing out of the Kluane Ranges to the northwest of Kluane Lake blocked north-flowing drainage in Shakwak trench and resulted in a higher than present lake level (Turner *et al.*, 2016). We see a record of this at the Lewis Creek north (CA203201) and Lewis Creek south (CA203202) sections.

Till deposits preserved in the four Shakwak trench sections are interpreted to record glaciers from the St. Elias Mountains and possibly Ruby Range coalescing in and flowing NW up the trench. Outwash gravel at the Dutch Harbour (CA201901 and CA201902) and Goose Bay sites (CA201903) represent a retreating or stagnant ice front. These sites are located along ice marginal meltwater channels, further supporting the interpretation of ice stagnation. Glaciolacustrine sediments at the Dutch Harbour (CA201901 and CA201902) and Goose Bay sites (CA201903) are interpreted to be the result of sediment deposited into a glacial lake occupying Shakwak trench during deglaciation.

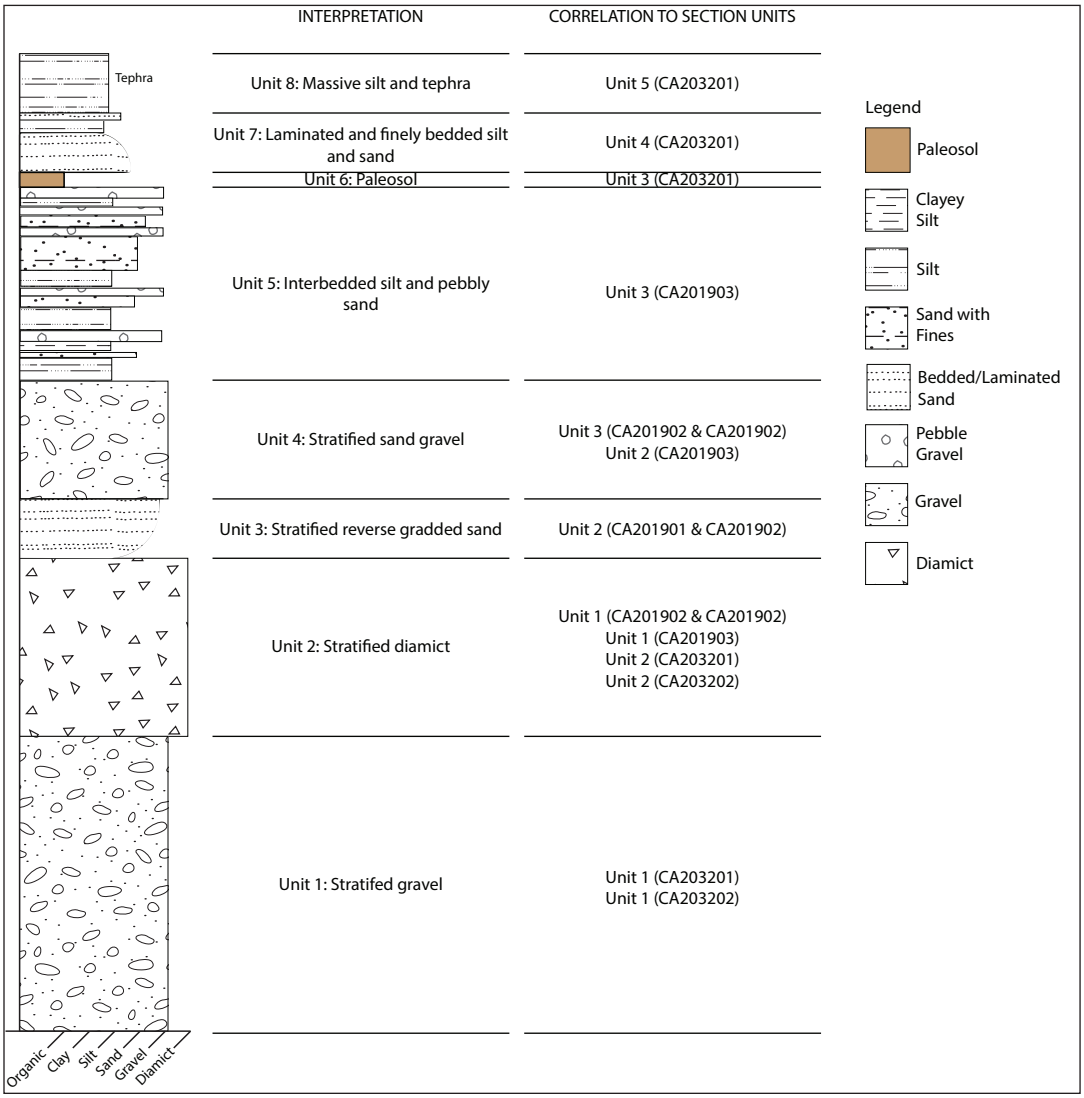

Figure 12. *Compilation of stratigraphy in Shakwak trench from five sites. To the right of the stratigraphic column are unit interpretations and the units that correlate to the individual sections investigated along Shakwak trench.*

Surficial geology landscape model

A general model for the surficial geology of the landscape in the study area has been developed to aid in the discussion of which surficial materials would be expected at each landscape position (Fig. 13). The distribution of surficial materials is primarily controlled by the steepness of slopes and the glacial history in a particular area. The most widespread active modern surficial process is colluviation, or downslope gravitational movement of materials. This, coupled with steep high-energy streams, results in unconsolidated surficial materials that are rapidly moved off-slope. The surficial geology for different landscape positions is discussed below.

Summits, ridges and plateaus

Summits and ridges are predominantly narrow features of bedrock and weathered bedrock. Although, some ridges, especially those at lower elevations, are wider and flatter. The thickness of weathered bedrock is typically <1 m except in the northwest part of the map area where thicknesses >1 m are common.

Loess veneers between 10 and 60 cm thick occur on low angle ridges, summits and plateaus. On plateaus, till blankets (>1 m thick) and veneers (<1 m thick) are common below the loess. Cryogenic mixing of till and loess is indicated by the presence of till clasts in frost boils at the surface. Where loess is present on summits, ridge tops and plateaus, it can dilute the geochemical signature of underlying bedrock and till.

Upper slopes

Upper slopes are located immediately below summit and ridge environments and are typically steep. Rare narrow benches follow bedrock stratigraphy and/or faults. Some of these bench features may be meltwater channels if they are located below the absolute glacial limit of ~1700–1800 m a.s.l. (Kennedy and Ellis, 2020). High slope angles result in rapid downslope movement of weathered bedrock by gravitational processes forming a discontinuous colluvial veneer (<1 m thick) between areas of exposed bedrock. Preservation of glacial sediment is possible on benches if they are below glacial limits. Also, thicker accumulations of colluvium can occur on benches. When soil sampling on upper slopes it should be noted if samples are taken on bench features below glacial limits to account for possible mixing of colluvium with glacial sediments.

Mid-slopes

These slopes are moderately steep. Colluvium accumulates in nearly continuous colluvial veneers (<1 m thick) with localized bedrock knobs protruding through colluvium. Colluvium is commonly loess-enriched on mid-slopes as it is washed off the steep upper slopes by surface water. As with upper slopes, there can be bench features at the mid-slope position and the same sampling considerations should be taken. Care should also be taken to sample materials that are not loess enriched at the mid-slope position to avoid masking till or bedrock geochemistry.

Lower slopes

At the lower slope position a dichotomy exists between valleys in the central Kluane Ranges and Shakwak trench, Duke River Valley and Ä'äy Chùu (Slims River) Valley. Valleys in the central Kluane Ranges are narrow, and the lower slopes are steeper than the lower slopes

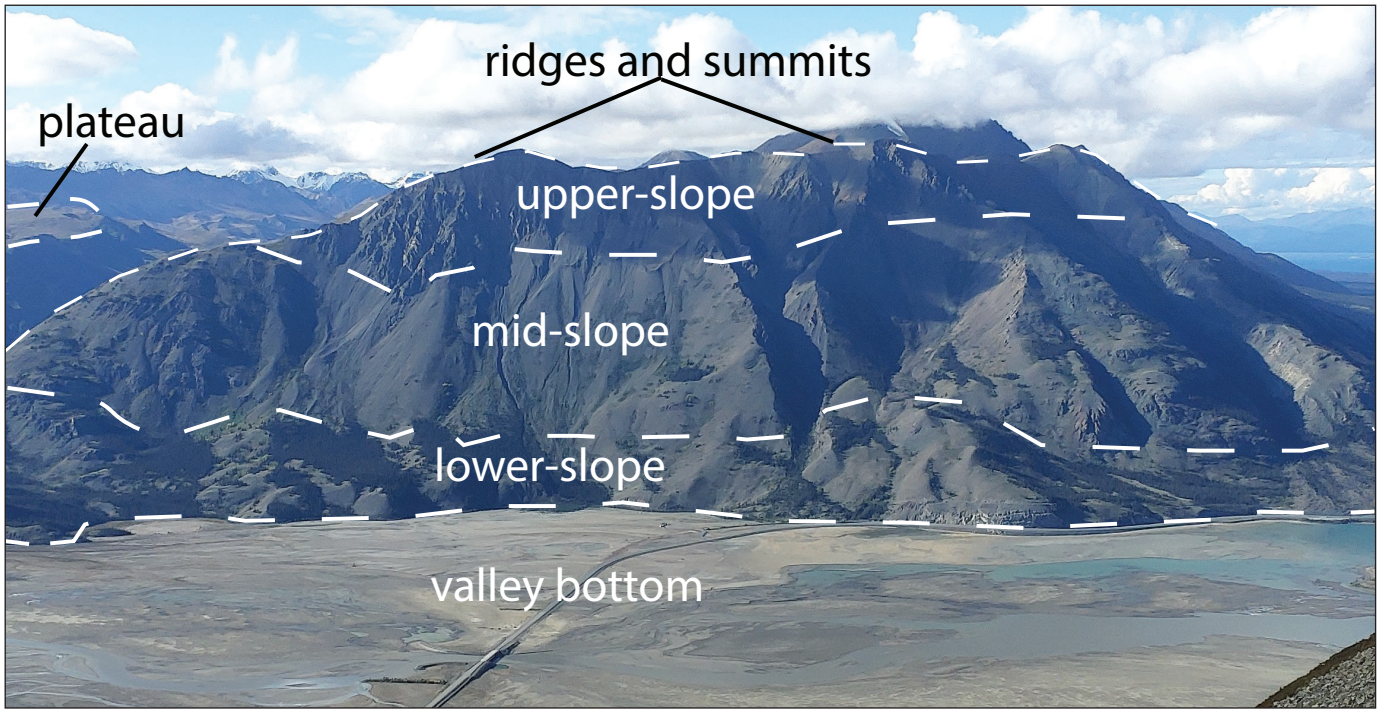

Figure 13. *Surficial geology landscape model superimposed over Sheep Mountain at the confluence of Ä'äy Chù Valley and Shakwak Trench. The valley bottom is the mouth of Ä'äy Chù Valley and the plateau on the left is Bullion Plateau.*

in Shakwak trench and Duke River Valley. Moderate slopes are characteristic of the lower slopes in valleys of the central Kluane Ranges. Thick accumulations of colluvium (>1 m) form nearly continuous aprons. Till and glacial fluvial sediments are rarely preserved at the surface and are typically covered by colluvium. Fluvial sediments can be found in rare pockets perched above the high-water mark.

Conversely, in Shakwak trench and Duke River Valley lower slopes are moderate to gentle. These slopes are characterized by colluvial and alluvial cones and the upper portions of fluvial fans that form thick deposits of colluvium and alluvium. Between fans and cones are thinner colluvial deposits that thicken as slope gradient decreases. There is a higher preservation potential for till on these slopes although it is commonly buried by fans cones and loess.

Geochemical sampling programs should target till where possible or colluvium sourced directly from bedrock. Colluvium derived from glacial sediments would not reflect the bedrock geochemistry and post depositional transport would confound efforts to vector back to the source of an anomaly. An effort should be made to avoid sampling loess and materials enriched by loess.

Valley bottoms

A trichotomy exists between the valley bottoms of Shakwak trench, Duke River and Ä'äy Chù and the valleys in the central Kluane Ranges. These differences can be thought of in terms of stream order. First and second order streams like those in the in the mountains (central Kluane Ranges) are steep and high energy, third and fourth order streams in larger valleys (Duke, Ä'äy Chù) are less steep and lower energy. Finally, Shakwak trench is both a structural basin as well as a higher order fluvial valley bottom.

The valley bottoms of the central Kluane Ranges are much narrower and have steeper gradients than the Duke River and Ä'äy Chù valleys and Shakwak trench. This results in higher energy streams with deeper bedrock incision and more cobble and boulder-rich fluvial deposits. Colluvium is prevalent at the edges of the valleys where it is deposited over fluvial gravel in fans and cones or in aprons between fans and cones. Targets for geochemical sample analysis should be limited to colluvium derived from bedrock or stream sediment samples in first or second order tributaries.

Valley bottoms of Duke River and Ä'äy Chù are characterized by broad braided rivers dominated by coarse sandy gravel. Some glaciofluvial material is preserved in terraces located above bedrock, but valley bottom sediments in these settings are primarily modern fluvial deposits. These sediments are more traveled and therefore more mixed than in higher order streams making them less suitable for geochemical sampling. Samples should be taken from incised streams near the mountain front.

The bottom of Shakwak trench is dominated by broad fans that are aggrading onto the gently-sloped valley sides and floor of the trench. Along the western side of Kluane Lake the dominant surficial materials are fluvial fan sediments and till. Till is more prevalent north of Destruction Bay and in the Burwash Landing area where linear glacial landforms (drumlins and flutes) dominate the landscape. Loess is ubiquitous in broad valley bottoms but is rarely thicker than 50 cm. South of Kluane Lake, ice stagnation topography dominates the landscape (hummocks, discontinuous ridges and kettle lakes). Sediment in this part of the trench comprises thick glaciofluvial and glaciolacustrine deposits with minor till. Streamlined features and thick till deposits suggest significant transport of surficial materials in valley bottom settings like Shakwak trench. Shakwak trench is a poor setting for geochemical sampling and samples should be taken in incised streams near the mountain front.

Geohazards

Permafrost

Permafrost is widespread but discontinuous in the central Kluane Ranges. It is most common on slopes with northeastern and northern aspects and on lower slopes or in valley bottoms. The distribution of permafrost varies widely as does its character (depth, thickness and ice content) based on topography, texture of surficial materials and surface cover. Solifluction lobes, revegetated active layer detachment landslide scars, tilting trees (drunken forest) and thermokarst thaw

ponds in the Burwash lowlands are good indicators that permafrost is present. Permafrost is also found in test pits dug where none of these features existed. Permafrost was commonly found 40–50 cm deep, but depths of 10–20 cm occurred where insulating vegetative cover exceeds 10 cm thick. Permafrost was found in a variety of different material types such as fluvial, course and fine-grained colluvium, fibric organics and tephra. Active layer detachment slides are common on the steep slopes in the study area, and are the result of saturated conditions at the bottom of the active layer.

Landslides

This region is characterized by steep valley walls as a result of rapid uplift and repeat glaciations. Steep slopes and highly fractured bedrock result in widespread slope failures such as debris flows and avalanches, rock avalanches and rock fall (Huscroft *et al.*, 2004; Blais-Stevens *et al.*, 2010). Abundant colluvium, outwash, till, and weathered bedrock are easily remobilized into debris avalanches and flows. Large scale landslides in the region have the potential to dam rivers in valley bottoms. This occurred at Vulcan Creek in 2014 in Kluane National Park (Brideau *et al.*, 2019). Lakes that form behind such dams could cause outburst floods if the landslide dam fails suddenly. Landslide hazards pose a risk to existing and future developments and linear infrastructure if mitigating steps are not taken.

Summary

Preliminary surficial geological mapping in the central Kluane Ranges demonstrates the importance of topography in the distribution of surficial materials. Distribution patterns of surficial materials are similar across the mapping area at high elevations. At lower elevations and in valley bottoms, there is variation between the narrow bedrock-controlled valleys of the central Kluane Ranges, the broader semi-confined floodplains of the Duke River and Ä'äy Chù valleys, and the broad Shakwak trench. Introduction of loess can provide additional complexities for soil sampling programs and care needs to be taken to avoid sampling loess where possible. Cryoturbation results in mixing of materials and it is important to recognize its distribution and intensity for accurate and effective analysis of soil geochemical exploration data. The character and distribution of permafrost is affected by slope, aspect, topography and surficial material texture. Permafrost is most common on slopes with north to northeast aspects and in valley bottoms and an average depth of 40–50 cm in the map area. Future infrastructure projects will need to understand the distribution and character of permafrost to avoid instability during and after construction.

Acknowledgments

Funding for this project was provided by Yukon Geological Survey, an NSERC discovery grant to B. Ward, and the Northern Scientific Training Program. Special thanks to Kenya Franz for all the amazing help in the field, Icefield Discovery for providing wonderful accommodations, and Kluane First Nation for supporting our work in their Traditional Territory. Finally, thanks to Derek Cronmiller for completing a thorough review of this paper and providing valuable insights and suggestions on improving the manuscript.

References

Blais-Stevens, A., Couture, R. and Page A., 2010. Landslide inventory along the Alaska Highway Corridor. Geological Survey of Canada, Open File 6654, DVD.

Bond, J.D. and van Loon, S. 2018. Yukon Placer Mining Industry 2015-2017. Yukon Geological Survey, 296 p.

Brideau, M.-A., Shugar, D.H., Bevington, A.R., Willis, M.J. and Wong, C., 2019. Evolution of the 2014 Vulcan Creek landslide-dammed lake, Yukon, Canada, using field and remote survey techniques. Landslides, vol. 16, p. 1823–1840, doi:10.1007/s10346-019-01199-3.

Clague, J.J., Luckman, B.H., Van Dorp, R.D., Gilbert, R., Froese, D., Jensen, B.J.L. and Reyes, A.V., 2006. Rapid changes in the level of Kluane Lake in Yukon Territory over the last millennium. Quaternary Research, vol. 66, p. 342–355, doi:10.1016/j.yqres.2006.06.005.

Colpron, M., Israel, S., Murphy, D., Pigage, L. and Moynihan, D., 2016. Yukon bedrock geology map. Yukon Geological Survey, Open File 2016-1, scale 1:1000000, map and legend.

Cronmiller, D. 2019. Surficial Geology, Stratigraphy, and Placer Deposits of the Ruby Range, Yukon Territory. Unpublished MSc/Phd ? thesis, Simon Fraser University, Burnaby, BC.

Denton, G.H. and Stuiver, M., 1967. Late Pleistocene Glacial Stratigraphy and Chronology, Northeastern St Elias Mountains, Yukon Territory, Canada. GSA Bulletin, vol. 78, p. 485–510, doi:10.1130/0016-7606(1967)78[485:LPGSAC]2.0.CO;2.

Duk-Rodkin, A., 1999. Glacial limits map of Yukon Territory. Exploration and Geological Services Division, Yukon Region, Indian and Northern Affairs Canada, Geoscience Map 1999-2..

Foster, G.L., Lunt, D.J. and Parrish, R.R., 2010. Mountain uplift and the glaciation of North America – a sensitivity study. Climate of the Past, vol. 6, p. 707–717, doi:10.5194/cp-6-707-2010.

Greene, A.R., Scoates, J.S. and Weis, D., 2004. Flood basalts of the Wrangellia Terrane, southwest Yukon: Implications for the formation of oceanic plateaus, continental crust and Ni-Cu-PGE mineralization. In: Yukon Exploration and Geology 2004, D.S. Emond, L.L. Lewis and G.D. Bradshaw (eds.), Yukon Geological Survey, p. 109–120. .

Howes, D.E. and Kenk, E., 1997. Terrain Classification System for British Columbia (Version 2). Recreational Fisheries Branch, Ministry of Environment and Surveys and Resource Mapping Branch, Ministry of Crown Lands, Province of British Columbia, Victoria, BC.

Hughes, O.L., Campbell, R.B., Muller, J.E. and Wheeler, J.O., 1969. Glacial limits and flow patterns, Yukon Territory south of 65 degrees north latitude. Geological Survey of Canada, Paper, 68–34, 9 p. and 1 map, scale 1:1000000, doi:10.4095/104733.

Huscroft, C.A., Lipovsky, P.S. and Bond, J.D., 2004. A regional characterization of landslides in the Alaska Highway corridor, Yukon. Yukon Geological Survey, Open File 2004-18.

Israel, S. and Cobbett, R., 2008. Kluane Ranges bedrock geology, White River area (Parts of NTS 115F/9, 15 and 16; 115G/12 and 115K/1, 2). *In:* Yukon Exploration and Geology 2007, D.S. Emond, L.R. Blackburn, R.P. Hill and L.H. Weston (eds.), Yukon Geological Survey, p. 153–167.

Israel, S., Murphy, D., Bennett, V., Mortensen, J. and Crowley, J., 2010. New insights into the geology and mineral potential of the Coast Belt in southwestern Yukon. *In:* Yukon Exploration and Geology 2010, K.E. MacFarlane, L.H. Weston and C. Relf (eds.), Yukon Geological Survey, p. 101–123.

Israel, S., Tizzard, A. and Major, J., 2006. Bedrock geology of the Duke River area, parts of NTS 115G/2, 3, 4, 6 and 7, southwestern Yukon. *In:* Yukon Exploration and Geology 2005, D.S. Emond, G.D. Bradshaw, L.L. Lewis and L.H. Weston (eds.), Yukon Geological Survey, p. 139–154.

Jackson, L., Ward, B., Duk-Rodkin, A. and Hughes, O., 1991. The Last Cordilleran Ice Sheet in Southern Yukon Territory. Géographie physique et Quaternaire, vol. 45, p. 341–354, doi:https://doi.org/10.7202/032880ar.

Jensen, B.J.L., Pyne-O'Donnell, S., Plunkett, G., Froese, D.G., Hughes, P.D.M., Sigl, M., McConnell, J.R., Amesbury, M.J., Blackwell, P.G., van den Bogaard, C., Buck, C.E., Charman, D.J., Clague, J.J., Hall, V.A., Koch, J., Mackay, H., Mallon, G., McColl, L. and Pilcher, J.R., 2014. Transatlantic distribution of the Alaskan White River Ash. Geology, vol. 42, p. 875–878, doi:10.1130/G35945.1.

Kennedy, K.E. and Ellis, S.E., 2020. Surficial geology of the northern Kluane Ranges (parts of NTS 115G/5, 6, 11, 12). Yukon Geological Survey, Open File 2020-5, 4 sheets, scale 1:50 000.

Kennedy, K.E. and van Loon, S. 2017. Preliminary investigations of placer gold settings in Arch Creek, Kluane district, southwestern Yukon. In: Yukon Exploration and Geology 2016, K.E. MacFarlane and L.H. Weston (eds.), Yukon Geological Survey, p. 103–115.

Lowdon, J.A., Wilmeth, R. and Blake, W. Jr., 1970. Geological Survey of Canada Radiocarbon Dates X. Geological Survey of Canada, Paper 70-2, 14 p.

Rampton, V., 1971. Late Pleistocene Glaciations of the Snag-Klutlan Area, Yukon Territory. ARCTIC, vol. 24, p. 277–300, doi:10.14430/arctic3142.

Turner, D.G., 2014. Pleistocene stratigraphy, glacial limits and paleoenvironments of White River and Silver Creek, southwest Yukon. Unpublished PhD thesis, Simon Fraser University, British Columbia, 140 p.

Turner, D.G., Ward, B.C., Froese, D.G., Lamothe, M., Bond, J.D. and Bigelow, N.H., 2016. Stratigraphy of Pleistocene glaciations in the St Elias Mountains, southwest Yukon, Canada. Boreas, vol. 45, p. 521–536, doi:10.1111/bor.12172.

Ward, B.C., Bond, J.D. and Gosse, J.C., 2007. Evidence for a 55–50 ka (early Wisconsin) glaciation of the Cordilleran ice sheet, Yukon Territory, Canada. Quaternary Research, vol. 68, p. 141–150, doi:10.1016/j.yqres.2007.04.002.

Yukon Geological Survey, 2020. Terrain Classification System Summary. *In:* Surficial data set. Yukon Geological Survey, http://data.geology.gov.yk.ca/Compilation/33#InfoTab, [accessed October, 2020].

Yukon Geological Survey

Yukon Geological Survey staff are located in two buildings in Whitehorse: the Elijah Smith Building at 300 Main Street, room 102, and the H.S. Bostock Core Library at Mile 918 on the Alaska Highway.

Branch Director

H.S. Bostock Core Library

Relf, Carolyn – Director, (867) 667–8892 carolyn.relf@yukon.ca

Operations

H.S. Bostock Core Library

Minor, Julie – Manager, Finance & Operations, (867) 667–8508 julie.minor@yukon.ca

Outreach

H.S. Bostock Core Library

Weston, Leyla – Outreach Geologist, (867) 393–7187 leyla.weston@yukon.ca

Regional Geology

H.S. Bostock Core Library

Colpron, Maurice – Head, Regional Geology, (867) 667–8235 maurice.colpron@yukon.ca
Ambrose, Tyler – Project Geologist, (867) 667–5175 tyler.ambrose@yukon.ca
Cobbett, Rosie – Project Geologist, (867) 455–2802 rosie.cobbett@yukon.ca
Moynihan, David – Project Geologist, (867) 455–2805 david.moynihan@yukon.ca
Skipton, Diane – Project Geologist, (867) 667–5175 diane.skipton@yukon.ca

Surficial Geology

Elijah Smith Building

Bond, Jeffrey – Head, Surficial Geology, (867) 667–8514 jeff.bond@yukon.ca
van Loon, Sydney – Placer Geologist, (867) 667–3408 sydney.vanloon@yukon.ca

H.S. Bostock Core Library

Kennedy, Kristen – Surficial Geologist, (867) 393–7188 kristen.kennedy@yukon.ca
Lipovsky, Panya – Surficial Geologist, (867) 667–8520 panya.lipovsky@yukon.ca

Minerals Geology

Elijah Smith Building

Casselman, Scott – Head, Minerals Geology, (867) 667–8192 scott.casselman@yukon.ca
Lewis, Lara – Economic Geologist, (867) 667–8518 lara.lewis@yukon.ca
Torgerson, Derek – Yukon Mineral Exploration Program, (867) 456–3828 derek.torgerson@yukon.ca
Eriks, Nicole – Economic Geologist, (867) 332–6040 nicole.eriks@yukon.ca

H.S. Bostock Core Library

Emberley, Justin – Core Library Manager, (867) 393–6492 justin.emberley@yukon.ca
Sack, Patrick – Metallogenist, (867) 667–3203 patrick.sack@yukon.ca

Editorial & Technical Services

Elijah Smith Building

MacFarlane, Karen – Head, Technical Services, (867) 667–8519 karen.macfarlane@yukon.ca
Elliot, Brett – Geological Spatial Database Administrator, (867) 667–8481 brett.elliot@yukon.ca
Staffen, Bailey – GIS Technician/Web Manager, (867) 456–6801 bailey.staffen@yukon.ca

Yukon Geological Survey
Energy, Mines and Resources
Government of Yukon